

**Local Site Effects in Archaeoseismology: Examples from the
Mycenaean Citadels of Tiryns and Midea (Argive Basin,
Peloponnese, Greece)**

Inaugural-Dissertation

zur

Erlangung des Doktorgrades

der Mathematisch-Naturwissenschaftlichen Fakultät

der Universität zu Köln



vorgelegt von

Héctor Roberto Hinojosa Prieto

aus Hermosillo, Sonora, Mexiko

Berichterstatter: Prof. Dr. K.-G. Hinzen

Prof. Dr. M. Melles

Tag der letzten mündlichen Prüfung: 18.01.2016

Abstract

The archaeological community has gained knowledge on how to document and diagnose damage by earthquake shaking to ancient man-made structures and how to estimate the intensity of past earthquakes, but has paid little attention to local site effects and its implications for the dynamic response of those structures. Qualitative studies of damage by earthquakes to ancient constructions surpass the amount of research on local site effects in the archaeoseismological literature. Yet, archaeoseismic observations are often based on a limited part of the mesoseismal area, on loosely constrained dated events, and sometimes on ambiguous evidence of earthquake damage. This mix of factors may lead to imprecise estimates of the size of past earthquakes and/or unrealistic earthquake environmental impacts if local site effects are ignored or over/undervalued. Hence, it is important not to rely solely on intensities based on archaeologically documented coseismic damage without a quantitative estimate of local site effects.

The present multidisciplinary study focuses on the Mycenaean citadels of Tiryns and Midea located in the Argive Basin (Peloponnese, Greece). The study is a key contribution to archaeoseismology because it provides a quantitative and deterministic method for estimating ancient local site effects and seismic hazard at an archaeological site. The proposed method permits the calculation of site-specific ground-motions, which are transformable into intensity values. The method requires input from archaeological, geoarchaeological, geophysical, geological, geotechnical, and historical studies. The over-or-underestimation of local site effects is minimized by removing accrued soils younger than the ancient walking horizon of interest. The method is applicable to archaeological sites worldwide with clear or unclear evidence of ancient earthquake damage, is scalable to any area size, and can help to decide on the location of new excavations targeting earthquake damage. The estimation of local site effects is carried out by computing synthetic seismograms for a reference rock-site located at each citadel, which are then used to accelerate regolith models for calculating surface amplification factors and related ground-motions. Earthquake source parameters of the hypothetical earthquakes are constrained from a seismotectonic model of the area. This study shows how to estimate ancient local site effects to test the Mycenaean earthquake hypothesis, which is based solely on archaeological and geomorphological field observations. The hypothesis suggests repeated earthquake damage to the Cyclopean fortification walls and enclosed buildings of Tiryns, Midea, and Mycenae during the end of the Late Bronze Age (LBA). The hypothesis has lacked evidence of written records of ancient earthquakes and of a town-wide devastation pattern; has left unexplained the strength and location of the potential causative earthquake(s); and has ignored the impact of local site effects. The results of the present study reveal new findings: the Tiryns and Midea citadels settled on weathered hard limestone while the outer constructions settled on cohesive-or-granular soils with variable shear strength and seismic site class categories corresponding to a lower and higher seismic hazard, respectively. Data from two field campaigns during the project coupled with available upfront information from the geophysical, geological, and geotechnical literature and

developed subsurface models show that the LBA ground conditions outside the fortification walls had a higher hazard than inside the walls, but archaeological findings do not reflect this. Active seismic sources at a distance greater than 40 km play a minor role. Local seismic sources in the Argolis are however critical, but are not confirmed seismically active. These findings weaken the plausibility of the Mycenaean earthquake hypothesis for Tiryns and Midea.

Zusammenfassung

In der Archäologie beschäftigten sich in den letzten Jahrzehnten eine ganze Reihe von Arbeiten mit der Dokumentation und Analyse potentieller Erdbebenschäden an archäologischen Befunden. Dabei wurden aber lokale seismische Standorteffekte kaum oder gar nicht berücksichtigt, obwohl diese im Hinblick auf Erdbebenschäden an bestehenden und antiken Bauwerken eine wichtige Rolle spielen. Qualitative Studien von Erdbebenschäden sind in diesem Bereich deutlich häufiger als quantitative Betrachtungen. Archäoseismologische Studien basieren häufig auf kleinräumigen Untersuchungen innerhalb der mesoseismischen Zone von Erdbeben und auf nur schwer zu datierenden Schadensbildern, die zudem nicht immer eindeutig seismogenen Ursprungs sind. Diese Ausgangslage kann mitunter zu fehlerbehafteten Abschätzungen der Stärke prähistorischer Erdbeben führen, besonders, wenn die lokalen Standorteffekte unberücksichtigt bleiben.

In dieser multidisziplinären Studie wird eine quantitative deterministische Methode entwickelt, um seismische Standorteffekte in archäoseismischen Untersuchungen zu berücksichtigen. Dabei werden standortspezifische Seismogramme simuliert, die es gestatten, die Intensität der Bodenbewegungen zur Zeit des potentiellen Erdbebenschadens abzuschätzen. Es werden neben archäologischen Daten geoarchäologische, geophysikalische, geologische und geotechnische Untersuchungen berücksichtigt. Zur Abschätzung realistischer Standorteffekte müssen Bodenschichten, die nach Eintritt des Schadens akkumuliert sind, im Modell entfernt werden. Die Methode kann auf unterschiedlichste archäologische Stätten angewandt werden und wird hier am Beispiel des mykenischen Palastes von Tiryns und der Akropolis von Midea in der Argolis, Peloponnes (Griechenland) entwickelt. Basierend auf archäologischen und einigen geomorphologischen Beobachtungen wurde vor mehr als 20 Jahren die Hypothese entwickelt, dass beide Zitadellen am Ende der späten Bronzezeit durch mehrfache Erdbebeneinwirkung zerstört wurden. Bauwerksschäden wurden dabei nur an Bauten innerhalb der kyklopischen Befestigungsmauern beider Zitadellen gefunden, aber bisher nicht an Bauten außerhalb, wie etwa der ausgedehnten Unterstadt von Tiryns. Ausgehend von eigenen, während zweier Feldkampagnen vor Ort erfassten und der Literatur entnommenen geophysikalischen, geologischen und geotechnischen Daten wurden Untergrundmodelle entwickelt, die zeigen, dass zur späten Bronzezeit auf Grund der lokalen Untergrundverhältnisse die seismische Gefährdung außerhalb der Befestigungsmauern deutlich höher lag als innerhalb, was sich aber so nicht in den archäologischen Befunden widerspiegelt. Seismische Quellen in Entfernungen größer als 40 km spielen dabei eine untergeordnete Rolle. Die lokalen Störungen der Argolis sind hingegen nicht gesichert als seismisch aktive Störungen zu betrachten, was die Plausibilität der Erdbebenhypothese im Hinblick auf Tiryns und Midea weiter schwächt.

Acknowledgements

I am greatly thankful to Prof. Dr. Klaus-G. Hinzen for giving me the opportunity to explore the exciting field of archaeoseismology during the HERACLES project. I am fortunate to have had him as my academic advisor. Many aspects of his supervision have made of my doctoral course my invaluable learning experience: his contagious interest in archaeoseismology, the willingness to share his extensive seismological knowledge, his keen eye for investigating interesting questions that gradually evolve into research topics, his openness and availability to engage in scientific and non-scientific discussions, and his patience and commitment to teach.

I am grateful to the Fritz Thyssen Foundation (Az. 10.11.2.39) and Gerda Henkel Foundation (AZ 25/F/11) for funding the HERACLES project; to Dr. Alkestis Papadimitriou (4th Ephorate of Prehistoric and Classical Antiquities, Nafplion) for permitting field work in the Argive Basin (Peloponnese, Greece); to Prof. Dr. Joseph Maran, Dr. Ursula Damm-Meinhardt, and Susanne Prillwitz for discussions about Mycenaean archaeology and for logistic support. I thank Prof. Dr. Martin Melles for participating as committee member and Prof. Dr. Bülent Tezkan for chairing the committee. I am also grateful to my wife, whose love, patience, and support were important towards reaching my goals. I thank GeoFact GmbH and FH Oldenburg for lending the horizontal geophones and GPS unit, respectively; to Dr. Eberhard Zangger for sharing the Greek borehole data; to the Institute of Geophysics and Meteorology of Cologne University for lending the seismic equipment; to R. Robl and group at the mechanical workshop of our institute for making the shear-wave aluminum source. I am very thankful to my colleagues Gregor Schweppe, Claus Fleischer, Dr. Sharon K. Reamer, Klaus Weber, Jana Tzislakis, Tatiana Kalytta, and Iris Schwellenbach for their kind support during both the field campaign and my stay at the Bensberg Seismological Station, all helped in one or another way. The participation of Dr. Pantelis Soupios is appreciated, who acquired and processed the TEM data, as well as the involvement of Prof. Dr. Bülent Tezkan and his student Nadine Haaf, who processed the TEM data set in the framework of a Master thesis project. I also thank Dr. Eleni E. Karagianni for sharing the velocity data of the Aegean region.

Table of contents

1	INTRODUCTION	1
1.1	Archaeoseismology.....	1
1.2	Background of the Mycenaean Civilization and the Earthquake hypothesis.....	4
1.2.1	The Mycenaean Civilization.....	4
1.2.2	The Mycenaean Earthquake Hypothesis.....	8
1.3	Local Site Effects in an Archaeoseismological Context.....	10
1.3.1	Overview of Local Site Effects.....	10
1.3.2	Importance of Local Site Effects in Archaeoseismic Research.....	13
1.4	Objective of the Research.....	15
1.5	Organization of the Dissertation.....	16
2	SETTING, GEOARCHAEOLOGY AND ARCHAEOSEISMOLOGY IN TIRYNS AND MIDEA	17
2.1	Setting of Tiryns and Midea.....	17
2.1.1	Tiryns.....	17
2.1.2	Midea.....	22
2.2	Geoarchaeological Perspective.....	25
2.3	Archaeoseismology: State of the Art.....	28
2.3.1	Postulated Evidence of Earthquake-Related Structural Damage to Tiryns and Midea...28	
2.3.2	Previous Examination of the Mycenaean Earthquake Hypothesis.....	34
3	GEOLOGICAL SETTING AND SEISMICITY OF THE ARGIVE BASIN	37
3.1	Geology.....	37
3.1.1	Near-Surface Geology at Tiryns and Midea.....	45

3.2	Seismicity.....	50
4	DYNAMIC PROPERTIES OF SOILS AND BEDROCK AT TIRYNS AND MIDEA AND GEOTECHNICAL PROFILES.....	57
4.1	Geotechnical Investigations.....	57
4.1.1	Previous Work.....	57
4.1.2	New Laboratory Tests.....	58
4.2	Geophysical Investigations.....	58
4.2.1	Previous Work.....	58
4.2.2	Seismic Refraction Tomography (SRT) Survey.....	64
4.2.3	Transient Electromagnetic Soundings.....	73
4.2.3.1	1D TEM Data Acquisition and Processing.....	74
4.2.3.2	Results and Interpretations of the 1D TEM survey.....	76
4.3	Geotechnical Profiles and Dynamic Properties of Soils and Bedrock	78
5	SYNTHETIC EARTHQUAKE RECORDS FOR NUMERICAL MODELING OF LOCAL SITE EFFECTS.....	82
5.1	Seismotectonic Model and Finite-Fault Models.....	84
5.1.1	Normal Faults in the Argive Basin and Patras–Corinth Continental Rift.....	84
5.1.2	Strike-Slip Faults in the Iria–Epidaurus Sinistral Transform fault system.....	87
5.1.3	Reverse Faults in the Hellenic Subduction Zone.....	88
5.1.4	Analytic Signal.....	89
5.2	Input Parameters of Numerical Modeling Methods.....	90
5.2.1	Shear-Wave Velocity Structure.....	91
5.2.2	Duration Model.....	94

5.2.3	The Kappa Parameter.....	96
5.2.4	Stress Drop ($\Delta\sigma$).....	97
5.2.5	Crustal Attenuation (<i>Q-factor</i>).....	97
5.3	Validation Model.....	101
5.4	Application of the Stochastic and the Green’s Function Methods: synthetic seismograms as input for acceleration.....	102
5.4.1	Normal Faulting Earthquakes in the Argive Basin.....	105
5.4.2	Normal Faulting Earthquakes in the Patras–Corinth Continental Rift.....	112
5.4.3	Strike-Slip Faulting Earthquakes in the Iria–Epidauros Sinistral Transform fault system.....	116
5.4.4	Reverse Faulting Earthquakes in the Hellenic Subduction Zone.....	118
6	FORWARD MODELING OF LOCAL SITE EFFECTS AT TIRYNS AND MIDEA.....	123
6.1	Dynamic Loading of Ground Surface.....	123
6.2	1D Forward Modeling of Local Site Effects with the Equivalent–Linear Model.....	125
6.2.1	Results and Interpretation.....	133
6.2.1.1	Variability of Amplification Factors.....	133
6.2.1.2	Estimated Surface Ground-motions and Intensity Values.....	138
7	DISCUSSION.....	150
7.1	The Role of Local Site Effects in the Mycenaean Earthquake Hypothesis Testing	150
7.1.1	Site Amplification and Surface Ground-Motions.....	150
7.1.2	Seismic Response of Mycenaean Structures.....	152
7.2	Can Earthquake Environmental and Archaeological Effects Be Assessed in the Argive Basin?.....	154

7.3	Criteria for Modeling Local Site Effects in Archaeoseismology.....	155
8	CONCLUSION AND RECOMMENDATIONS.....	158
	REFERENCES.....	163
	ONLINE RESOURCES.....	188
	APPENDIXES.....	189
	Appendix A.....	189
	Appendix B.....	190
	Appendix C.....	201
	Appendix D.....	209
	Appendix E.....	214
	ERKLÄRUNG.....	227
	LEBENS LAUF.....	228

List of Figures

- Figure 1.1 Examples of possible earthquake effects on ancient man-made structures.
- Figure 1.2 Schematic workflow of quantitative archaeoseismic modeling.
- Figure 1.3 Map of the Aegean Sea region showing Mycenaean sites.
- Figure 1.4 Distribution of shallow drill cores near Tiryns and coastline reconstruction.
- Figure 1.5 Schematic representation of the seismic wave refraction processes.
- Figure 1.6 Conceptualized models of geomorphologic groups for local site response.
- Figure 1.7 Conceptualized geomorphologic model of Tiryns and Midea.
- Figure 2.1 Digital Elevation Model and elevation profile of the Argive Basin.
- Figure 2.2 Terrain slope map of the Tiryns hill and vicinity.
- Figure 2.3 Panoramic views of Tiryns and geoarchaeological cross-sections.
- Figure 2.4 Archaeological plan of Tiryns superimposed on the bedrock elevation map.
- Figure 2.5 Archaeological plan of Midea superimposed on the surface topography map.
- Figure 2.6 Terrain slope map of the Midea hill and vicinity.
- Figure 2.7 Reconstructed paleocoastlines, ancient Lake Lerna deposits, and distribution of boreholes of the Greek Service of Land Improvement (GSLI).
- Figure 2.8 The floruit phases of painted pottery at Tiryns in relation to percent of building destructions.
- Figure 2.9 Current situation of the Cyclopean walls of Tiryns and Midea.
- Figure 2.10 Standard Spectral Ratios and Horizontal-Vertical Spectral Ratios for Tiryns and Midea.
- Figure 3.1 Simplified geologic map of the Argive Basin.
- Figure 3.2 Composite lithostratigraphic column of the Argive Basin.
- Figure 3.3 Map of shallow and deep geologic boreholes in the Argive Basin.

- Figure 3.4 Explained deep geologic boreholes in the Argive Basin.
- Figure 3.5 Detail geologic map of the eastern Argive Basin.
- Figure 3.6 Geologic profile illustrating the geometry of the cohesive and granular soils and the bedrock structure between Tiryns and Midea.
- Figure 3.7 Field structural geologic data of the Tiryns hill (bedrock).
- Figure 3.8 Representative stratigraphic column of Tiryns and Midea.
- Figure 3.9 Simplified structural geologic map and cross-section of the Midea ridge.
- Figure 3.10 Neotectonic map of the Peloponnese, Greece, showing the distribution of active faults, and both historical and instrumentally recorded earthquakes.
- Figure 3.11 Neotectonic setting of the Argive Basin–Argolic Gulf half-graben.
- Figure 4.1 Geophysical surveys in the Argive Basin and Argolic Gulf.
- Figure 4.2 Previous onshore geophysical surveys near the Tiryns citadel.
- Figure 4.3 Geophysical surveys at Tiryns superimposed on the archaeological plan.
- Figure 4.4 Computed v_{s30} map of the Argive Basin using the Wald and Allen (2007) method.
- Figure 4.5 Computed v_{s30} map of Tiryns and Midea using the Stewart et al. (2104) method.
- Figure 4.6 Deployment of seismic refraction tomography survey at Tiryns.
- Figure 4.7 Three-dimensional view of the v_p and v_s tomograms deployed at Tiryns.
- Figure 4.8 Two-dimensional v_p structure models of Tiryns.
- Figure 4.9 Two-dimensional v_s structure models of Tiryns.
- Figure 4.10 Resulting Poisson ratio (ν) plots of Tiryns.
- Figure 4.11 Resulting v_p/v_s ratio plots of Tiryns.
- Figure 4.12 TEM deployment in the Argive Basin.
- Figure 4.13 Distribution of 1D TEM stations in the Argive Basin.

- Figure 4.14 Final 1D TEM inverted models.
- Figure 4.15 Geotechnical profiles at Tiryns.
- Figure 4.16 Geotechnical profiles at Midea.
- Figure 4.17 Geotechnical profile of the area between Tiryns and Midea.
- Figure 5.1 Active normal faulting in the Argive Basin and eastern Gulf of Corinth.
- Figure 5.2 Active strike-slip faults in the Iria–Epidauros Sinistral Transform fault system.
- Figure 5.3 Active compressional faults in the Hellenic Subduction Zone.
- Figure 5.4 Analytic signal used a synthetic input source in this study.
- Figure 5.5 Shear-wave velocity model of the Aegean continental crust.
- Figure 5.6 1D models of v_s , v_p , and density adopted in this study.
- Figure 5.7 Path duration models adopted in this study.
- Figure 5.8 Adopted 1D Q_s and Q_p model used in the Green's Function approach.
- Figure 5.9 Maps of the Aegean Moho.
- Figure 5.10 Validation example of the 06/12/2012 local earthquake M_w 4.3.
- Figure 5.11 Summary of all estimated maximum horizontal PGA values.
- Figure 5.12 Summary of all estimated intensity values.
- Figure 5.13 Stochastically simulated seismograms of some local extensional earthquakes.
- Figure 5.14 Acceleration response spectra for reference station at Tiryns and Midea.
- Figure 5.15 Three-Component synthetic accelerogram of reference station at Tiryns and Midea.
- Figure 5.16 Three-Component synthetic velocity seismograms of reference station at Tiryns and Midea.
- Figure 5.17 Three-Component synthetic displacement seismograms of reference station at Tiryns and Midea.

- Figure 5.18 Stochastically simulated horizontal accelerograms of the Xylokaastro normal faults with reference station at Tiryns and Midea.
- Figure 5.19 Three-Component synthetic acceleration seismograms of the three Xylokaastro normal fault scenarios with reference station at Tiryns and Midea simulated with the Green's Function method.
- Figure 5.20 Three-Component synthetic velocity seismograms of the three Xylokaastro normal fault scenarios with reference station at Tiryns and Midea simulated with the Green's Function method.
- Figure 5.21 Three-Component synthetic displacement seismograms of the three Xylokaastro normal fault scenarios with reference station at Tiryns and Midea simulated with the Green's Function method.
- Figure 5.22 Stochastically simulated horizontal accelerograms of strike-slip faults in the Iria–Epidauros Sinistral Transform fault system with reference station at Tiryns and Midea.
- Figure 5.23 Three-Component synthetic acceleration seismograms of the Iria–Epidauros1 strike-slip fault with reference station at Tiryns and Midea simulated with the Green's Function method.
- Figure 5.24 Three-Component synthetic velocity seismograms of the Iria–Epidauros1 strike-slip fault with reference station at Tiryns and Midea simulated with the Green's Function method.
- Figure 5.25 Three-Component synthetic displacement seismograms of the Iria–Epidauros1 strike-slip fault with reference station at Tiryns and Midea simulated with the Green's Function method.
- Figure 5.26 Example of stochastically simulated horizontal acceleration seismograms of an interface and an intraplate compressional earthquake of the Hellenic Subduction Zone with reference station at Tiryns and Midea.
- Figure 5.27 Three-Component synthetic acceleration seismograms of an interface and an intraplate compressional earthquake of the Hellenic Subduction Zone with reference station at Tiryns and Midea simulated with the Green's Function method.
- Figure 5.28 Three-Component synthetic velocity seismograms of an interface and an intraplate compressional earthquake of the Hellenic Subduction Zone with

reference station at Tiryns and Midea simulated with the Green's Function method.

Figure 5.29 Three-Component synthetic displacement seismograms of an interface and an intraplate compressional earthquake of the Hellenic Subduction Zone with reference station at Tiryns and Midea simulated with the Green's Function method.

Figure 6.1 Selected shear modulus and damping ratio curves for soils and bedrock.

Figure 6.2 Seismic microzonation at Mycenaean Tiryns.

Figure 6.3 Seismic microzonation at Mycenaean Midea.

Figure 6.4 Seismic microzonation along the Tiryns-Midea profile.

Figure 6.5 Workflow of 1D forward modeling of local site effects in archaeoseismology.

Figure 6.6 Examples of site-specific 1D Equivalent-Linear response analysis modeled with input accelerograms computed with the Stochastic and the Green's Function methods and both 1D average and gradient v_s models.

Figure 6.7 Summary of calculated surface amplification factor for all modeling sites using input accelerograms computed with the Green's Function approach.

Figure 6.8 Summary of maximum surface acceleration values for all modeling sites using input accelerograms computed with the Green's Function approach.

Figure 6.9 Summary of resulting surface ground-motions for all modeling sites using input accelerograms computed with the Green's Function approach.

Figure 6.10 Calculated surface acceleration time histories using a 1D average v_s model and input accelerograms computed with the Green's Function approach.

Figure 6.11 Calculated surface acceleration time histories using a 1D gradient v_s model and input accelerograms computed with the Green's Function approach.

Figure 6.12 Summary of intensity values using the average and gradient v_s models and input accelerograms computed with the Green's Function approach.

List of Tables

- Table 1.1 Chronological chart of the Late Helladic period.
- Table 1.2 Some well-documented damaging earthquakes with observable site effects.
- Table 2.1 Summary of Late Bronze Age stratigraphic archaeological data.
- Table 3.1 Unified Soil Classification System (USCS) chart.
- Table 3.2 Summary of estimated earthquake hazard and ground motion parameters for the Argive Basin (Peloponnese, Greece).
- Table 3.3 Seismic hazard level and expected Peak Ground Acceleration for the Argive Basin, Tiryns, and Midea.
- Table 5.1 Alternative procedures for estimating earthquake-induced ground motion.
- Table 5.2 Criteria to define normal faults traces in the Argive Basin.
- Table 5.3 Seismic fault parameters of 12 assumed earthquakes on normal faults in the Argive Basin and Patras–Corinth Continental Rift.
- Table 5.4 Seismic fault parameters of 6 assumed strike-slip earthquakes in the Iria–Epidaurus Sinistral Transform fault system.
- Table 5.5 Seismic fault parameters of 9 assumed compressional earthquakes in the Hellenic Subduction Zone.
- Table 5.6 Path duration models adopted in the stochastic simulation of finite-faults.
- Table 5.7 Available κ values for Greece.
- Table 5.8 Adopted earthquake stress drop values according to seismic source.
- Table 5.9 Available crustal attenuation (Q) values for Greece.
- Table 6.1 Geotechnical site class categories adopted in this study.

1. INTRODUCTION

1.1 Archaeoseismology

Archaeoseismology, also known as earthquake archaeology, is a subdiscipline of seismology that investigates pre-instrumental earthquakes that, by affecting sites of human occupation and their surroundings, have left their physical mark in ancient man-made structures unearthed by archaeological excavations or pertaining to the monumental heritage (Hinzen, 2011). These physical marks, relevant for archaeoseismic research, are occasionally (i) displacements along shear planes directly linked to the earthquake fault plane or its branches; (ii) off-fault-shaking effects including fractured building elements, tilted walls, shift of building elements, lateral distorting, braking and overthrow of walls, rotations of vertically oriented objects; (iii) the secondary shaking effects lateral spreading, mass wasting, and cyclic mobility as a consequence of soil liquefaction; and (iv) archaeologically detected abandonment of a site and evidence of repair and rebuilding. Figure 1.1 shows examples of structural damage documented in various archaeological sites around the world. Sometimes, a number of these seismogenic marks are found either in one or various chronologically stacked destruction horizons so-called *earthquake strata*, a term introduced by British archaeologist Sir Arthur Evans in the 1920's (Evans, 1928). The expressions 'earthquake-indicators' (Karcz and Kafri, 1978), "destruction" layers (Rapp, 1986), and 'earthquake-horizon' (French, 1996) are surrogates of the term *earthquake stratum*. Despite that the archaeological community widely uses the term earthquake stratum; they seem not to have established a systematic methodology for identifying and appraising archaeoseismic damage to man-made objects (Buck, 2006). Archaeological (i.e., coins, inscriptions, characteristic objects, and pottery) and/or historical material generally can assist to date possible seismic events (Ambraseys, 1971; Bottari et al., 2009; Stiros, 2010).

Archaeoseismology brings together the efforts of seismologists, archaeologists earthquake engineers, civil engineers, geologists, geoarchaeologists, architects, and historians (Schreiber et al., 2012; Jusseret, 2014) towards the assessment of archaeoseismic evidence, the expansion of both the pre-instrumental and instrumental earthquake catalogue and the assessment of the seismic hazard of a region (Caputo and Helly, 2008; Bottari et al., 2009; Caputo et al., 2010). Specific questions investigated by archaeoseismology are (i) how probable are seismic ground motions, or secondary earthquake effects, as the cause of damage observed in man-made structures from the past; (ii) when did the damaging ground motion occur, and (iii) what can be deduced about the nature of the causing earthquake (Hinzen, 2011).



Figure 1.1: Examples of deformations and damage which possibly are earthquake effects: (A) Horizontally deformed wall of a crusader fortress build on top of the Dead Sea Transform Fault in the Jordan Valley; (B) deformed vault of a Roman sewer in Cologne, Germany; (C) toppled columns of a Byzantine church in Sussita located above the Sea of Galilee; (D) toppled column of the great palace in Petra, Jordan; (E) moved block in an arch of the Nimrod fortress in the Golan Heights; (F) shifted blocks of an analemma of a Roman theatre in Pinara, SW Turkey; (G) moved blocks of a corner wall of a Roman monument in Patara, SW Turkey; (H) shifted blocks of a Roman grave house in Pinara, SW Turkey; (I) spall of block corners, same object as in (G); (J) broken and horizontally displaced fortification wall of the Roman Tolbiacum (Zülpich, Germany); (K) rotated Lycien sarcophagus in Pinara, SW Turkey. (Photos by Hinzen, 2011).

Archaeoseismology utilizes data and techniques different from those of conventional seismology and earthquake geology, which rely on instrumental and historical records, and structural data, respectively (Bottari et al., 2009). It is challenging to determine the clear cause of structural damage in archaeological records due to the fact that various natural causes might yield similar looking damage patterns and anthropogenic action can also create similar damage or permanent deformation (Nikonov, 1988; Hinzen et al., 2012). Nonetheless, established qualitative archaeoseismic criteria have helped to distinguish seismic-induced

structural damage to ancient structures from other natural and/or anthropogenic causes (Karcz and Kafri, 1978; Rapp, 1986; Stiros, 1996; Ambraseys, 2005; Galadini et al., 2006; Buck, 2006; Marco, 2008; Bottari et al., 2009; Caputo et al., 2010; Hinzen, 2011; Hinzen et al., 2011). Nowadays, excavation-parallel three-dimensional (3D) laser scans accompanied by a quantitative damage analysis allow a fast and accurate identification, classification and quantification of structural damage at a site, and can assist archaeological work during excavation (Schreiber et al., 2012; Hinzen et al., 2010, 2012). Moreover, the 3D surface meshes derived from the same scan data become the basis for numerical models (i.e., Finite or Discrete Element Models) of the both large and small man-made structures such as rooms, aqueducts, wells, walls, and terracotta vessels and figures (Hinzen et al., 2010; Hinzen et al., 2011; Schreiber et al., 2012; Hinzen, 2012; Hinzen et al., 2015).

Archaeoseismic investigations have evolved from a qualitative (i.e., Rapp, 1986; Di vita, 1995; Guidoboni and Bianchi, 1995; Stiros, 1996; Bottari et al., 2009; Rodriguez-Pascua et al., 2011; Sintubin, 2011; Gorduño-Monroy et al., 2012a, 2012b; Jusseret et al., 2013; Stiros and Phytharouli, 2014) to quantitative approach (i.e., Hinzen, 2005; Galadini et al., 2006; Caputo et al., 2010; Tendürüs et al., 2010; Banselam et al., 2010; Hinzen, 2009, 2011; Hinzen et al., 2010, 2011, 2013a, 2015, submitted). The qualitative approach examines the typology of earthquake effects in architectural remains (Stiros, 1996), sometimes including the landscape that surrounds the site (Rodriguez-Pascua et al., 2011). This kind of approach presents advantages and disadvantages. For instance, the criterion of Stiros (1996) identifies earthquake-related structural damage to man-made structures strictly from archaeological data provided the elimination of natural and/or anthropogenic causes; however, the technique leaves unanswered various cases of destruction of architecture and abandonment of the site and it does not account for the effects of co-seismic morphological changes to the ground surface. The criterion of Rodriguez-Pascua et al. (2011) utilizes both the observed “seismic deformation pattern” of the ground surface and the toppled patterns of archaeological artifacts in order to construct a theoretical strain ellipsoid for the archaeological site under investigation, but does not determine the source parameters of the causative fault. So, the major assumptions are that the observed toppled pattern(s) is co-seismic and that the resulting surficial expression of the morphogenic fault has remained unaltered. Then, the systematically derived theoretical strain ellipsoid is compared with the historical-to-present tectonic stress field pattern, active faults or nearby active seismic zones in order to gain a deeper insight of the potential earthquake source(s). Conversely, quantitative archaeoseismic studies of toppled columns strongly suggests that it is not straightforward to deduce a reliable back azimuth toward the earthquake source based on the deformation and toppled patterns of man-made structures (Hinzen, 2009, 2012). Therefore, is not possible to establish a direct link between the orientation of a fallen object and the tectonic stress field of a past earthquake. The method of Rodriguez-Pascua et al. (2011) has rather limited quantitative applicability; so conclusive interpretations derived from their approach should be cautiously considered. Buck (2006) provides a literature review and a thorough examination of the several qualitative methodologies adopted to appraise archaeoseismic damage. She concludes that, when using the universal identification criteria (e.g., “check-list” approach), interpretations of qualitative observations are commonly subjective and with a lack of human

and physical context of the site. Therefore, she proposes a project-specific interdisciplinary approach to objectively assess archaeoseismic damage.

Moreover, the systematically designed quantitative archaeoseismic approaches of Galadini et al. (2006) and Hinzen et al. (2011) test ‘archaeoseismic evidence’ before considering it reliable for quantitative comparison against the observed damage structures. These methods propose an analytical/numerical modeling procedure for a given archaeoseismic project. The approach is to build upon available upfront and/or newly collected geotechnical, geological, geophysical, geoarchaeological, archaeological, and historical data (Figure 1.2). In most cases, newly collected field or laboratory data (e.g., geological, geophysical, and geotechnical) is tailored to answer specific archaeoseismic questions (Hinzen, 2011). Following the quantitative procedure, an archaeoseismic project likely becomes unique in its own way (cf. Buck, 2006). An up-to-date summary of archaeoseismological studies using advanced measuring methods and quantitative numerical modeling is given by Hinzen et al. (2011). Galadini et al. (2006) discuss in detail the methodologies and procedures in archaeoseismological research.

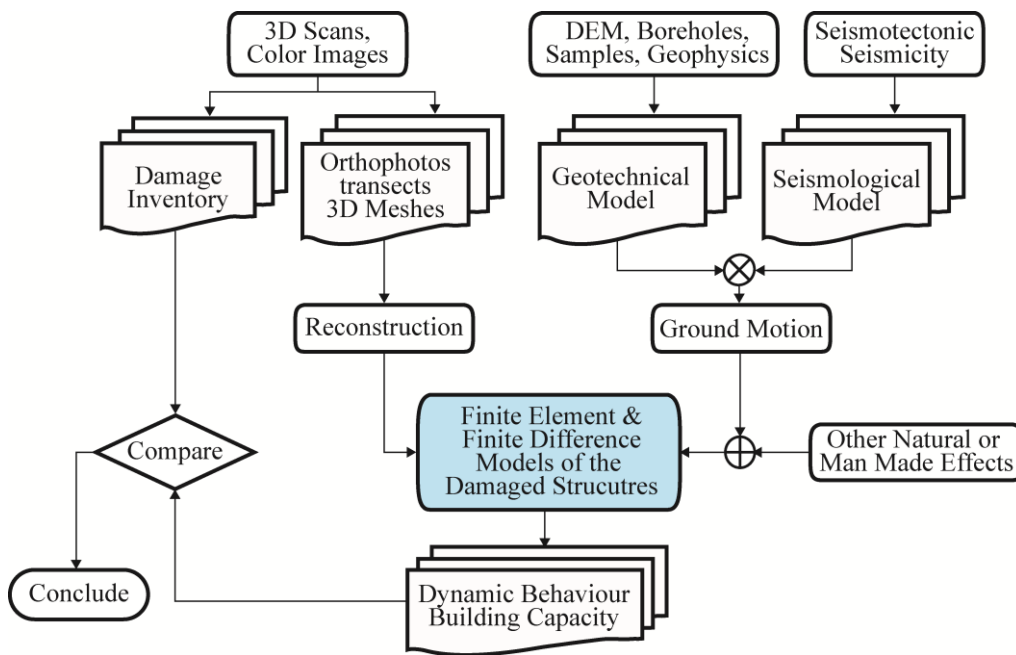


Figure 1.2: Schematic workflow of quantitative archaeoseismic modeling (after Hinzen et al., 2011).

1.2 Background of the Mycenaean Civilization and the Earthquake Hypothesis

1.2.1 The Mycenaean Civilization

The Mycenaean culture is the first “high civilization” in Europe. The term “Mycenaean” derives from the fortified citadel of Mycenae, located in the Argive Basin of the Peloponnese (Greece), which was first excavated during the mid-1870s by the German excavator Heinrich Schliemann (Hemingway and Hemingway, 2000; Spathari, 2001). Several excavations followed after Schliemann lead by British and Greek archaeologists (Klein, 1997; Spathari, 2001). Spathari (2001) narrates the history of the Mycenae Acropolis and gives an overview of the archaeological record. Klein (1997) provides a detail summary of the excavators at

Mycenae. The term “Mycenaean” is also used for the characteristic material culture of the Late Bronze Age (LBA) in parts of ancient Greece, (i.e., on the Peloponnese and parts of the mainland).

The Mycenaean civilization emerged *ca.* 1700/1650 BCE (proto-palatial period) and flourished between *ca.* 1425 to 1200 BCE (palatial period). After the demise of the palaces followed the post-palatial period from *ca.* 1190 to 1050 BCE which eventually led to the disappearance of the characteristic features (Middleton, 2008, 2012; Maran, 2010; Galanakis, 2012). These cultural phases define the Late Helladic (LH) or Mycenaean period. The term “Late Helladic” originally refers to a system of relative chronological dating on the Greek mainland which is based on the development of the Mycenaean painted pottery. Nowadays, it is also commonly used to indicate the date of a site or of other material remains (Table 1.1) (Galanakis, 2012).

Table 1.1: Chronological chart (from Demakopoulou, 2012) with subdivisions of the Late Helladic (LH) period according to ceramic phases (after Galanakis, 2012).

			1100 BCE	
		Late Helladic (LH) IIIC	1200 BCE	Post-palatial period
		Late Helladic (LH) IIIB	1300 BCE	
	Late Bronze Age (LBA)	Late Helladic (LH) IIIA	1400 BCE	Palatial period (Late Mycenaean)
		Late Helladic (LH) IIB	1500 BCE	
Bronze Age		Late Helladic (LH) IIA	1600 BCE	Pre-palatial period (Early Mycenaean)
		Late Helladic (LH) I	1700 BCE	
	Shaft Grave Period		1600–1450 BCE	
	Middle Bronze Age (MBA)	Middle Helladic period	2000–1600 BCE	
	Early Bronze Age (EBA)	Early Helladic period	3200–2000 BCE	
	Neolithic Period		7 th –4 th millennia BCE	

The Mycenaean civilization were bold traders of goods, fierce warriors, and great engineers who designed and built remarkable palaces, tombs, and infrastructure such as roads and dams (Hemingway and Hemingway, 2000). According to Homer (*ca.* 800 BCE), King Agamemnon from Mycenae was leader of the Achaeans (i.e., all Greeks) in their siege of Troja, but this is not a historical fact and therefore cannot be dated precisely (Spathari, 2001). The Mycenaean civilization coexisted and overlapped, respectively, with the two neighboring civilizations on Crete (Minoan Culture) and on the Cyclades (Cycladic Culture), with influences in both ways (Hemingway and Hemingway, 2000).

The collapse of the Mycenaean palaces occurred as a systematic breakdown of socio-political relationships that held ‘palatial’ societies in their own provinces and possibly overseas with predominant powers (Middleton, 2008, 2012). This development, which is heralding the Iron Age, is also found in the Near East, even though not simultaneously but over a certain length of time. In Greece, it can be generally observed, that during the post-palatial period many settlements were abandoned or shrank into small villages (Middleton, 2008, 2012; Galanakis, 2012), which has to be explained as evidence for a diminishing population. This tendency

continued into the Early Iron Age to which some scholars also refer as the ‘Dark Ages’ (Drake, 2012).

The Mycenaean syllabic script so-called Linear B, the earliest proven form of ancient Greek language, was used for administrative purposes and vanished with the demise of the palaces. Evidence comes from clay tablets found at Mycenae, Midea, Pylos, Thebes, Knossos, and Cydonia (Walberg, 1998; Demakopoulou et al., 1996; Hemingway and Hemingway, 2000; Middleton, 2008; Demakopoulou, 2012; http://en.wikipedia.org/wiki/Linear_B). Unfortunately, the absence of other forms of Mycenaean texts precludes archaeologists and historians from gaining insight into events and social processes that might have foreshadowed the collapse of the Mycenaean palatial society (Middleton, 2008, 2012). An overview of the Mycenaean culture and society during the main periods is given by Galanakis (2012). Middleton (2008, 2012) offers a contextualized, broader, and in-depth analysis of the Mycenaean palatial society before and after its collapse.

The causes of the decline of the Mycenaean civilization remain a controversy. Competing anthropogenic reasons, health disasters (i.e., plagues and epidemics), and natural disaster(s) are some of the suggested hypotheses to explain the extraordinary changes during this cultural epoch (Middleton, 2008, 2012; Galanakis, 2012). Anthropogenic causes include overstretch, economic changes, internal problems, and warfare (Iakovidis, 1986; Martin, 1996; Middleton, 2008, 2012; Drake, 2012). Plague and epidemics remain a possible factor, but there is still a lack of evidence for them in the archaeological remains (Middleton, 2008, 2012). Natural disasters of regional proportion that include earthquakes (Papanastassiou et al., 1993; Kilian, 1996; Stiros and Jones, 1996; Nur and Cline, 2000; Nur and Burges, 2008), climatic changes (Bryson et al., 1974; Kaniewski et al., 2010; Drake, 2012), and volcanic eruptions (Force, 2008) are considered probable given that Mycenaean sites settled near Late Neogene–Quaternary volcanoes of the Hellenic arc and seismic sources already active since at least Miocene times (Papanikolaou and Royden, 2007; Royden and Papanikolaou, 2011). Ancient tsunamis have not been invoked as potential cause for the demise of the Mycenaean civilization. Yet, tsunamis have affected the island of Crete during the LBA period (McCoy and Heiken, 2000) and much later in historical times (Shaw et al., 2008), and have left marks in the Argive Basin’s coastline long before and after the Palatial Period (Ntageretzis, 2014). Middleton (2008, 2012) argues that natural disasters cannot account for the collapse of the Mycenaean palatial society because there is archaeological evidence of survival, recovery, and continuing occupation at a certain number of Mycenaean sites. He concludes that collapse ensues from several causes (many discussed in his dissertation), determined by specific reasons distressing individual societies.

The Mycenaean strongholds include the monumental fortified citadels of Mycenae, Tiryns, Midea, and Argos, settled in the Argive Basin of the Argolis Peninsula (Peloponnese, Greece) (Figure 1.3). Other contemporaneous and prominent Mycenaean centers include Thebes and Gla north of Corinth, Athens located east of Corinth, Pylos west of the Messenian Gulf in southwestern Peloponnese, and the recently discovered Kalamianos harbor-town located on the coastline of the Saronic Gulf southeast of Corinth (Tartaron et al., 2011). Together, these

sites, some of them monumental, established the centers of administrative, religious, economic, and social life for their local or regional communities, and shared political and economic affairs throughout the Mediterranean realm from Spain to the Levant through a system of commercial and cultural exchange (Hemingway and Hemingway, 2000; Galanakis, 2012; Demakopoulou, 2012). Mycenaean local workshops manufactured functional objects of pottery and bronze, luxury items such as gold and silver jewelry, carved gems, vases of precious metals and stone, and glass ornaments (Hemingway and Hemingway, 2000), as well as weapons containing gold, silver, bronze, and lead inlays (Stos-Gale and Gale, 1982). The local lead-silver mines from Laurion, Attica Peninsula of the Saronikos Gulf, were exploited from at least as early as Middle Helladic times to the Late Helladic IIIC period (Stos-Gale and Gale, 1982).

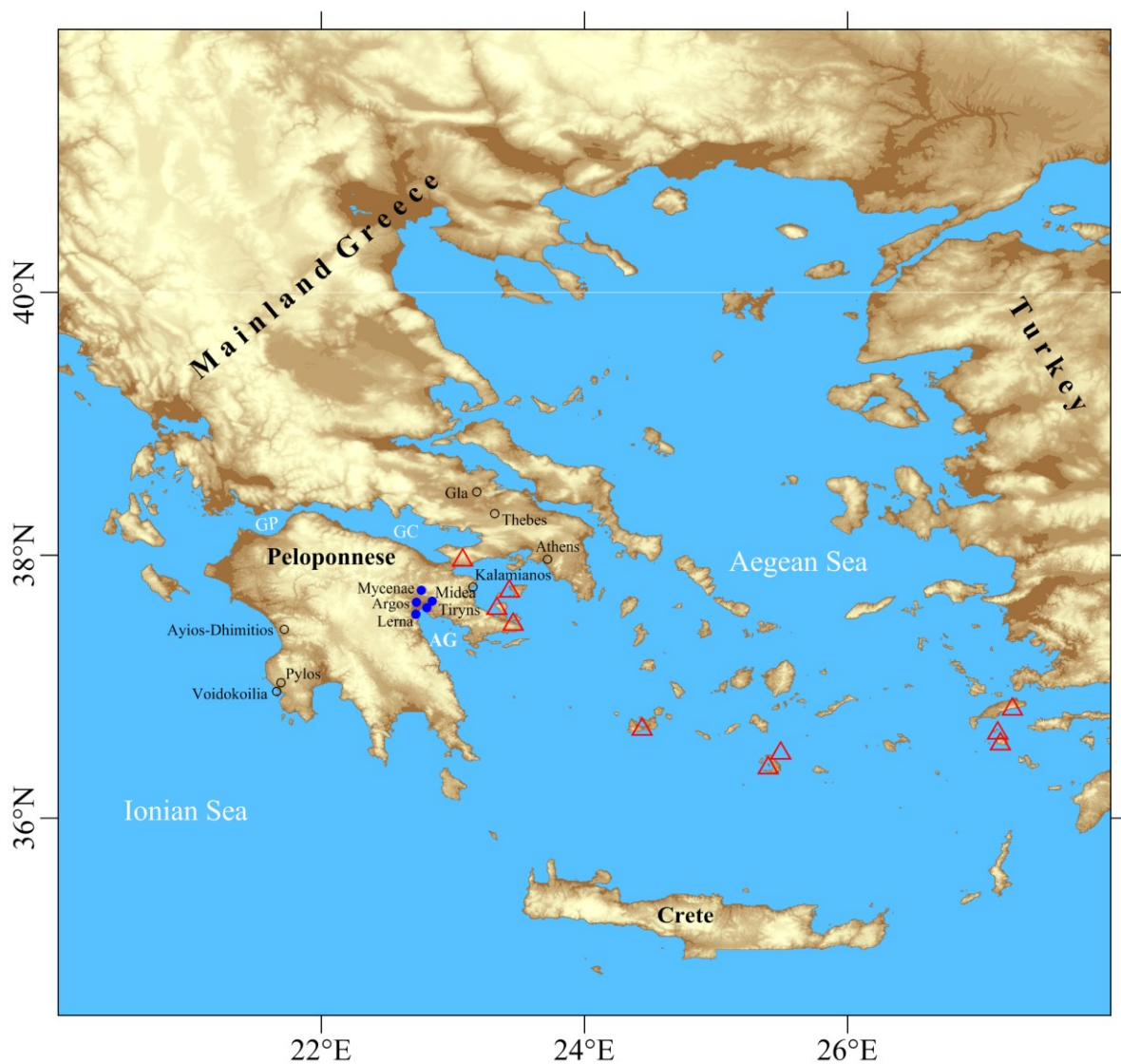


Figure 1.3: Map of the Aegean Sea region showing Mycenaean sites mentioned in this study marked by blue solid-circles (i.e., sites within the Argive Basin of the Argolis Peninsula, Peloponnese, Greece) and empty circles (i.e., sites outside the Argive Basin). AG = Argolic Gulf; GC = Gulf of Corinth; GP = Gulf of Patras. Red triangles represent active volcanoes of the Hellenic arc.

1.2.2 *The Mycenaean Earthquake Hypothesis*

Already in 1926 and 1946, British and French archaeologists Sir Arthur Evans and Claude Schaeffer, respectively, put forward the idea that earthquakes might have caused severe destruction at LBA sites in Aegean and Eastern Mediterranean regions at the end of the LBA (Jusseret and Sintubin, 2013; Jusseret, 2014). To a great extent, these ideas were accepted rather uncritically which might be explained by the high reputation of both excavators. In the 1970s and 1980s, archaeologists unearthed destruction layers which they interpreted as *earthquake strata* in LBA ruins of contemporaneous Mycenaean sites inside (Kilian, 1978, 1988, 1996; Åström and Demakopoulou, 1996; French, 1996) and outside the Argolid (cf. Nur and Cline, 2000). This was parallel with geomorphologic field observations around Mycenaean sites located in the Argive Basin that supported the seismogenic hypothesis (Papanastassiou et al., 1993; Zangger, 1994; Gaki-Papanastassiou et al., 1996; Maroukian et al., 1996). Further, the seismogenic hypothesis is supported by Nur and Cline (2000) who evoke an ‘earthquake storm’ during ca. 1225-1175 BCE (e.g., LH period: Table 1) caused by (yet unidentified) active faults in the Aegean and Eastern Mediterranean regions; however, these workers acknowledge that other forces may have been in concert with the ‘earthquake storm’ and that the seismic activity could explain partial or total destruction of the several sites. These destruction layers have played an important role. Due to their interpreted regional synchronism and territorial context, the destruction layers have been envisioned by archaeologists and pre-historians as catastrophic markers in Mycenaean history and archaeology (Kilian, 1996; Åström and Demakopoulou, 1996; French, 1996; Nur and Cline, 2000; Nur and Burgess, 2008). Subsequent qualitative (Stiros and Jones, 1996; Nur and Cline, 2000; Nur and Burgess, 2008; Sintubin, 2011) and quantitative (Papadopoulos, 1996; Hinzen et al., 2013b; Hinzen et al., 2015; Hinzen et al., submitted) archaeoseismic research has tested the Mycenaean earthquake hypothesis. Clearly, this hypothesis has evolved from being a mere archaeological interpretation to a fully-testable hypothesis, but certain earthquake source parameters have remained unexplained since its proposal. Still, without quantitative archaeoseismic proof, archaeologists, geoarchaeologists, and geomorphologists continue to consider destructive earthquakes during the LH period with high probability. Overall, the Mycenaean earthquake hypothesis remains poorly tested by quantitative archaeoseismological techniques (Hinzen et al., 2013b; Hinojosa-Prieto and Hinzen, 2015).

The earthquake(s) that might have caused total or significant damage to several monumental Mycenaean structures during the Mycenaean palatial period (Kilian, 1980; Papanastassiou et al., 1993; Zangger, 1994; Kilian, 1996; French, 1996; Åström and Demakopoulou, 1996; Sampson, 1996; Walberg, 1998; Papadimitriou, 2001; Walberg, 2001; Demakopoulou, 2012) are thought to have occurred within the seismically active Aegean Sea region (Nur and Cline, 2000). Seismogenic causes of building damage have been put forward, but only documented and described in a qualitative way following archaeological excavations at Tiryns (Kilian, 1980, 1996), Midea (Åström and Demakopoulou, 1986, 1996), and Mycenae (French, 1996). Geomorphological field observations suggest that the nearby Mycenae normal fault was the causative fault for the supposed synchronized destruction of Tiryns, Midea, and Mycenae during ca. 1200 BCE (Papanastassiou et al., 1993; Gaki-Papanastassiou et al., 1996; Maroukian et al., 1996). A summary of the proposed structural damage at Tiryns, Midea and

Mycenae is presented and discussed in chapter 2. Nevertheless, several of the aforementioned (section 1.1) destruction marks remain unobserved at these important sites. For instance, these include displacements along shear planes directly linked to the earthquake fault plane or its branches, fractured building elements, shift of building elements, braking or fracturing of blocks or walls, spalling of block corners, rotations of vertically oriented objects, and soil liquefaction.

Various paleoclimate proxy records indicate that climatic changes probably influenced the LBA cultural collapse and the drop in population in later centuries inferred from a scarcity of archaeological data for occupation relative to other periods. Particularly, colder sea surface temperatures and arid land conditions might have led to a decline in precipitation across the Eastern Mediterranean that triggered lows in agricultural productivity (Bryson et al., 1974; Weiss, 1982; Kaniewski et al., 2010; Drake, 2012). Field evidence of ancient volcanic eruptions and tsunamis have been found in the early LBA archaeological stratigraphy of various pre-Mycenaean sites of the Minoan civilization (Papadopoulos, 2011), which waning stages overlapped with the Mycenaean civilization. For instance, the Thera (Santorini) eruption, dated to 1660–1613 BCE (Manning et al., 2006) and to 1627–1600 BCE (Friedrich et al., 2006), devastated the Minoans and other civilizations in Eastern Mediterranean regions (McCoy and Heiken, 2000). However, despite of the close proximity of Mycenaean sites to active volcanoes (i.e., Methana, Poros, Aegina, Santorini), mapped volcanic deposits from prehistoric eruptions (Fytikas et al., 1976; Innocenti et al., 1981; Pe-Piper et al., 1983; McCoy and Heiken, 2000; Force, 2008; Pe-Piper and Piper, 2013) do not occur at or within their vicinity.

Moreover, tsunami studies have defined tsunamigenic zones in the Aegean Sea region and documented tsunami deposits (i.e., tsunamiites) in coastal strips of the Gulf of Corinth, the Messenian and the Laconian Gulfs of the Peloponnese, Santoniri Island, and Crete (McCoy and Heiken, 2000; Shaw et al., 2008; Papadopoulos et al., 2014; Ntageretzis, 2014). A recent study documents paleo-tsunamiites at four neighboring coring locations onshore the Argolic Gulf, located just 1 to ~2 km south of the Tiryns citadel (Ntageretzis, 2014) (Figure 1.4). Radiocarbon dating of material retrieved from these cores suggest potential episodic tsunamigenic activity at least since the 5th millennium BCE up to the 17th century AD and establishes local event chronostratigraphies and correlations on a local to supra-regional scale. However, the geographic location and elevation of the paleo-tsunamiites found in cores TIR4, TIR3, TIR10, and TIR5 (Ntageretzis, 2014) plot under the waters of the Argolic Gulf according to the position of the ancient coastline at different times in history (Figure 1.4) (Zangger, 1993; van Andel et al., 1990b). Therefore, these deposits should be interpreted with caution. Despite that the whole Hellenic subduction zone and related volcanic arc represent a tsunami hazard for Greece, the absent record of paleo-tsunamiites and past volcanic deposits in the Mycenaean archaeological stratigraphy of Tiryns and Midea excludes tsunamis and volcanic eruptions as possible causes for the downfall of the Mycenaean civilization, especially the palatial culture.

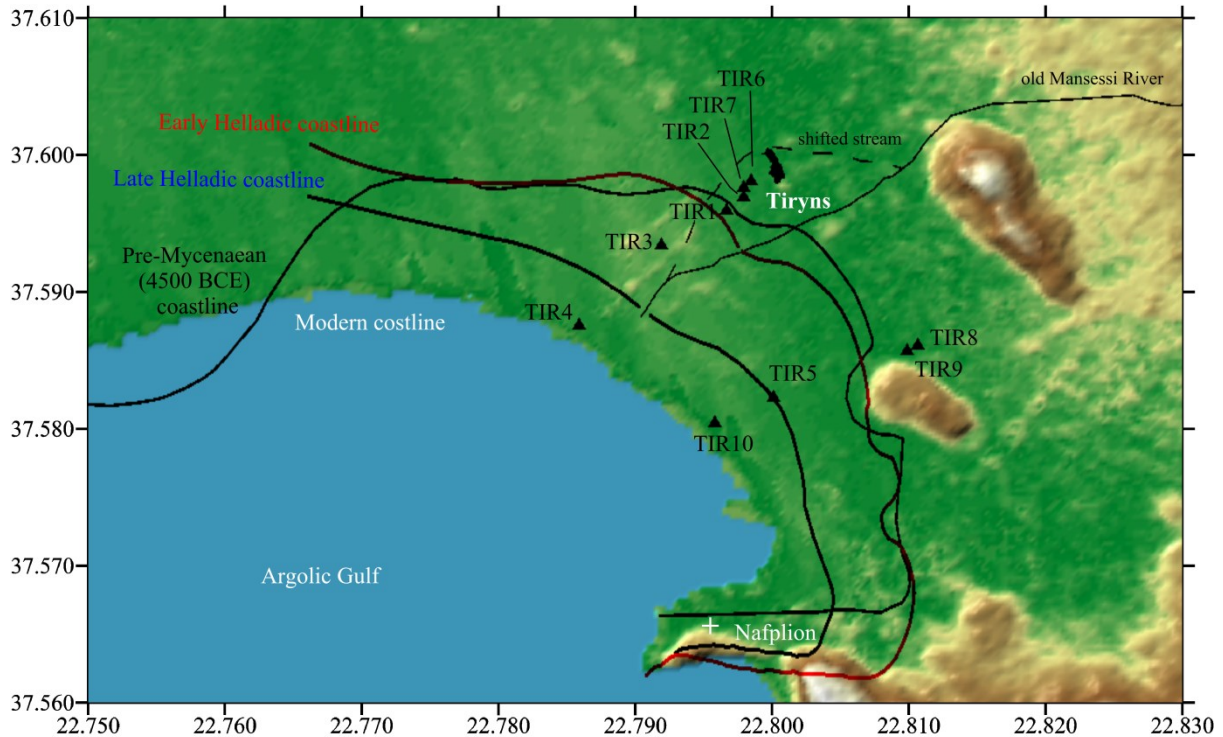


Figure 1.4: Location of shallow cores (< 10 m) drilled by Ntageretzis (2014) in the eastern coastal strip of the Argive Basin and reconstruction of the Argolic Gulf coastline at different times in history (after Zangger, 1993). Identified and radiocarbon dated paleo-tsunamiites are in cores TIR4, TIR3, TIR10 and TIR5.

1.3 Local Site Effects in an Archaeoseismological Context

1.3.1 Overview of Local Site Effects

For a long time, earthquake records have shown that surface ground motions recorded at a given site can vary noticeably even over small inter-site distances (Reid, 1910; Hough et al., 1990; Aki, 1993; Lermo and Chávez-García, 1994; Chávez-García and Cuenca, 1996; Boore, 2004; Messaudi et al., 2012). Ground shaking, and possibly induced structural damage to man-made structures, is strongly influenced by the rupture mechanism of an earthquake source, the effects of the path traveled by seismic waves, and the surface and underground structure of the site where the ground motion is recorded. Each of these three elements (i. e., source, path and site) is a seismological topic in its own right and has been investigated by experts in the field for many years (e.g., Boore, 2004; Thompson et al., 2012; Boore and Thompson, 2014). When a geologic fault ruptures below the earth's surface, seismic energy (body waves) radiates by the earthquake source in a spherical pattern; however, the radiation pattern of a shear rupture is non-spherical. These body waves are refracted and reflected when they reach the interface between geologic materials with different wave velocities. So, by the time the seismic rays reach the ground surface multiple refractions have often bent the seismic rays to a nearly upright direction (Kramer, 1996) (Figure 1.5). Even though seismic waves might travel through tens or hundreds of kilometers of rock and often less than 100 m of soil, the soil deposit strongly influences the characteristics of the ground surface motion (Kramer, 1996).

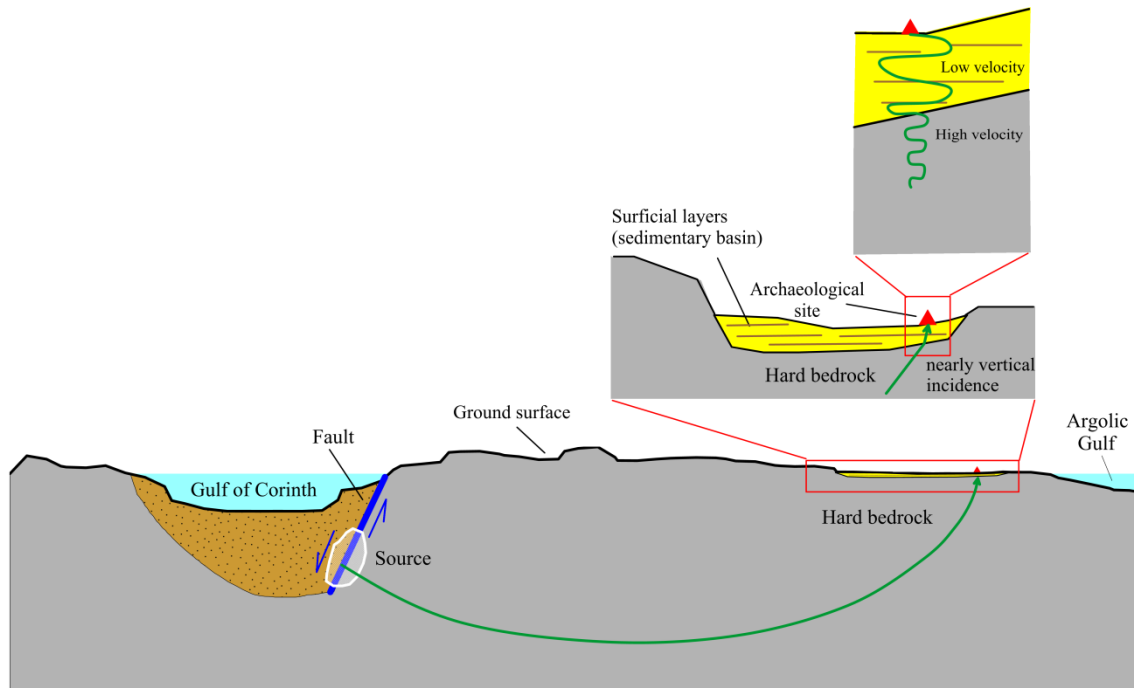


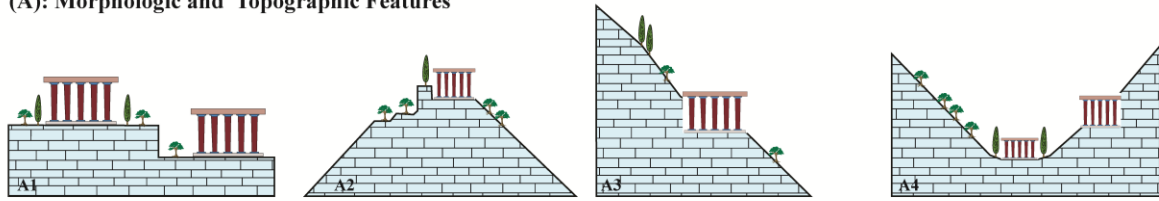
Figure 1.5: (*Lower panel*) Refraction processes that produces steep incidence of seismic wave near the ground surface (after Kramer, 1996) adapted for the Gulf of Corinth–Argive Basin profile, Peloponnese, Greece, after Rigo et al. (1996), Latorre et al. (2004) and Flotté et al. (2005). (*Middle and Upper panels*) Zoomed areas where seismic wave amplification occurs due to the transition from higher velocity rock (higher impedance) to lower velocity sediments (lower impedance) (adapted after Kramer, 1996; Şafak, 2001).

The underground geologic structure, consolidation, variation of the groundwater table, variation of material mechanical properties in the near-subsurface, the presence of heterogeneities and discontinuities, and surface topography can influence amplitude (may amplify or deamplify motion), the frequency content (may shift to higher or lower), and the duration of strong shaking (Boore, 1972; Davies and West, 1973; Geli et al., 1988; Kramer, 1996; Şafak, 2001; Boore, 2004; Bensalem et al., 2010; Chen et al., 2011). The amplification of seismic waves is due to the impedance contrast between horizontally layered sediments and overlying soils (lower impedance) and the underlying bedrock (higher impedance) (Figure 1.5) (Şafak, 2001; Cornou and Bard, 2003). Soil response depends on the type, thickness, and stiffness of soil. Recognized and subject of intensive investigation for many years, this concept is referred to as “local site effects” (Aki, 1993; Boore, 2004). The geomorphologic conditions that influence the local site response are illustrated schematically in Figure 1.6 following the categorization of Panzera et al. (2013); however, a sub-category label (A1 to C4) is introduced in this figure to distinguish between geomorphologic scenarios in subsequent discussions.

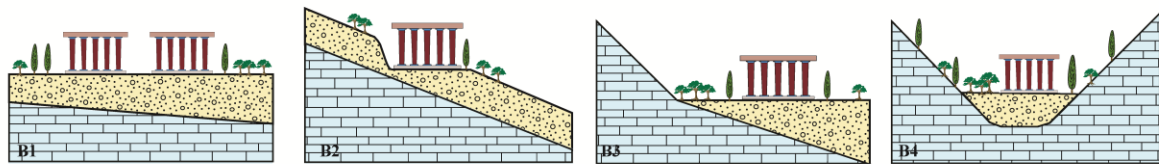
Seismic ground motion and related ground amplification are major factors influencing the degree of damage to infrastructure (Aki, 1993; Atkinson and Boore, 1995; Chávez-García and Cuenca, 1996; Kawase, 2003; Fritsche and Fäh, 2009). A common scenario of seismic wave amplification occurs during the seismic loading of soil deposits that overlie relatively harder bedrock (Mohraz, 1976; Bard and Bouchon, 1985; Şafak, 2001; Fletcher and

Boatwright, 2013). Some well-known examples are listed in Table 1.2. Nowadays, earthquake engineering practice requires the estimation of the level of ground motion and ground amplification for a given site in order to assess the seismic vulnerability of infrastructure and the susceptibility of soils during future earthquakes (Raptakis et al., 2000; Şafak, 2001; Hashash and Park, 2001; Kawase, 2003; Sørensen et al., 2006; Koçkar and Akgün, 2012; Maufroy et al., 2015); however, the evaluation of local site effects is quite sparse in quantitative archaeoseismology. Examples of archaeoseismic investigations that consider local site effects include Hinzen (2005), Fäh et al. (2006), Harbi et al. (2007), Bottari et al. (2008), Hinzen and Weiner (2009), Hinzen et al. (2013a), and Hinzen et al. (submitted).

(A): Morphologic and Topographic Features



(B): Typology and Geometry of Sediments



(C) Presence of Water-Bearing Strata, Landslides, Structural Discontinuities and Cavities

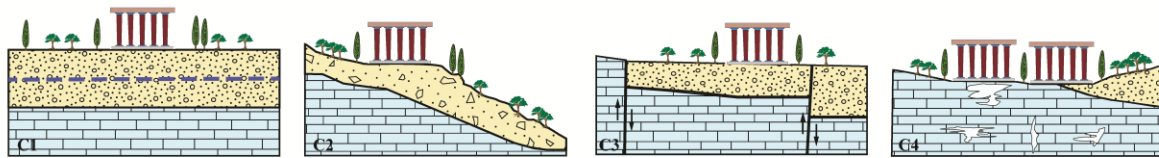


Figure 1.6: Sketch illustrating the conceptualized main geomorphologic categories (A to C) with the corresponding possible scenarios (sub-categories A1 to C4, respectively) for local site response (modified after Panzera et al., 2013).

Table 1.2 Some well-documented damaging earthquakes with observable site effects.

Event	Magnitude	Depth (km)	Reference
San Francisco, California in 1906	$(M_w = 7.7-7.9)^a$	$(10.0 \pm 2)^a$	Reid (1910), Zoback (2006) ^d
Northern Belgium in 1938	$M_s = 5.0 \pm 0.3$	19 ± 4	Nguyen et al. (2004)
Michoacán, Mexico in 1985	$M_s = 8.1$	17.0	Campillo et al. (1989)
Loma Prieta, California in 1989	$M_s = 7.1$	12.0	Chin and Aki (1991)
Northridge, California in 1994	$M_w = 6.7$	17 ± 1	Pitarka and Irikura (1996)
Kobe, Japan in 1995	$M_w = 6.9$	17.0	Wald (1995), Kawase (1996)
Athens, Greece in 1999	$M_w = 5.9$	15.0	Roumelioti et al. (2004)
Kocaeli, Turkey in 1999	$M_w = 7.4$	16.0	Sekiguchi and Iwata (2002), Rathje et al. (2003)
Wenchuan, China in 2008	$M_s = 8.0$	14.0	Wen et al. (2010)
Baja California Norte, Mexico in 2010	$M_w = 7.2$	4.0	earthquakes.usgs.gov
Port-au-Prince, Haiti in 2010	$M_w = 7.0$	13.0	earthquakes.usgs.gov
Offshore Concepcion, Chile in 2010	$M_w = 8.8$	22.9	earthquakes.usgs.gov
Christchurch, New Zealand in 2010	$M_w = 7.0$	12.0	earthquakes.usgs.gov
Eastern Turkey in 2011	$M_w = 7.1$	18.0	earthquakes.usgs.gov
Offshore Honshu, Japan in 2011	$M_w = 9.0$	29.0	earthquakes.usgs.gov
Linqiong, China in 2013	$M_w = 6.5$	14.0	earthquakes.usgs.gov
Bandar Bushehr, Iran in 2013	$M_w = 6.4$	12.0	earthquakes.usgs.gov
Iquique, Chile in 2014	$M_w = 8.2$	25.0	earthquakes.usgs.gov
East of Kudi, Nepal in 2015	$M_w = 7.8$	8.2	Bilham (2015)

1.3.2 Importance of Local Site Effects in Archaeoseismic Research

The primary objectives of a quantitative archaeoseismic investigation are to estimate the nature of the ground motion that caused the damage (Hinzen et al., 2011) and to obtain information about the nature of the earthquake source that caused the ground motion (Galadini et al., 2006). Hinzen et al. (submitted) point out that archaeoseismic observations are often limited to a small portion of the mesoseismal area and the correlation of damage across several neighboring sites is often hindered by uncertainties in dating the damaging events (Galadini et al., 2006; Jusseret et al., 2013). These factors can strongly bias the estimation of the strength of ancient earthquakes; therefore, the consideration and systematic assessment of local seismic site effects becomes critical in an archaeoseismic study (Hinzen et al., submitted).

In principle, neglecting ground amplification in archaeoseismological studies might lead to overestimation of the size of an ancient damaging earthquake (Hinzen, 2011). For seismic ground motion simulations, the use of only one horizontal component as earthquake input signal in site response analysis can lead to significant underestimation of seismic site response (Chen et al., 2011); and the dynamic soil properties (e.g., density, shear wave velocity, damping) should (preferably) be measured *in-situ* (Meng, 2007). Hence, if the goal is to estimate local site effects in archaeoseismology, it is appropriate to implement some of the quantitative tools used in earthquake engineering (cf. Galadini et al., 2006). The estimation of surface ground motion can be done empirically with records of actual earthquakes (cf. Hinzen et al., submitted) or numerically with the stochastic or the Green's function methods (Somerville and Moriwaki, 2003). Field tests and analytical/numerical models can assess the characteristics of seismic site amplification (Chávez-García et al., 1997; Şafak, 2001; Hinzen et al., submitted). They involve recording and analyzing the dynamic response of sites using active sources, ambient noise, and actual earthquakes.

Analytical/numerical models are convenient in quantitative archaeoseismology because they can develop an understanding of seismic wave propagation characteristics of sedimentary basins when instrumentally recorded earthquake records and/or macroseismic intensity data from historical records are absent (Hashash and Park, 2001; Hinzen, 2005; Berilgen, 2007; Bottari et al., 2008; Karastathis et al., 2010a, 2010b). These models require a conceptualized geotechnical model containing the geometry of all soil layers from bedrock to surface, their dynamic properties, the incident bedrock motions, and ‘realistic’ synthetic earthquake records particularly obtained from rock-sites. Synthetic earthquake ground motions are calculated based on source parameters (i.e., rupture length, rupture width, seismic moment (M_o), and moment magnitude (M_w)) linked to a seismotectonic model representative of the region of interest. Posteriorly, these synthetic ground motions are used as the earthquake input signal for the calculation of site amplifications and the resulting site-specific surface ground motion.

An environmental connection existed between Mycenaean citadels and their surrounding landscape. The relationship between isolated hard-rock ridges (i.e., outcropping bedrock) bordered by cohesive or granular soils was a condition frequently met for the design and construction of Mycenaean citadels (e.g., Tiryns and Midea) (Demakopoulou, 1995). Archaeological excavation data from Tiryns (Maran, 2010) indicate that a settlement (so-called Lower Town) developed on the sediments/soils that are deposited in angular unconformity against the Tiryns ridge (bedrock); however, in absence of archaeological excavation data at the foothills of the Midea ridge the existence of an adjacent settlement is uncertain, although it is considered as likely. Therefore, following the classification scenario for local seismic response of Panzera et al. (2013), the citadels of Tiryns and Midea correspond to the combination of geomorphologic sub-categories A2 and B3 (i.e., bedrock/ridge rising above sediments/soils) (Figure 1.6). In theory, the natural topographic relief of the Tiryns and Midea ridges and the bordering sediments are considered natural features expected to influence the local seismic response of the ground surface. Figure 1.7 illustrates a conceptualized geomorphologic longitudinal model of Tiryns and Midea; but several architectural features (i.e., cyclopean walls, reconstructed buildings, etc.) are omitted for visualization purposes and the soil-bedrock interface is represented only schematically. The geometry of the soils and the depth to bedrock are appropriately defined in subsequent chapters based on available and newly collected geologic and geophysical information.

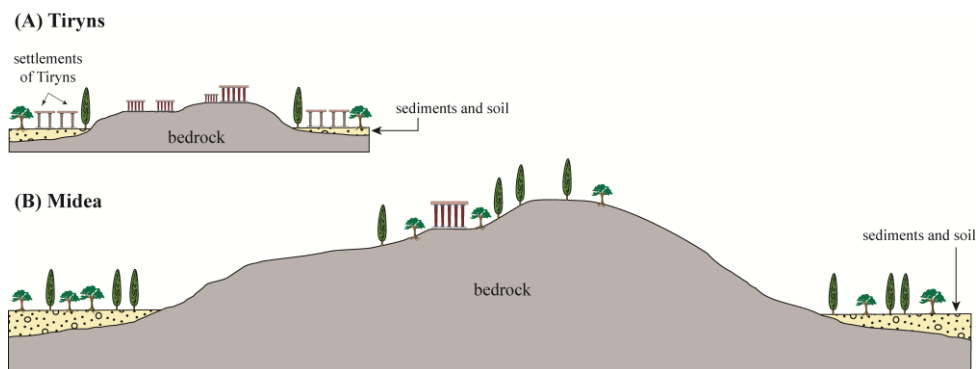


Figure 1.7: Conceptualized geomorphologic cross-sectional model of the Mycenaean citadels of Tiryns (A) and Midea (B) (not to scale).

1.4 Objective of the Research

In Greece, archaeological and geoarchaeological studies are quite abundant (Tourloukis and Karkanis, 2012 and references there in) in comparison to archaeoseismic investigations (Stiros and Jones, 1996; Nur and Cline, 2000; Buck, 2006; Tendürüs et al., 2010; Jusseret et al., 2013; Hinzen et al., 2013b; Hinzen et al., 2015; Hinzen et al., submitted). Further, several quantitative local seismic site effect investigations have been conducted only in response to recent damaging earthquakes that have destroyed both historical and modern infrastructure (i.e., Gariel et al., 1991; Pitilakis et al., 1992; Pedersen et al., 1994; Lachet et al., 1996; Chávez-García et al., 1996; Roumelioti et al., 2004a; Maufroy et al., 2015; Bilham, 2015). Conversely, the quantitative assessment of local seismic site effects in archaeoseismology is still in its early stages (Hinzen, 2005; Fäh et al., 2006; Bottari et al., 2008; Hinzen and Weiner, 2009; Hinzen et al., submitted). Recently, Hinzen et al. (submitted) investigated the local seismic site effects at both Mycenaean Tiryns and Midea using empirical data from instrumentally recorded earthquakes and ambient noise, and forward modeling. The forward modeling of seismic local site effects using synthetic earthquake records (as input acceleration) coupled with estimated dynamic properties of soils and bedrock from archaeological sites of interest is rare in archaeoseismology. Particularly, the quantitative assessment of local site effects should be done in a site-specific basis to account for the surficial and underground geologic and topographic conditions at and around the archaeological site(s) of interest. The term site-specific basis means that, for a given place, a one-dimensional (1D) geotechnical model of the near-surface is created for estimating local site effects.

The goal of the present archaeoseismic study is to perform numerical forward modeling of the local seismic site effects particularly ground amplification from the sediment cover and related surface ground-motion in order to test the earthquake hypothesis. The influence of both the near-surface geologic and topographic conditions is investigated on a site-specific basis. The backbone of this parametric study comprises (i) a seismotectonic model containing onshore and offshore active seismic sources near to citadels of Tiryns and Midea; (ii) a geologic model of each citadel and surroundings; and (iii) a comprehensive site-specific geotechnical model of each citadel that accounts for both the reconstructed walking horizon during the palatial period and the dynamic material properties of the near-surface materials required to (iv) forward model the local site effects. This has been outlined during the 2013 Seismological Society of America Annual Meeting conference in Salt Lake city, Utah, USA (Hinzen et al., 2013b: HERACLES project [**H**ypothesis-**T**esting of **E**arthquake **R**uined **A**rgolid **C**onstrutions and **L**andscape with **E**ngineering **S**eismology]). This dissertation follows the proposed multidisciplinary quantitative methodology of Hinzen et al. (2011). In particular, Greece is an ideal place to conduct quantitative archaeoseismic research because it is seismically active and contains the remains of numerous monumental man-made structures of ancient civilizations that date into the third millennium (Caputo and Helly, 2008; Hinzen et al., 2013b). The remains of the two neighboring Mycenaean citadels of Tiryns and Midea are the subject of study in this dissertation because they (i) have an extensive excavation history, over 120 and 80 years for Tiryns and Midea, respectively; (ii) both citadels are located on isolated outcropping bedrock ridges with contrasting underground geologic structure,

topographic conditions, and surrounding soil-type despite of their geographic proximity; (iii) both citadels are contemporaneous and representative of Mycenaean architecture; and (iv) the archaeological interpretation that both citadels might have been damaged (synchronously) by regional earthquakes during the palatial period merits its examination because it remains poorly evaluated and tested with quantitative archaeoseismic techniques.

1.5 Organization of the Dissertation

Chapter two highlights the setting and the current geoarchaeological and archaeoseismological understanding of the Mycenaean citadels of Tiryns and Midea. The geology of the Argive Basin and seismicity of nearby seismic sources are discussed in chapter three in order to establish the relationship between the near-surface conditions around the sites and the seismic sources. The geophysical and geotechnical properties of the soils and bedrock are presented and discussed in chapter four based upon previous and new geophysical investigations relevant to this study. These material properties coupled with available geologic, geotechnical and geophysical information are used to develop a comprehensive geotechnical model of the Tiryns and Midea citadels, which is required in the subsequent chapters devoted to 1D forward modeling of local site effects. Chapter five deals with the generation of synthetic earthquake records needed for the simulation of site-specific surface ground-motion and the estimation of seismic local site effects. Chapter six presents the methodology, results and interpretations of the numerical modeling of local site effects at Tiryns, Midea, and the area between them. Chapter seven discusses the implications for the Mycenaean earthquake hypothesis in light of the examined postulated archaeoseismic evidence and the overall modeled local site effects. Finally, chapter eight provides the dissertation conclusion and recommendations.

2. SETTING, GEOARCHAEOLOGY AND ARCHAEOSEISMOLOGY OF TIRYNS AND MIDEA

The neighboring Mycenaean citadels of Tiryns and Midea were built on isolated, prominent natural hard-rock ridges surrounded by topographic highs. The distance between both citadels is about 7.0 km and both were interconnected with other Mycenaean centers by a network of roads (Demakopoulou, 2012). Both citadels share the same geography, but contrasting topographic and geologic settings (Figure 2.1). By the LH IIIB period (i.e., palatial period), fortification walls of Cyclopean-style encircled the citadels; hence reaching the status of acropolis following Demakopoulou (1995). Tiryns and Midea were presumably important strongholds of Mycenae, which is considered the regional political core (Balcer, 1974; Middleton, 2008; Maran, 2004a, 2004b, 2010).

2.1 Setting of Tiryns and Midea

2.1.1 Tiryns

Tiryns overlooks the south-widening Argolic Gulf as it stands on an elongated north-northwest trending, ~300 m long limestone ridge (bedrock) rising above the alluvial soils of the southeastern Argive Basin (Zangger, 1994; Maran, 2010) (Figure 2.1). The proximity of the Tiryns citadel to the Argolic Gulf, which opens into the Aegean Sea, and its participation in long-distance trading highlight Tiryns' socio-economic role as a major Mediterranean harbor in the Late Bronze Age (LBA) (Maran, 2010). Archaeological excavations at Tiryns brought to light palatial architecture (Schliemann, 1886; Kilian, 1983, 1988, 1990; Maran, 2004a, 2004b, 2006, 2010) composed of several complexes. These include the Lower Citadel (LC) in the north and the Upper Citadel (UC) in the center of which the Great Megaron (the Palace) is located, and the East and South Galleries built on the eastern and southern flanks of the ridge, respectively. The current elevation of these three complexes increases from north (~15.0 m a.s.l.) to south (~28.0 m a.s.l.). Currently, the Cyclopean walls of Tiryns are preserved at maximum 9.9 m high and about 7.0 m thick, but were probably somewhat higher during the palatial period. The wall circuit is about 750 m long and encloses an area of nearly 18,500 m² (Papadimitriou, 2001). Fallen blocks of the Cyclopean wall are still scattered on the eastern and northern flanks of the Tiryns ridge. In this dissertation, these fallen blocks are interpreted to be in their original collapsed position (Figure 2.1). The west wall was restored along its entire length, but segments of the eastern side remain in the fallen condition described by H. Schliemann in 1886 (Hinzen et al., 2013b). As part of the HERACLES project, 3D laser scans of the northeast section of the damaged wall in Tiryns have been taken. These images will serve as a base for numeric modeling of the disaggregation processes (Hinzen et al., 2013b).

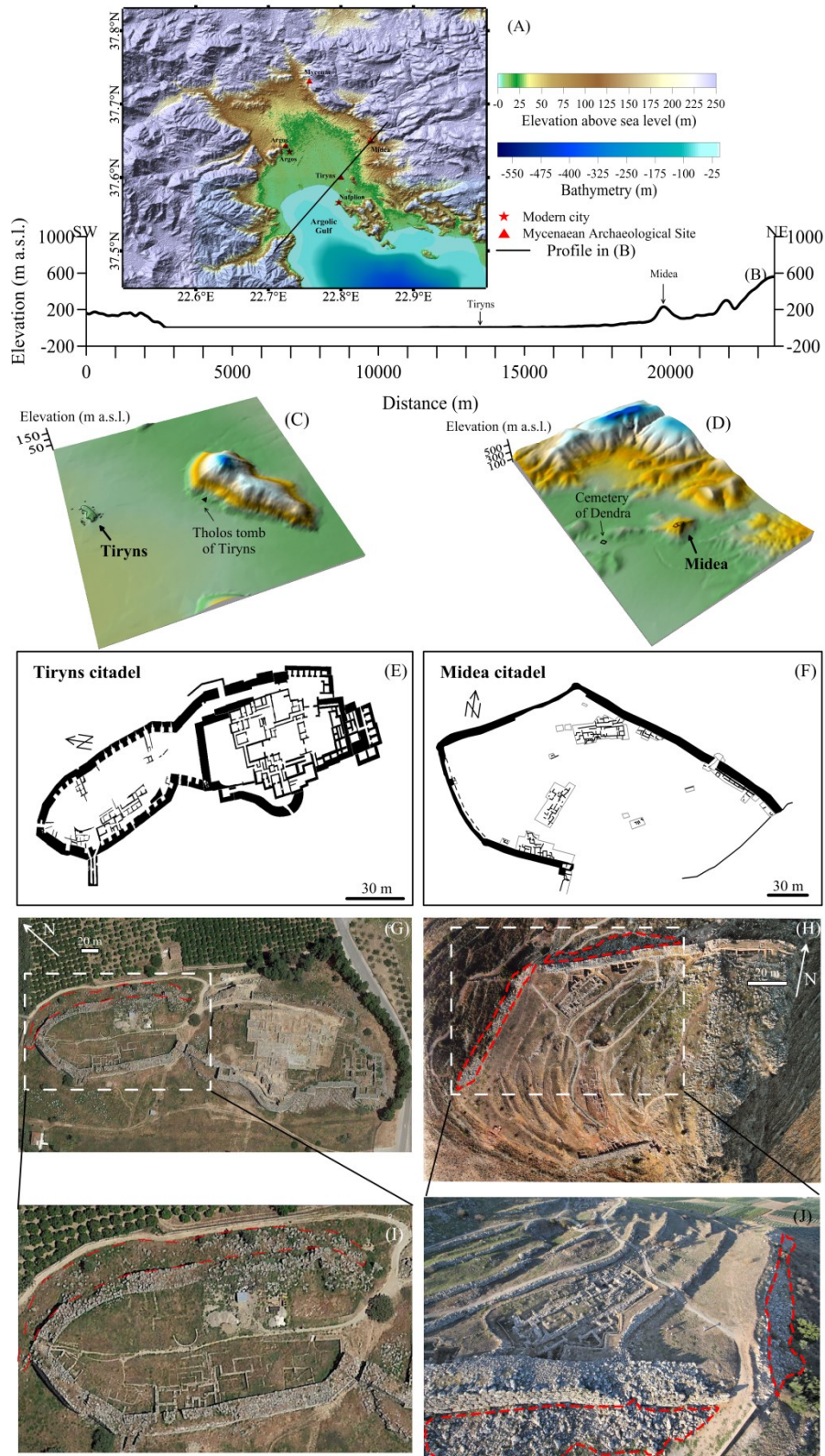


Figure 2.1: (A) Digital Elevation Model (DEM) of the Argive Basin and (B) elevation profile crossing the Argolic Gulf and both Tiryns and Midea citadels. DEM of the surroundings of (C) Tiryns and (D) Midea. Archaeological plan of (E) Tiryns (after Maran, 2010) and (F) Midea (after Demakopoulou, 2012). (G and H) Aerial photographs showing both citadels and (I and J) the location of collapsed Cyclopean walls in Tiryns and Midea, respectively, marked with red dashed. Aerial Photographs of Tiryns and Midea from Google Earth[®] and K. Xenikakis in Demakopoulou (2012), respectively.

A terrain slope analysis of the Tiryns hill and vicinity indicates that the slope angle varies from 5-45°. Specifically, the fortification walls were not built on slope steeper than 40°, as shown in Figure 2.2. The terrain slope angle was computed using the grid-calculus tool included in the software SURFER® (version 10.7.972) by Golden Software, Inc. based on the digitalization of 1.0 m resolution topographic charts made by the Hellenic Military Geographical Service (HMGS, 1951).

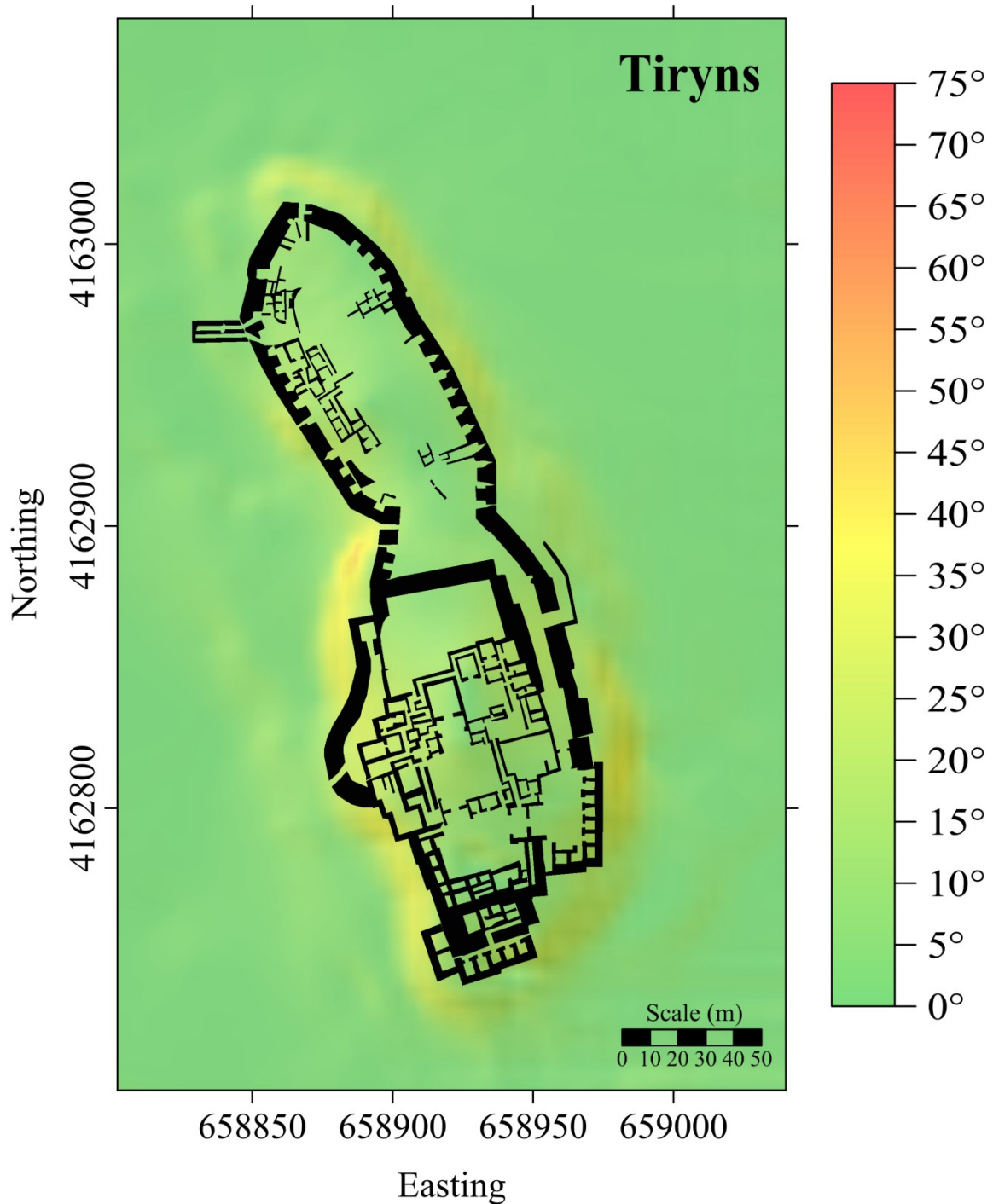


Figure 2.2: Terrain slope map of the Tiryns hill and vicinity.

Archaeological excavation data of Kilian (between 1976 and 1986) suggest that Tiryns was first inhabited in the Neolithic Age (7th–4th millennium BCE). Building activity and settlement spanned the whole Bronze Age period, with the earliest architectural remains dating back to the Early Bronze Age (EBA) (*ca.* 2000–2900 BCE) (Kilian, 1980, 1983, 1988; Papadimitriou, 2001). The excavation/trenching work of H. Schliemann (between 1884 and 1885) in the UC dug through a layer of soil between 3.0 to 6.5 m thick deposited over the weathered and fractured limestone bedrock. A recent empirical determination of site effects estimates the presence of a 3.0 to 4.0 m thick fill and/or wall remnants between the present surface and the top of the limestone in the southern UC and the Southern Gallery (Hinzen et al., submitted). It is assumed that the lower levels of this layer contain material that is either older or contemporary with the palatial period covered by a very thin top soil. Together, the excavations of H. Schliemann and W. Dörpfeld (1884-1885), W. Dörpfeld and G. Karo (1905-1914), K. Müller and H. Sulze (1926-1929), N. Verdelis with U. Jantzen and J. Schäfer (1957-1974), K. Kilian (1975-1986), and J. Maran (1997 to present) (Papadimitriou, 2001) suggest that the Mycenaean settlement, at least within the UC, was built on material presumably of ruins of pre-existing buildings of the LH IIIB late period. Hence, this material acts as the foundation of several palatial buildings in the UC. In the LC, Schliemann's trenches dug through soil and reached the bedrock between 0.5 to 2.7 m to as much as 5.0 m deep in the northern edge. The archaeological excavation data from the LC indicate superimposed settlement phases (Kilian, 1980, 1983, 1988; Maran, 2010). Some Mycenaean rooms of the palatial period seem to have been built on bedrock (western LC) and some on pre-existing ruins (eastern LC). The remains of the Mycenaean palatial architecture are shown in Figure 2.3. Papadimitriou (2001) provides a detailed chronology of the excavation history at Tiryns.

Excavations inside the fortification walls of Tiryns (Schliemann, 1886) and a terrain model of the site and surrounding landscape (Falter, 2012) reveal the bedrock depth and topography. The summit of the Tiryns ridge is rather flat and the soil slope outside the citadel dips gently seawards (Falter, 2012). During the LH period, Tiryns was surrounded by the Lower Town (LT) settlement of yet unknown proportions (Zangger, 1994; Maran, 2010). At < 5.0 m depth, an archaeogeophysical survey detected magnetic and electrical resistivity anomalies interpreted as architectural ruins (Hübner and Giese, 2006) and later confirmed by an excavation which assigned them as LT settlements (Maran, 2010). Figure 2.4 shows the archaeological plan of Tiryns citadel superimposed on the bedrock elevation map inside the citadel and the distribution of the excavated LT settlement. Both geomorphological and geoarchaeological stratigraphic studies of Zangger (1993, 1994) propose that the LT was inundated by a single catastrophic earthquake-related flash-flood *ca.* 1200 BCE (i.e., earthquake postulated by Kilian [1980]) which deposited flood deposits. However, Maran's more recent interpretation of new evidence shows that the flood deposits actually represent a sequence of periodic flooding events spanning likely a longer period within the 13th century BCE and he therefore refutes the possibility of a single flashflood event (Maran, 2004b).

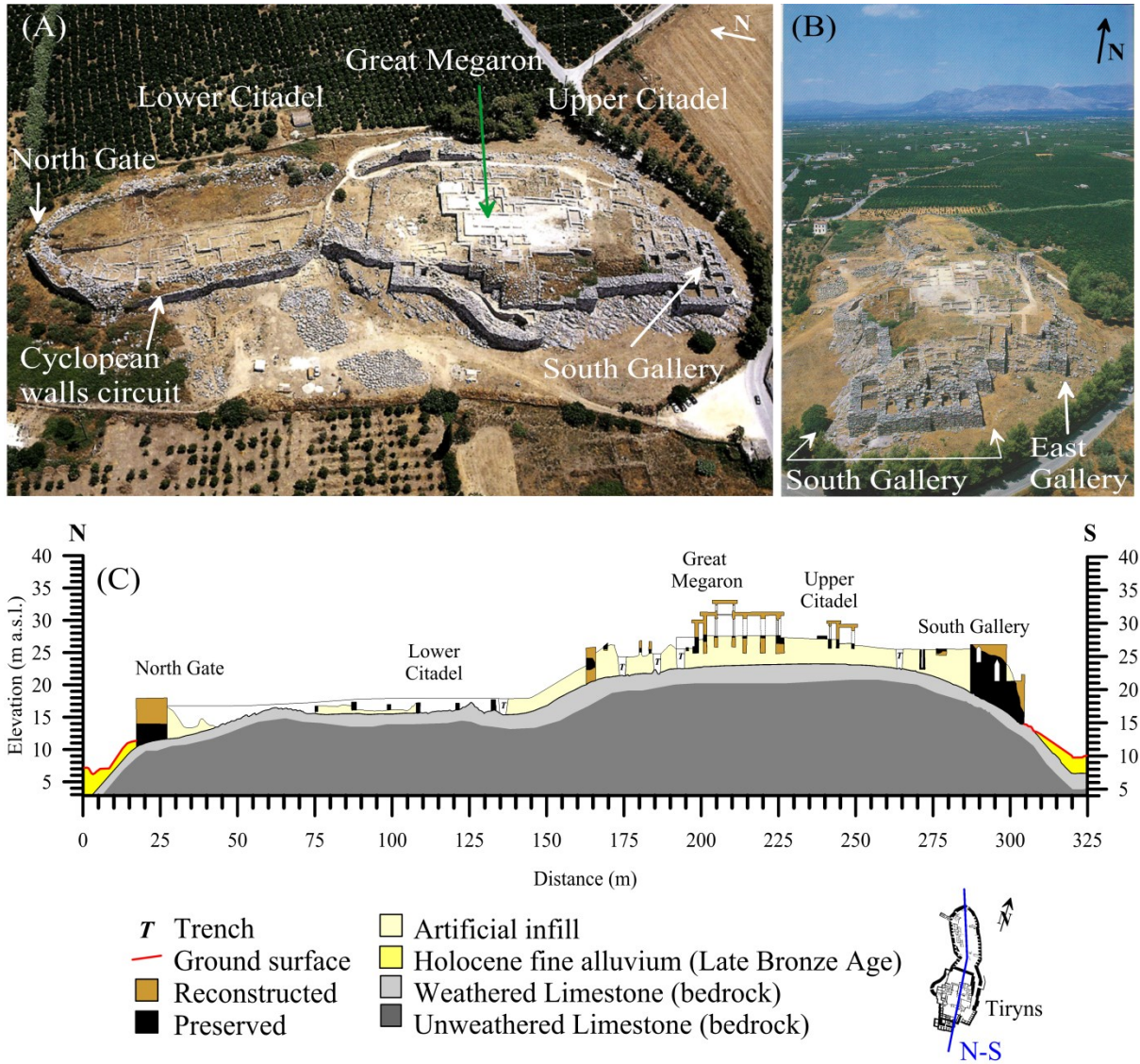


Figure 2.3: Panoramic views of Mycenaean Tiryns from west (A) and south (B) (aerial photographs by Daskalopoulou and Patrikianos in Papadimitriou, 2001). Interpreted North-South (C) geoarchaeological cross-section with Mycenaean palatial buildings outlined after the excavation and reconstruction work of Schliemann (1886) (after Hinojosa-Prieto and Hinzen, 2015).

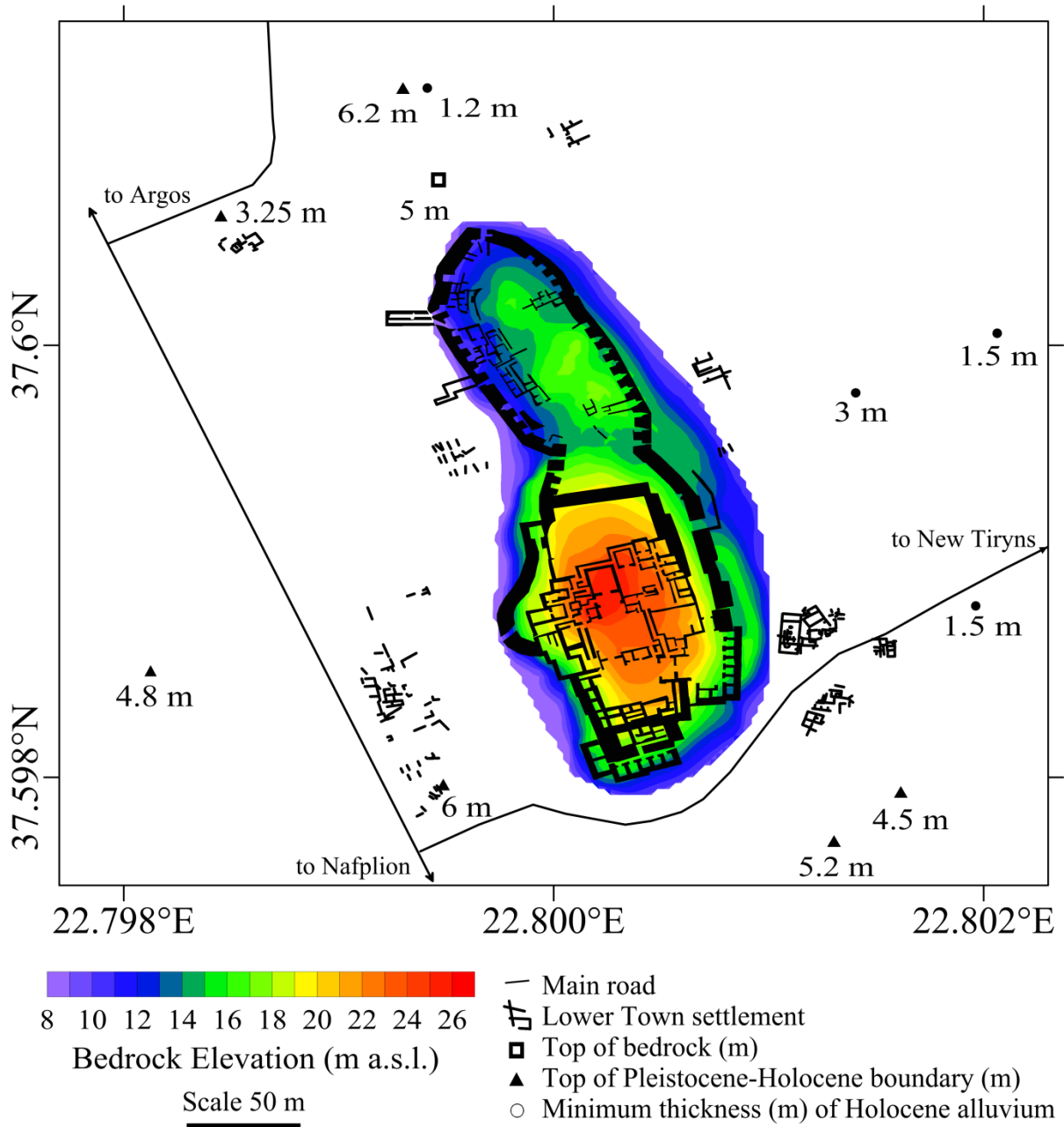


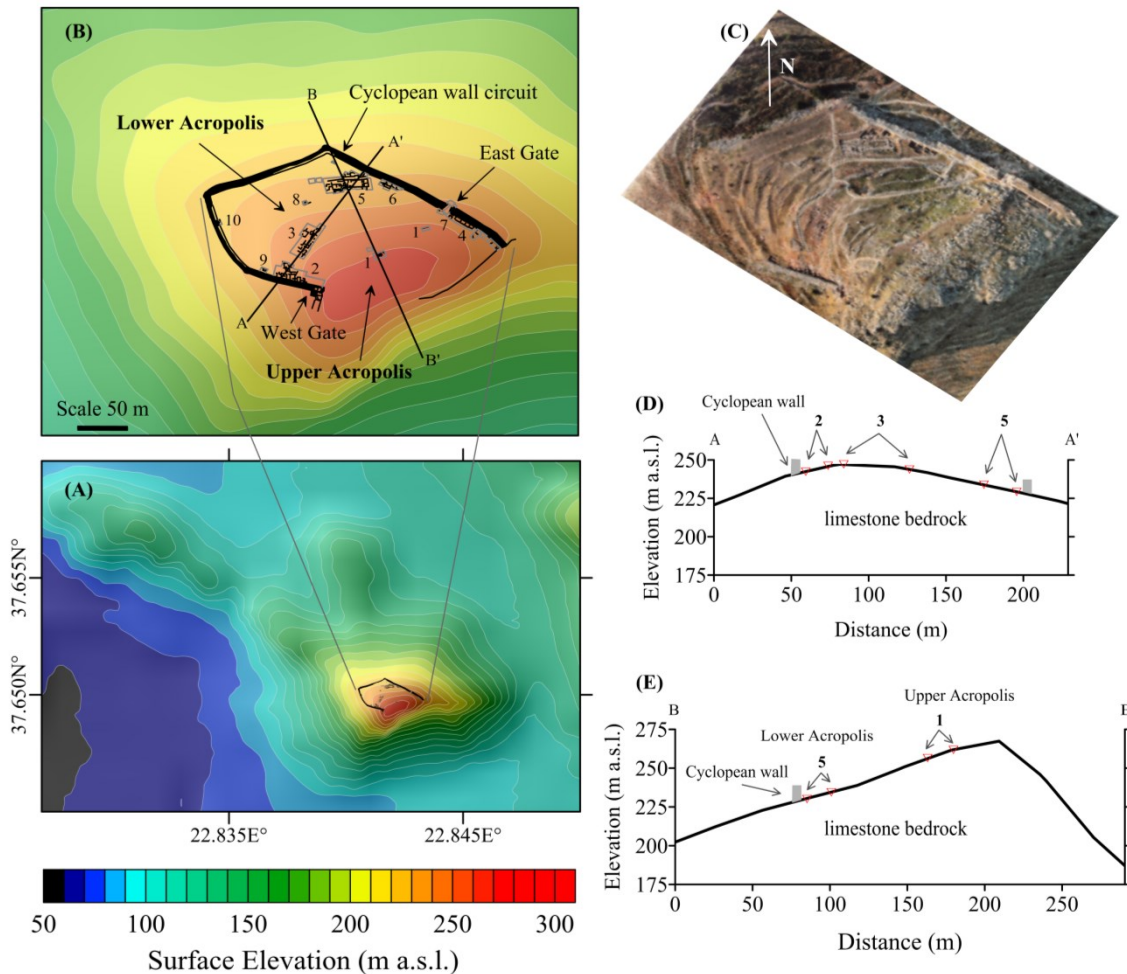
Figure 2.4: Archaeological plan of Tiryns (Maran, 2010) superimposed on the bedrock elevation (Klessing, unpublished data; Falter, 2012). Also shown are the excavated settlements of the Lower Town (after Maran, 2010), location of available shallow boreholes shown by squares, triangles, and circles (after Zangger, 1993) planned to reach the top of Late Pleistocene clays (see legend for symbols).

2.1.2 Midea

The Mycenaean citadel of Midea is located nearly 12.0 km southeast of Mycenae and 7.0 km northeast of Tiryns. The Midea citadel overlooks the entire Argive Basin including the Argolic Gulf as it was built partly on a hilltop and hillside of a prominent 2000 m long ridge (Demakopoulou, 2012). This ridge trends north-northwest, reaches a maximum altitude of 268 m (a.s.l.), and is composed of highly weathered, karstified, crystalline limestone faulted against continental flysch deposits. The ridge rises above the Upper Pliocene–Quaternary steep terrace deposits of the northeastern Argive Basin.

Archaeological excavations at the Midea citadel have so far focused in areas inside the wall circuit (Demakopoulou et al., 1994, 1996; Walberg, 1998, 2001; Demakopoulou et al., 2012). A detail survey measured the extension and elevation of the Cyclopean wall (Fischer, 1986). As part of the HERACLES project, 3D laser scans of the damaged wall in Midea were taken to assist in the numerical modeling of the fragmentation process, of which results will be presented in a separate study. The excavation data indicate that Midea was occupied in the Final Neolithic to Early Byzantine period and that important economic, administrative, military, and ritual activities took place during its climax in Mycenaean times (Walberg, 2001; Demakopoulou, 2012). Midea comprises a lower and an upper natural level separated by a rocky slope dividing the citadel into the Lower and Upper Acropolis, respectively (Demakopoulou, 2012). The Mycenaean architecture of Midea was erected on karstic limestone bedrock. The structure comprises various room compounds fortified by Cyclopean walls and gates built at the southern and northeastern flanks of the ridge (Persson, 1931; Åström and Demakopoulou, 1986, 1996; Åström et al., 1988, 1990, 1992; Demakopoulou et al., 1994, 1996; Demakopoulou, 1995; Walberg, 1998, 2001; Demakopoulou, 2012). Figure 2.5 shows the archaeological plan of Midea overlaid on the surface topography map.

The structures in the Lower Acropolis include the Megaron Complex located in the northern part next to a small Building; a Complex of Buildings in the middle interpreted as both living and working areas; a two-storey Building Complex found next to the West Gate and against the southern Cyclopean wall used as storerooms and workshops; and two narrow passages (“syrinx”) crossing through the thickness of the west section of the Cyclopean wall, which were used as sally ports. The Upper Acropolis was considered a “Palace Area” by the first excavator of Midea, Axel Persson, who found a few Mycenaean structural remains (Demakopoulou, 2012). Other structures comprise the Complex of Rooms in the area of the East Gate that were also used as workshops and storerooms and other structural remains of pre-Mycenaean times showing that pre-Mycenaean settlements of Midea established on the summit. It is postulated that an earthquake at *ca.* 1200 BCE and associated fire damaged the Megaron Complex and the Buildings adjacent to the Gates; however, occupation of the whole Midea site continued afterwards (Walberg, 1998, 2001; Demakopoulou, 2012). The Cyclopean wall was built in LH IIIB middle; its circuit is 450 m long, 5.0 to 7.0 m thick, partially preserved up to a height of 7.0 m, and enclosing an area of 24,000 m² (Fischer, 1986; Walberg, 2001; Demakopoulou, 2012). Large limestone boulders were used for the inner and outer façades, while the interior of the wall contained a filling of much smaller stones. At the points where the wall changes its direction, it has small curving protrusions or bastions that strengthen the fortification. The fortification wall is truncated by the natural steep limestone cliff at the southern and eastern flanks (Demakopoulou, 2012), implying that the Mycenaean recognized the cliff as a natural barrier against intruders. Blocks of the collapsed Cyclopean wall are still scattered on the steep northern slope and current excavations continue to unearth more remnants of the collapsed wall.



pre-Mycenaean times (4800 -1600 BCE): End of 13th century BCE: 13th-12th century BCE:

- | | | |
|------------------------------|------------------------|---|
| 1 Building and other remains | 2 Building Complex | 5 Megaron Complex |
| | 3 Complex of Buildings | 6 Remains of the Mycenaean and Late Roman periods |
| | 4 Complex of Rooms | 7 Inner gate |
| | | 8-10 Building remains and sally port |

Figure 2.5: (A) Archaeological plan of Mycenaean Midea (Demakopoulou, 2012) superimposed on the surface topography map. (B) Enlarged view of the archaeological plan. (C) Aerial photograph of the fortified area of Midea (aerial photo by K. Xenikakis in Demakopoulou, 2012). (D) Southwest-Northeast and (E) Northwest-Southeast topographic profiles showing the limits of excavated and unreconstructed buildings inside the Cyclopean walls.

A terrain slope analysis of the Midea hill and vicinity shows that the slope angle varies from 5-75°. Particularly, the Cyclopean walls were not erected on slope steeper than 40°, as shown in Figure 2.6. The terrain slope angle map was computed similar to the one for Tiryns. An excavated destruction layer principally defined by partially collapsed structures such as walls, buildings, and gates has been interpreted to represent earthquake-related structural damage which occurred during the LH IIIB2 period *ca.* 1200 BCE (Åström et al., 1990; Åström and Demakopoulou, 1996), roughly contemporary with that at Tiryns (Figure 2.1 G-J). The current condition of the Cyclopean wall of Midea is thought to represent the original collapsed position. The East and the West Gates are positioned opposite to each other. A

Cyclopean ramp led to the East Gate. This gate seems to have been the main entrance to the citadel as it led to the Upper Acropolis and the Lower Terraces in the northwest. The West Gate gave access to the southwest area of the Lower Acropolis. This gate contained a bastion measuring 11×11 m and between the bastion and the steep cliff is an exterior court to which led a small built ramp (Demakopoulou, 2012).

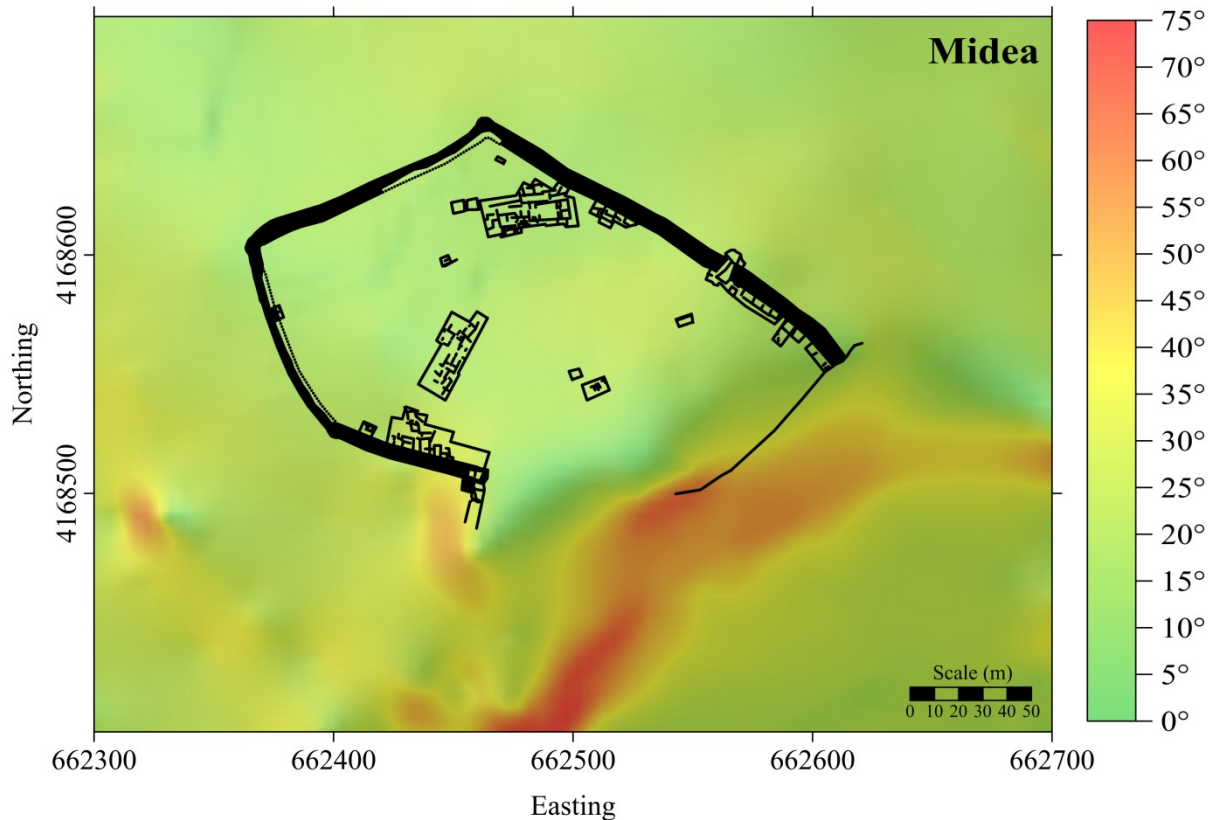


Figure 2.6: Terrain slope map of the Midea hill and vicinity.

Up to this date, the only excavation works outside Midea are the ones that uncovered and documented the so-called royal Cemetery of Dendra (Persson, 1931). This cemetery is located about 1.5 km northwest of Midea, and it is named after the adjacent modern village of Dendra (see Figure 2.1D) (Demakopoulou, 2012). Excavations comprised a monumental Tholos tomb (beehive-shaped), sixteen Chamber tombs, and burials of horses of the Mycenaean period. The cemetery was built in Holocene coarse-grained alluvial fan deposits almost at the present ground surface. It is here assumed that the paleoelevation of the Mycenaean walking horizon in the vicinity of Midea has remained relatively unchanged. This is supported by both a depositional history and paleo-landscape study of the Argive Basin (van Andel et al., 1986, 1990a; Zangger, 1993). Demakopoulou (2012) provides a current synopsis of the history and archaeology of Midea.

2.2 Geoarchaeological Perspective

Previous geoarchaeological investigations in the Argive Basin–Argolic Gulf region have focused on various topics. These include landscape changes of climatic (Zangger, 1993, 1994) and anthropogenic origin (Balcer, 1974; Maroukian et al., 1996, 2004); archaeological

stratigraphy, morphotectonic, and geomorphologic observations (Papanastassiou et al., 1993; Zangger, 1993, 1994; Maroukian et al., 1996, 2004; Georgiou and Galanakis, 2010); microfacies analysis through petrographic examinations of samples from Cyclopean blocks of carbonates and siliciclastic decorative stones from the Tiryns citadel and adjacent outcrops (Varti-Matarangas et al., 2000; Varti-Matarangas and Matarangas, 2000); localized archaeogeophysical surveys (van Andel and Lianos, 1984; van Andel et al., 1993; Hübner and Giese, 2006; Zananiri et al., 2010a, 2010b; Mitropoulos and Zananiri, 2010); holistic significance and classification of Mycenaean single chamber tombs (Dirlik, 2012); and more recently paleo-tsunamis (Ntageretzis, 2014). Specially, the studies that discuss the landscape evolution and Mycenaean archaeological stratigraphy (Kraft et al., 1977; van Andel et al., 1986, 1990a; Zangger, 1993, 1994; Ntageretzis, 2014) are central for reconstructing the paleo-surface and paleo-coastline and characterizing the soil-types (texture, grain size, and origin) representative of the eastern Argive Basin during the Mycenaean palatial period. This information is crucial for the assessment of local seismic site effects, which are discussed in subsequent chapters.

Noticeable shoreline shifts and terrestrial modifications occurred in the Argive Basin at least since the Pliocene (van Andel and Lianos, 1984; van Andel et al., 1990b). Particularly, the sedimentological record around Tiryns resembled a swampy soil environment with a much closer shoreline by the end of the LBA, the height difference of the Tiryns citadel with respect to its surroundings was slightly higher than today (Zangger, 1993, 1994). Throughout the Bronze Age, the coastline retreated to its present-day location due to both soil erosion farther inland and sediment re-deposition in a shallow bay, and a former east-west running stream fluctuated from south to north of Tiryns which deposited flood sediments and coarse gravel and sand deposits (Zangger, 1994, 1994; Maran, 2004b) (Figure 2.7). Despite of intermittent alluviation since *ca.* 3000 BCE, torrential flooding around Tiryns during the LBA, and coastal changes, the landscape in the central, northern, and eastern parts of the Argive Basin has remained relatively unchanged since the Bronze Age period (Zangger, 1993). Moreover, fertile soils in the basin were already available to the Mycenaean in response to a period of local slope erosion of the adjacent sources (van Andel et al., 1986, 1990a; Zangger, 1993, 1994). A stable landscape during the LBA is also reported in the southern Argolid, 40-50 km southeast of Tiryns (Pope and van Andel, 1984).

Conversely, also during Mycenaean times, the westernmost coastal strip of the Argive Basin was dominated by a natural beach barrier that separated an ancient small shallow (< 6.5 m deep) freshwater lake, so-called Lake Lerna, from the Argolic Gulf (Zangger, 1993). The geologic record shows a 6.0 to 6.5 m thick marine sequence of Quaternary fine-grained sediments at the former Lake Lerna (Zangger, 1993). Sediments include a lower Early Pleistocene yellow and brown paleosols interlayered with dark grey mud passing into a Holocene hard red bed, with pedogenic calcite concretions, capped by 1.0 to 1.20 m thick dark brown and bluish gray-to-black clays with peat and humus. The former expanse of the Lake Lerna covered the western half of the coastal plain from the Early Holocene onwards (Zangger, 1993). Various presumable active normal faults coincide with the proposed location of Lake Lerna (Figure 2.7A). The proximity of natural water reservoirs to fault

escarpments or pronounced geomorphologic expressions and the human presence at such water bodies are a common feature in areas of recent tectonic activity (King and Bailey, 2006).

The Mycenaeans took advantage of the landscape and the geology. They built luxurious acropolises and infrastructure on the surrounding soils (Demakopoulou, 1995; Maran, 2004a, 2004b, 2006, 2010). The soft and arable Upper Pliocene–Quaternary fluvio-torrential–alluvial deposits were used for agricultural purposes (van Andel et al., 1990a; Zangger, 1993; Beaufils, 2000), the construction of Tholos and Chamber tomb cemeteries (Dirlik, 2012; Karkanas et al., 2012), harbor towns (Maran, 2010; Tartaron et al., 2011), a dam (Balcer, 1974; Maroukian et al., 2004), bridges, and drainage and irrigation systems (Hemingway and Hemingway, 2000). Crouch (1996) establishes that both pre-historic and historic Greek cities/settlements followed a series of urban location determinants fixed to geographic setting and karstic geology: these include a defensible site, at a juncture of best water and soil resources, in arable land, on a trade route, suitable for a central palace or urban network, and at a focus of maximum variations.

The Upper Pliocene–Quaternary sedimentary deposits in many Greek sedimentary basins had a significant human impact, as reflected in Mycenaean burial practices. The time period of earliest and latest Mycenaean chamber tomb dates between 1675 BCE to between 1320–1160 BCE (Dirlik, 2012). The burial practices depended on the ability of removing unconsolidated surficial sediments for the building of both, the Tholoi (for royalty) and large Chamber tombs (for families) into a hillside to an underground chamber (Dirlik, 2012; Karkanas et al., 2012). A plethora of Mycenaean Tholos tombs and Chamber tombs exist in the Peloponnese. In the Argive Basin, the Tholos Tombs of Tiryns were within the domain of the Tiryns Acropolis, the Cemetery of Dendra which contains several Tholos and Chamber tombs likely belonging to the Midea Acropolis (Figure 2.1 C-D), and the Mycenae Acropolis had the largest number of tombs within its realm (Mee and Cavanagh, 1984, 1990). Although recognized during archaeological excavations, structural damage (i.e., collapse of roof, dome and/or pillars) to Mycenaean tombs has been assigned to anthropogenic causes (burglary) and soil erosion, but not explicitly documented (Cavanagh and Laxton, 1981; Dirlik, 2012). Conversely, other tombs, like the Treasury of Atreus and the Tomb of Aegisthus at Mycenae, show no signs of structural damage (French, 1996). The abundance and distribution of Mycenaean tombs reveal the geoarchaeological significance of Late Neogene–Quaternary sediments at any given Mycenaean hub. The architectural and engineering achievements of the Mycenaean civilization were possible due to their novel techniques and the availability of construction stone/materials obtained from local quarries as well as their infrastructure (cf. Balcer, 1974; Beaufils, 2000; Varti-Matarangas et al., 2000; Spathari, 2001; Tartaron et al., 2011; Dirlik, 2012).

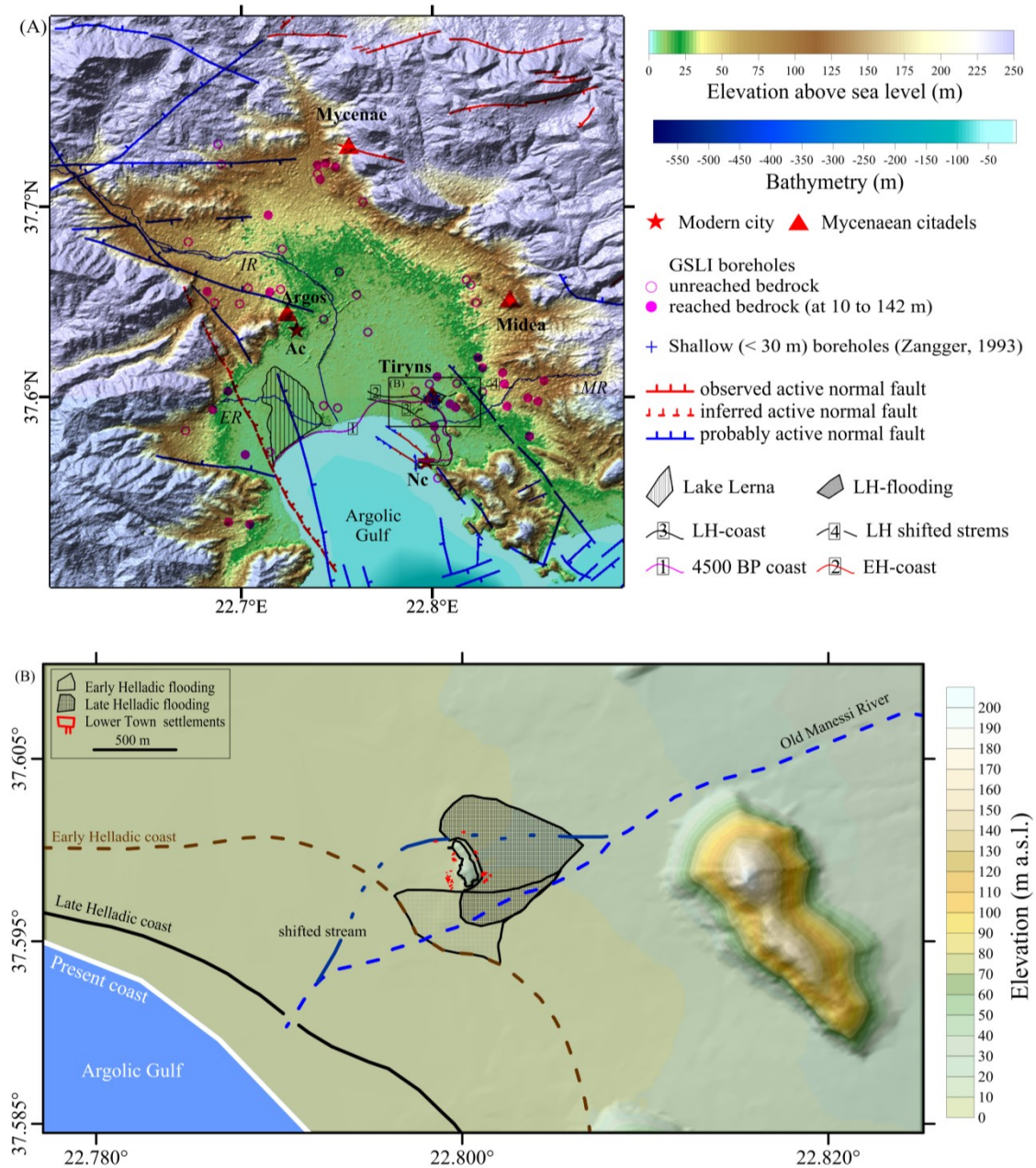


Figure 2.7: (A) Terrain map of the Argive Basin showing the reconstructed paleocoastlines, the location of the ancient Lake Lerna deposits according to Zangger (1993, 1994) and the distribution of boreholes of the GSLI (unpublished data). (B) Reconstruction of Early and Late Helladic coastlines of the eastern Argolic Gulf, flood deposits and ruins of the Lower Town settlement in the vicinity of Tiryns according to Zangger (1993, 1994). Ac = Argos city. Nc = Nafplion city. IR, ER and MR = Inachos, Erasinos and Manessi Rivers, respectively.

2.3 Archaeoseismology: State of the Art

2.3.1 Postulated Evidence of Earthquake-Related Structural Damage to Tiryns and Midea

Historical records suggest that several strong to great earthquakes ($6 \leq M_w \leq 8.5$) have occurred in regions onshore and offshore the Peloponnese, Greece (Ambraseys, 1996; Ambraseys and Jackson, 1990; Papazachos et al., 2000; Ambraseys, 2005, 2006; Stiros, 2010). The historical seismicity of Greece is well-documented back to the year 1000 CE

(Ambraseys and Jackson, 1990; Kouskouna and Makropoulos, 2004) and moderately-documented back to 550 BCE (Di Vita, 1995; Ambraseys, 1996; Papazachos et al., 2000b; Papazachos and Papazachou, 2003). Evidence of seismic activity before 550 BCE might only be extracted from archaeological excavations and paleoseismic studies. Written sources confirming the occurrence of earthquakes in the Mycenaean palatial period do not exist (Ambraseys and Jackson, 1990; Ambraseys, 1996; Kilian, 1996). Instead, the ‘destructive earthquakes’ that presumably occurred during the LH palatial period (Kilian, 1996; Åström and Demakopoulou, 1996; French, 1996; Nur and Cline, 2000; Nur and Burges, 2008) continue to remain speculative rather than evident. These past earthquakes are merely postulated based on archaeological excavation data and field observations from various fortified Mycenaean acropolises throughout Greek territory that show a contemporaneous life-and-destruction cycle occasionally attributed to seismogenic causes. Neither pre-historical (Middleton, 2008, 2012) nor historical information (Kouskouna and Makropoulos, 2004; Stiros, 2010) from Greece provides records for widespread exodus and devastation of civilizations in the aftermath of destructive earthquakes.

The Mycenaean earthquake hypothesis proposes the coseismic structural collapse of several important Mycenaean citadels including Tiryns (Kilian, 1988, 1996), Midea (Åström and Demakopoulou, 1996), Mycenae (French, 1996), Thebes (Sampson, 1996), Teichos Dymaion, Pylos, Nichoria, The Menelaion, Lefkandi, Iolkos, Kydonia, and Knossos (Nur and Cline, 2000) during the LBA, based on destruction layers with supposed indications of earthquake damage. These strata are separated by time intervals in the order of several decades during the palatial and post-palatial periods suggesting that more than one earthquake might have caused the structural damage to Mycenaean settlements (Kilian, 1996; Åström and Demakopoulou, 1996; Stockhammer and French, 2009; Mühlenbruch, 2013; Damm-Meinhardt, in press).

In general, the evidence presented by archaeologists includes tilted and curved walls, human skeletons lying under the debris of presumably collapsed walls and a large assemblage of broken pottery apparently toppled off by ground shaking forces (Kilian, 1996; Åström and Demakopoulou, 1996; French, 1996). Morphotectonic field observations from the eastern Argive Basin suggest the reactivation of the Mycenae normal fault, possibly 5.0 km long, along the eastern flank of Mycenae dated *ca.* 1190 BCE (Papanastassiou et al., 1993; Gaki-Papanastassiou et al., 1996; Maroukian et al., 1996). The dating of this event is based on Mycenaean potsherds found at the lowermost horizon of the fluvio-torrential sediments deposited upstream of the fault scarp. Although both the age and the Mycenaean authenticity of these potsherds have been visually confirmed, no physical dating is available and thus this interpretation remains debatable. Table 2.1 provides a summary of stratigraphic archaeological data used to define destruction layers at several Mycenaean sites. Discrepancies in the dates of the destruction layers arise from site to site likely due to the fact that they were not contemporaneous and/or that the dating of pottery style carries an uncertainty in the order of decades.

Table 2.1: Summary of Late Bronze Age stratigraphic archaeological data interpreted to represent earthquake strata of some Mycenaean sites.

Mycenaean Site	Dated Destruction-layer(s)	Archaeological Evidence	Reference
Tiryns	destruction layers at <i>ca.</i> 1250 BCE, <i>ca.</i> 1200/1190 BCE and in later 12. century BCE (LH IIIC Advanced)	Tilted and curved walls and foundations, immediate building repair after destruction; fallen and broken pottery including figures, figurines, vessels, bowls, tiles; human skeletons of a woman and child presumably killed by a collapsing building; fires. Differential subsidence in coastal Argive Basin. Particularly, the structural collapse of Tiryns is attributed to the <i>ca.</i> 1200 BCE earthquake.	Kilian (1980, 1988, 1996)
Midea	end of LH IIIB2 period (<i>ca.</i> 1200/1190 BCE)	Skeleton of a young girl with skull and backbone smashed under fallen rocks found in one room near the East Gate; fire/ash layer, collapsed, tilted and curved walls, collapsed buildings and East Gate; postulated abandonment of the citadel; broken pottery assemblages; objects such as pottery, clay figurines, stone and bronze tools and an important gold bead found in fill presumably fallen from the upper floor.	Åström et al. (1990); Åström and Demakopoulou (1996); Demakopoulou (2012)
Mycenae	middle of LH IIIB period (<i>ca.</i> 1250 BCE)	Two skeletons inside Mycenae citadel, one skeleton in the adjacent Panagia Houses, and several skeletons in the Plakes House just ~100 m north of Mycenae citadel; building repair work in Mycenae citadel. Site located ~16 km north of Tiryns.	French (1996)
Thebes	LH IIIB period (<i>ca.</i> 1250 BCE)	Carbonized wood/ash layer due to long-lasting fire, collapse of a two-storey building and walls; burned skeleton of a young woman with cracked skull by the collapsed roof; broken mud-bricks and scattered pottery and furniture. Site located 92 km north of Tiryns.	Sampson (1996)
Kalamianos	unconstrained destruction layer(s) (undated)	Extensive number of collapsed stone walls, collapsed roofs, broken ceramic vessels; subsided coastline causing partial submerging of the settlement; postulated abandonment at <i>ca.</i> 1200 BCE due to destruction of the town by yet unknown causes, though human and seismic catastrophe are considered but remain to be ruled out. Site located ~ 35 km northeast of Tiryns.	Tartaron et al. (2011); Dao (2011)

More than one earthquake, of yet unknown parameters, is attributed to the documented structural damage of LH IIIB–C architecture observed at Tiryns and Midea (Kilian, 1983, 1988, 1996; Papanastassiou et al., 1993; Åström and Demakopoulou, 1996; Gaki-Papanastassiou et al., 1996; Maroukian et al., 1996; Nur and Cline, 2000; Nur and Burges, 2008; Hinzen et al., 2015). These include two earthquakes (and possibly a third one) during the palatial period and one earthquake in the post-palatial period (Kilian, 1996; Stockhammer and French, 2009; Mühlenbruch, 2013; Damm-Meinhardt, in press) which presumably damaged the Tiryns citadel. Respectively, they are deduced from three destruction layers dated to LH IIIB Middle (*ca.* 1250 BCE), LH IIIB Final (*ca.* 1200/1190 BCE), and LH IIIC Advanced (later 12th BCE) on the basis of stylistic pottery dating. After the structural collapse of the buildings and related conflagration inside the Tiryns citadel at *ca.* 1200 BCE, the occupation continued although there were definitely major changes. Similarly, settlement continuation is found at Midea and Mycenae after the postulated earthquake at the end of the palatial period (Middleton, 2008, 2012; Demakopoulou, 2012). Figure 2.8 displays the relation of the development of painted pottery and architectural phases at the LC of Tiryns as seen by the excavator (Kilian, 1996).

As mentioned before, the structural collapse of the Cyclopean walls of Tiryns is also taken as archaeoseismic evidence in this study. The preserved position of several fallen blocks of Cyclopean walls from Mycenaean Tiryns and Midea is illustrated in Figure 2.9. However, it

remains unclear if the collapse occurred in response to earthquakes during the LH IIIB, LH IIIC, later, or not due to earthquakes.

A major destruction layer at the neighboring Midea citadel has been interpreted as a sign of a destructive earthquake at the end of the LH IIIB2 period, *ca.* 1200/1190 BCE (Åström and Demakopoulou, 1996; Demakopoulou, 2012). This destruction layer is characterized by ashy, grey soil, mixed with charcoal and other burnt organic material, a skeleton found under debris, and the collapse apparently of the walls (Åström and Demakopoulou, 1996). Intuitively or under mutual influence, archaeologists continue to assume that the *ca.* 1200/1190 BCE earthquake caused the coseismic structural collapse of both Tiryns and Midea citadels; thus marking the transition from the Mycenaean palatial period to the post-palatial period. This is a valid, but yet untested, assumption because both citadels are only 7.0 km apart. Archaeological evidence supports the contemporary existence of both Tiryns and Midea citadels (Demakopoulou, 2012); so both might share the same history of events. The citadels of Mycenae (French, 1996) and Thebes (Sampson, 1996) also show destruction layers attributed to the same postulated earthquake at *ca.* 1200/1190 BCE.

Moreover, excavation data from several Greek well-documented archaeological sites strongly suggest earthquake-related structural damage to buildings that pre-date and post-date the Mycenaean civilization. To name a few, these include the EBA (*ca.* 3200–2050 BCE) sites of Ayios-Dhimitrios and Voidokoilia located in southwestern Peloponnese (Zachos, 1996); Thebes located north of the city of Corinth (Sampson, 1996); and at least three towns in west Crete (365 CE) (Stiros, 2010). The combination of the postulated earthquake-related structural damage observed at pre-Mycenaean, Mycenaean and post-Mycenaean sites yield a catalog of pre-historic earthquakes in the EBA and LBA with an apparent gap in the MBA cultural period. This gap is probably due to a lack of evidence for settlement structures during this period (built over Mycenaean times).

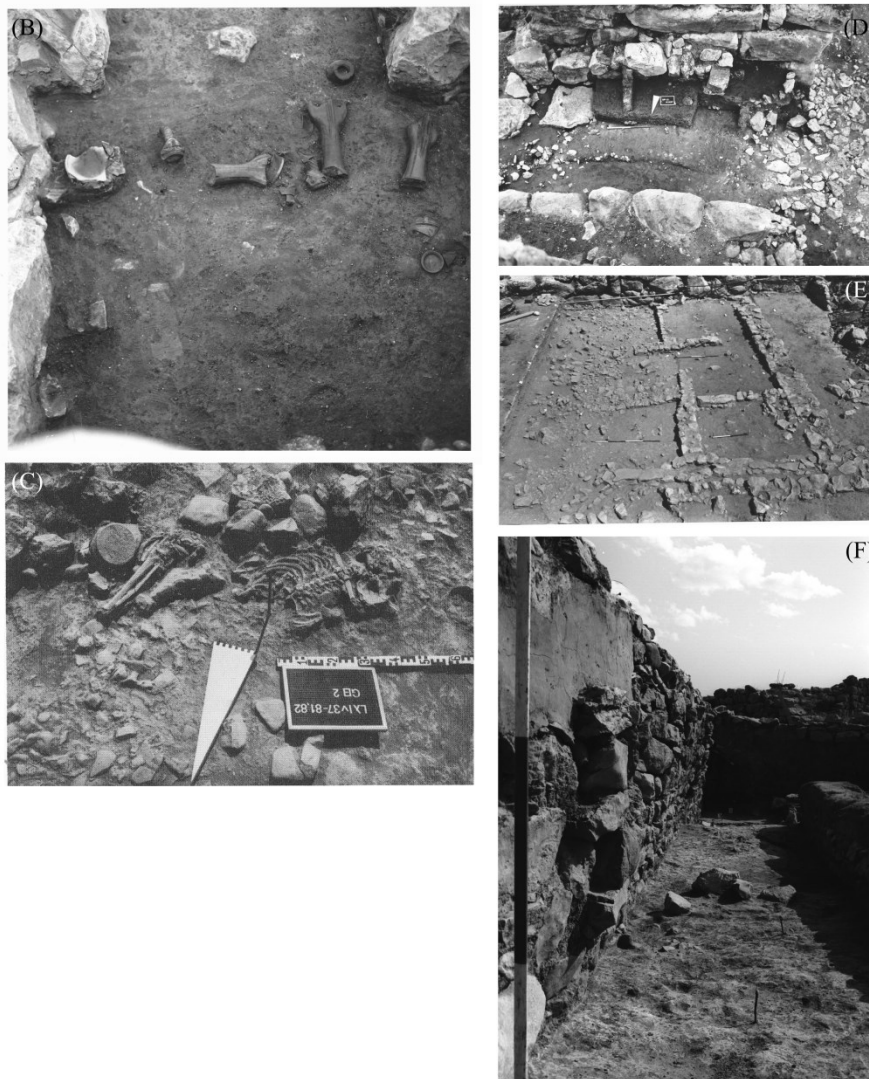
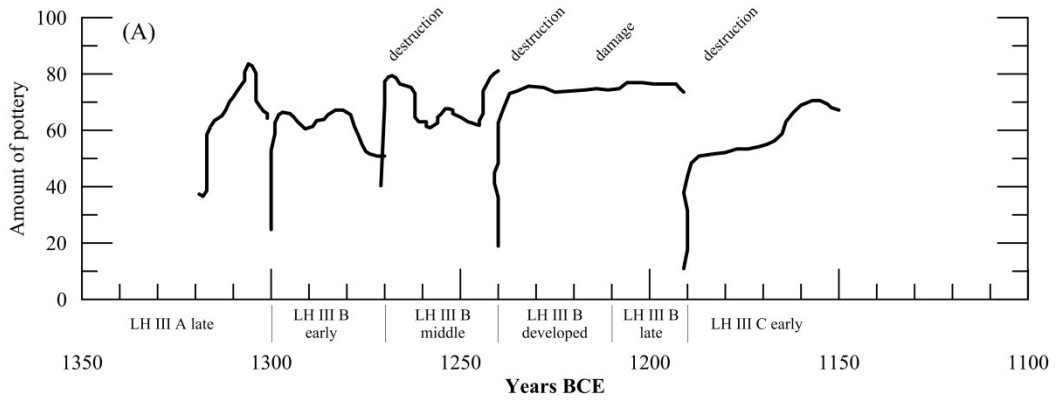


Figure 2.8: (A) The floruit phases of painted pottery at Mycenaean Tiryns in LH IIIA late to LH IIIC early in relation to percent of building destructions (after Kilian, 1988, 1996). (B) Excavation photographs of Room 110 in the LC showing Mycenaean terracotta figures and vessels (photograph courtesy of the German Archaeological Institute [DAI]–Athens [Ti-1976-140-54]). (C) Skeletons of a woman and child killed and buried presumably by fallen walls (photograph courtesy of the DAI–Athens [80.9/67–68]) (scale 1.0 m, white triangle points north). (D) Curved and collapsed walls at the Main Gate of the UC (photograph courtesy of the DAI–Athens [Ti-1983-019]). (E) Undulating walls and corners not at right angles in Building X inside the LC (photograph courtesy of the DAI–Athens [Ti-1980-012-04]). (F) Westward and eastward tilted walls of corridor in Building VI inside the LC (photograph courtesy of the DAI–Athens [Ti-1980-017-64]).

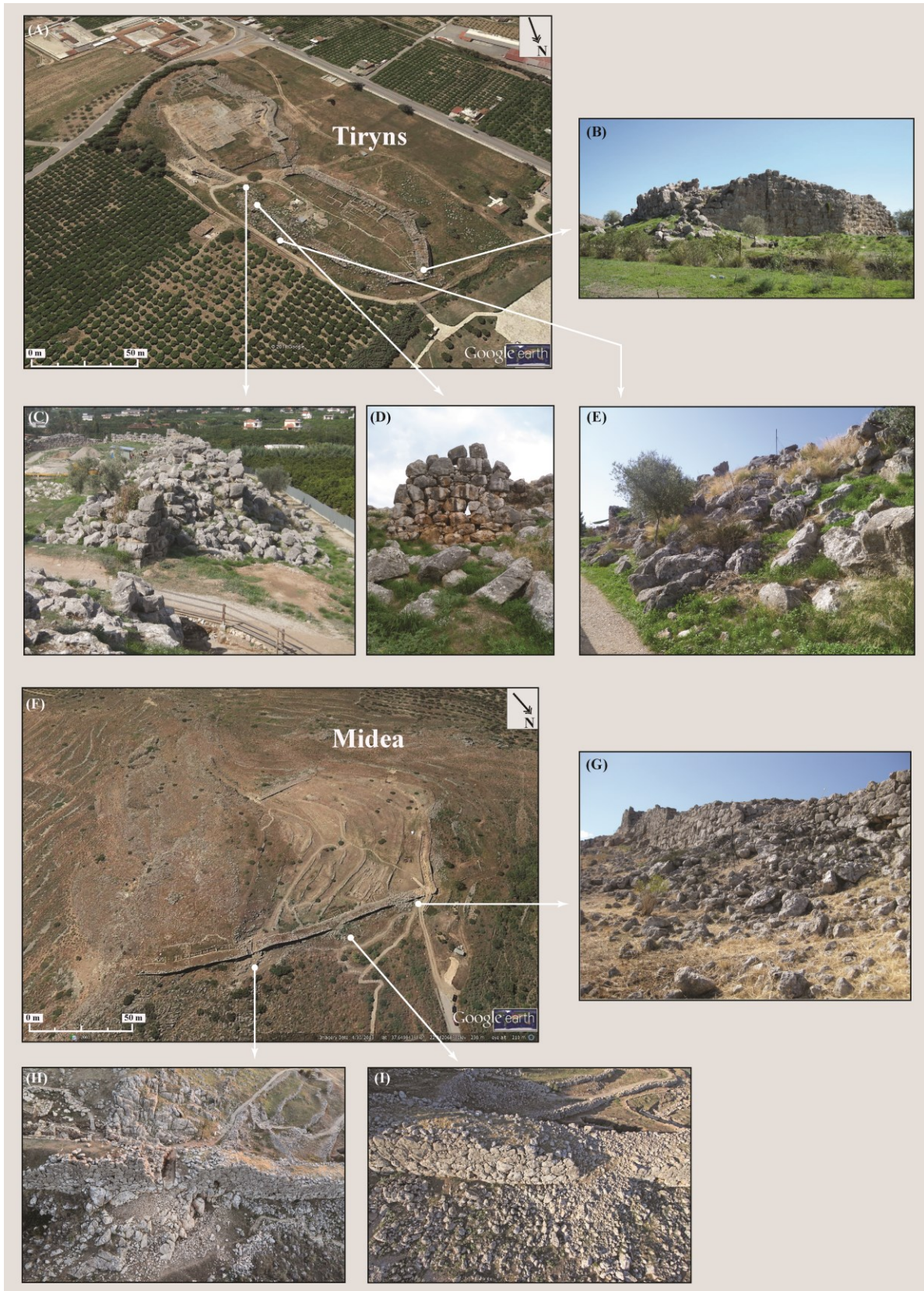


Figure 2.9: Satellite photograph of the Tiryns and Midea citadels showing the position of several collapsed blocks of the Cyclopean wall of Tiryns (A to E) and Midea (F to I). Photograph credits: author (B), K.-G. Hinzen (C, D, G, and E) and K. Xenikakis (H and I).

2.3.2 Previous Examination of the Mycenaean Earthquake Hypothesis

A few archaeoseismological studies have examined the Mycenaean earthquake hypothesis, and some detailed geophysical-geotechnical investigations (tailored to local site effects) shed some light on the behavior of the ground surface under seismic loading in the Argive Basin. These studies include the following ones.

Kalytta (2014) determined empirical local site effects at the Tiryns and Midea citadels caused by local earthquakes ($M_L \leq 4.3$) with epicentral distances < 100 km. Eighteen seismic events were selected from the earthquake database of Voigt (2013) and processed using the reference-site Standard Spectral Ratio (SSR) and the non-reference Horizontal-Vertical Spectral Ratio (HVSR) methods. Site amplification factors were determined for locations inside and outside the citadels using the SSR method with the reference station located at Tiryns hill. The amplitude of the HVSR peak at the resonance frequency was also determined for the same stations. Figure 2.10 summarizes the main spectral peaks determined from both methods. In Tiryns, the SSR method yields an amplification factor of 8.5 at a frequency of 6.5 Hz on a flat region containing unconsolidated stream deposits directly northeast of the citadel. Topographic amplification effects are detected at Midea. The station at the southern foothill yields an amplification factor of 6.6 (N component) at a frequency of 34.0 Hz attributed to a 2.0 to 3.0 m thick layer of Quaternary sediment over bedrock. The station at the hilltop produces ground motion amplifications of a factor of 2.0 to 3.0 at frequencies between 1.0 to 3.0 Hz. Also in Midea, the direction of incoming ground motion likewise affects the level of amplification related to topographic site effects. The combination of the SSR and HVSR methods allowed the distinction between geologic and topographic site effects at both citadels (Kalytta, 2014).

Hinzen et al. (2015) tested the probability of toppling Mycenaean terracotta figures and clay vessels found in a room within the LC of Tiryns. In their numerical simulations, the artifacts stand on a bench and are excited by seismic ground motions based on instrumentally recorded Greek earthquakes and find that the simulated thrown position of the toppled objects do not match the original spots found by the excavators; therefore, refuting the hypothesis of Kilian (1980, 1996) that these figures and vessels were toppled by an earthquake. Papadopoulos (1996) utilizes 20th century seismic intensities and their frequency distribution to calculate the probability that at least one earthquake (intensity > 6) occurred in one of all the Mycenaean regions in a time interval of 30 and 100 years during the end of the late LBA period. The calculated probability ranges between 0.744 and 0.990 for 30 years and between 0.992 and 0.999 for 100 years. Nur and Cline (2000) and Nur and Burges (2008) argue that the rupture of one or more $M_w \geq 6$ earthquakes closely-spaced in time (decades) could have caused the partial or total structural damage to several LBA man-made structures during the end of the LBA in Aegean and Eastern Mediterranean regions. These authors rely on superimposed patterns of instrumental seismicity and maximum intensity of seismic ground motion against the location of several LBA major sites; however, this rather qualitative method only highlights a long-known and obvious fact (e.g., Mycenaean citadels are located 40 to 300 km from active seismic source zones). Although not tailored to tackle archaeoseismological questions, the recent detailed geophysical–geotechnical studies of Karastathis et al. (2010a,

2010b) determine that the cohesive sandy-clayey soils in the coastal zone of Nafplion city are prone to strong ground-motion amplification of up to 4.5 at soils-sites of B class (i.e., rock) and subsequent highly probable soil-liquefaction during the rupture of shallow strong local earthquakes ($M_w \geq 6.3$) with an epicentral distance ≤ 70 km from Tiryns. These workers identify nearby strike-slip faults in the southeastern Argolis Peninsula and normal faults in the eastern Gulf of Corinth as potential sources. Due to the close proximity to Tiryns (< 3.0 km) and nearly similar soil site conditions, these studies provide clues about the possible seismic response during dynamic loading of the Pleistocene–Holocene soils that occur around the Tiryns citadel. Other seismic site amplification studies, done for class C soil-sites (i.e., very stiff soil–hard soft soils or soft rock), in adjacent Late Neogene–Quaternary structural basins with geological conditions comparable to the Argive Basin yield mean site amplification factors of nearly 1.5 to 5.5 for the 1.0 to 10.0 Hz frequency range (Gariel et al., 1991; Pitilakis et al., 1992; Margaris and Boore, 1998; Roumelioti et al., 2004a).

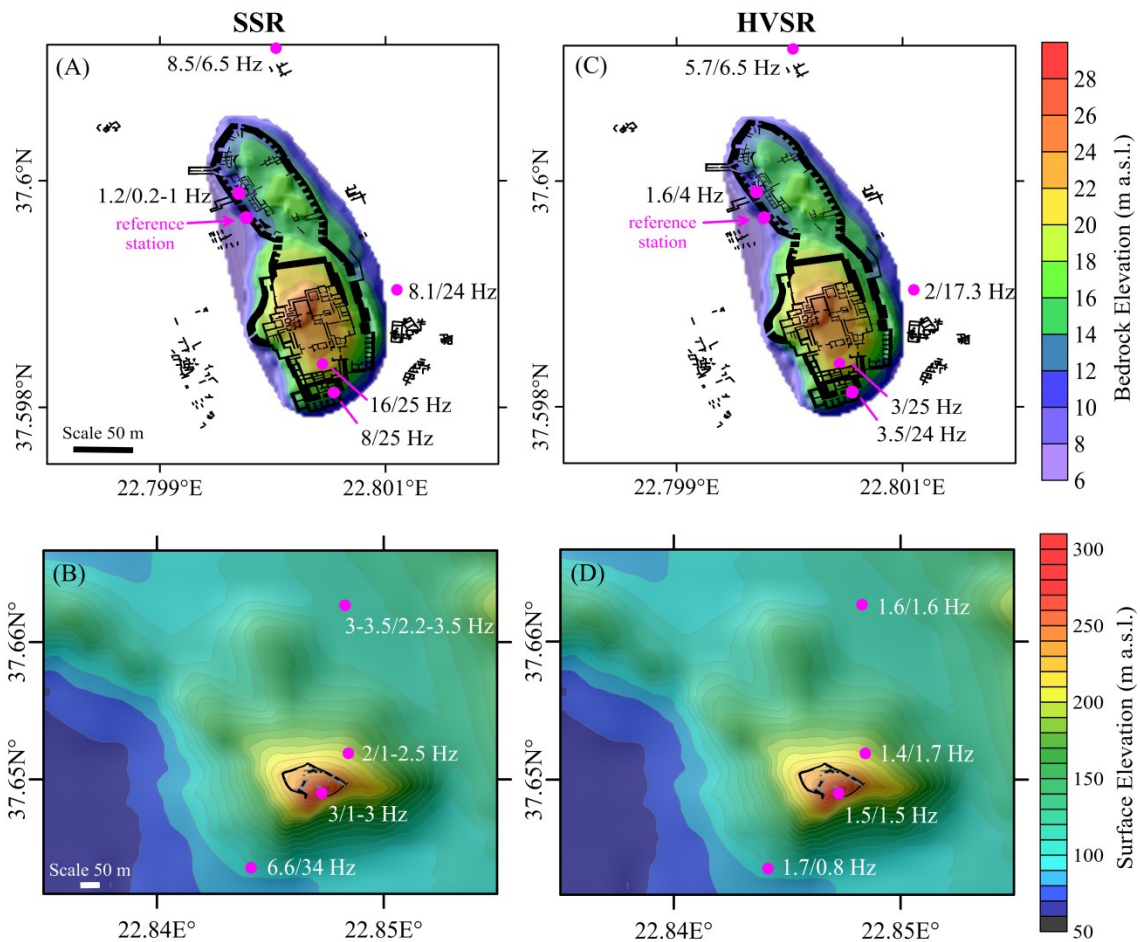


Figure 2.10: (Left column) Site amplification factors determined with the reference-site Standard Spectral Ratio (SSR) method for Tiryns (A) and Midea (B). (Right column) Amplitude of Horizontal-Vertical Spectral Ratio (HVSR) peak at the resonance frequency for Tiryns (C) and Midea (D). The magenta circles mark the location of the stations. Numbers next to the stations give the amplification factor for the N-S component and the frequency at which it is observed using the SSR method and the amplitude of the HVSR peak at the resonance frequency, respectively (data after Kalytta, 2014). Archaeological plan of Tiryns and Midea after Maran (2010) and Demakopoulou (2012), respectively.

Recently, Hinzen et al. (submitted) determined small to moderate local seismic site effects at Tiryns and Midea from the combined results from, small local earthquakes ($1.6 < M_w < 4.9$), measurements of ambient noise, and 1D forward modeling. The earthquake data was recorded at ten stations during a nine month deployment, the ambient noise was measured at 182 single stations and six station arrays, and 1D forward modeling was done using an acceleration sweep signal (input time series) with logarithmically increasing frequencies from 0.2 to 20 Hz and varying levels of ground-motion (0.01, 0.1, 0.25, 0.5, and 0.8 *g*). Forward modeling predicts factors of 2.0 and 2.3 at 2.2 and 5.6 Hz, respectively, in the LC of Tiryns and an amplification factor of 2.0 at 6.5 Hz at a site in its UC. Spectral ratios of local earthquake signals at the same sites referred to records at a station at the base of the Tiryns hill show smaller amplifications at the LC (1.4 at 6.2 Hz) and basically no amplification at the UC site. Specially, the LT of Tiryns was at a higher hazard level than the citadel itself, including the Cyclopean walls, which are built on the outcropping limestone (Hinzen et al., submitted). Further, the results from spectral ratios and forward modeling from measuring sites at the foothills of the Midea ridge yield amplifications smaller than 2.0 (with respect to the reference station at Tiryns) between 0.2 to 20.0 Hz. Amplifications increase upslope up to 2.1 and 3.0 at the flank of the hill and its summit, respectively. These are the maximum values of a broad peak in the amplification functions of the horizontal components of both locations between 0.8 Hz and 3.5 Hz. They attributed these amplifications due to topographic effects of the nearly 270 m high ridge.

3. GEOLOGIC SETTING AND SEISMICITY OF THE ARGIVE BASIN

3.1 Geology

The Argive Basin (AB) is in the western Argolis Peninsula of the Peloponnese, Greece. The geologic record of the Argolis Peninsula includes several tectonic events: Mesozoic rifting, passive margin evolution, ophiolite emplacement leading to the closure of oceanic tracks in the west and east and continental collision followed by middle Cenozoic-to-present normal faulting and arc volcanism (Jacobshagen, 1986; Clift and Robertson, 1990). Further, the basement of the AB consists of an assemblage of folded and tectonically fractured thrust sheets stacked during the Alpine orogeny. Structurally, from bottom to top these include (i) the basal 1700 m thick Upper Triassic–Upper Jurassic Lower Unit, (ii) followed by the roughly 300 m thick Middle Upper Jurassic–Early Eocene Middle Unit, and (iii) the approximately 500 m thick Upper Jurassic–Upper Cretaceous Upper Unit. The Lower Unit is composed of the Pantokrator Limestone (~1000 m thick) *ca.* 245-164 Ma overlaid by the Kimmeridgian to Tithonian (*ca.* 155-145 Ma) greenschist facies clastic Potami Formation (~700 m thick) (Bachmann and Risch, 1979; Jacobshagen, 1986; Clift and Robertson, 1990; Photiades and Skourtsis-Coroneou, 1994; Saccani et al., 2003; Photiades, 2010). The Middle Unit is composed of an Albian-Cenomanian to Paleocene-Middle Eocene (*ca.* 99-40 Ma) Mesoautochthonous Carbonate Sequence (~100 m thick) overlaid by post-Early Eocene (*ca.* 58-40 Ma) continental flysch deposits (< 200 m thick) (Tataris et al., 1970; Photiades and Skourtsis-Coroneou, 1994; Clift, 1996; Saccani et al., 2003; Photiades, 2010). The Upper Unit consists of an Upper Jurassic (*ca.* 161-145 Ma) ophiolitic *mélange* (< 100 m thick) capped by a Middle Cenomanian to Middle Maastrichtian (*ca.* 96-67 Ma) Carbonate Sequence (~300 m thick), in turn covered by Middle Turonian to Middle Maastrichtian (*ca.* 90-67 Ma) ~50 m thick Pelagic sediments (Photiades and Skourtsis-Coroneou, 1994; Saccani et al., 2003; Photiades, 2010).

The outcropping bedrock of the AB is folded, tectonically fractured, and moderately-to-highly weathered (Jacobshagen, 1986; Apostolidis and Koutsouveli, 2010; Photiades, 2010). The bedrock is mainly composed of Triassic–Upper Cretaceous strongly karstified limestones thrust against Paleogene continental flysch deposits (Papastamatiou et al., 1960; Tataris et al., 1970). It is in angular unconformity with an Upper Pliocene–Quaternary sedimentary sequence of terrestrial and marine origin of poorly known thickness and geometry (van Andel et al., 1990a, 1990b, 1993; Zangger, 1993; Apostolidis and Koutsouveli, 2010).

The southern edge of the AB is a 10 km long coastline and marks the Pliocene–Pleistocene sediment wedge of the Argolic Gulf (AG). Both the AB and the AG form a south-widening, fault-bounded Late Neogene–Quaternary extensional sedimentary basin (van Andel et al., 1990b, 1993; Photiades and Skourtsis-Coroneou, 1994; Papanikolaou et al., 1994; Mitropoulos and Zananiri, 2010; Georgiou and Galanakis, 2010). Sedimentation in the AB started in the Pliocene (Zangger, 1993) with seasonal rivers draining the surrounding Upper Triassic–Eocene bedrock (van Andel et al., 1990, 1993a, 1990b; Maroukian et al., 2004). Consolidated marl, sandy marl, conglomerates and sandstones of continental and lacustrine origin and some volcanic clasts make up the Upper Pliocene sediments (van Andel et al., 1993; Clift, 1996). The Quaternary sediments are composed of a well consolidated

Pleistocene sequence of > 20 m thick marine transgressive/regressive of clays, sands, silts, and gravels followed by terrestrial alluvial terraces (Zangger, 1993). This sequence is covered by Holocene unconsolidated marsh to fluvio-torrential-alluvial surface deposits of coastal and terrestrial origin composed of chaotically interbedded clays, silts, sandy-silts, sandy-clays, sandy-gravels, subordinate pebbly gravel-silts and lesser silty-sands (Tataris et al., 1970; Kraft et al., 1977; van Andel et al., 1990b, 1993; Zangger, 1993; Apostolidis and Koutsouveli, 2010; Ntageretzis, 2014). The geomorphologic nature of these sediments is diagnostic of a debris-flow-dominated alluvial fan (Boggs, 2001). Holocene subsidence rates in the AB increase from north to south along its western and eastern flanks from 50-100 to 10-150 cm/ka, respectively, while the center subsides slower (10-20 cm/ka) (Finke, 1988). Figure 3.1 and Figure 3.2 show a simplified geologic map and a composite lithostratigraphic column of the whole AB, respectively.

Deep boreholes (≥ 40 m) drilled by the Greek Service of Land Improvement (GSLI, unpublished data) around the AB and shallow borings (≤ 30 m) drilled around the Tiryns archaeological site (Zangger, 1993; Ntageretzis, 2014) constrain the subsurface stratigraphy of the AB and the Tiryns site, respectively (Figure 3.3). The deep boreholes are presented and described in detailed in Figure 3.4. They clearly indicate an irregularly thick Late Neogene–Quaternary clastic sequence with extremely heterogeneous texture unconformably deposited on uneven shallow-to-deep bedrock likely due to the tectonic history of the area. Similarly, the shallow borings of Zangger (1993) and Ntageretzis (2014), which they described in detailed, illustrate that the soil-bedrock boundary deepens away from the Tiryns ridge.

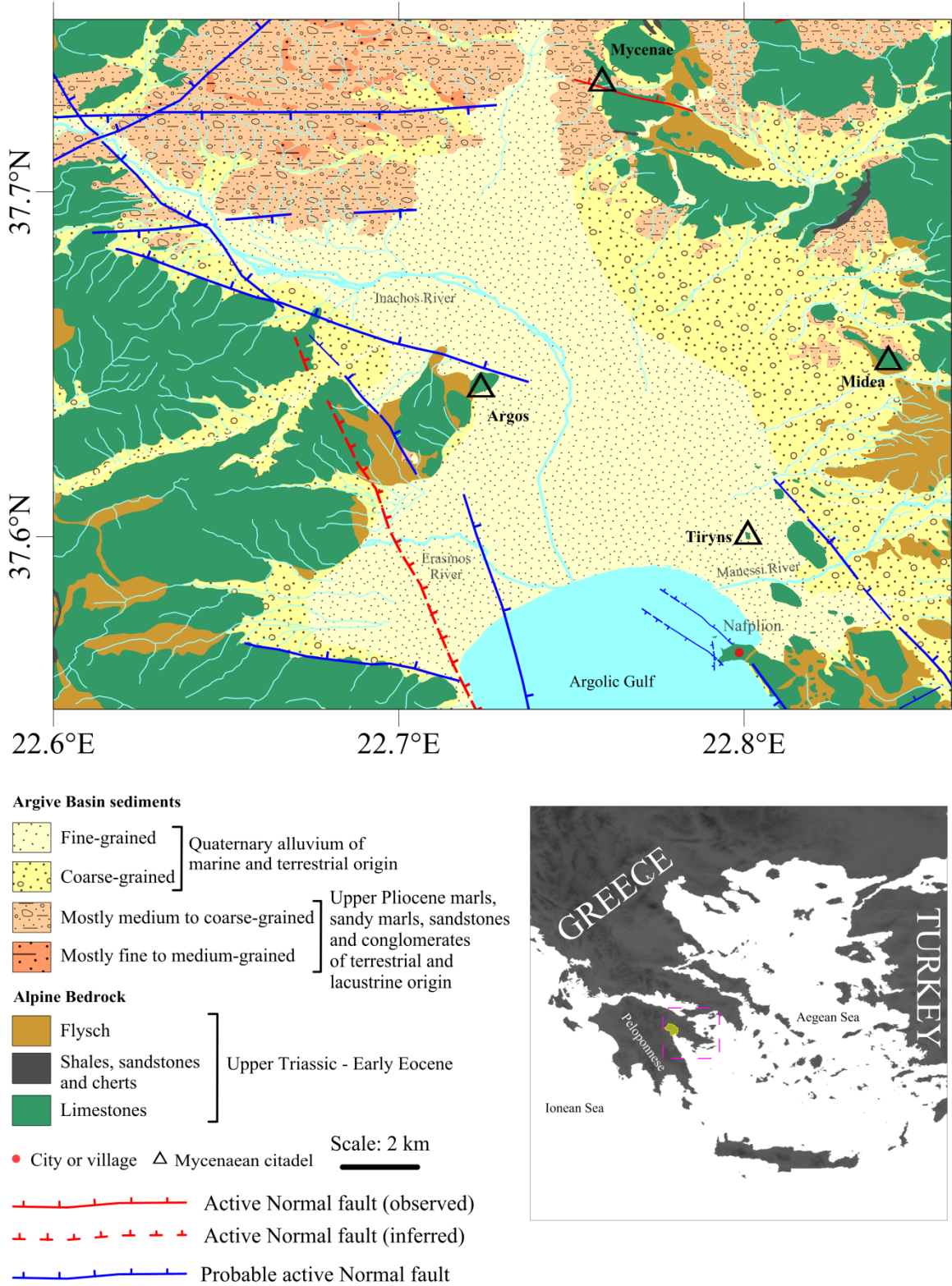


Figure 3.1: Simplified geologic map of the Argive Basin of the Argolis Peninsula (Peloponnese, Greece) (*top*) (after Papastamatiou et al., 1960; Tataris et al., 1970; Georgiou and Galanakis, 2010). Overview map (*bottom-right corner*) of Greece highlighting the location of the Argive Basin (yellow) within the Argolis Peninsula (magenta square).

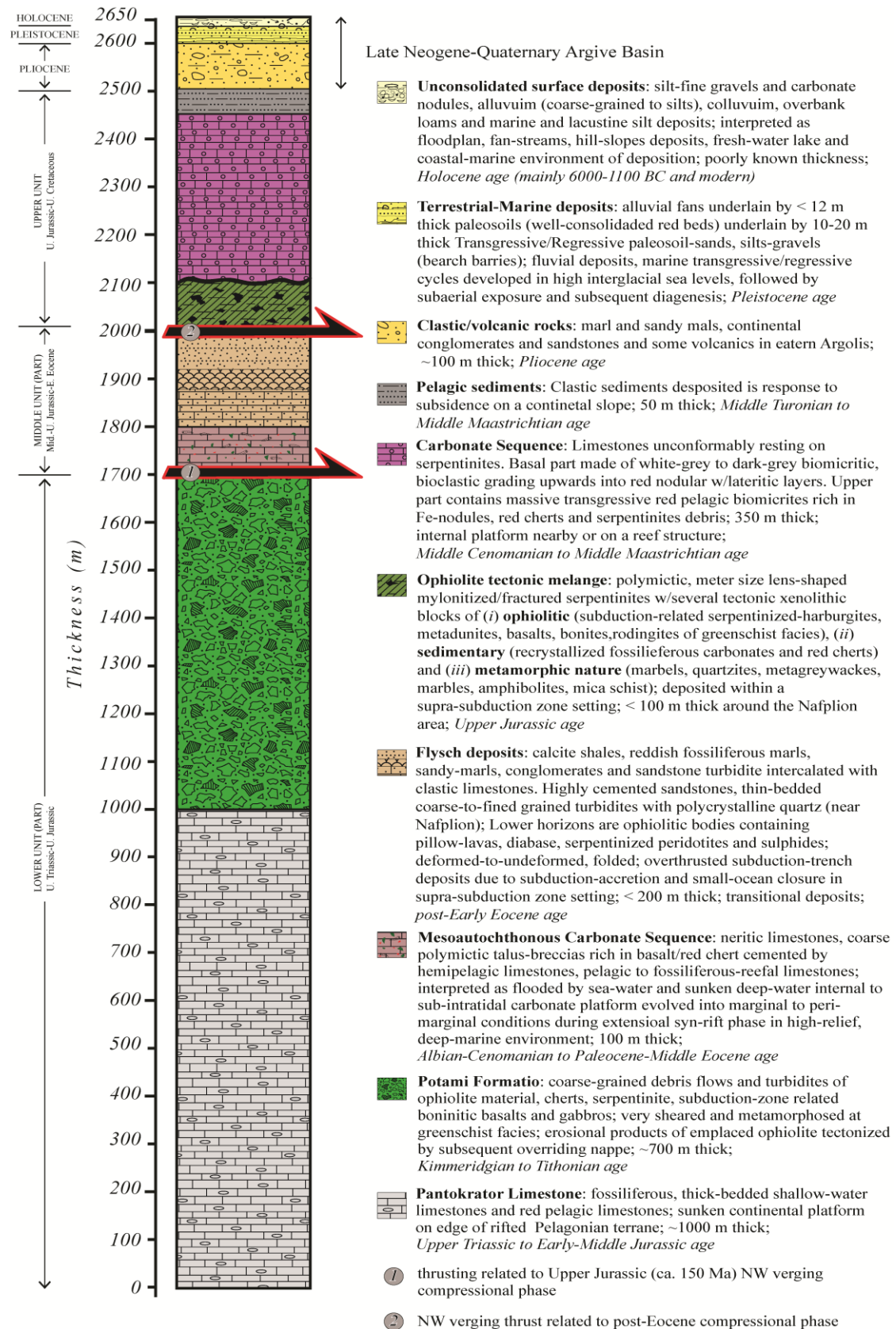


Figure 3.2: Composite lithostratigraphic column of the Argive Basin of the Argolis Peninsula (Peloponnese, Greece) (compiled from Papastamatiou et al., 1960; Tataris et al., 1970; Kraft et al., 1977; Craft and Robertson, 1990; Zangger, 1993; van Andel et al., 1993; Photiades and Skourtis-Coroneou, 1994; Clift, 1996; Saccani et al., 2003; Photiades, 2010).

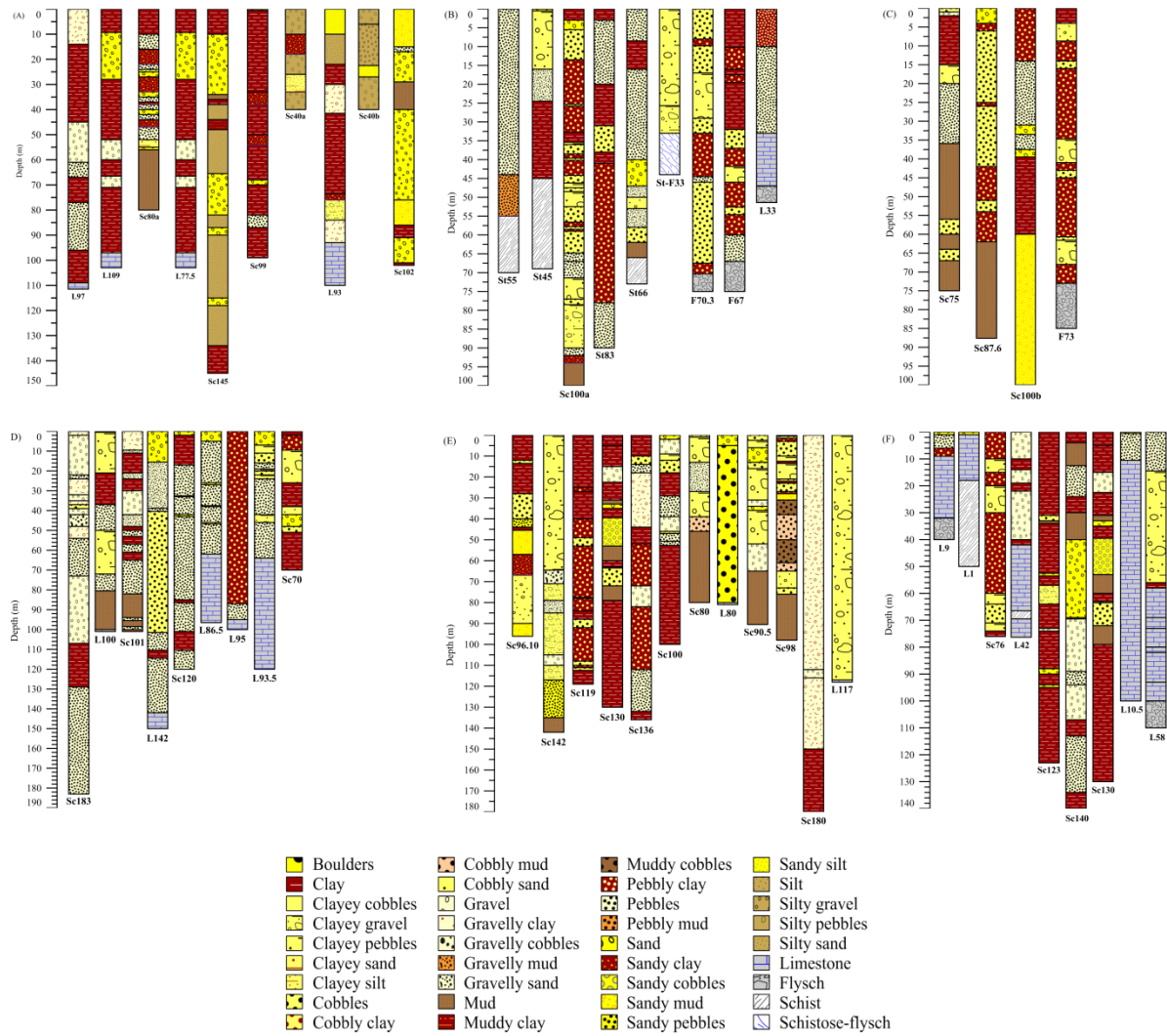


Figure 3.4: Explained deep geologic boreholes drilled in the Argive Basin of the Argolis Peninsula (Peloponnese, Greece). The alphanumeric label at the base of each borehole corresponds to the same label as in Figure 3.3A.

In particular, the alluvial soils that surround the Mycenaean citadels of Tiryns and Midea are geomorphologically distinct. The soils surrounding Tiryns define the flat topography and are fine-grained mainly characterized by clays, silty clays, muds, clayey silt, fine sands, sandy gravels, and coastal sand dunes (Papastamatiou et al., 1960; Tataris et al., 1970; van Andel et al., 1990a, 1990b, 1993; Zangger, 1993; Apostolidis and Koutsouveli, 2010; Ntageretzis, 2014). The soils surrounding Midea represent alluvial fan deposits closer to the sediment source primarily composed of marls, sandy marls, very coarse sands, very coarse gravels, and pebbly to coarse conglomerates (Tataris et al., 1970; van Andel et al., 1990a, 1990b, 1993; Zangger, 1993; Apostolidis and Koutsouveli, 2010). Thus, the soils around Tiryns and Midea classify as *cohesive soils and granular soils*, respectively, following the Unified Soil Classification System (see Table 3.1). Further, from the geotechnical earthquake engineering point of view, the shear-wave velocity (v_s) is lower for the soils around Tiryns and higher for the soils around Midea. This is a trend observed in adjacent continental basins of comparable geologic and geomorphologic setting (Koçkar and Akgün, 2012; Stewart et al., 2014) and at a

global scale (Wald and Allen, 2007). The transition from cohesive to granular soils is best defined by a northwest-southeast trending stratigraphic contact that passes northeast of Tiryns. This can be seen in the detailed geologic map of eastern AB (Figure 3.5). Furthermore, in an archaeoseismological context, the ground surface and undulating bedrock vary significantly within the area encompassing Tiryns and Midea (Figure 3.6). These factors are expected to impose local seismic site effects during dynamic loading of the ground surface.

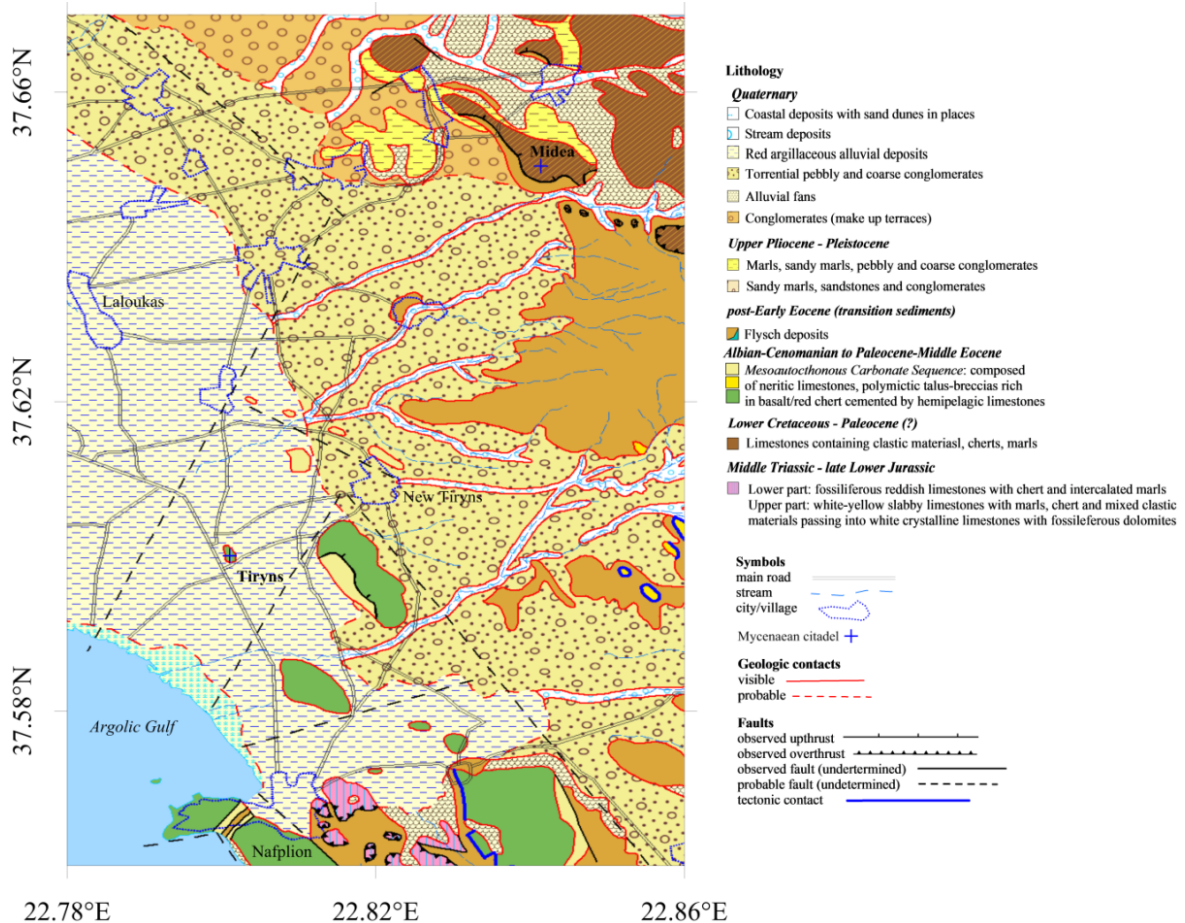


Figure 3.5: Geologic map of the eastern Argive Basin of the Argolis Peninsula (Peloponnese, Greece) depicting the location of the Mycenaean citadels of Tiryns and Midea (modified after Tataris et al., 1970).

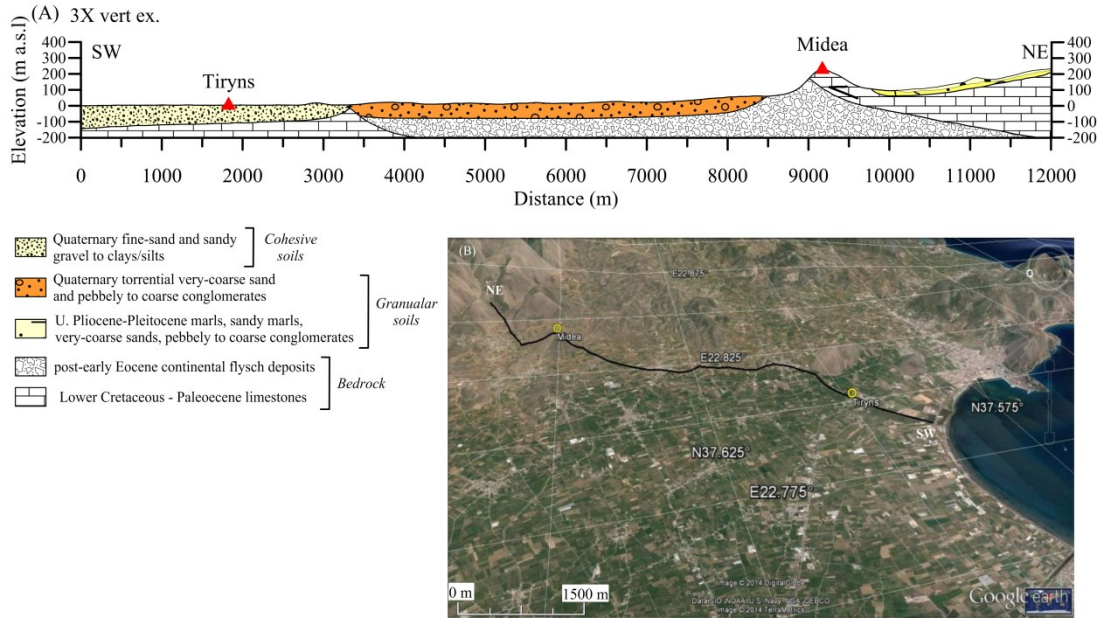


Figure 3.6: (A) Geologic profile illustrating the geometry of the cohesive and granular soils, and the bedrock structure between Tiryns and Midea. (B) Satellite photo from Google Earth® showing the orientation of the geologic profile with view from the west at an eye altitude of 1.70 km and elevation exaggeration of 3×.

Table 3.1: Soil classification used in engineering and geology to describe the texture and grain size of unconsolidated soil deposits by the Unified Soil Classification (USC) system (from ASTM D 2487).

Major divisions		USCS Group symbol	USCS Group name	Void ratio Min. Max.
Coarse grained (granular) soils more than 50% retained on or above No. 200 (0.075 mm) sieve	gravel > 50% of coarse fraction retained on No. 4 (4.75 mm) sieve	GW	Well graded gravel, sandy gravel, with little or no fines	0.26 0.46
		GP	Poorly graded gravel, sandy gravel, with little or no fines	0.26 0.46
		GM	Silty gravels, silty sandy gravels	0.18 0.28
		GC	Clayey gravels, clayey sandy gravels	0.21 0.37
	sand ≥ 50% of coarse fraction passes No. 4 sieve	SW	Well graded sands, gravelly sands, with little or no fines	0.29 0.74
		SP	Poorly graded sands, gravelly sands, with little or no fines	0.30 0.75
		SM	silty sand	0.33 0.98
		SC	clayey sand	0.17 0.59
Fine grained (cohesive) soils 50% or more passing the No. 200 sieve	silt and clay liquid limit < 50	ML	inorganic silts, silty or clayey fine sands, with slight plasticity	0.26 1.28
		CL	inorganic clays, silty clays, sandy clays of low plasticity	0.41 0.69
		OL	organic silts and organic silty clays of low plasticity	0.74 2.26
	silt and clay liquid limit ≥ 50	MH	inorganic silt of high plasticity, elastic silt	1.14 2.10
		CH	inorganic clay of high plasticity, fat clay	0.63 1.45
		OH	organic clay of high plasticity, organic silt	1.06 3.34
Highly organic soils	Pt	peat		

3.1.1 Near-Surface Geology at Tiryns and Midea

In this study, structural geologic mapping was done at six well-exposed outcrops (numbered 1 to 6) along the western and southern flank of the Tiryns limestone ridge or bedrock (Figure 3.7A) and at adjacent topographic highs (i.e., outcropping bedrock). The eastern flank of the Tiryns ridge was highly vegetated during the field campaign. The studied outcrops contain primary geologic structures such as ordinary parallel joints, conjugate joint sets, and various previously undocumented sedimentary structures discussed by Hinojosa-Prieto and Hinzen (2015). Collectively, both the available and new geologic data are essential for interpreting the seismic velocities of the limestone bedrock and for the construction of a comprehensive geotechnical model of the Tiryns archaeological site.

Available shallow borings (Zangger, 1993) and the detailed structural geologic mapping (Hinojosa-Prieto and Hinzen, 2015) at the Tiryns ridge indicates (i) that the geologic contact between the Quaternary fine-grained soils and the bedrock is an angular unconformity; (ii) no evidence of faulting was found at the surface; (iii) the limestones vary from mudstones to wackestones under Dunham's classification of carbonates; and (iv) that the nearly 300 m long limestone ridge is composed of shallow to moderate, south-dipping, thickly to very thickly bedded, tectonically jointed, low-energy, poorly-fossiliferous limestone beds. Clearly, the weathered joints and all karstic features indicate limestone dissolution; which might have started as early as the Upper Cretaceous or during the opening of the AB in the Late Neogene. Figure 3.7B shows an example of a typical outcrop (#3) with the nearly orthogonal geometric relationship between the bedding planes and the joint planes. Figure 3.7C illustrates that bedding in all outcrops strikes dominantly E-W with variations to the NS and SE and dips consistently southwards. Three groups of joints are identified on the basis of type and orientation, as seen in Figure 3.7D: (i) a dominant population of planar joints oriented EW; (ii) also planar joints oriented NE-SW; and (iii) conjugate joint sets oriented NW-SE, which are the least abundant. Both the wide spacing between the bedding planes and the joints creates naturally equidimensional blocks of limestone that permitted the Mycenaeans the quarrying of large blocks suitable for the construction of the cyclopean wall (see Figure 3.7B) (cf. Varti-Matarangas et al., 2000; Beaufils, 2000; Tartaron et al., 2011) and other infrastructure (Karo, 1934; Balcer, 1974; Maroukian et al., 2004; Dirlik, 2012).

The sedimentary structures observed at the Tiryns locality include algae, calcified gastropod shells, disarticulated gastropod shells, thin fine-grained calcite veins, thick coarse-grained calcite veins, geopetal structures, bedding planes and karstic features such as potholes and vugs near bedding planes, pressure dissolution seams and rillenkarren. Some of these karstic features have also been mapped at the Kalamianos harbor town located 35 km northeast of Tiryns (Tartaron et al., 2011). The bedding-joint network, the sedimentary structures and all the karstic features affect the rock mass quality of the limestone bedrock formation; therefore, they are interpreted to contribute to its natural porosity and overall hydrologic permeability of the bedrock formation.

Detailed structural geologic mapping south-southeast and east of the Tiryns citadel documents several active and probably active normal dip-slip faults of presumed Late Neogene–

Quaternary age (Georgiou and Galanakis, 2010). In addition, a postulated buried normal fault detected by a three-dimensional (3D) gravity survey occurs about 2 km south of Tiryns (Karastathis et al., 2010a, 2010b). The geologic mapping at the Tiryns citadel does not provide evidence of gravitational movements along observed fractures.

Shallow borings (< 30 m depth) and trenches immediately outside the Tiryns citadel reveal the stratigraphy down to the Late Pleistocene–Holocene stratigraphic boundary (Zangger, 1993, 1994; Ntageretzis, 2014), and coupled with available upfront geotechnical (Apostolidis and Koutsouveli, 2010) and geophysical data (Karastathis et al., 2010a, 2010b) the top of the bedrock is identified. The stratigraphy within the vicinity of the Tiryns citadel comprises 0.30 to 4.0 m of post-Mycenaean soils of which 0.50 to 3.0 m are modern gravelly topsoil covering Holocene fine-grained alluvium 3.0 to 7.0 m thick. The alluvium is composed of chaotically interbedded, poorly sorted heterogeneous fine-grained soils with textures including silts, sandy-silts, sandy-clays, minor pebbly gravel-silts and lesser silty-sands deposited in the second-half of the LH IIIB period either during or shortly after the construction of the final palace (Zangger, 1993, 1994). The alluvium overlays < 8.0 m thick Late Pleistocene well-consolidated red clays/silts (paleosoils) of poorly estimated thickness and geometry prior to this study (chapter 4 discusses this aspect). Finally, these paleosols are unconformably deposited over weathered, highly fractured, thickly-bedded, and shallowly south-dipping *ca.* 97-94 Ma limestone bedrock (Hinojosa-Prieto and Hinzen, 2015). Figure 3.8A illustrates the geologic stratigraphy of Tiryns.

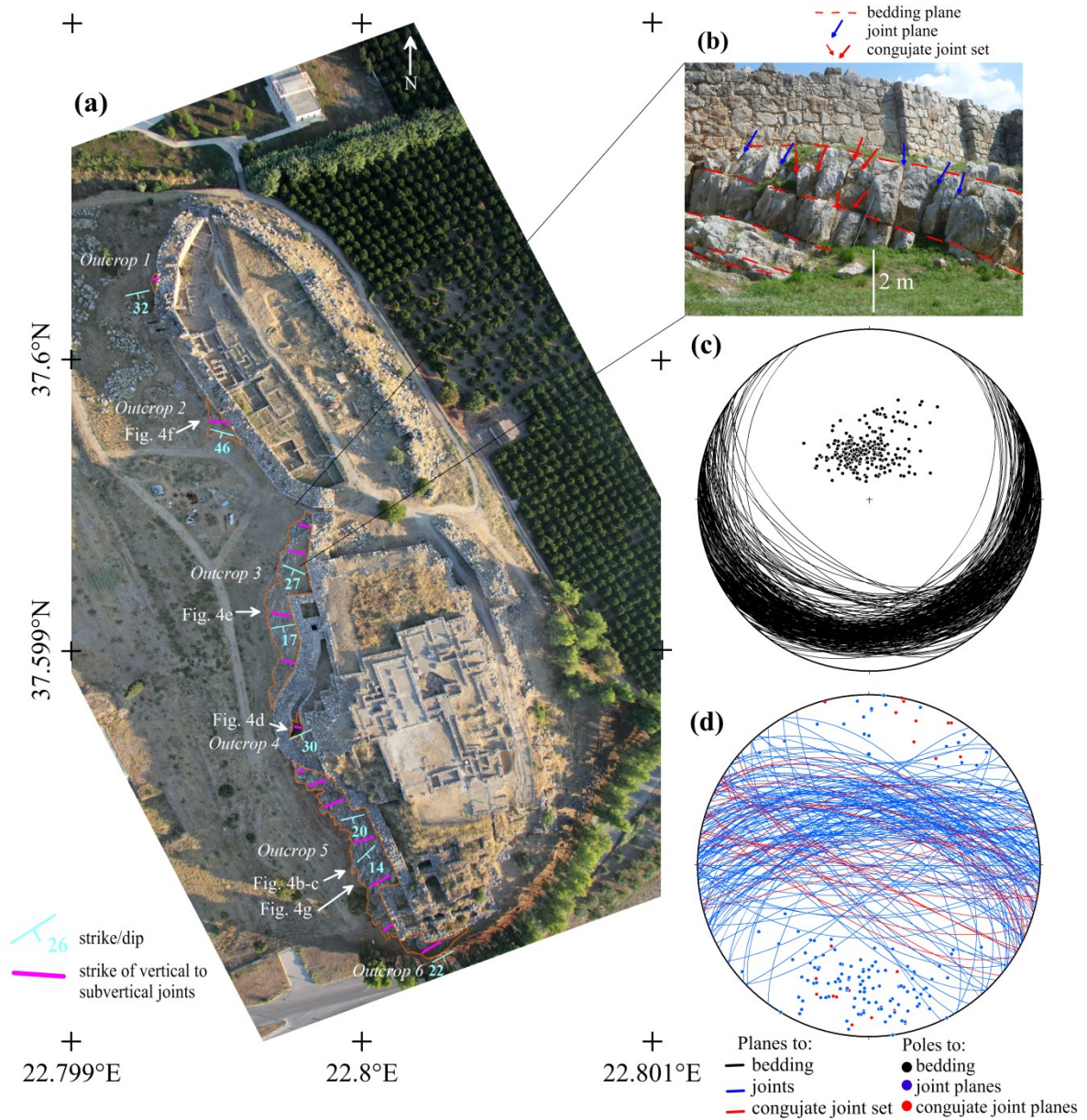


Figure 3.7: (A) Structural geologic data of Tiryns bedrock imposed on aerial photo of the Tiryns citadel. (B) Geometric relationship between joint planes and bedding planes (scale = 2 m long stick). Equal-area stereonet projections of (C) bedding planes and (D) joint planes.

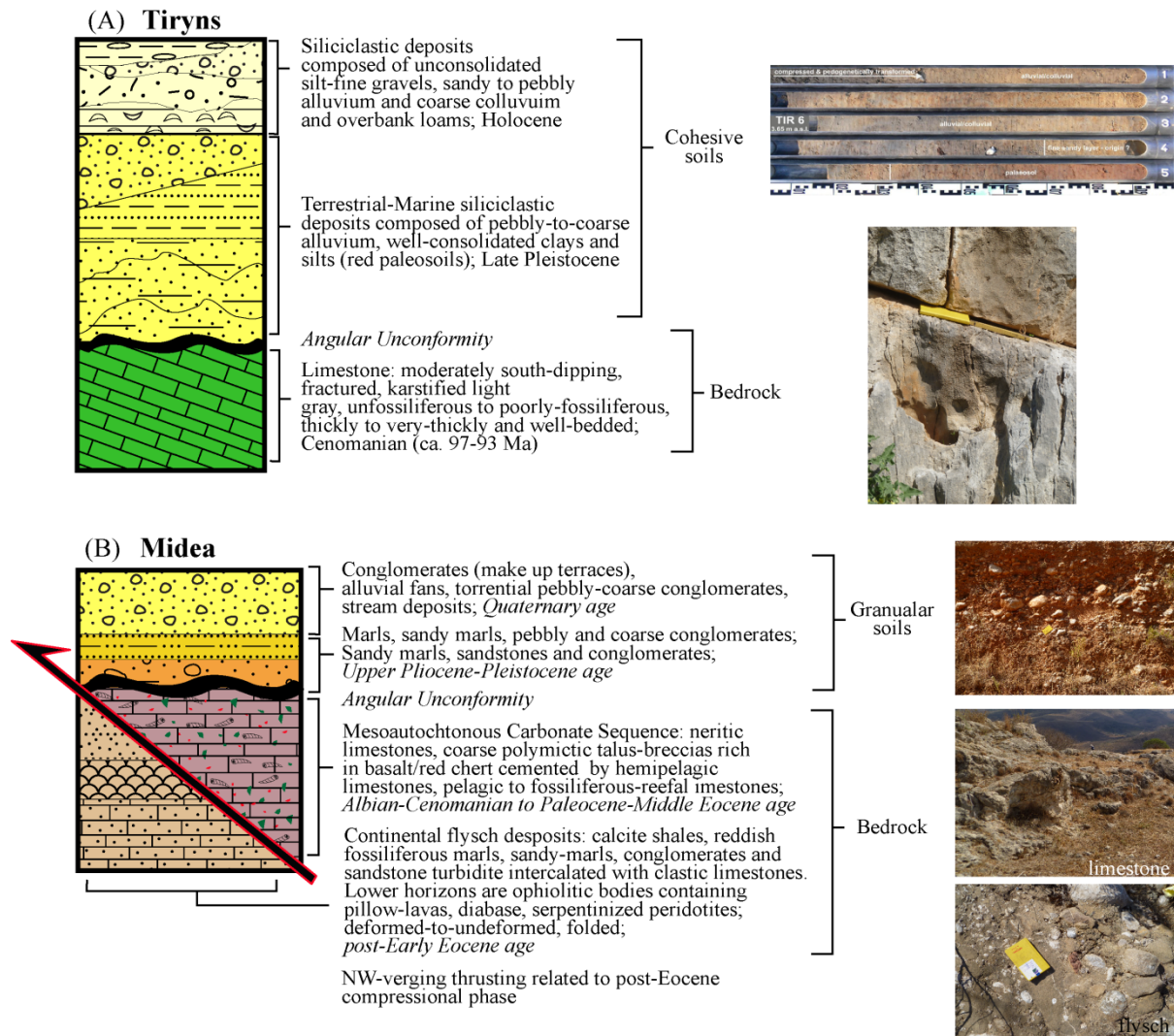


Figure 3.8: Representative stratigraphic column of the vicinity of (A) Tiryns and (B) Midea (after Tataris et al., 1970; Kraft et al., 1977; Zangger, 1993; van Andel et al., 1990a, 1990b, 1993; Clift, 1996; Hinojosa-Prieto and Hinzen, 2015; GSLI, unpublished data). Uppermost photograph taken from Ntageretzis (2014), other ones from the author.

The Midea ridge, where the Midea citadel was built on, is structurally controlled by a northwest-trending, northeast-dipping inactive thrust fault (Figure 3.9) (Tataris et al., 1970). The fault is parallel to the ridge's long axis; therefore the bedrock underneath the Midea citadel is clearly heterogeneous. From bottom to top, the Midea ridge is partly composed of post-Early Eocene continental flysch deposits thrust against Lower Cretaceous-Paleocene clastic limestones, which in turn are covered by Albian-Cenomanian to Paleocene-Middle Eocene neritic limestones and polymictic talus-breccias rich in basalt/red chert cemented by hemipelagic limestones. The flysch is the most heterogeneous hard-rock in the AB (Apostolidis and Koutsouveli, 2010). The flysch consists of sandstones, quartzites, calcareous schist sandy-marls, siltstones, and conglomerates with intercalations of limestones. At localities near thrust faults, flysch is semi-metamorphic with olistholiths of varying grain-size and compositions (e.g., limestones, dolomites, sandstones, ophiolites, etc.). Weathered,

strongly karstified highly-fractured, thickly-bedded, white to pink fossiliferous, crystalline limestones crop at the Midea archaeological site (Tataris et al., 1970; Photiades, 2010).

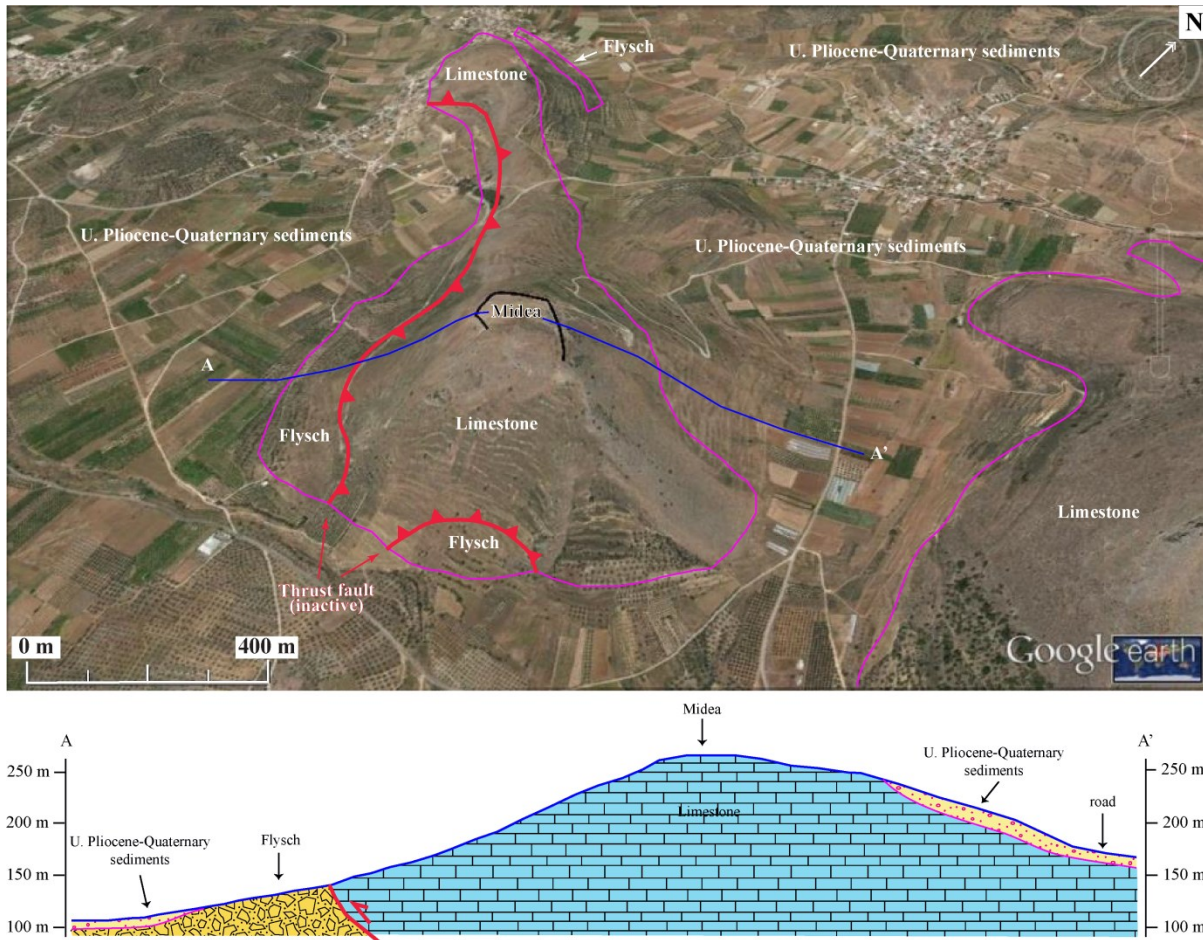


Figure 3.9: Simplified structural geologic map (*top*) and geologic cross-section (*bottom*) of the Midea ridge, viewing from the southeast at an eye altitude of 1.70 km. The black line on the summit of the ridge corresponds to the location of the Cyclopean walls of the Midea citadel. Satellite photo from Google Earth® with 2× vertical exaggeration. The flysch and overlying Upper Pliocene–Quaternary sediments are undifferentiated; see Figure 3.8B for differentiated geologic units. Geology from Tataris et al. (1970).

The undeformed sediments that occur at the flanks of the Midea ridge are made up of a 20 to 65 m thick Upper Pliocene–Quaternary well-consolidated terrigenous continental clastic sequence overlying along an angular unconformity on pre-Oligocene carbonate-flysch bedrock. The sediments are composed of a basal Upper–Pliocene to Pleistocene marls, sandy-marls, sandstones, and pebbly-and-coarse conglomerates and make up the terraces. The Quaternary sediments are alluvial fan deposits characterized by pebbly-and-coarse conglomerates and sands, which also make up terraces. Ephemeral streams incise the terraces (Figure 3.5) and contribute to the sediment budget of the AB (Zangger, 1993). Three deep boreholes located east of the Midea ridge and near the Cemetery of Dendra penetrated between 75 to 100 m depth and reveal a clastic sequence comprised of marine muds nearly 35 m thick overlain by coarse-grained clastic layer of terrestrial origin (GSLI, unpublished data) (Figure 3.4). Other boreholes scattered between the Tiryns and Midea citadels reached the

bedrock between depths of 33 to 83 m (Figures 2.2A and 3.4). These boreholes plot outside the surficial extent of LBA alluvial toe mapped by Zangger (1993). The representative stratigraphic column of the Midea citadel is also shown in Figure 3.8B. Both archaeological excavations (Åström et al., 1988, 1990, 1992; Demakopoulou et al., 1994, 1996; Demakopoulou, 2012) and geologic field observations indicate that the Midea citadel was built directly on (limestone) bedrock. Though, a very thin soil layer (still) caps the archaeological ruins and is thought to be post-Mycenaean.

3.2 Seismicity

The instrumental seismicity period of Greece is well-documented since the deployment of the first seismograph in 1897 in Athens (Ambraseys and Jackson, 1990; Kouskouna and Makropoulos, 2004; <http://www.gein.noa.gr/en/general>). Historical records suggest that three local moderate to large magnitude earthquakes had an impact on the city of Nafplion, which is located next to Tiryns (Ambraseys and Jackson, 1990; Ambraseys, 1996; Papazachos and Papazachou, 2003). Figure 3.10 illustrates the distribution of historic and instrumental earthquakes within and near the Peloponnese, Greece.

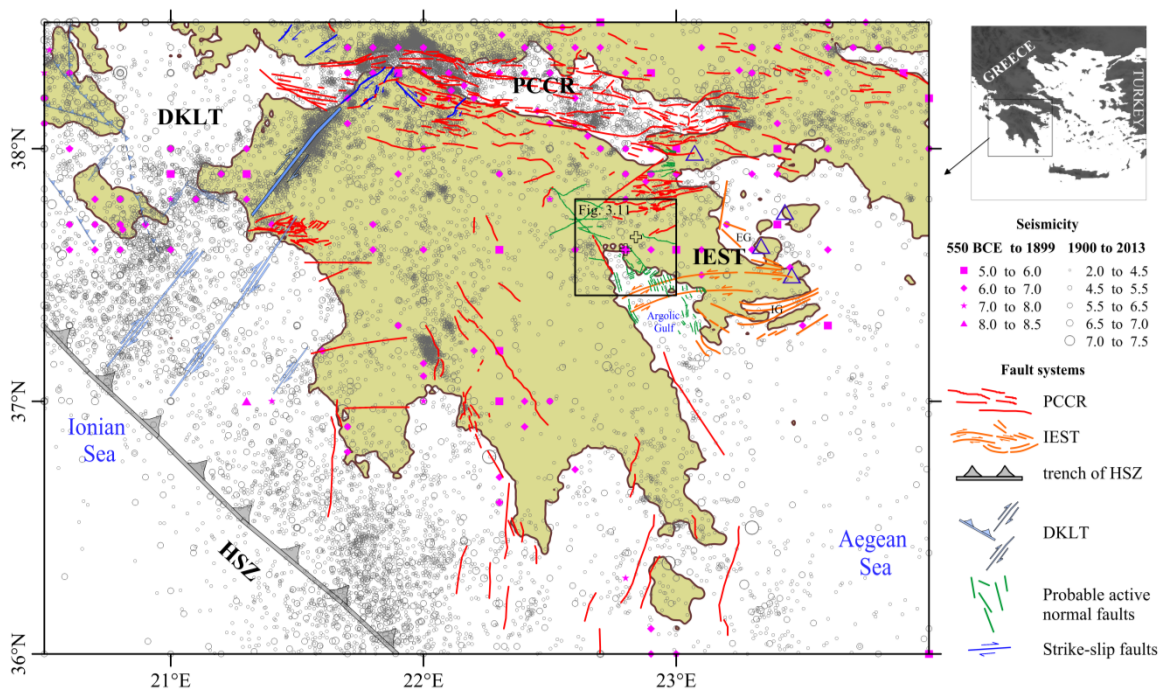


Figure 3.10: Seismicity of the Peloponnese from 550 BCE to 1899 taken from The University of Athens, Greece (UOA) and Aristotle University of Thessaloniki, Greece (AUTH) catalogs and from 1900 to 2013 taken from the AUTH catalog. Blue triangles indicate volcanoes of the active Hellenic volcanic arc. Black hollow-crosses indicate Mycenaean Tiryns and Midea citadels. EG = Epidaurus Graben. IG = Idhra Graben.

The Aegean Sea and continental Greek territory contain seismically active zones of the fragmented Aegean microplate. The seismicity of the Aegean microplate is the highest in the Mediterranean region; however, due to the complex tectonic situation its seismicity pattern is rather diffuse (McKenzie, 1972, 1978; Makropoulos and Burton, 1984; Papazachos, 1980; Taymaz et al., 1990; Papanikolaou and Royden, 2007; Taymaz et al., 2007). Seismogenic

zonation for onshore and offshore Greek territory including the Peloponnese has been done based on the focal distribution of shallow to deep earthquakes (< 180 km) (Papazachos, 1980; Papazachos and Papaioannou, 1993; Papaioannou and Papazachos, 2000) and more recently on the basis of onshore geological and neotectonic data, and offshore seismic reflection profiles (Papoulia et al., 2014). Weak and strong mainshocks and aftershocks are common within the uppermost 20 km of the Peloponnese (Hatzfeld et al., 1989; Hatzfeld and Martin, 1992; Hatzfeld et al., 1993a, 1993b; Hatzfeld, 1994; Molnar et al., 2007). The seismogenic zonation work of Papoulia et al. (2014), specific to the Peloponnese and its offshore environment, emphasizes that the interaction of a NNW-SSE oriented 92 km long, inactive extensional detachment fault (Papanikolaou and Royden, 2007) and a NW-SE trending ~ 60 km long active normal fault along the western and eastern coast of the AG, respectively, are the dominant structures that can explain the current low level and shallow seismicity supposedly under an E-W oriented extensional stress regime. In this view, the AB is the onshore continuation of the AG (van Andel and Lianos, 1984; van Andel et al., 1990b, 1993).

The AB contains observed and inferred normal faults, some traditionally considered as active and others as probably active faults (Papastamatiou et al., 1960; Tataris et al., 1970; Papanastassiou et al., 1993; Papanikolaou et al., 1994; ECPFEO, 1996; Georgiou and Galanakis, 2010). The AB is surrounded by well-known active source zones located as far as ≤ 150 km (Papadopoulos and Kijko, 1991; Papazachos and Papaioannou, 1993; Papaioannou and Papazachos, 2000; Makris et al., 2004; Karastathis et al., 2010a, 2010b; Makropoulos et al., 2012; <http://geophysics.geo.auth.gr>; www.geophysics.geol.uoa.gr). The well-known active source zones include the Patras-and-Corinth Continental Rift (PCCR) system passing into the dextral Kefhalonia-Lefkada Transform Fault (DKLT) system in the Ionian Sea in the north; the oceanic trench of the Hellenic Subduction Zone (HSZ) offshore western and southern Peloponnese with its downgoing slab extending underneath the AB; and the Iria–Epidaurus Sinistral Transform fault system (IEST) located in the southeast Argolis Peninsula. The location of the AB and the potential seismic sources are shown in Figure 3.10. Late Neogene–Quaternary sedimentary basins of the Peloponnese, including the AB, show a much lower seismic activity than these surrounding source zones; nevertheless seismicity within the Argolis Peninsula includes crustal earthquakes and events down to 150 km depth in the downgoing slab (Figure 3.11) (Papazachos et al., 1988; Lyon-Caen et al., 1988; Papadopoulos and Kijko, 1991; Hatzfeld et al., 1989; Hatzfeld and Martin, 1992; Hatzfeld et al., 1993a, 1993b, 2000; Papazachos et al., 2000a; Makris et al., 2004; Voigt, 2013).

In an archaeoseismological context, the seismic scenario of the AB during Mycenaean times is likely to be the same as it is today because the active tectonic setting of the Peloponnese has remained unchanged since the Pliocene (*ca.* 5.3 Ma) according to regional geologic (Papanikolaou et al., 1994), seismologic (Hatzfeld, 1994; Papazachos et al., 2000b), and geodynamic studies (Papanikolaou and Royden, 2007; Royden and Papanikolaou, 2011). Moreover, the aforementioned seismogenic zones are considered potential seismic hazard to all Mycenaean sites located in the AB. However, the moderate to strong earthquakes in the western PCCR and the adjacent DKLT (Koukouvelas et al., 1996; Sachpazi et al., 2000;

Konstantinou et al., 2009) are much less likely to have caused damage to Mycenaean sites in the AB due to the relatively large epicentral distances.

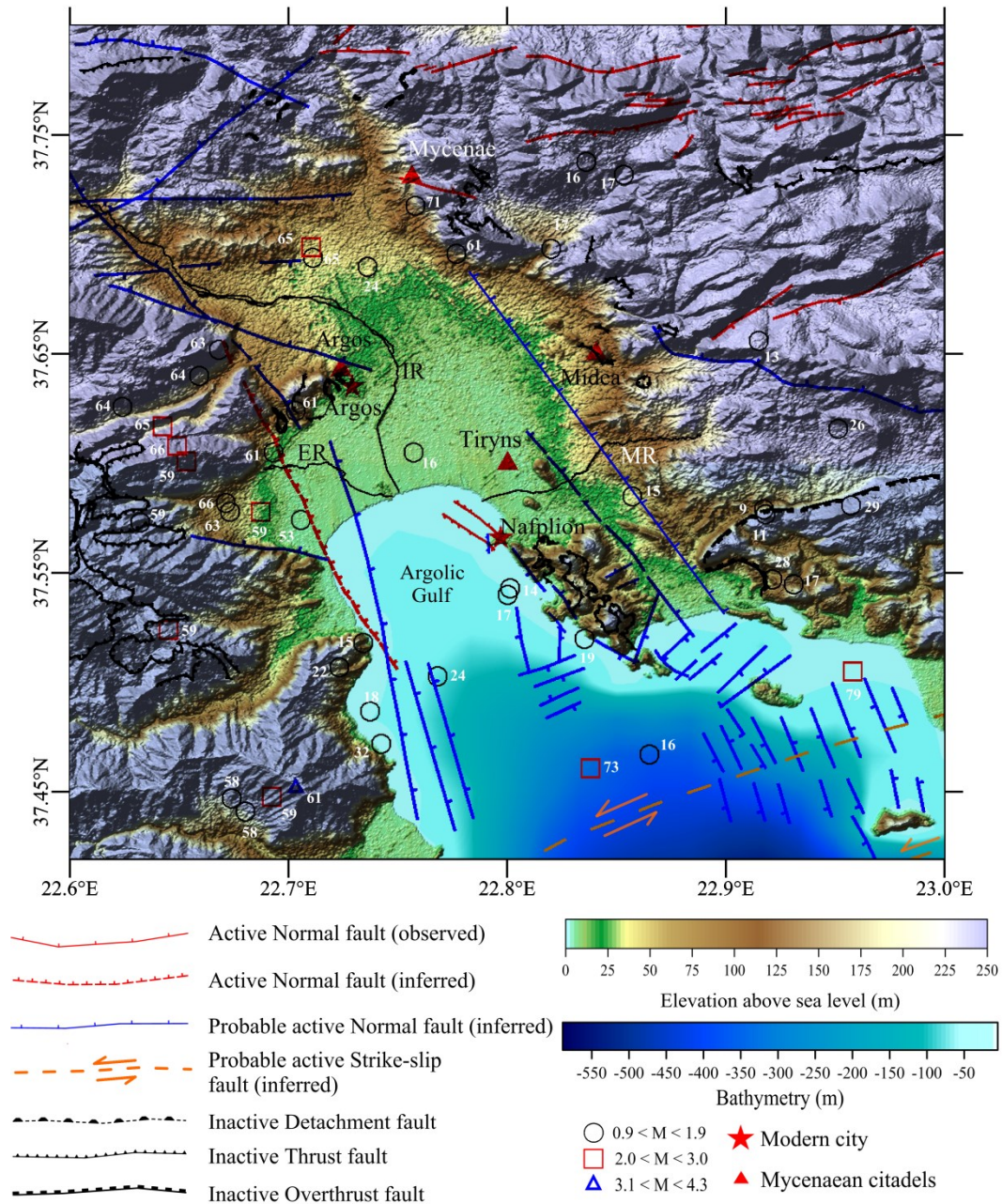


Figure 3.11: Neotectonic setting of the Argive Basin–Argolic Gulf sedimentary basin. Instrumental seismicity from Hatzfeld et al. (1989), UOA catalog, and this study. Depth (km) of hypocenter is marked next to epicenter symbol. Fault traces from Papastamatiou et al. (1960), Tataris et al. (1970), van Andel et al. (1993), Papanikolaou et al. (1994), ECPFEO (1996), Hatzfeld et al. (1999), and Georgiou and Galanakis (2010). Inactive faults in black. Terrain model from the Shuttle Radar Topography Mission (SRTM) 3 arc-second resolution. Bathymetry model from the National Oceanic Atmospheric Administration (NOAA) Geodas data.

Major active normal faults of the PCCR are geologically expressed as 12 to 40 km long segments (Pavlidis and Caputo, 2004; Pavlidis et al., 2006; Pacchiani and Lyon-Caen, 2010; Karastathis et al., 2010a) and are arranged in an en-echelon pattern (Flotté et al., 2005). Normal faults located along the southern shoreline strike WNW-ESE and dip northwards at

moderately to steep angles (50-70°) (Koukouvelas et al., 1996; Rigo et al., 1996; Armijo et al., 1996; Bernard et al., 1997; Le Meur et al., 1997; Hatzfeld et al., 2000; Micarrelli et al., 2003; Latorre et al., 2004; Konstantinou et al., 2009; Pacchiani and Lyon-Caen, 2010). Active offshore steeply-dipping antithetic normal faults exist along the northern shoreline, but are less active than the southern ones (Goldsworthy et al., 2002; Moretti et al., 2003). The Patras and Corinth continental rifts are connected by an active onshore NE-SW trending small sinistral strike-slip fault system (Flotté et al., 2005) and together form the asymmetric E-W trending PCCR that separates the Peloponnese from central Greece (Hatzfeld et al., 1993, 2000; Goldsworthy et al., 2002; Moretti et al., 2003). Thus, uplift and subsidence occur along the southern and northern coastlines, respectively (Armijo et al., 1996). The PCCR ruptures diachronously from east to west (Sachpazi et al., 2003).

Fault plane solutions of moderate and strong shallow earthquakes (≤ 15 km depth) exhibit an E-W trending normal faulting pattern and cause the current north-south oriented crustal extension (e.g., Rigo et al., 1996; Bernard et al., 1997; Hatzfeld et al., 2000). This is corroborated by geodetic measurements across the PCCR yielding a rate of crustal extension that decreases from west to east from 16 to 11 mm/yr, respectively (Clarke et al., 1997; Avallone et al., 2004). Long recurrence periods for large earthquakes on normal faults along the southern coastline of the Gulf of Corinth are implied on the basis of observed tectonic strain buildup (< 1 mm/yr) across such faults (Avallone et al., 2004).

The seismicity in the HSZ is caused by the subduction of the African oceanic lithosphere under the Aegean microplate (e.g., Peloponnese and the Aegean Sea). This seismic belt is located about 70 to 150 km offshore of the southwestern and southern Peloponnese, respectively, with hypocenters down to 200 km depth (McKenzie, 1972, 1978; Makropoulos and Burton, 1984; Hatzfeld et al., 1989; Taymaz et al., 1990; Papazachos, 1996; Hatzfeld and Martin, 1992; Hatzfeld, 1994; Papazachos and Nolet, 1997; Papazachos et al., 2000a; Kiratzi and Louvari, 2003; Meier et al., 2004; Bohnhoff et al., 2004; Roumelioti et al., 2009; Becker et al., 2010). The African lithosphere converges NNW with the Aegean microplate at a rate of approximately 10 mm/yr (McClusky et al., 2000). Deformation along the Hellenic oceanic trench is taken up by reverse faulting and low-angle thrust faulting with microseismicity occurring in both the overriding and downgoing plates and macroseismicity along the plate interface (Comninakis and Papazachos, 1980; Hatzfeld and Martin, 1992, 1993a, 1993b; Papazachos, 1996; Papazachos et al., 2000a; Kiratzi and Louvari, 2003; Meier et al., 2004; Bohnhoff et al., 2004; Roumelioti et al., 2009; Becker et al., 2010). Microseismic and P- and S-wave tomography studies show that the African slab subducts gently at $\sim 10^\circ$ beneath the Peloponnese for about 200 km measured from the trench and then plunges steeply (25–45°) at a depth of 50–70 km down to 150 km depth (Hatzfeld et al., 1989; Hatzfeld and Martin, 1992; Hatzfeld et al., 1993a, 1993b; Hatzfeld, 1994; Papazachos and Nolet, 1997). The slab kink is near the AB–AG structure. Further towards the volcanic arc, weak to strong earthquakes with normal faulting mechanisms are abundant within the overriding plate and lesser along the subduction plate interface (Hatzfeld et al., 1989, 1993a, 1993b; Papazachos et al., 2000a). This reflects the current crustal extension in the Aegean Sea region and extension of the subducting African slab parallel to the plate interface. Additionally, compressional stress axes

of intermediate depth events (40–80 km) show pure thrusting due to locking where the slab kinks underneath the AB.

The IEST crustal fault system in the Argolis Peninsula remains poorly understood. Both historical (Ambraseys and Jackson, 1990; Papadopoulos et al., 2000; Papazachos and Papazachou, 2003) and instrumental records from local (Makris et al., 2004) and regional seismic networks (Drakopoulos and Srivastava, 1970; Ambraseys and Jackson, 1990; Makropoulos et al., 2012; geophysics.geo.auth.gr) show low seismicity levels with weak to strong crustal earthquakes and events down to 120 km depth. Yet, an accurate seismo-tectonic model for the IEST is unavailable due to a scarcity of fault plane solutions. However, the current structural geologic model consists of sinistral transtensional and normal faults. This model builds upon scarce onshore geologic field observations (Clift and Robertson, 1990; Clift, 1996), marine seismic reflection surveys (van Andel and Lianos, 1984; van Andel et al., 1990b, 1993), several nearby seismicity studies (Hatzfeld et al., 1989, 1992, 1993a, 1994, 2000), and a recent morphotectonic analysis (Vassilopoulou, 2010). The morphotectonic study of Vassilopoulou (2010) focuses in the whole southern Argolis Peninsula and documents an ESE-WNW and EW orientation of faulting zones. The morphotectonic study builds upon ground and remote sensing data, relating to tectonics and geology, coupled with computer-based terrain analysis. Further, the IEST consists of two postulated E-W trending sinistral transform faults, so-called Iria and Epidaurus faults, in the southeastern Argolis Peninsula and presumably affect Holocene scree deposits and Alpine bedrock (van Andel and Lianos, 1984; Clift and Robertson, 1990; van Andel et al., 1993; Vassilopoulou, 2010). These faults might submerge into the waters of the AG; thus, the IEST offsets the easternmost normal faults of the AG in an en-echelon pattern and are interpreted to accommodate a southward increment in the extension rate (van Andel et al., 1993). Additionally, the normal faults of the AG are truncated by Late Neogene–Quaternary high-angle normal faults that bound the E-W trending Idhra graben in the south (van Andel and Lianos, 1984; van Andel et al., 1993) and the WNW-ESE oriented Epidaurus graben in the north (Makris et al., 2004). The crustal seismicity in the IEST region is currently interpreted as the result of transtension and extensional stress fields imposed by the adjacent PCCR system due to the rearrangement of eastwards escaping crustal blocks in response to the NNW compression of western Peloponnese (Clift and Robertson, 1990; van Andel et al., 1993; Makris et al., 2004; Drakatos et al., 2005).

Despite that the AB region shows low levels of seismicity (e.g., Ambraseys and Jackson, 1990), its high seismic impedance along the soil–bedrock interface and its immediate proximity to the aforementioned seismic source zones (Hinojosa-Prieto and Hinzen, 2015) justifies its consideration in seismic hazard analyses. Seismic hazard studies, for specific areas within the AB, have focused on assessing the risk of landslide and soil-liquefaction potential, as well as probabilistic engineering ground motion parameters and earthquake hazard parameters which are summarized in Table 3.2.

Table 3.2: Summary of the type of estimated earthquake hazard and ground motion parameters for the Argive Basin (Peloponnese, Greece).

Parameter	Reference
<i>Earthquake hazard related</i>	
maximum regional magnitude	Papadopoulos and Kijko (1991)
activity rate of seismic events	Papadopoulos and Kijko (1991)
mean return period	Papadopoulos and Kijko (1991)
parameter <i>b</i> of the magnitude-frequency relationship	Papadopoulos and Kijko (1991)
probability of occurrence of $M_{\min} \geq 6.0$ event between years 1993-2002	Papazachos and Papaioannou (1993)
minimum magnitude ($M_{\min} \geq 6.0$) at 0-180 km depth range	Papazachos and Papaioannou (1993)
macroseismic intensity (in Modified Mercalli scale)	Papaioannou and Papazachos (2000)
<i>Ground motion related</i>	
Arias intensity	Tselentis and Danciu (2010a)
peak-ground acceleration and velocity	Papaioannou and Papazachos (2000) Tselentis and Danciu (2010a) Skarlatoudis et al. (2013)
cumulative absolute velocity	Tselentis and Danciu (2010a)
Newmark's displacement hazard	Tselentis and Danciu (2010a)
broad zonation of high-attenuation and amplification	Skarlatoudis et al. (2013)

The AB is located above the low-velocity mantle-wedge at the southwestern limit of the back-arc region of the HSZ (Hashida et al., 1988; Skarlatoudis et al., 2013). The seismic hazard is higher for areas located within the fore-arc region than in the back-arc ones (Papadopoulos and Kijko, 1991; Papazachos and Papaioannou, 1993; Papaioannou and Papazachos, 2000). The forearc region exhibits a lower attenuation causing the level of predicted response-spectra in the fore-arc areas to be almost 10 times higher than those in the back-arc areas (Hashida et al., 1988; Skarlatoudis et al., 2013). The back-arc region exhibits a high attenuation of seismic waves from shallow and intermediate depth events (Hashida et al., 1988; Skarlatoudis et al., 2013). Skarlatoudis et al. (2013) link the low attenuation in fore-arc region to the presence of the high-velocity (*high-Q*) subducting African slab and the high attenuation in back-arc region to current volcanic activity and associated low-velocity (*low-Q*) mantle-wedge above the subducting African slab.

At the basin scale, the susceptibility level of earthquake-induced soil-liquefaction for the AB is moderate in zones with fine-grained Quaternary soils and very low in zones with coarse-grained Pleistocene soils (Papathanassiou et al., 2010). At the site-scale, the marshy deposits of the suburban limits of the city of Nafplion can present non-linear soil amplification behavior and a high soil-liquefaction risk in the event of a shallow strong earthquake (e.g., $M_w \geq 6.3$) in either the adjacent PCCR or the IEST source zones (Karastathis et al., 2010a, 2010b). Soil-liquefaction is likely to happen within a water-saturated clayey layer between 6-12 m depth due to a low water-table (10 m depth) (Karastathis et al., 2010a, 2010b). This coastal area is just < 2.0 km south-southwest of the Tiryns citadel. Depending on the foci location, the seismic waves of a subduction-related in-slab strong earthquake may not be attenuated when they reach the surface in the back-arc region if they do not pass through the low velocity/*low-Q* mantle wedge pocket located under the AB (Skarlatoudis et al., 2013). This type of event likely poses a seismic hazard; and perhaps can produce soil amplification and related soil liquefaction.

In regional seismic hazard maps of Greece, the AB is considered a zone of low seismic hazard levels (Papadopoulos and Kijko, 1991; Tselentis and Danciu, 2010a; Papathanassiou et al., 2010). Conversely, at the local scale, seismic hazard levels within the basin vary from very low to high due to the contrasting near-surface geologic conditions resulting in various levels of expected Peak Ground Acceleration (PGA) (Papadopoulos and Kijko, 1991; Tselentis and Danciu, 2010a; Apostolidis and Koutsouveli, 2010; Karastathis et al., 2010a, 2010b; Papathanassiou et al., 2010; USGS, 2014). Table 3.3 compiles available expected PGA values and the corresponding seismic hazard level for the localities of Tiryns and Midea and the AB as a whole. The consensus is that the larger and more active seismogenic faults outside the AB are likely to pose a higher hazard than the smaller and possibly active local faults within or underneath the AB. Nevertheless, the presumably active local faults mapped in the AB are also considered in this study; despite that earthquakes have not been assigned to any of these faults.

Table 3.3: Seismic Hazard Level (SHL) and expected Peak Ground Acceleration (PGA) values for the Argive Basin and the vicinity of Tiryns and Midea. (SHL refers to an informally relative scale defined by the tabulated references).

SHL	PGA (g)	Probability of exceedance	Place	Reference
Low to High	0.16–0.50	10% over 50 year period	Argive Basin	Tselentis and Danciu (2010a)
Low ^a	0.16 ^b	10% over 50 year period ^b	Argive Basin	a = Papadopoulos and Kijko (1991) b = Papathanassiou et al. (2010)
Low High	0.31 0.40–0.50	10% over 50 year period	Tiryns–Nafplion city within Midea	Tselentis and Danciu (2010a)
Low	-	-	nearby Midea	Papadopoulos and Kijko (1991)
Low	0.16	-	~3 to 4 km south of Tiryns	Apostolidis and Koutsouveli (2010)
Very low to Low	0.036–0.217	-	~1.5 to 2 km south of Tiryns	Karastathis et al. (2010a, 2010b)
Very Low to Low	0.16–0.24	10% over 50 year period	Pleistocene soils within Midea	Papathanassiou et al. (2010)
Moderate	0.24		Holocene soils within Tiryns	
Moderate	0.16		Latest Holocene soils within Tiryns	
-	0.24	10% over 50 year period	Argolis Peninsula & East-Central Peloponnese	U.S. Geological Survey (USGS, 2014)

4. DYNAMIC PROPERTIES OF SOILS AND BEDROCK AT TIRYNS AND MIDEA AND GEOTECHNICAL PROFILES

Dynamic properties of the soils and bedrock at and around Tiryns and Midea, and geologic profiles are derived in this chapter. The dynamic properties of the near-surface materials are required to estimate seismic site effects. The dynamic properties include the shear-wave velocity (v_s), stiffness (G/G_{max}) and damping ratio (ζ) curves as a function of strain of the materials that compose the stratigraphic model. The soil geometry and the density of the soils and bedrock are also necessary parameters. The geological units considered in the present study are evaluated on the basis of new (see chapter 3) and available upfront geologic mapping (Papastamatiou et al., 1960; Tataris et al., 1970; Georgiou and Galanakis, 2010; Photiades, 2010), boreholes (GSLI, unpublished data; Zangger, 1993; Ntageretzis, 2014), geotechnical data (Marinos and Hoek, 2001; Marinos et al., 2006; Sabatakakis et al., 2008; Apostolidis and Koutsouveli, 2010; Karagianni et al., 2010; Marinos and Tsiambaos, 2010; Tziallas et al., 2013), and in-situ geophysical measurements near to Tiryns and Midea (Hübner and Giese, 2002; Karmis, 2008; Karmis et al., 2010; Karastathis et al., 2010a, 2010b; Zananiri et al., 2010a, 2010b; Ntageretzis, 2014; this study). As part of the HERACLES project, a seismic refraction tomography (SRT) (Hinojosa-Prieto and Hinzen, 2015) and a transient electromagnetic (TEM) survey (Soupios et al., 2014) were performed to investigate the seismic velocity and resistivity structure of the subsurface materials and the underground geology at and around Tiryns and Midea.

4.1 Geotechnical Investigations

4.1.1 Previous Work

The engineering geological map of Nafplion city and wider area by Apostolidis and Koutsouveli (2010) identifies 18 earth materials. Their study illustrates the relative shear strength of the soils and the degree of alteration from weathering and fracturing in the outcropping bedrock composed mainly of limestone and subordinate conglomeratic-flysch: weaker and stiffer soils occur around Tiryns and Midea, respectively. The estimation of the strength, stiffness, and rock mass quality factor is evaluated by measuring the uniaxial compressive strength of the rock mass (σ_{ci}); the Young's modulus of intact rock (E_i) that measures the resistance to deformation; the point loading index ($I_{s(50)}$) which calculates the intact rock strength index as opposed to the rock mass (Rusnak and Mark, 1999; Sabatakakis et al., 2008); and the Geological Strength Index (GSI) which relates the properties of intact rock elements to those of the overall rock mass, but is only applicable to heterogeneous rocks such as flysch (Marinos and Hoek, 2001). The strength of outcropping limestone and flysch in Greece comes from recent geotechnical laboratory measurements of σ_{ci} , E_i , and $I_{s(50)}$ (Sabatakakis et al., 2008; Karagianni et al., 2010; Marinos and Tsiambaos, 2010) and suggest the following. The E_i measured on limestone and flysch corresponds to poor to fair and poor to strong rock mass quality, respectively, following Barton (2007). Following the criteria of Marinos and Hoek (2001), the σ_{ci} measured on limestone and flysch correspond to medium strong-strong and weak rock mass strength, respectively; the $I_{s(50)}$ measured on limestone corresponds to a strong intact rock mass; and the here estimated GSI values for the conglomeratic-flysch of the Argive Basin are between 25–30 corresponding to a fair rock mass strength.

4.1.2 New Laboratory Tests

Three gray-color limestone and three ammonico rosso limestone samples were collected for geotechnical laboratory analysis conducted by the Institute of Geotechnical Engineering at the University of Aachen, Germany. The grey-color limestone samples are representative of the Tiryns hill (e.g., Tiryns' bedrock) and part of the cyclopean blocks that make up the fortification wall. The samples of the ammonico rosso limestone are observed in less abundance in the cyclopean walls and in walls of the South Gallery of Tiryns. Average values of 2637 kg/m^3 and 22 GPa were obtained for the density (ρ) and E_i , respectively. The gray limestones yield E_i values from 22 to 33.5 GPa that correspond to poor to fair rock mass quality following Barton (2007); while ammonico rosso limestones yield lower E_i values (i.e., 10-21 GPa) indicative of lower rock quality. The complete laboratory measurements are listed in Appendix B.

4.2 Geophysical Investigations

4.2.1 Previous Work

In recent years, onshore geophysical studies have been performed near the cities of Argos (Zananiri et al., 2010a, 2010b) and Nafplion (Karmis, 2008; Karastathis et al., 2010a, 2010b; Ntageretzis, 2014) as well as within (Hübner and Giese, 2002; this study) and outside (Ntageretzis, 2014) the limits of the Tiryns archaeological site. Additionally, marine seismic reflection profiles have been completed for the western AG (van Andel et al., 1990b) and offshore Nafplion (Mitropoulos and Zananiri, 2010). Figure 4.1 shows the surficial extend of these surveys. Overall, these surveys target environmental (primarily) and archaeological issues. Geophysical investigations have not been conducted neither at or adjacent to the Midea archaeological site prior to the HERACLES project.

Zananiri et al. (2010b) performed a pseudo-3D magnetic survey (i.e., total field and gradient magnetic readings) in the Agora archaeological site located within the limits of the ancient city of Argos (Figure 4.1). The survey covered an area of $2,300 \text{ m}^2$ using a 1.0 m station-spacing. The results suggest the presence of buried man-made structures likely indicating ancient inhabitation ruins, remnants of small buildings, and road foundations.

The multi-method geophysical campaign of Karastathis et al. (2010a, 2010b) deployed within the suburban area of Nafplion (Figure 4.2) provides information about the soil–bedrock depth and morphology, the depth of the groundwater table, and the minimum sediment thickness of the Pliocene–Quaternary cover. The geophysical campaign was tailored to understand the geotechnical engineering and hydrologic conditions for a liquefaction hazard study. The campaign consisted of a Multichannel Analysis of Surface Waves (MASW), seismic reflection, both v_p (compressional P-wave) and v_s (horizontally polarized shear-wave) seismic refraction, and three-dimensional (3D) gravity on Quaternary alluvium equivalent to the one at Tiryns. The MASW results show v_s from 100-500 m/s and 500-1000 m/s for the Quaternary soils and limestone bedrock, respectively. The refraction survey yields v_p between 320-740 m/s and v_s between 120-320 m/s for the soils; and v_p between 1600-3000 m/s and v_s of 600 m/s for the bedrock. Nearly 1.5 km south of Tiryns, low v_p values and high Poisson ratios were detected beyond 5.0 m depth within a Quaternary sandy-silt/silty layer

interpreted as saturated soils due to a shallow groundwater table. Both the seismic reflection profiles and the 3D gravity survey of Karastathis et al. (2010a, 2010b) suggest limestone bedrock topography varying from 60 to 200 m depth and likely affected by two, parallel, buried south-dipping inactive low-angle normal faults (Karastathis et al., 2010a).

Electrical resistivity tomographies (ERT) and TEM soundings (Karmis, 2008; Karmis et al., 2010) measured near Tiryns (Figure 4.2) also indicate an irregular bedrock topography varying from 40 to 145 m depth. A nearly 100 km² two-dimensional (2D) marine seismic reflection survey in the western AG reveals Pliocene–Quaternary reflectors (unconformities), several N-S trending normal and reverse faults, and uplifted limestone blocks at 300–500 m depth (van Andel et al., 1990b). A smaller (13.5 km²) 2D marine seismic reflection survey also reveals reflectors offshore Tiryns and Nafplion (Mitropoulos and Zananiri, 2010) (Figure 4.1). Conclusively, the spatially distributed onshore and more widely distributed offshore geophysical surveys suggest undulating bedrock topography likely due to either the opening of the Argolic Gulf in the Late Neogene or to older tectonic events. Yet, the soil–bedrock interface remains poorly mapped in most parts of the Argive Basin.

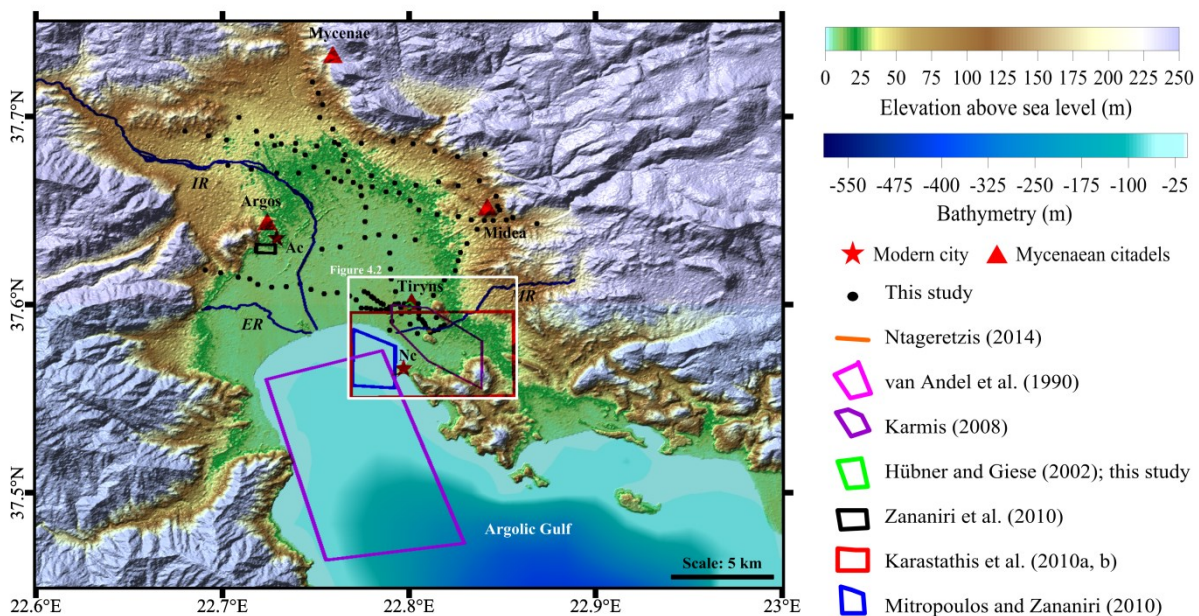


Figure 4.1: Geophysical surveys in the Argive Basin–Argolic Gulf region of the Argolid Peninsula (Peloponnese, Greece). Ac = Argos city; Nc = Nafplion city.

The uppermost 5.0 m depth of the fine-grained Holocene alluvium flanking the western and northern sides of Tiryns were reached with a 2D magnetic survey and several 1D vertical electrical soundings (VES) (Hübner and Giese, 2006). The magnetic and resistivity anomalies at the west side were suggestive of building structures buried at 4.0 m depth (Hübner and Giese 2006) which were later confirmed by an archaeological excavation (Maran, 2010). On the north side, a high-resistivity anomaly surrounded by lower-resistivity values was also interpreted as a buried building structure, but remains unexcavated. More recently, at 140–200 m west of Tiryns, two shallow ERT transects (≤ 12.0 m) located next to two shallow

(< 10.0 m depth) soil cores do not reach bedrock and only corroborate the occurrence of soils (Ntageretzis, 2014). Figure 4.3 displays the location of the magnetic, VES, and ERT surveys. The scarcity of onshore and offshore geophysical data calls for more geophysical investigations in the Argive Basin particularly at and around important archaeological sites such as Tiryns and Midea. Shallow geophysical prospecting can help map the thickness of sedimentary strata, identify underground geologic structures, and discontinuities in the bedrock that influence local site effects; clarify areas of archaeological potential at the planning stage or at an early stage of an ongoing excavation (Zananiri et al., 2010b); and can facilitate ongoing and future archaeoseismic research (Galadini et al., 2006). Both SRT and TEM soundings can provide useful information about the near-surface required to assess local site effects at specific sites. These methods are adopted in this study and discussed in sections 4.2.2 and 4.2.3, respectively.

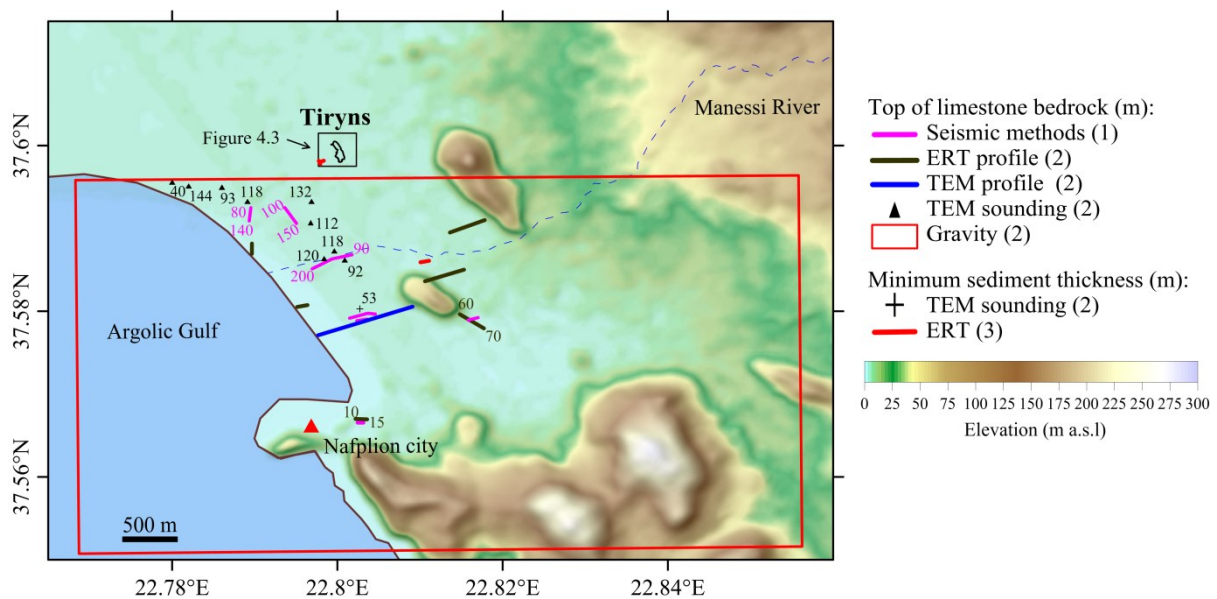


Figure 4.2: Previous onshore geophysical surveys within the greater city of Nafplion. The depth (m) to the top of the bedrock (limestone) and the minimum sediment thickness of the Upper Pliocene–Quaternary sediments is indicated by the number next to the geophysical method used. (1) = Karastathis et al. (2010a); (2) = Karmis et al. (2010); (3) = Ntageretzis (2014). TEM = Transient Electromagnetic; ERT = Electrical Resistivity Tomography. Seismic methods include Vertical Seismic Profiling, Multiple Analysis of Surface Waves, Refraction and Reflection profiles.

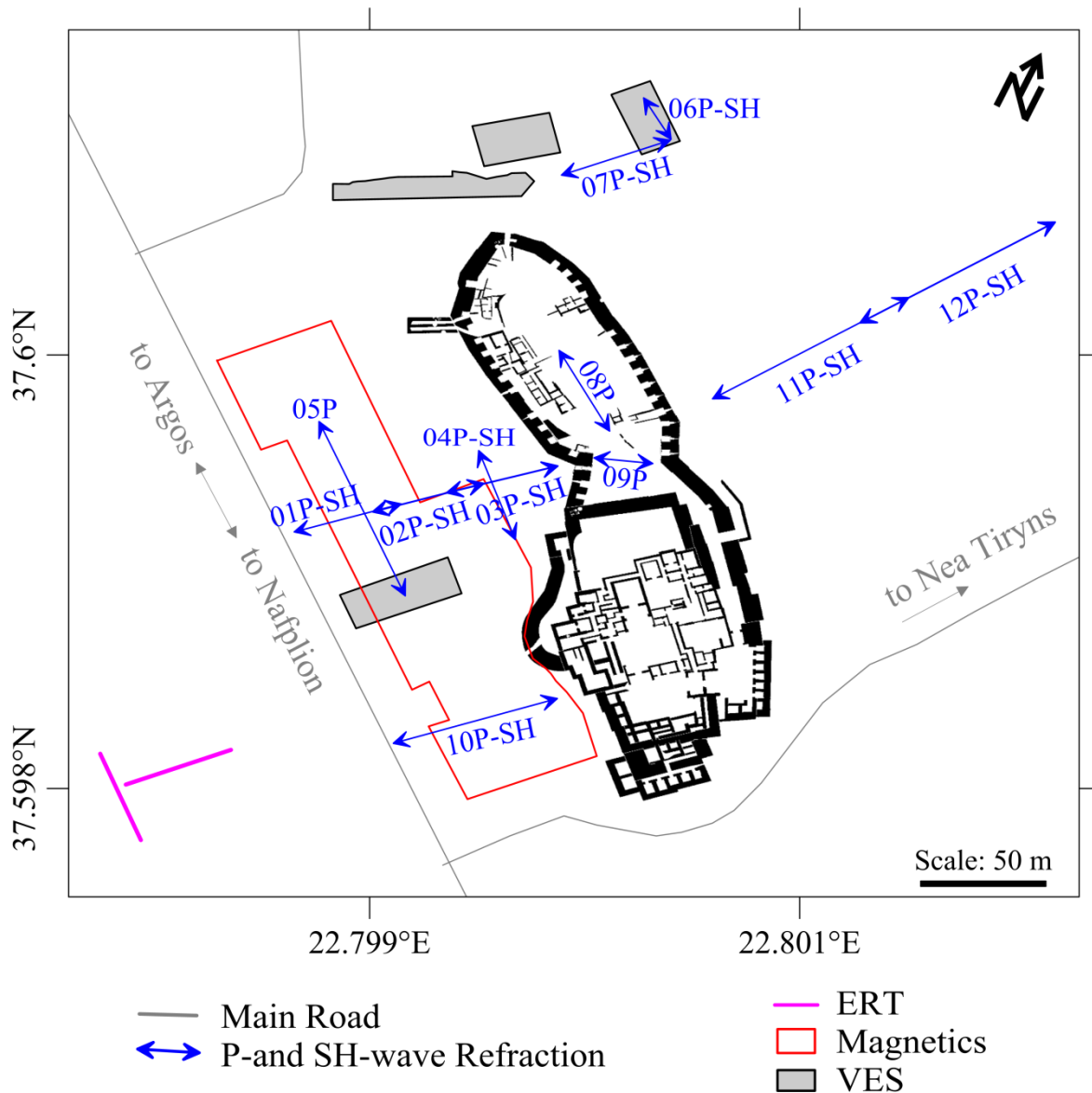


Figure 4.3: Seismic refraction tomography survey of P-and SH-wave data (this study), magnetic and vertical electrical sounding (VES) surveys of Hübner and Giese (2002), and electrical resistivity tomography (ERT) transects of Ntageretzis (2014) superimposed on the archaeological plan of the Tiryns citadel.

Synthetic v_s data for the whole Argive Basin is available for the uppermost 30 m of the subsurface, the so-called v_s^{30} . Values of v_s^{30} can be estimated with empirical relations based on a global proxy (Wald and Allen, 2007) or, if available, from a local proxy (Stewart et al., 2014). The resulting product is a map of v_s^{30} . This approach is widely adopted in engineering practice when v_s data are unavailable for a given site or region. Maps of v_s^{30} are attractive because they provide a rapid way of mapping seismic site conditions for a large surface area, and the data can be used for building codes and for the calibration of ground motion prediction equations (Wald and Allen, 2007; Stewart et al., 2014). Explicitly, these maps correlate “modern” topographic slope with empirical field data in the form of geologic, geotechnical and/or seismic information to compute a synthetic v_s^{30} . So for archaeoseismological purposes one must know upfront how much sediment/soil must be

removed in order to reconstruct ancient walking horizons. Nonetheless, this method is not applicable in this case because the resulting synthetic v_s^{30} map yields unrealistic v_s results. For instance, the Tiryns ridge does not appear on the resulting v_s^{30} map (Figure 4.4) because the algorithm to compute synthetic v_s^{30} uses a 30 arcsec topographic grid (i.e., low resolution for this case study).

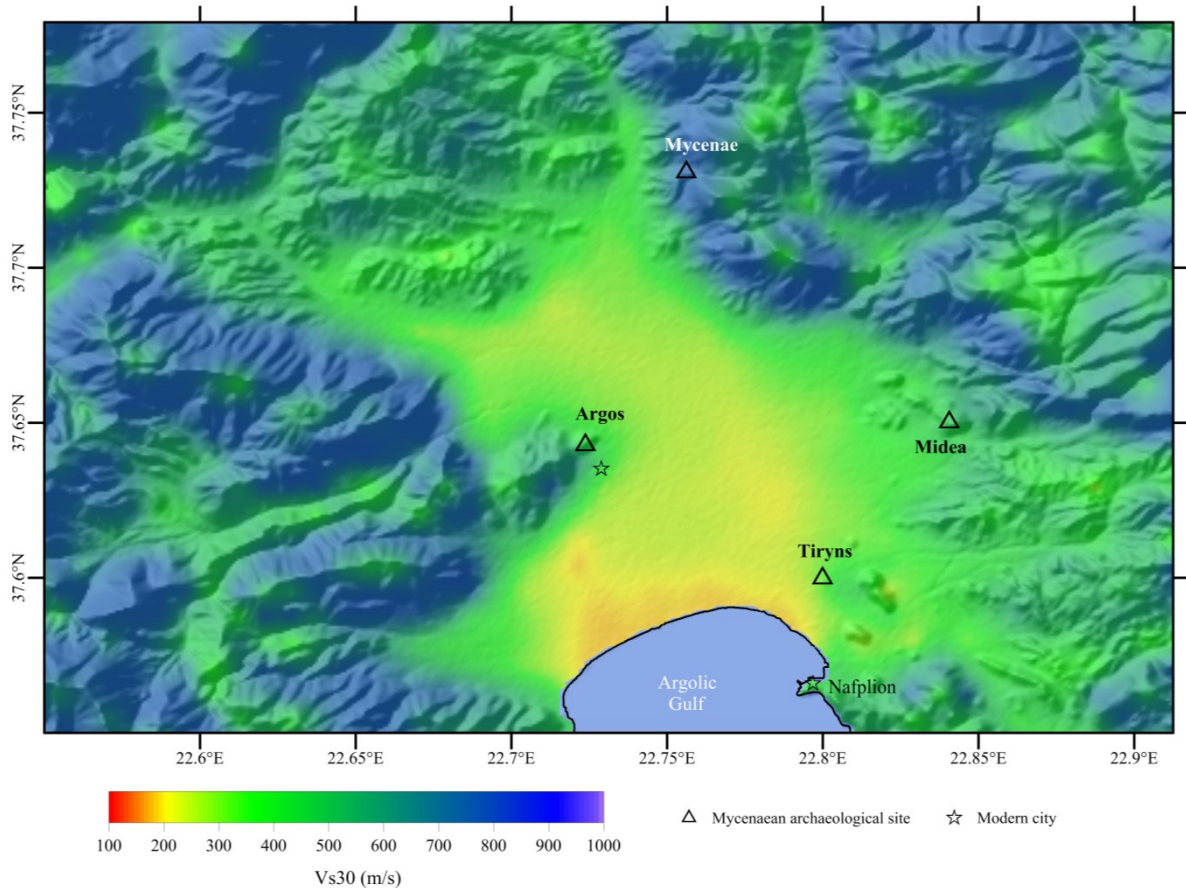


Figure 4.4: Synthetic v_s^{30} map of the Argive Basin of the Argolid Peninsula (Peloponnese, Greece) computed with the v_s^{30} -topographic slope approach of Wald and Allen (2007).

More recently, Stewart et al. (2014) developed a local dataset and geologic-and terrain-based empirical relationships to estimate v_s^{30} for Quaternary sediments and both Tertiary and Mesozoic rock sites on Greek territory. The local proxies of Stewart et al. (2014) were derived using a Greek database. The database contains information regarding local surface geology, geomorphic site conditions, and surface gradient at 30 and 3 arcsec resolutions from 314 sites scattered throughout Greece; however, with little data from the Argive Basin. A detail description of the empirical equations and methodology is given in Stewart et al. (2014). Following the empirical relations for Quaternary sediments and Tertiary and Mesozoic rock sites proposed by Stewart et al. (2014), a synthetic v_s^{30} map is created for the vicinity of Tiryns and Midea archaeological sites (Figure 4.5). An advantage of this proxy over the topographic slope proxy (Wald and Allen, 2007) is that it produces a *material-type* customized synthetic v_s^{30} map for local regions of Greece resulting in more accurate and reliable v_s^{30} values within the applicable region (Stewart et al., 2014). Examination of the

resulting v_s^{30} map using the methodology of Stewart et al. (2014) yields the following results: (i) the synthetic v_s^{30} values of both Tiryns (~790 m/s) and Midea (900 m/s) ridges are only in slight contrast with the v_s^{30} values of the surrounding sediments (620-810 m/s). However, the differences in v_s^{30} are attributed to the wide range of v_s^{30} for tectonized Tertiary rock sites (200 to 1000 m/s with a mean of 456 m/s) and tectonized Mesozoic rock sites (300 to 1200 m/s with a mean of 589 m/s) (Stewart et al., 2014); (ii) the computed v_s^{30} values for both the sediments and the Tiryns and Midea ridges are realistic according to the v_s^{30} categories of NEHRP (2003); and (iii) the synthetic v_s^{30} are comparable with v_s obtained from previous seismic refraction surveys (Karastathis et al., 2010a, 2010b; Hinojosa-Prieto and Hinzen, 2015); therefore, the synthetic v_s^{30} values are tentative for areas lacking directly determined v_s data. The v_s^{30} map in Figure 4.5 yields higher v_s^{30} for the soils around Tiryns than the v_s^{30} map in Figure 4.4. This discrepancy is attributed to the different algorithms to compute v_s^{30} : the algorithm of Stewart et al. (2014) uses an empirical equation derived from geologic-and terrain-based data (3 arcsec topographic grid) while the algorithm of Wald and Allen (2007) uses an empirical equation solely based on topography (30 arcsec topographic grid). The digital elevation model used in Figure 4.5 corresponds to the eastern Argive Basin and was obtained from the digitalization of 1-m resolution topographic charts of the Hellenic Military Geographical Service (HMGS, 1951) using a commercial digitalization and georeferencing mapping software (Didger[®]) by Golden Software, Inc.

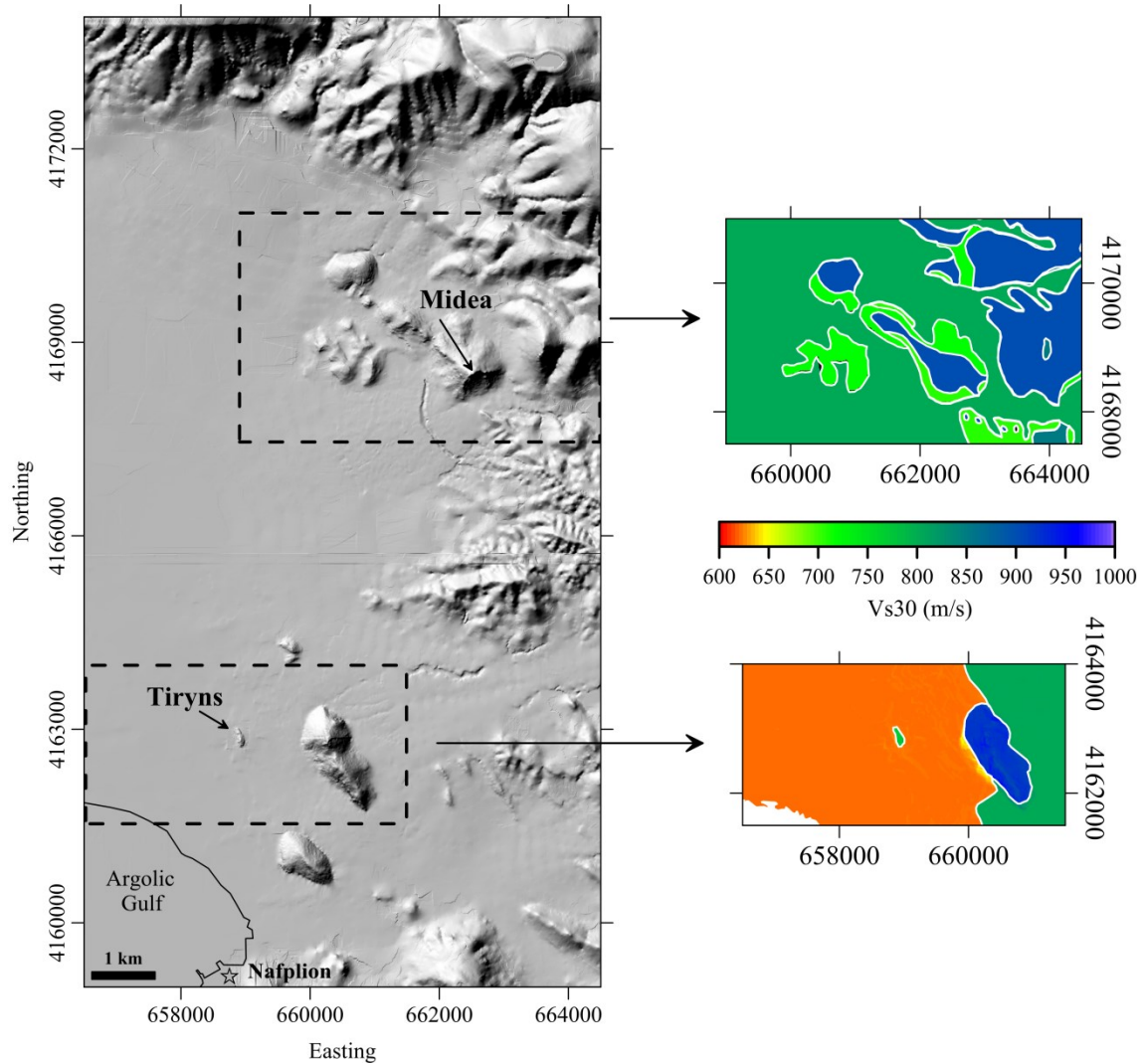


Figure 4.5: Synthetic v_s^{30} map of the vicinity of Tiryns and Midea located in the Argive Basin of the Argolid Peninsula (Peloponnese, Greece) computed with the Geologic-and Terrain-based proxies of Stewart et al. (2104).

4.2.2 Seismic Refraction Tomography (SRT) Survey

During the HERACLES project, a v_p and v_s SRT survey was performed within the limits of the Tiryns archaeological site (Hinojosa-Prieto and Hinzen, 2015). The SRT survey was done in order to (i) derive the v_p and v_s structure and acoustic impedance contrast in the near surface; (ii) to estimate the soil thickness and geometry accumulated prior to the LH IIIB period; (iii) to map the depth and morphology of the soil–bedrock interface; (iv) to compute several elastic moduli parameters such as Poisson ratio (ν), shear modulus (μ), Young’s modulus (E), and bulk modulus (k); and (v) to evaluate the strength of the bedrock with the geotechnical rock mass quality factor. Particularly, v_s is the key geotechnical parameter that controls the dynamic response of the soil to the earthquake excitation primarily consisting of shear-waves propagating from the bedrock up to the ground surface (Kramer, 1996). The elastic moduli coupled with the mechanical parameters, geologic, and archaeological constitute the basis of a comprehensive 2D geotechnical model of Tiryns and Midea. However, SRT was not performed at the Midea archaeological site because the Midea citadel

was built on outcropping bedrock similar to the one at Tiryns. Thus, values for v_s , ρ , material strength for the granular soils in the basin, and for the Midea ridge are assigned based on available upfront geotechnical (e.g., Marinos et al., 2006; Sabatakakis et al., 2008; Apostolidis and Koutsouveli, 2010; Karagianni et al., 2010; Marinos and Tsiambaos, 2010; Tziallas et al., 2013), geologic (Tataris et al., 1970; Piper et al., 1978; Zangger, 1993; Photiades, 2010; GSLI, unpublished data; this study), and directly determined v_s on flysch from northern Peloponnese (Tselentis et al., 2007) and correlative limestones south of Midea (Karastathis et al., 2010a, 2010b).

Twelve v_p and nine v_s profiles were collected (Figure 4.3) using a 24 channel ABEM Terraloc Mk6 v2 seismograph (Figure 4.6). Details of the measurements, data processing and results are given by Hinojosa-Prieto and Hinzen (2015). However, these published results do not include all the 2D tomograms due to the limited space imposed by the journal's guidelines. For consistency in the presentation of the results, this sub-section provides all the seismic refraction tomograms performed by the SRT survey including the resulting Poisson ratio (ν) plots and v_p/v_s plots. Figure 4.7 shows the v_p and v_s profiles plotted in a 3D view with the same velocity scale for direct comparison. For visualization purposes, all v_p and v_s tomograms, ν plots, and v_p/v_s plots are shown individually in Figure 4.8, 4.9, 4.10, 4.11, respectively.



Figure 4.6: Deployment of the seismic refraction tomography survey. (A) Seismograph unit and profile. (B) Aluminum plate source to generate P-waves. (C) Surveying of geophone and shotpoint locations with differential GPS unit. (D) Coupling of SH-wave aluminum source to the ground surface. (E) Leveling of horizontal geophone. (F) Hammer-horizontal impact aluminum source from both left and right sides to generate SH-waves from each side (Photo credits: HERACLES project).

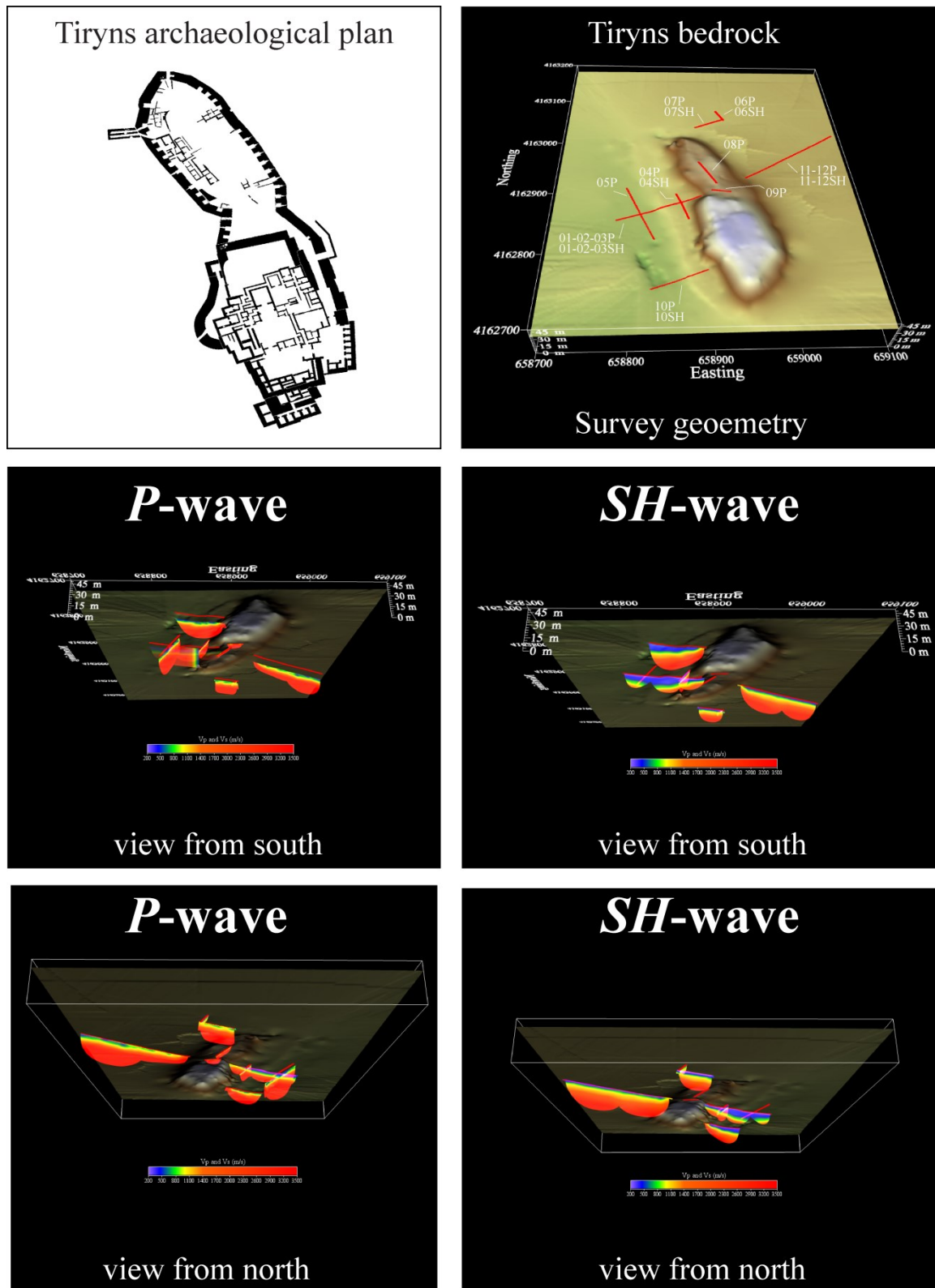


Figure 4.7: 3D view of the v_p and v_s tomograms deployed within the limits of the Tiryns citadel. All tomograms are seen from underneath.

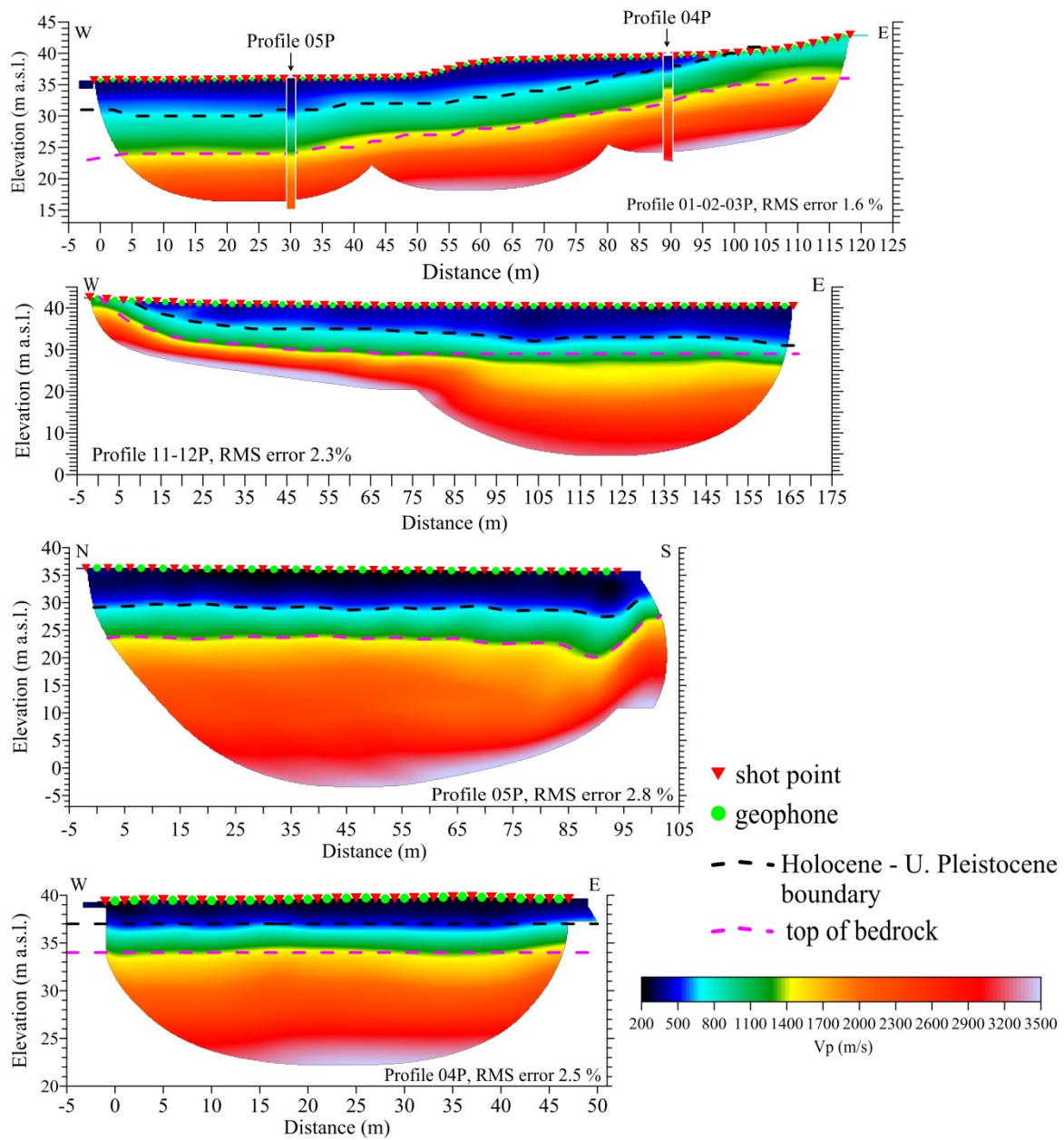


Figure 4.8: P-wave (v_p) velocity structure models from Tiryns. The black and pink dashed lines in all tomograms indicate the interpreted position and geometry of the Holocene–Upper Pleistocene interface and the soil–bedrock interface, respectively. All tomograms are plotted with the same color scale. Figure 4.7 shows the location of intersecting v_p tomograms. RMS = Root Mean Square error.

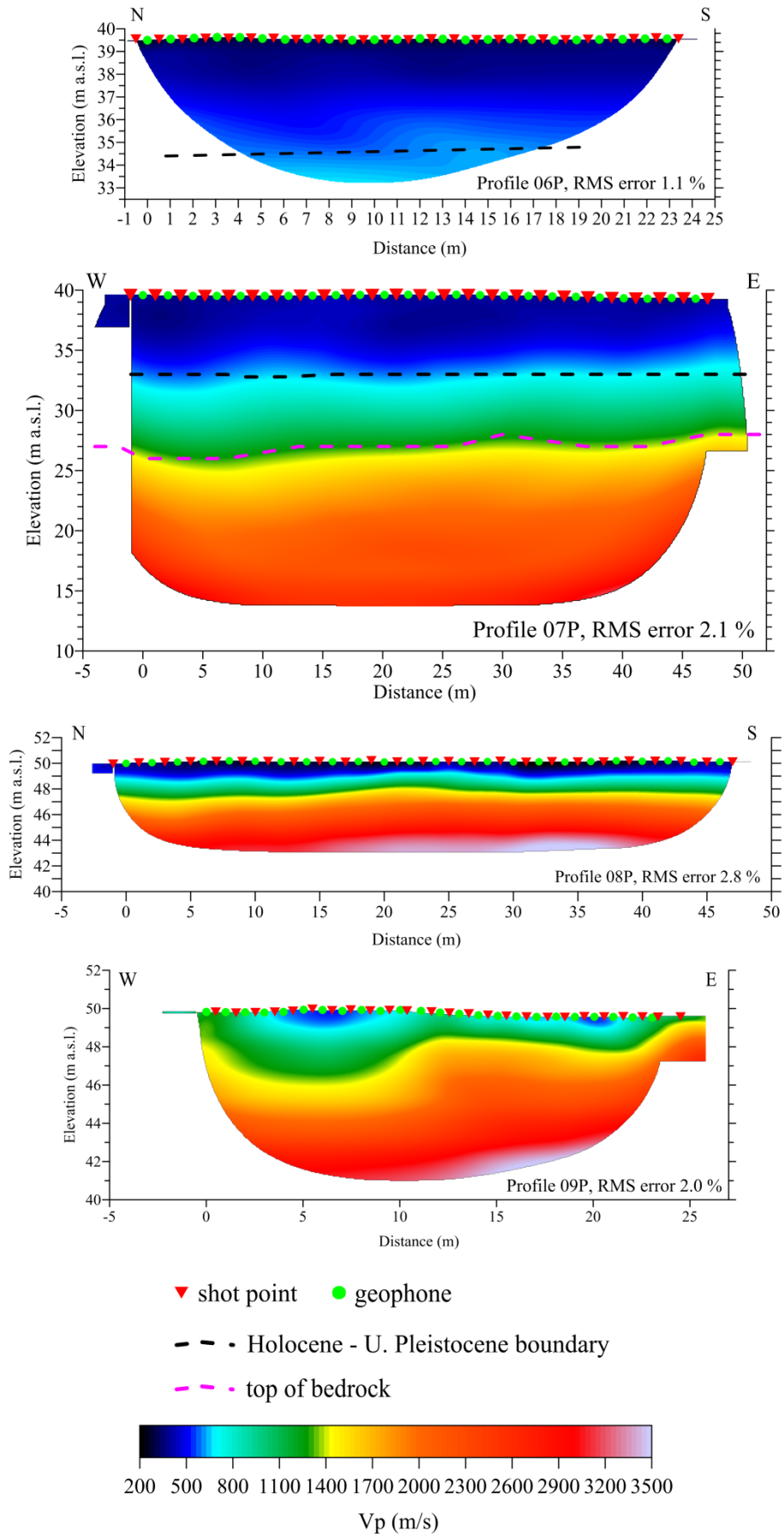


Figure 4.8 continued.

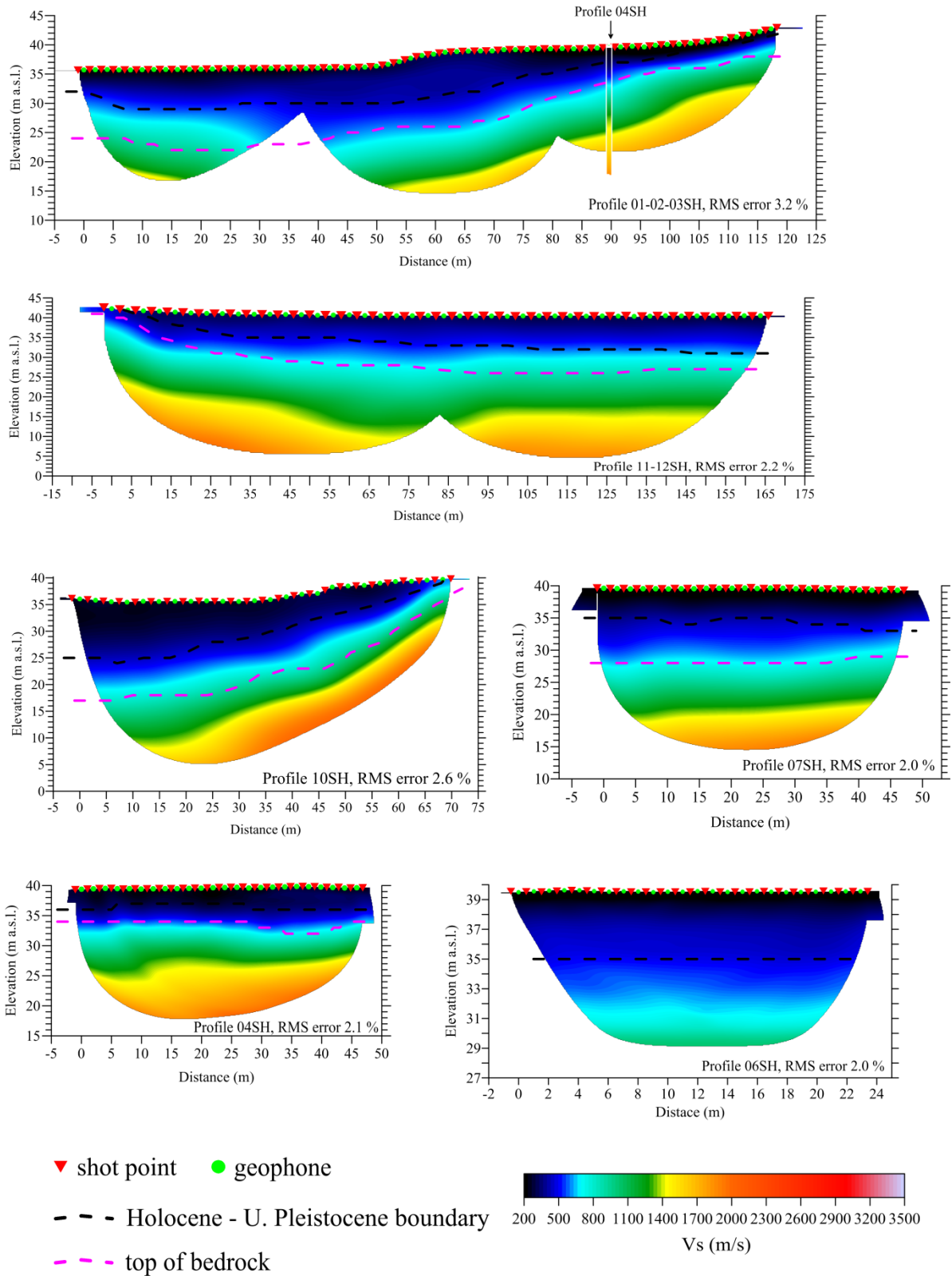


Figure 4.9: SH-wave (v_s) velocity structure models from Tiryns. The black and pink dashed lines in all tomograms indicate the interpreted position and geometry of the Holocene–Upper Pleistocene interface and the soil–bedrock interface, respectively. All tomograms are plotted with the same color scale. Figure 4.7 shows the location of intersecting v_s tomograms. RMS = Root Mean Square error.

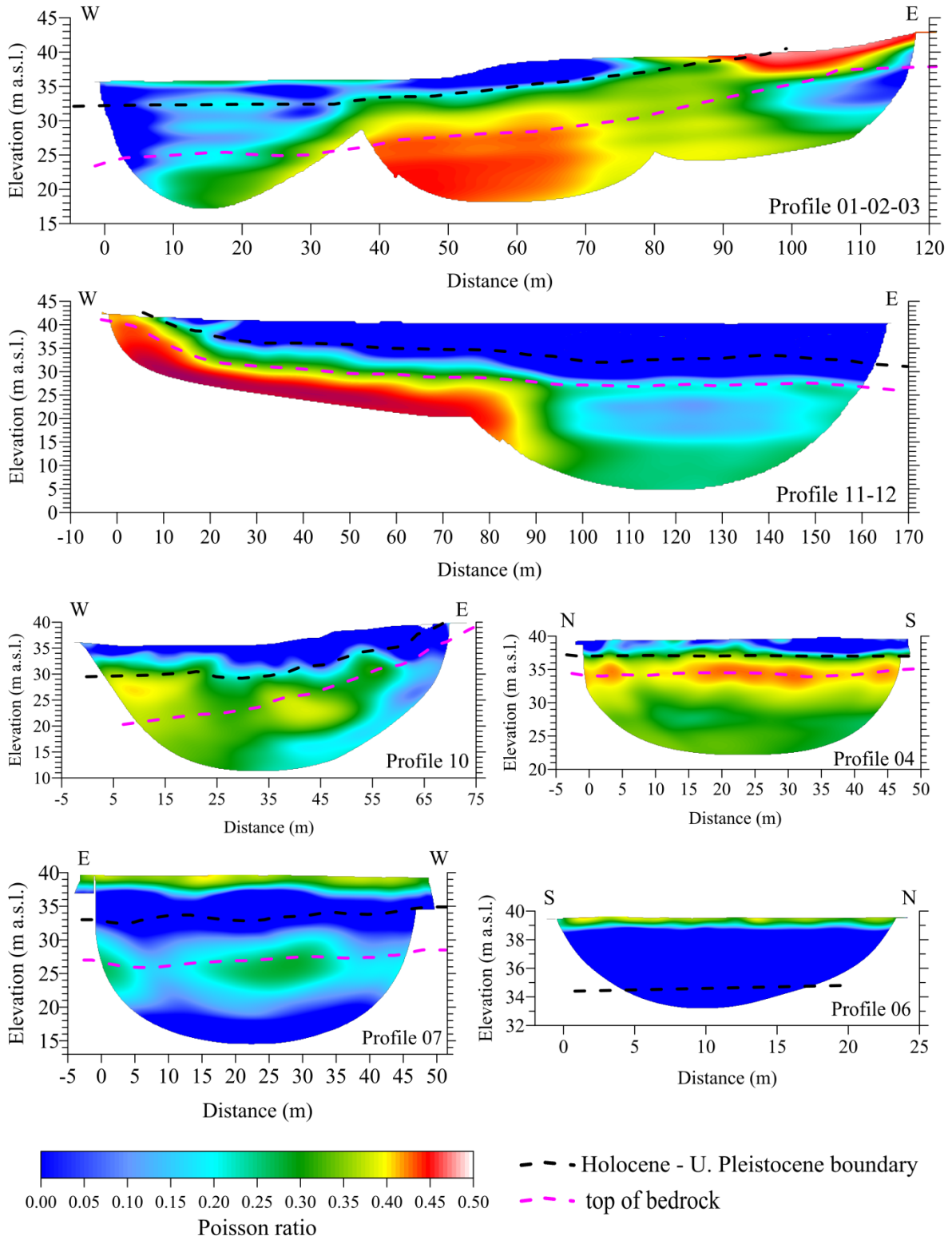


Figure 4.10: Poisson ratio (ν) plots computed from all v_p and v_s tomograms from Tiryns.

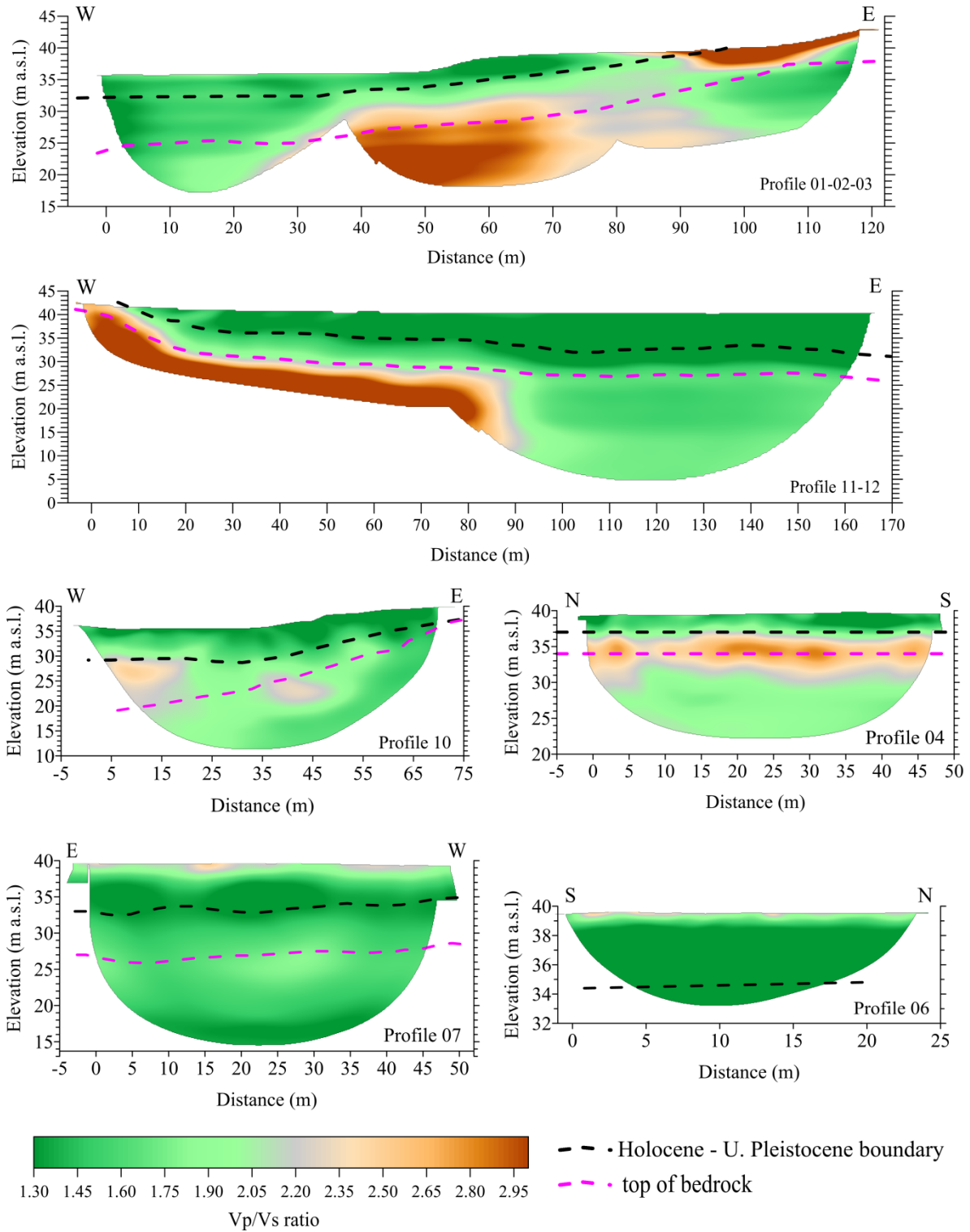


Figure 4.11: v_p/v_s ratio plots computed from all v_p and v_s tomograms from Tiryns.

The previously unpublished v_p and v_s tomograms shown in this section do not change the interpretations and conclusions reached by Hinojosa-Prieto and Hinzen (2015) which are briefly summarized as follows:

- The SRT survey imaged the thickness and geometry of the Late Pleistocene–Holocene fine-grained soils, and the depth and morphology of the soil–bedrock interface. The depth of investigation reaches up to 30 m;
- From top to bottom, the v_p and v_s range from 200–3500 m/s and 120–2000 m/s, respectively:
 - ✓ the Holocene alluvium shows v_p between 300–600 m/s resulting in a calculated mean of 430 m/s and v_s between 185–450 m/s (mean of 300 m/s);
 - ✓ the Late Pleistocene clays/silts have a v_p between 600–1295 m/s (mean of 835 m/s) and v_s between 400–800 m/s (mean of 575 m/s);
 - ✓ and the gradual change from weathered to fresh limestone bedrock is marked by v_p between 1400–3500 m/s (global mean of 2270 m/s) and v_s from 800–2000 m/s (global mean of 1235 m/s); finally, the calculated mean v_p and v_s for the weathered and the fresh portions of the limestone bedrock are 2850 and 1470 m/s and 1893 and 995 m/s, respectively;
- From the geotechnical engineering point of view, the results of all v_s tomograms that detected the limestone bedrock suggest a calculated mean v_s of 855 m/s for the uppermost 30 m. This classifies the Tiryns archaeological site as a class B site (i.e. “Rock”) under the NEHRP (2003) site class definition; however, both a high v_p and v_s impedance contrast (5 and 4, respectively) exists between the Quaternary soils and the bedrock despite that it is a rock site;
- The top of the bedrock varies from 2 to 7 m in the east and 7 to 17 m deep in the west;
- The v values from east-west oriented profiles show that the soil–bedrock boundary is locally water-saturated near to the ridge before it transitions laterally to intermediate and to undersaturated conditions as far as 100 m away;
- Geologic faulting is not identified neither by the v_p and v_s tomograms nor by the detailed structural geologic mapping

4.2.3 Transient Electromagnetic (TEM) Soundings

The TEM method has been successfully applied to map the distribution of electrical resistivity and conductivity of both the soils and bedrock in various Late Neogene–Quaternary sedimentary basins of distinct depositional environment (Karmis et al., 2010; Souplos et al., 2013; Kanta et al., 2013; Mollidor et al., 2013; von Papen et al., 2013; Yogeshwar et al., 2013; Yogeshwar, 2014). The fine to coarse grained sediments of the Argive Basin (Apostolidis and Koutsouveli, 2010) were deposited unconformably on moderately to highly weathered, deformed, and tectonically fractured Alpine bedrock (Photiades, 2010; Apostolidis and Koutsouveli, 2010). This lithologic contrast translates into a good conductor (e.g., conductive clastic deposits) over a poor conductor of electrical current (e.g., hard-rock bedrock). A 1D TEM sounding survey was deployed in the Argive Basin in order to map the thickness, geometry, internal resistivity structure of the sedimentary cover, and the depth to bedrock.

4.2.3.1 1D TEM Data Acquisition and Processing

The TEM-Fast 48 instrument was used with a single-loop dimension of 25×25 m in some locations and 50×50 m in others. Figure 4.12 shows the portable TEM-Fast 48 system instrumentation and the typical field setup. The system was set to a transmitting current of up to 4 Amperes with 32 or 36 active time gates (depending on the depth of penetration) from 8 to $2048 \mu\text{s}$ and a stacking time of about 4 minutes. The TEM data were collected in three field campaigns in the year of 2013 (June 15-17, August 5-7, and December 15-20) by Professor Pantelis Soupios at the Laboratory of Geophysics and Seismology of the Technical Educational Institute of Crete, Greece.

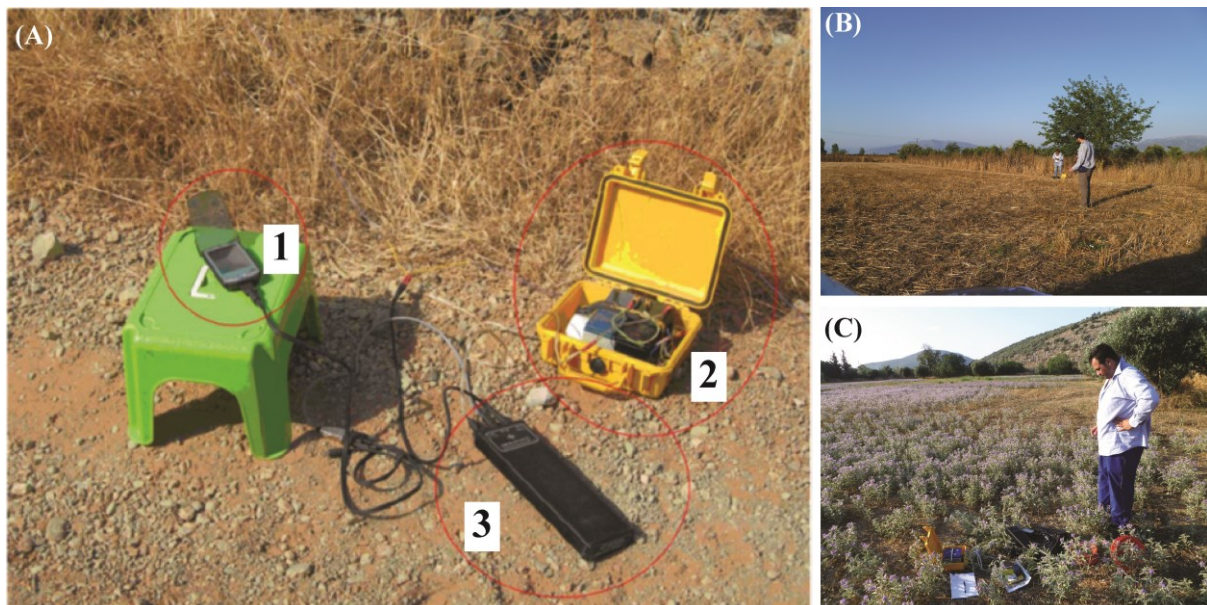


Figure 4.12: (A) TEM instrumentation composed of palmtop PC (1), external power supply (2), and the TEM-Fast 48 system (3). Example of a TEM single-loop deployment on (B) flat terrain and adjacent to (C) a hard-rock ridge.

The 1D TEM survey consists of a total of 151 stations distributed throughout the Argive Basin with a station spacing varying from 200-750 m (Figure 4.13). Several TEM stations line up along a profile. There is a total of 10 profiles labeled P1 to P10 and with different azimuths. To reduce the influence of noise sources, the TEM sounding locations were chosen away from power and telephone lines, pipelines, operating or abandoned boreholes, roads, metallic fences, among other sources of cultural noise. To avoid aliasing effects from high frequency radio sources and to improve the signal to noise ratio, TEM soundings were repeated three times at each station. The stations were numbered in an ascending order and the first, second and third measurements at a given station were given the suffix A, B and C, respectively. The measurement with the minimum Root Mean Square error, from each station was chosen for modeling and inversion of 1D geoelectrical resistivity soundings. TEM-Fast 48 raw data from a total of 142 TEM soundings (out of the 151 soundings) were consistently pre-processed (e.g., editing and smoothing) prior to inversion. These steps were done with the integrated TEM-RES software package. The geographic coordinate of the selected TEM measurement/station is listed in Appendix B (Table 4.2). The TEM measurements performed

inside the limits of the Tiryns archaeological site were rejected because of noisy data caused by metallic fences, buried pipes and a major road.

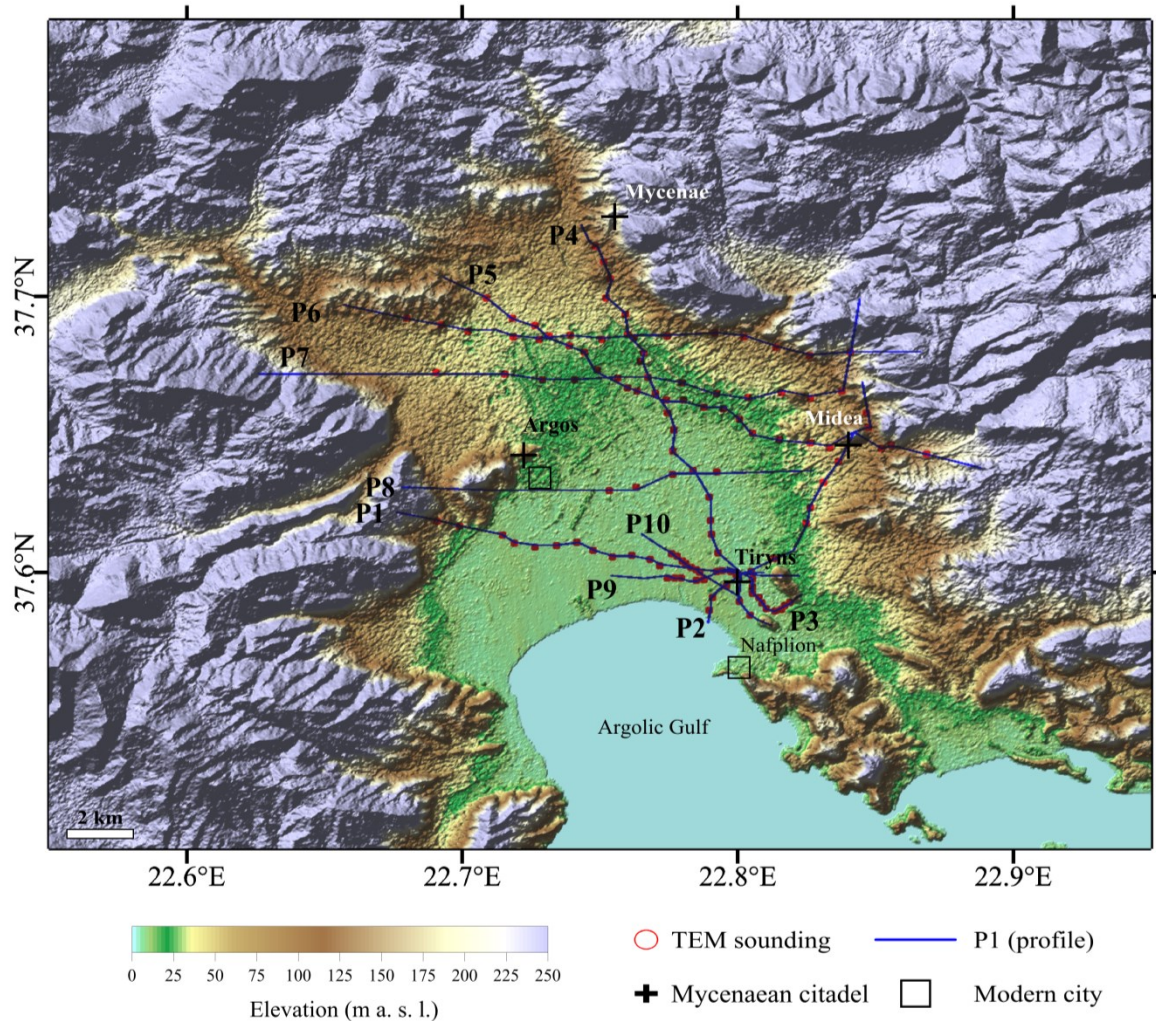


Figure 4.13: Map of the 1D TEM deployment in the Argive Basin of the Argolid Peninsula (Peloponnese, Greece). The geographic coordinate of each TEM station and selected measurement for 1D inversion is listed in Appendix B.

The interpretation of 1D TEM data set is based primarily on 1D inversions in which the resistivity of the model only varies with depth (one-dimension) (Scholl, 2005; Haroon et al., 2014). The 1D TEM data were inverted by Haaf (2015) using the 1D algorithm *EMUPLUS* of Scholl (2005). *EMUPLUS* utilizes three different 1D inversion techniques including Occam’s R1 and R2, Marquardt–Levenberg and Monte–Carlo. The Occam’s R1 and R2 technique uses a minimum number of model parameters to explain the data. In order to obtain a multi-layered smooth model, the Occam’s inversion implemented for the first (R1) and second order (R2) smoothness is used (Constable et al., 1987). The R1 defines “roughness” as the summed differences between adjacent layers of a N -layer case and R2 defines the total change in differences with depth (Constable et al., 1987; Scholl, 2005; Yogeshwar et al., 2013). The R1 and R2 Occam’s inversion models typically differ in zones where the model is not supported by the data. The Marquardt–Levenberg technique aims to find a simple subsurface model

with smooth structure consisting only of a few layers which are derived visually from the Occam's inversion model (Scholl, 2005; Yogeshwar, 2014). For the Occam's and Marquardt–Levenberg inversions, a homogenous earth model with a specified number of layers is used as an initial model. The Monte–Carlo technique incorporates random models to fit the measured data. Each model parameter of a preliminary best-fit model is perturbed randomly by a pre-defined percentage value and if the data-fit falls within a pre-defined acceptance range, the model is kept as equivalent otherwise a separate Marquardt–Levenberg inversion is performed and the procedure is repeated (Yogeshwar, 2014). Equivalent models still rely on the initial model, but they provide an estimate of the non-linear model parameters variances (Yogeshwar, 2014). The theory of Occam's R1 and R2, Marquardt–Levenberg and Monte–Carlo inversions are discussed in detail by Scholl (2005) and Yogeshwar (2014). The adopted multi-method inversion procedure and algorithm (*EMUPLUS*) have been applied successfully to various 1D TEM data sets collected in terrestrial (von Papen et al., 2013; Yogeshwar et al., 2013; Haroon et al., 2014) and marine (Mollidor et al., 2013) environments under different geometric configurations.

4.2.3.2 Results and Interpretations of the 1D TEM Survey

Figure 4.14 shows an example of the final 1D TEM inversion models calculated with the Occam's R1 and R2, Marquardt–Levenberg and Monte–Carlo techniques with their corresponding topographic profile for Tiryns and Midea. The remaining final 1D TEM inversion models are shown in Figure B1 of Appendix B. The results consistently show a shallow three-layer case scenario: upper, middle and lower layer with resistivity values from 10-120, 0.1-1200, and 40-140 Ω -m, respectively. The lower layer is interpreted as the half-space (i.e., bedrock). However, as expected, the resulting depth-resistivity structure varies noticeably from station to station (Haaf, 2015). The maximum depth of investigation is estimated from the depth at which the Occam's R1 and R2 inversion models start to depart (Haaf, 2015). The upper and middle layer gained well-resolved depths and resistivities, but the lower layer is rather poorly resolved in some cases. The poorly-resolved lower layer is due to the removal of transients prior to the inversion step because of large errors at late times (deeper depths) in the field data. Further, the size of the loop array may have been too small to penetrate large portions of bedrock. Therefore, while the resistivity structure of the Late Neogene–Quaternary sedimentary cover is well-constrained across the basin, the soil–bedrock boundary and the transition from weathered to unweathered bedrock are difficult to detect with the resulting 1D inversion models. Nonetheless, the available boreholes assist in the interpretation of the 1D TEM inversion models.

Around Tiryns, a conductive middle layer is bounded by a more resistive upper and lower layer. Several adjacent sections show this resistivity pattern (Haaf, 2015). The resistive upper layer has also been identified with vertical electrical soundings immediately outside the fortification walls of Tiryns (e.g., Hübner and Giese, 2006). Conversely, the three-layered resistivity structure varies noticeably around Midea (Figure 4.14). For instance, TEM station 101B located ~1000 m northeast of Midea shows a thin (~ 5 m) middle conductive layer bounded by a resistive upper (20 m thick) and a lower layer. Conversely, station 108B

located ~1000 m southeast of Midea shows a 30 m thick resistive middle layer bounded by a less resistive upper layer (5 m thick) and a lower layer.

The interpretation of the 1D TEM inverted models is guided by the aforementioned boreholes (see chapter 3, Figure 3.4), surficial geology, and insights from available upfront TEM soundings, electrical resistivity tomography profiles, seismic profiles, and a gravity survey (see Figure 3.2). The resulting three-layer resistivity structure around Tiryns is interpreted as follows: the upper, middle, and lower layers correspond to the Holocene alluvium, the Upper Pleistocene clays/silts/muds, and the weathered and fractured portion of the bedrock. The 1D TEM inverted models from stations near Tiryns (e.g., stations A010C, A009C, A028C) indicate that the soil–bedrock interface varies between 30 to 50 m depth at about ~250 to 600 m away from the Tiryns hill. This is consistent with seismic refraction data (Hinojosa-Prieto and Hinzen, 2015). The resulting three-layer resistivity model around Midea is interpreted as follows: the upper and middle layers correspond to the whole Upper Pliocene–Quaternary clastic heterogeneous sequence. The lower layer corresponds to the moderately to highly weathered and fractured bedrock composed of limestone thrust against conglomeratic flysch.

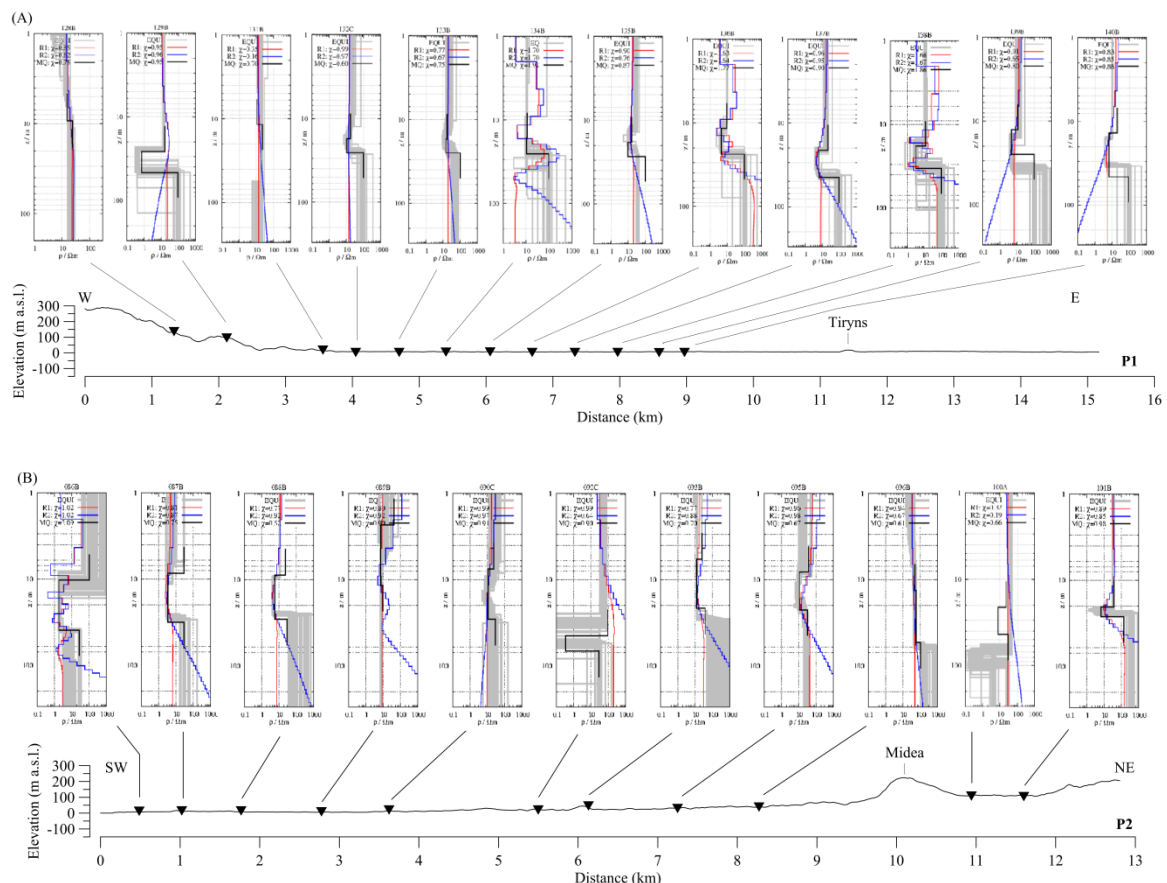


Figure 4.14: 1D TEM models inverted with the Occam’s R1 (red line) and R2 (blue line), Marquardt–Levenberg (black line) and Monte–Carlo (grey line) techniques (from Haaf, 2015) plotted along corresponding topographic profile crossing (A) Tiryns and (B) Midea.

4.3 Geotechnical Profiles and Dynamic Properties of Soils and Bedrock

The previously presented geotechnical descriptions of the soils and bedrock, v_s , and 1D resistivity data coupled with geologic information (chapter 3) are interpreted collectively in order to create geotechnical profiles that traverse the archaeological sites of Tiryns and Midea and the area between them. The results are shown in Figures 4.15, 4.16, and 4.17, respectively. The profiles depict (i) the type and geometry of the soils; (ii) the depth to the soil–bedrock interface; (iii) and account for the Mycenaean walking horizon after removing post-Mycenaean sediments mapped by Zangger (1993, 1994). Then, each lithologic unit in each profile is assigned its corresponding v_s (in m/s), density (in g/cm^3), G/G_{max} curve, and ζ curve. Finally, several 1D geologic models are extracted from the resulting geotechnical profiles and are used as modeling sites for the 1D forward modeling of local site effects. The adopted G/G_{max} and ζ curves used in the estimation of local site effects correspond to fine-grained sands, clays/silts, coarse-grained gravels and hard-rock bedrock, and are taken from Seed and Idriss (1970), Seed and Sun (1989), Weber (2007), and Chandler et al. (2005a, 2005b), respectively. The theoretical background of the selected G/G_{max} and ζ curves is discussed in chapter 6 and the curves are shown in Figure 6.2.

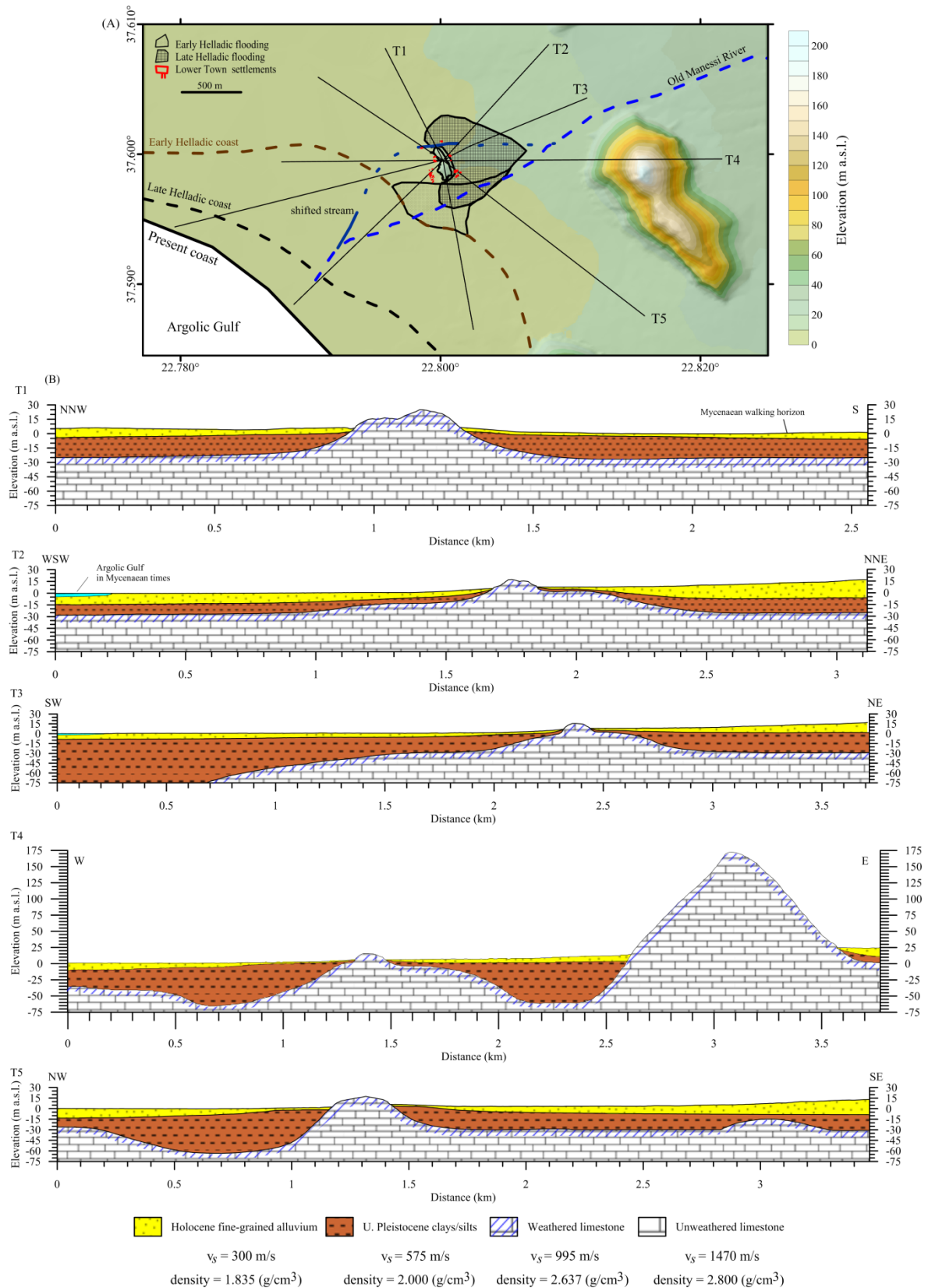


Figure 4.15: (A) Terrain map showing the location of the (B) geotechnical profiles at Mycenaean Tiryns with corresponding average v_s (m/s) and density (g/cm^3) for each material. The Early and Late Helladic coastlines and flooding areas are after Zangger (1994). $3\times$ vertical exaggeration.

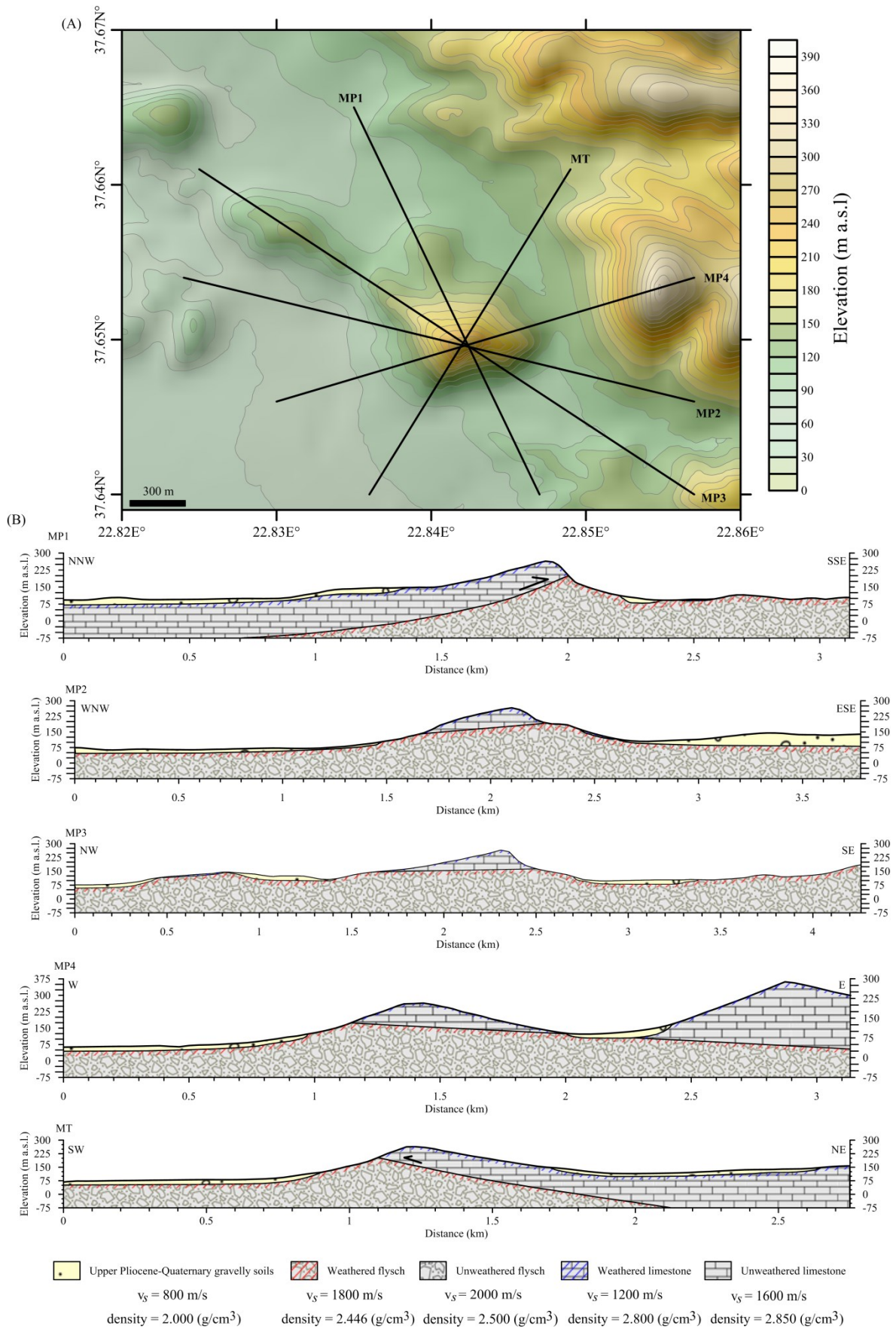


Figure 4.16: (A) Terrain map showing the location of the (B) geotechnical profiles at Mycenaean Midea with corresponding average v_s (m/s) and density (g/cm^3) for each material. No vertical exaggeration.

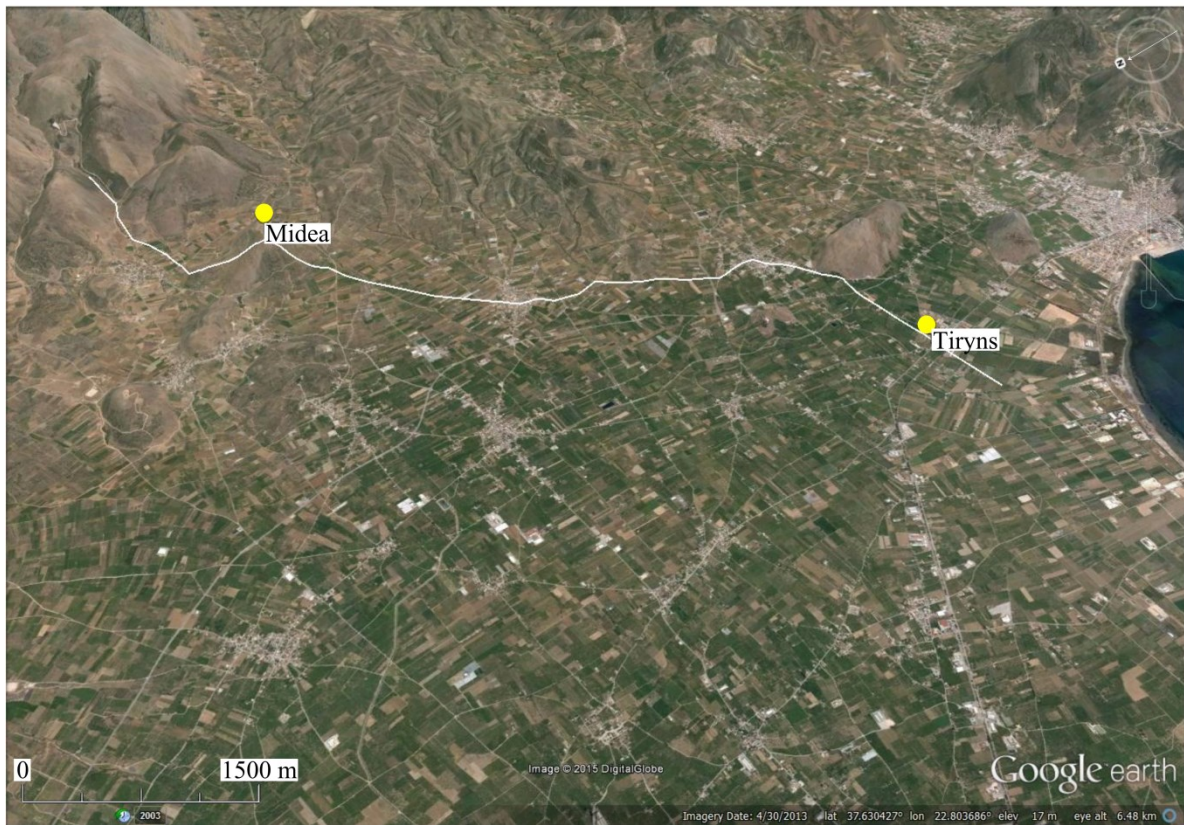
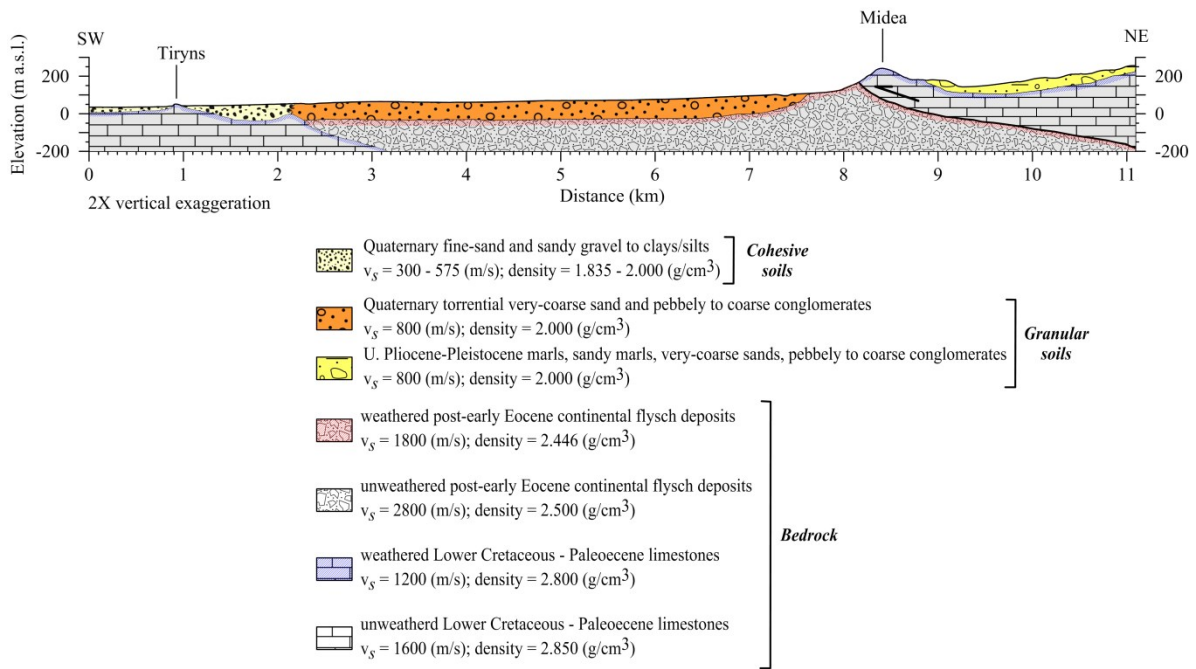


Figure 4.17: (Upper panel) Tiryns–Midea geotechnical profile with corresponding v_s (m/s) and density (g/cm^3) for each material. (Lower panel) Satellite photograph from Google Earth® with view looking towards the east-southeast. 3× vertical exaggeration.

5. SYNTHETIC EARTHQUAKE RECORDS FOR NUMERICAL MODELING OF LOCAL SITE EFFECTS

A data set of synthetic earthquake records is developed following a deterministic approach. Seismic ground-motions can be estimated with an empirical ground-motion model and with numerical ground-motion models. Numerical ground-motion models can be made with the stochastic and the Green's function methods. The empirical model requires actual recordings of earthquakes while the numerical models allow the computation of a synthetic earthquake record(s) in the absence of strong-motion earthquake records measured at or near the site of interest. Each method yields different results because the source, travel wave path, and site conditions are accounted for by different modeling parameters. Somerville and Moriwaki (2003) give a comparison of the empirical, stochastic, and Green's function methods to estimate seismic ground-motion (Table 5.1). The stochastic and the Green's function simulation methods are widely used in earthquake engineering practice (Somerville and Moriwaki, 2003) and have been recently applied in quantitative archaeoseismology (e.g., Hinzen, 2005; Caputo et al., 2010).

Table 5.1: Alternative procedures for estimating earthquake-induced ground-motion (modified after Somerville and Moriwaki, 2003).

	Method	Earthquake Source	Path (wave propagation)	Site
	Empirical	Seismic Moment or Magnitude	Distance	Geological category
Numerical	Stochastic	Source spectrum	Attenuation function, e.g., $\frac{1}{R} - \frac{1}{R^2}$, or empirical. Duration varies with R. Anelastic Q . No distinct body waves or surface waves.	kappa (κ) or f_{\max}
	Green's function	Shear dislocation, slip time function specified on fault	Green's function including body waves, surface waves, anelastic Q .	kappa (κ); empirical or theoretical receiver function

The stochastic method models ground-motion as a time sequence of band limited white noise (Somerville and Moriwaki, 2003). A Fourier spectral model of the ground-motion is created, starting with a model of the source spectrum and modifying its shape by factors that represent wave propagation effects. The stochastic method is described in detail by Beresnev and Atkinson (1997), and implemented in the FINSIM computer code of Beresnev and Atkinson (1998). The method uses a crustal attenuation (Q) model and a duration model to simulate propagation effects. The source area (fault area) is divided into subsources. Subsource time series are created assuming a ω^2 spectrum following the method of Boore (1983, 2003). The propagation to the observation point (or site) is calculated with duration and attenuation operators (Boore and Atkinson, 1987). The FINSIM code uses a summation procedure so that the rupture propagates from the hypocenter and activates the subsources as it passes them. A random component is included in the subsource trigger times (Beresnev and Atkinson, 1997, 1998). The stochastic method has been applied successfully to large earthquakes of different character, such as in western and eastern North America and South America (Atkinson, 1995; Beresnev and Atkinson, 1997), and even to smaller events down to moment magnitude (M_w) of 6 (Castro et al., 2001; Roumelioti et al., 2004a).

The Green's function method is a more mathematically rigorous procedure that contains fewer simplifications in comparison with the stochastic method. The Green's function method uses scaling relations for earthquake source parameters in conjunction with the elastodynamic representation theorem to construct ground-motion time histories in the time domain without resorting to assumptions about the shape of the source spectrum (Somerville and Moriawaki, 2003). This involves summation over the fault surface of the convolution of the slip time function on the fault with the Green's function for the appropriate depth and distance. This summation process is based on linear superposition and does not account for nonlinear soil effects. Calculation of the Green's functions requires knowledge of the crustal velocity structure and Q between the source and the site (Kramer, 1996). Moreover, the simulation procedure is used to develop synthetic ground-motion on "engineering bedrock". This ground-motion is then used as input into a soil response analysis to obtain the ground motion at the soil surface. The Green's function method is implemented by Wang (1999) in his algorithm consisting of two computer codes: *qscmp08* and *qsgrn08*. The *qscmp08* code computes the synthetic seismograms (two horizontal and vertical) once the seismogram Green's function of a layered half-space earth model has been computed with the *qsgrn08* code. The algorithm is numerically stable and high-frequency synthetic seismograms (e.g., near-field motions) can be computed for modeling local site effects.

The adopted deterministic approach to model seismic loading at the Tiryns and Midea archaeological sites is as follows:

- (1) construction of a seismotectonic model of active faults segments or seismogenic sources including normal, strike-slip, and reverse faults with a planar and rectangular fault geometry;
- (2) calculation of theoretical M_w and down-dip rupture width (DRW) for normal fault segments based on the empirical relation derived from a local database for *Aegean-type normal faults* (Pavlidis and Caputo, 2004) and from a worldwide database that includes all types of slip (Wells and Coppersmith, 1994);
- (3) assignment of DRW of faults and M_w for strike-slip fault segments based on the empirical relation of Wells and Coppersmith (1994) derived from a worldwide database that includes all types of slip;
- (4) calculation of theoretical surface fault rupture length and DRW of subduction-related reverse faults using the empirical relation of Papazachos et al. (2004), Strasser et al. (2010), and Blaser et al. (2010) derived from different worldwide data sets;
- (5) and calculation of synthetic ground-motion parameters based on the proposed faults using both the stochastic and Green's function modeling techniques. The ground-motion parameters include pseudo-acceleration response spectra and acceleration seismograms with the stochastic technique; and acceleration, velocity, and displacement seismograms with the Green's function technique. For each simulation, the observation point is placed on outcropping bedrock; in this case inside the fortification walls of Tiryns and Midea. Both observation points classify as site class B ("rock") under the NEHRP (2003) site class definition (Hinojosa-Prieto and Hinzen, 2015). The resulting synthetic earthquake records are used as rock outcropping ground motions in the forward modeling of site-specific local site effects.

5.1 Seismotectonic Model and Finite-Fault Models

The seismicity pattern and seismicity levels of the Argive Basin (AB) and surroundings have been presented in Chapter 3. The seismotectonic model consists of four seismogenic zones that are here considered potential seismic hazards to all Mycenaean sites located in the AB. The seismogenic zones include the (i) AB; (ii) the eastern limit of the Patras-and-Corinth Continental Rift (PCCR) system located ~40 km north of the AB; (iii) the Iria–Epidauros Sinistral Transform (IEST) fault system located 25 to 35 km southeast of the AB; and (iv) the Hellenic Subduction Zone (HSZ). Normal faults exist in the AB and PCCR, strike-slip faults in the IEST, and reverse faults in the HSZ. Further, any of these faults is a potential seismogenic source. Considering the distance between the fault source and the observation sites (i.e., Tiryns and Midea), the observation sites are subjected to strong short-period (high-frequency) motion from earthquakes triggered by faults in the AB and IEST and to strong long-period (low-frequency) motion from larger earthquakes triggered by more distant faults including those located in the PCCR and HSZ.

5.1.1 Normal Faults in the Argive Basin and Patras–Corinth Continental Rift

It is important to discuss the criteria to classify normal faults in the Argive Basin–Argolic Gulf region because of their proximity to Mycenaean Tiryns and Midea. The tectonic setting of the Argive Basin–Argolic Gulf structure remains poorly understood. Submarine, steeply-dipping normal faults linked to E-W and NNW-trending extension during the Pliocene to Pleistocene and mildly folded and faulted Pliocene submarine sediments have been detected in marine seismic reflection profiles in the Argolic Gulf; however, there is no evidence of fault movement for the past 1 Ma (van Andel et al., 1990b; Papanikolaou et al., 1994; Piper and Perissoratis, 2003; Mitropoulos and Zananiri, 2010). Onshore seismic reflection and refraction profiles ~2 km south of Tiryns (Karastathis et al., 2010a, 2010b) and refraction profiles around Tiryns and several boreholes (Hinojosa-Prieto and Hinzen, 2015) detect uneven bedrock topography but not evidence of faulted Quaternary sediments. Particularly, the surface traces of normal faults in the AB have been observed and inferred on the basis on local surficial geologic, geomorphologic, and neotectonic observations and classified as active or probably active without further confirmation and without clearly defining the term ‘active’ (Table 5.2) (Papastamatiou et al., 1960; Tataris et al., 1970; Papanastassiou et al., 1993; Papanikolaou et al., 1994; ECPFEO, 1996; Georgiou and Galanakis, 2010). The studies lack information about subsurface fault geometry and paleoseismic investigations are non-existent. Thus, the certainty of existence of Quaternary normal faults in the AB differs from fault to fault (see Table 5.2). While the geomorphic expression of normal faults is noticeable on the hard-rock, hilly terrain outside the sedimentary plain, it is highly questionable inside the plain. Fault scarp data from normal faults, of presumed Pliocene to Quaternary age, collected at outcropping bedrock indicate a NW-SE oriented extensional stress field (Georgiou and Galanakis, 2010), consistent with the pattern seen offshore. The earthquake catalogue for Greece extending for the period from 550 BCE to 2013 (<http://geophysics.geo.auth.gr>; Makropoulos et al., 2012) and local, short-term seismic experiments (e.g., 45-51 days: Hatzfeld et al., 1989, 1993a, 1993b; Makris et al., 2004; 9 months: this study) show scarce and diffuse, shallow (≤ 40 km), minor to light earthquake activity in the Argive Basin–Argolic Gulf region; and direct links between these weak

earthquakes and specific normal faults cannot be made in the lack of both clustering events and of any fault plane solutions. Poorly documented nearby historical events cannot be taken as conclusive evidence of fault-activity in the basin. The current data about the existence of normal faults in the AB is rather premature, insufficient, and inaccurate to portray active and/or probably active faults, e.g., < 130,000 years old following Machette (2000). This line of reasoning also applies to the poorly documented strike-slip faults of the IEST. However, for the sake of testing the Mycenaean earthquake hypothesis and aware of the speculative nature of fault-activity in the AB, several fault segments are still taken as ‘capable or potential sources’ due to their close proximity to Mycenaean Tiryns and Midea. On the other hand, fault-activity on the seismogenic sources in the eastern Gulf of Corinth and the HSZ is well-documented and the sources are active.

Table 5.2: Criteria to define active and potentially active normal faults in the Argive Basin. Segments with code given in bold have least uncertainties.

Fault Segment Code	Criteria	Observations	Reference
ABNF-1	neotectonic mapping; marine seismic reflection surveying	active; inferred surface fault trace; clear geomorphic expression; talus cones deposits on downthrown block; absent fault scarp onshore; imaged faults offshore and displaced marine reflectors	ECPFEO (1996); van Andel et al. (1993)
ABNF-2	instrumental seismicity; marine seismic reflection surveying	probable active; inferred surface fault trace; clear geomorphic expression; absent fault scarp; imaged faults and displaced marine reflectors; bathymetric-geomorphologic survey	Hatzfeld et al. (1989, 1993, 2001); Hatzfeld (1999); van Andel et al. (1993); Papanikolaou et al. (1994)
ABNF-3	geologic surveying; neotectonic mapping	probable active; inferred surface fault trace; clear geomorphic expression; talus cones deposits on down-thrown block; absent fault scarp	Papastamatiou et al. (1960); ECPFEO (1996)
ABNF-4	geologic surveying	probable active; inferred surface fault trace; inferred geomorphic expression; buried/eroded scarp?	Tataris et al. (1970)
ABNF-5	neotectonic mapping	active; observed surface fault trace; clear geomorphic expression; talus cones deposits on downthrown block; absent fault scarp	ECPFEO (1996)
ABNF-6	neotectonic mapping	active; observed surface fault trace; clear geomorphic expression; talus cones deposits on downthrown block; absent fault scarp	ECPFEO (1996)
ABNF-7	neotectonic mapping; geomorphologic surveying	probable active; inferred surface fault trace; clear geomorphic expression; talus cones deposits on downthrown block; absent fault scarp	ECPFEO (1996); Papanastassiou et al. (1993)
ABNAF-4	structural geologic mapping	probable active; inferred surface fault trace; buried/eroded scarp?; inferred geomorphic expression based on adjacent visible fault scarps; the middle portion (5 km long) is mapped and the remaining 15 km (both extremes) are excessively inferred	Georgiou and Galanakis (2010)
Mycenae fault	neotectonic mapping; geomorphologic surveying	active; observed surface fault trace; clear geomorphic expression; talus cones deposits on downthrown block; visible fault scarp	ECPFEO (1996); Papanastassiou et al. (1993)

The currently active EW-trending normal faults in eastern PCCR are related to NS-oriented extension (e.g., Hatzfeld, 1994; Rigo et al., 1996; Armijo et al., 1996; Bernard et al., 1997; Hatzfeld et al., 2000). The lengths of known active normal faults in the southern coastal strip of the PCCR vary from 12 to 40 km (Pavlidis et al., 2006; Karastathis et al., 2010a). Faults strike W-NE, dip N at moderate to steep angles, reach up to 40 km long, and are as close as about 40 km to the AB. The faults are clearly active and typically produce moderate to strong

earthquakes (Rigo et al., 1996; Bernard et al., 1997; Goldsworthy et al., 2002; Moretti et al., 2003; Pavlides and Caputo, 2004). The geomorphic expression or geological fault length of a normal fault is taken to represent the potential surface rupture length (SRL). The SRL (in km) of each modeled fault is taken from available studies in the AB and the PCCR (see Table 5.3) and is used to estimate the potential M_w . Then, M_w is used to estimate the potential DRW (in km). The DRW is calculated using the global empirical relation of Wells and Coppersmith (1994) for all types of slip:

$$DRW = 10^{(-1.01 + (0.32 \cdot M_w))} \quad (1)$$

M_w is calculated using the global empirical relationship of Wells and Coppersmith (1994) (equation 2) also for all type of slip and the empirical relation of Pavlides and Caputo (2004) (equation 3) derived only for *Aegean-type normal faults*:

$$M_w = 5.08 + 1.16 \cdot \log(SRL) \quad (2)$$

$$M_w = 5.48 + 0.9 \cdot \log(SRL) \quad (3)$$

The strike and dip, SRL, DRW, and M_w of all the modeled normal faults are shown in Table 5.3. The surface expression of the normal faults and their location relative to Mycenaean Tiryns and Midea citadels are shown in Figure 5.1.

Table 5.3: Seismic fault parameters of twelve assumed earthquakes on normal faults in the AB and PCCR.

Source	Fault Name	Strike/dip	SRL (km)	(WC94) DRW (km)	(WC94) M_w	(PC04) M_w	Reference
AB	ABNAF4	323/75W	20	13	6.6	6.7	GG10
	ABNF1	329/75E	16	12	6.5	6.6	vA93; E96
	ABNF2	342/75E	20	13	6.6	6.7	vA93; E96
	ABNF3	286/75NNE	11	10	6.3	6.4	E96
	ABNF4	325/75NE	12	10	6.3	6.5	E96
	ABNF5	261/75S	7	8	6.1	6.2	E96
	ABNF6	250/75SE	8	9	6.1	6.3	E96
	ABNF7	285/75SW	15	11	6.4	6.5	E96
	Mycenae fault	245/42NE	5	7	5.9	6.1	P93; E96
PCCR	Xylokaastro-1	295/30NE	30	15	6.8	6.8	K10a, K10b
	Xylokaastro-2	295/40NE	30	15	6.8	6.8	K10a, K10b
	Xylokaastro-3	295/50NE	30	15	6.8	6.8	K10a, K10b

vA93: van Andel et al. (1993); P93: Papanastassiou et al. (1993); WC94: Wells and Coppersmith (1994); E96: ECPFEO (1996); P96: Papazachos (1996); PC04: Pavlides and Caputo (2004); K10a: Karastathis et al. (2010a); K10b: Karastathis et al. (2010b); GG10: Georgiou and Galanakis (2010)

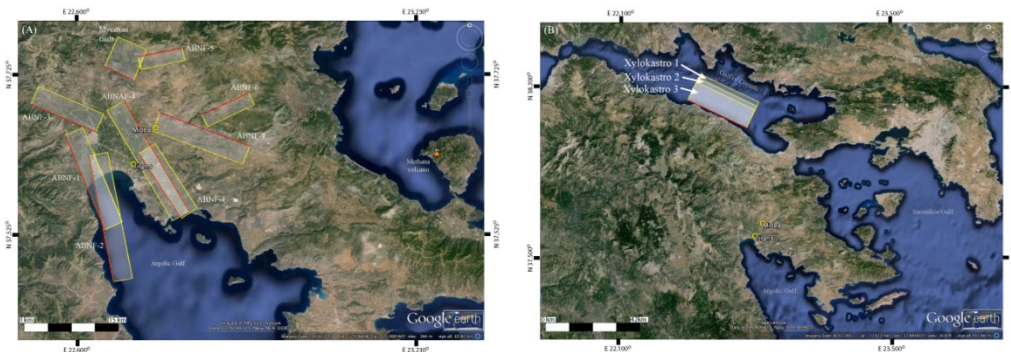


Figure 5.1: Map of Late Neogene–Quaternary active normal faulting in the (A) Argive Basin (AB) and (B) eastern Patras–Corinth Continental Rift (PCCR). Red lines indicate linear segments fitted to the trend of the fault. Rectangle indicates the surface projection of the fault. Xylokaastro-1, Xylokaastro-2, and Xylokaastro-3 dipping at 30°, 40°, and 50°, respectively. The location of the Tiryns and Midea citadel is indicated by the circle.

5.1.2 Strike-Slip Faults in the Iria–Epidaurus Sinistral Transform fault system

The westernmost tip of the E-W trending Iria and Epidaurus sinistral strike-slip faults is at 20 and 40 km E-SE from Tiryns and 21 and 39 km from Midea, respectively. The SRL of each fault is taken from the literature (Clift, 1990; Makris et al., 2004; Vassilopoulou, 2010; Karastathis et al., 2010a, 2010b) and is used to calculate the potential DRW and M_w using the empirical relation of Wells and Coppersmith (1994) (equations 1 and 2). Table 5.4 shows the SRL, DRW, and M_w for the Iria fault, Epidaurus fault, and the combination of both fault segments into the Iria–Epidaurus fault segment. The Iria and Epidaurus faults bound the northern flank, a ~45 km long E-W oriented topographic high (Vassilopoulou, 2010).

Table 5.4: Seismic fault parameters of six assumed earthquakes on strike-slip faults in the IEST.

Fault Name	Strike/dip	SRL (km)	(WC94) DRW (km)	(WC94) M_w	Reference
Iria1	266/75N	24	13	6.7	CR90; K10a; K10b
Iria2	266/90N	24	13	6.7	CR90; K10a; K10b
Epidaurus1	275/75N	19	12	6.6	CR90; K10a; K10b
Epidaurus2	275/90N	19	12	6.6	CR90; K10a; K10b
Iria-Epidaurus1	270/75N	43	17	7.0	CR90; K10a; K10b
Iria-Epidaurus2	270/90N	43	17	7.0	CR90; K10a; K10b

CR90: Clift and Robertson (1990); WC94: Wells and Coppersmith (1994); K10a: Karastathis et al. (2010a); K10b: Karastathis et al. (2010b)



Figure 5.2: Map of active Iria and Epidaurus strike-slip faults in the Iria-Epidaurus Sinistral Transform (IEST) fault system of southeastern Argolis Peninsula. Red lines indicate linear segments fitted to the trend of the fault. Rectangle indicates the surface projection of the fault. Both faults are modeled with a dip of 75° and 90°. The location of the Tiryns and Midea citadel is indicated by the circle.

5.1.3 Reverse Faults in the Hellenic Subduction Zone

The modeled reverse faults are linked to the seismicity in response to the subduction of the African oceanic lithosphere under the Aegean microplate. The reverse faults are divided into shallow and deep sources. The shallow ones occur parallel to the Hellenic oceanic trench, therefore are the more distant ones and trigger intraplate earthquakes. The deeper source faults occur down-dip along the subduction-zone plate interface and trigger interface earthquakes directly underneath the AB. Figure 5.3 illustrates the location and surface projection of the reverse faults with respect to Tiryns and Midea.

The SRL and DRW of the reverse faults are based on M_w between 7.6 and 8.5. These measures are taken from instrumental earthquakes (Papazachos et al., 2000a; <http://geophysics.geo.auth.gr>; www.geophysics.geol.uoa.gr) and modeled paleoearthquakes (Stiros, 2010). The SRL and DRW are computed using the global scaling empirical relations of earthquake source parameters of Papazachos et al. (2004) (equations 4 and 5), Strasser et al. (2010) (equations 6 to 9), and Blaser et al. (2010) (equations 10 and 11):

$$SRL = 10^{((0.55 \cdot M_w) - 2.19)} \quad (4)$$

$$DRW = 10^{((0.31 \cdot M_w) - 0.63)} \quad (5)$$

$$SRL = 10^{(-2.477 + (0.585 \cdot M_w))} \quad (6, \text{ for interface earthquakes})$$

$$DRW = 10^{(-0.882 + (0.351 \cdot M_w))} \quad (7, \text{ for interface earthquakes})$$

$$SRL = 10^{(-2.35 + (0.562 \cdot M_w))} \quad (8, \text{ for intraplate earthquakes})$$

$$DRW = 10^{(-1.058 + (0.356 \cdot M_w))} \quad (9, \text{ for intraplate earthquakes})$$

$$SRL = 10^{(-2.81 + (0.62 \cdot M_w))} \quad (10)$$

$$DRW = 10^{(-1.79 + (0.45 \cdot M_w))} \quad (11)$$

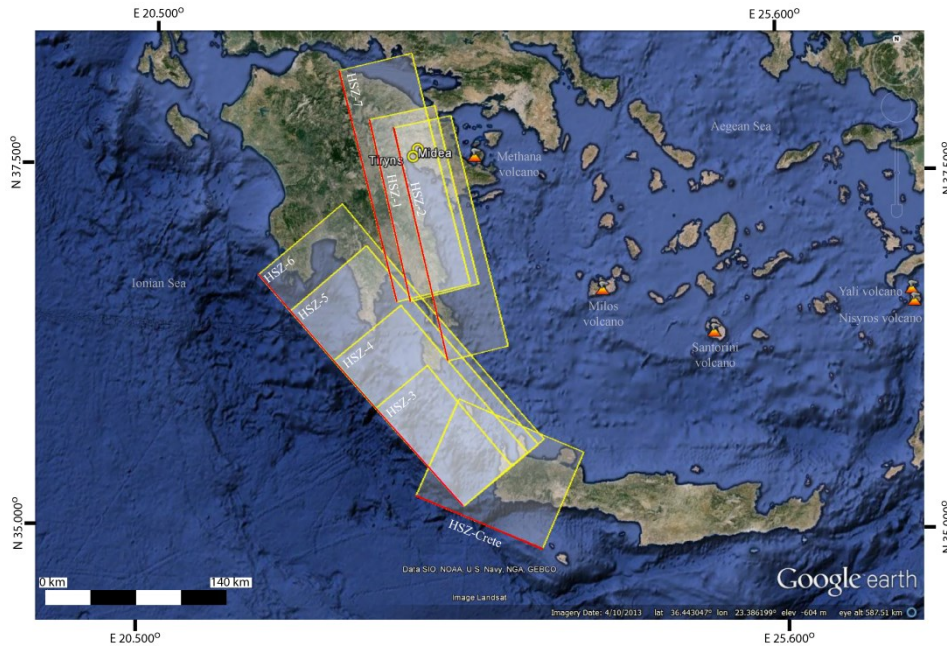


Figure 5.3: Map of active reverse faults in the Hellenic Subduction Zone (HSZ). Red lines indicate linear segments fitted to the trend of the fault. Rectangle indicates the surface projection of the fault. Faults under the Tiryns and Midea citadels (circles) plot along the subduction-zone interface. Offshore faults correspond to intraplate faulting along the Hellenic oceanic trench.

The empirical formulas of Papazachos et al. (2004) and Blaser et al. (2010) were derived using an earthquake M_w range of 6.7 to 9.3 and 6.1 to 9.5, respectively, and do not distinguish between interface and intraplate events. Contrary, Strasser et al. (2010) differentiate between interface and intraplate events and derived empirical formulas for each type of event using an M_w range of 6.3 to 9.4 and 5.9 to 7.8, respectively. Thus, it is expected to obtain noticeable variability in both the fault length and fault width. Table 5.5 shows the seismic fault parameters of the assumed interface and intraplate compressional earthquakes.

A reverse fault offshore southwestern Crete, Greece, is of particular interest to this study because it might have triggered the great Crete earthquake at AD 365 with M_w 8.5 or M_w 8.3 according to Stiros (2010) and Shaw et al. (2008), respectively. Although the proposed time of rupture of this fault post-dates the Mycenaean palatial period (i.e., LH IIIB), this fault is modeled here because of the seismic site effects that might induced in the eastern AB if it had ruptured during the LH IIIB. If the computed M_w 8.5 is taken, this historical earthquake is the largest event reported in Greek seismicity catalogs. Elastic dislocation analysis of coastal uplift data coupled with historical, archaeological, radiocarbon, seismological, and large-scale tectonic data suggests that this fault might have triggered the M_w 8.5 earthquake at AD 365 causing ~9 m coastal uplift in western Crete and widespread destruction (Stiros, 2010). Elastic dislocation modeling on this fault finds a good match between the observed and calculated vertical crustal displacements based on the following computed fault parameters: 292.5°/40°NE strike and dip, 70 km hypocenter, 105 km fault length, 100 km fault width, 16 m slip, seismic moment (M_0) of 5.04×10^{21} Nm, and a corresponding M_w 8.5 (Stiros, 2010). However, the fault length and fault width used by Stiros (2010) result in a rather shorter SRL compared to the computed SRL using the global empirical scaling relations of Papazachos et al. (2004) and Blaser et al. (2010) (see Table 5.4.). This discrepancy can be attributed to the modeling assumptions adopted by Stiros (2010).

Table 5.5: Seismic fault parameters of nine assumed earthquakes on reverse faults in the back-arc region (BAR) and along-arc region (AAR) of the HSZ. IFE = Interface event. IPE = Intraplate event.

Source	Fault Name	Strike/dip*	M_w	SRL (km)			DRW (km)			Reference
				(P04)	(Str10)	(B10)	(P04)	(Str10)	(B10)	
BAR, IFE	HSZ-1	346/45NE	7.9	143	139	122	66	78	58	H89; P00
BAR, IFE	HSZ-2	346/45NE	8.1	184	183	163	76	91	72	H89; P00
AAR, IPE	HSZ-3	312/25NE	7.6	98	83	80	53	44	43	P96
AAR, IPE	HSZ-4	312/25NE	8.0	162	-	141	71	-	65	P96
AAR, IPE	HSZ-5	312/25NE	8.2	209	-	188	82	-	79	P96
AAR, IPE	HSZ-6	312/25NE	8.3	237	-	217	88	-	88	P96
BAR, IFE	HSZ-7	346/40NE	8.1	184	183	163	76	91	72	H89; P00
AAR, IPE	HSZ-Crete	292.5/40NE	8.5	305	-	288	101	-	108	modified from S10
AAR, IPE	HSZ-Crete	292.5/40NE	8.5	105	-	-	100	-	-	as suggested by S10

P04: Papazachos et al. (2004); Str10: Strasser et al. (2010); B10: Blaser et al. (2010); H89: Hatzfeld et al. (1989); P96: Papazachos (1996); P00: Papazachos et al. (2000); S10: Stiros (2010)

5.1.4 Analytic Signal

Analytic input signals have been used as sources of ground-motion in several quantitative archaeoseismic studies to address seismogenic-related effects on ancient man-made structures (Caputo et al., 2010; Hinzen et al., 2010; Hinzen et al., 2013a). In the present study, a logarithmic sweep signal is also used as an input for acceleration, in addition to the

previously presented synthetic earthquake records. The duration of the analytic input signal is 30 s with start and end frequencies of 0.2 Hz and 20 Hz, respectively, which covers the frequency range of engineering interest. The maximum amplitude is 0.1 g. The analytic input signal is defined by equation (12)

$$s(t) = \sin[\theta(t)] = \sin[K \cdot (e^{-t/L} - 1)] \quad (12)$$

where

$$K = \frac{\omega_1 T}{\ln\left(\frac{\omega_1}{\omega_2}\right)}, L = \frac{T}{\ln\left(\frac{\omega_1}{\omega_2}\right)} \quad (13)$$

where $\omega_1 = 1.25664$ and $\omega_2 = 125.664$ resulting in $K = -8.18626$ and $L = -6.51442$. The signal is shown in Figure 5.4.

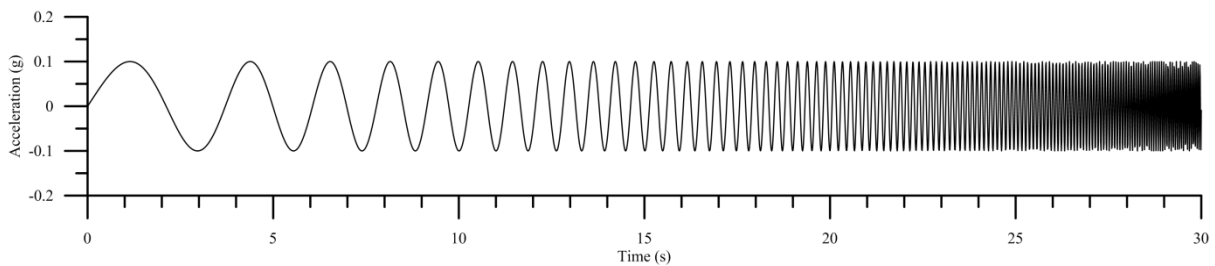


Figure 5.4: Analytic signal used in this study as a synthetic input source in the modeling of seismic site effects.

5.2 Input Parameters of Numerical Modeling Methods

The stochastic method requires the earthquake location, M_w , M_o , rupture size, rupture duration, kappa (κ , a near-surface attenuation parameter), stress drop ($\Delta\sigma$), crustal attenuation (Q -factor), crustal shear-wave velocity (v_s), and crustal density for the numerical modeling of finite-fault segments. In order to model the synthetic earthquake, the Green's function method requires the calculation of the Green's functions of a multi-layered half-space earth model and the representation of the earthquake source by an arbitrary number of rectangular dislocation planes or sub-faults. Several parameters are required to calculate the Green's function: source-observation configuration (e.g., equidistant radial distances and equidistant source depths), time sampling (e.g., number of time samples, time window, and corner frequency of source spectrum), wave number integration (e.g., slowness cut-off, sampling rate of the wavenumber integration, and factor for suppressing the time domain aliasing), and multi-layered half-space model (e.g., number and thickness of layers and the compressional-wave (v_p), shear-wave velocity (v_s), density, and quality factor of the compressional (Q_p) and shear-wave velocities (Q_s) of each layer that makes up the half-space model. The parameters to calculate the synthetic earthquake source are M_o , $\Delta\sigma$, geographic coordinates and depth of the upper reference point for the strike direction, the length, and the width of the rectangular fault segment, the mean strike, mean dip, and the mean rake angle of the fault segment, the position of the nucleation point, the rupture velocity, and the location of the observation point(s).

5.2.1 Shear-Wave Velocity Structure

The Aegean lithosphere is strongly heterogeneous due to its complex tectonic evolution. The current distribution of seismic velocities is influenced mostly by tectonic and magmatic processes active since the Eocene (Endrun et al., 2008). The Argolis Peninsula is at the edge of the back-arc area of the active Hellenic volcanic arc. The forearc and back-arc areas of the Hellenic volcanic arc exhibit low and high attenuation of seismic waves, respectively (Skarlatoudis et al., 2013). This causes a difference in ground motions in forearc areas of a factor of ~ 10 in response-spectra plots compared to back-arc areas. This phenomenon is linked to the presence of high-velocity (high- Q) slab amplification on seismic waveforms in forearc regions; while for back-arc regions is linked to high temperature due to volcanic activity and low-velocity (low- Q) mantle-wedge attenuation due to a significant percentage partial melt above the subducting African slab (Karagianni et al., 2005; Skarlatoudis et al., 2013). Active crustal-scale faults that affect the periphery of the Peloponnese and the Alpine brittle structures (cracks, fractures, and joints) linked to compressional forces of the orogeny and related ophiolitic nappe emplacement process riddle the Peloponnesian crust (Molnar et al., 2007).

The crustal velocity structure of Greece is known from seismic investigations varying from global, regional to local scales. Karagianni et al. (2005) and Endrun et al. (2008) provide a summary of the studies that have measured the velocity structure of the broader Aegean region. P-wave tomography imaged the lithosphere down to 160 km depth (Papazachos et al., 1995). Kalogeras and Burton (1996) used Rayleigh wave group velocities along paths from different source regions in the broader Aegean towards a station in Athens, Greece. The S-wave velocity structure was resolved down to 70 km depth. Papazachos and Nolet (1997) used S-and P-wave traveltimes to create a 3D image down to 150 km depth of the Aegean region. Bourova et al. (2005) used fundamental mode Rayleigh wave and Love phase velocities from teleseismic sources to develop tomographic images at depth slices of 50, 70, 100, and 200 km. Karagianni et al. (2005) derived a high-resolution 3D S-wave tomographic image of the crust–uppermost mantle for the Aegean region with good seismic ray path coverage for the whole Argolis Peninsula including the Argive Basin. Endrun et al. (2008) used fundamental mode Rayleigh wave-wave dispersion with the Aegean region to determined average dispersion curves along seismic ray paths and developed 1D S-wave velocity models down to 250 km depth along the Hellenic forearc and a north-south trending profile traversing the whole Aegean Sea.

Localized 3D passive seismic tomographies of v_p and v_s data (Le Meur et al., 1997; Tiberi et al., 2000; Latorre et al., 2004; Drakatos et al., 2005), 2D active marine reflection/refraction studies (Sachpazi et al., 2003; Clément et al., 2004; Zelt et al., 2004, 2005), gravity (Tiberi et al., 2001), magnetotelluric (Lazaridou-Varotsou and Papanikolaou, 1987; Pham et al., 2000), and microseismic data (Rigo et al., 1996; Hatzfeld et al., 1989, 1992, 1993a, 2000; Makris et al., 2004) performed in several regions outside the AB provide a robust idea of the crustal velocity structure and crustal thickness around the AB. However, the results of Karagianni et al. (2005) offer the highest spatial resolution compared to the aforementioned studies, with the exception of Papazachos and Nolet (1997). This stems on the fact that surface wave

measurements are sensitive to the structure of the lithosphere and asthenosphere and can yield high radial resolution in this depth range (Endrun et al., 2008). In addition, the aforementioned studies used a reduced number of stations and sources, the distribution of sources is less homogeneous, the seismic ray path coverage is lesser for the Argive Basin, or the choice of method (1D and along ray paths between station-pair) simply excludes the AB. For the 3D S-wave tomographic image of the crust–uppermost mantle, Karagianni et al. (2005) used previously determined averaged Rayleigh wave group velocities fundamental mode by Karagianni et al. (2002) from a database consisting of 185 regional earthquakes. The average group velocity was determined using the method of frequency time analysis for each epicenter–station ray path (Karagianni et al., 2002) to develop the local group velocity for different periods over the Aegean area covered by the seismic ray paths. Also, for every gridpoint ($0.5^\circ \times 0.5^\circ$ spacing), a local dispersion curve was defined and inverted using a non-linear inversion method to derive 1D shear-wave velocity–depth models which were later interpolated to create the 3D image. Figure 5.5 shows the spatial variation of v_s within the crust–uppermost mantle.

The above studies do not detect a crustal low-velocity zone under the AB; however, a low-velocity zone exists at mid-crustal depths (10–20 km) in the northwestern Greece (Papazachos et al., 1995) and westernmost Peloponnese (Papazachos and Nolet, 1997; Endrun et al., 2008), in the northern Aegean Sea between 50–100 km depth (Bourova et al., 2005), in the SE Aegean Sea–SW Turkey region at lower crustal depths (20–40 km) (Kalogerias and Burton, 1996), and in the southern and central Aegean Sea between 30–40 km depth (Karagianni et al., 2005). Therefore, it is assumed that the thermal imprint of active volcanism is possibly minor under eastern Peloponnese; so the lower crustal velocity remains relatively colder (faster) compared to other Aegean regions. The ophiolitic belt in the eastern Peloponnese probably contributes to the locally faster velocity structure. Following the 3D v_s structure model of Karagianni et al. (2005), the v_s for the eastern AB varies from ~ 3.4 – 3.9 km/s from 6–40 km depth. The selected v_s value for the 0–6 km depth range is 2.1 km/s after trial-and-error in the model validation. The combination of these two v_s models results in the adopted crustal v_s model for this study. This crustal v_s model is within the ranges of the aforementioned v_s studies covering the Aegean region and global models including the PREM of Dziewonski and Anderson (1981) and the CUB shear velocity model of the crust–upper mantle created at the University of Colorado, Boulder (<http://ciei.colorado.edu/~nshapiro/MODEL/>) by Shapiro and Ritzwoller (2002). Figure 5.6 shows the adopted crustal v_s model compared to other v_s models, as well as the adopted v_p and density models required for the simulations of seismograms.

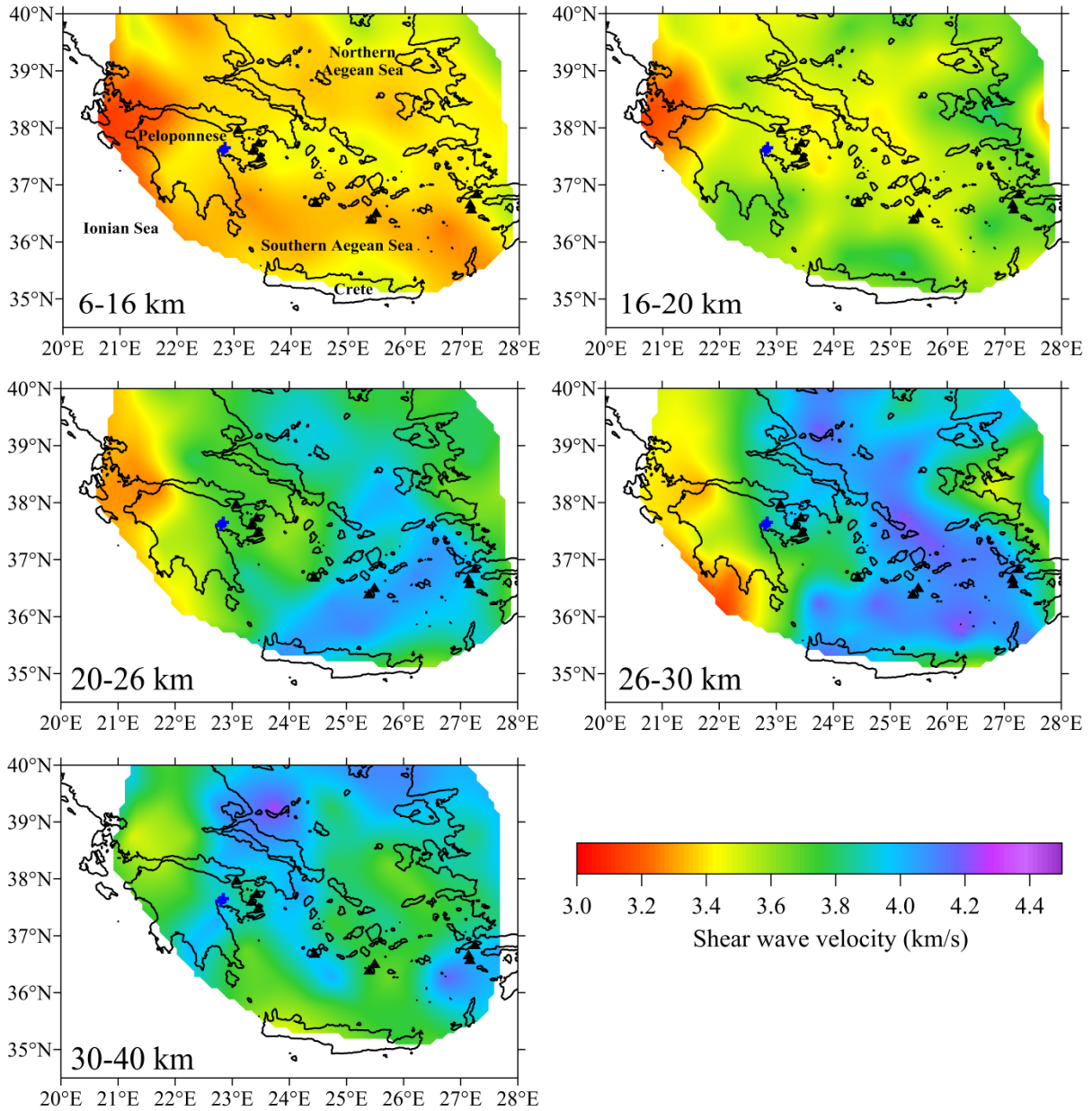


Figure 5.5: Depth slices of the shear wave velocity model for the crust in the Aegean area (data courtesy of Lena Karagianni). Crosses correspond to the location of Tiryns and Midea and triangles to the active volcanoes of the Hellenic arc.

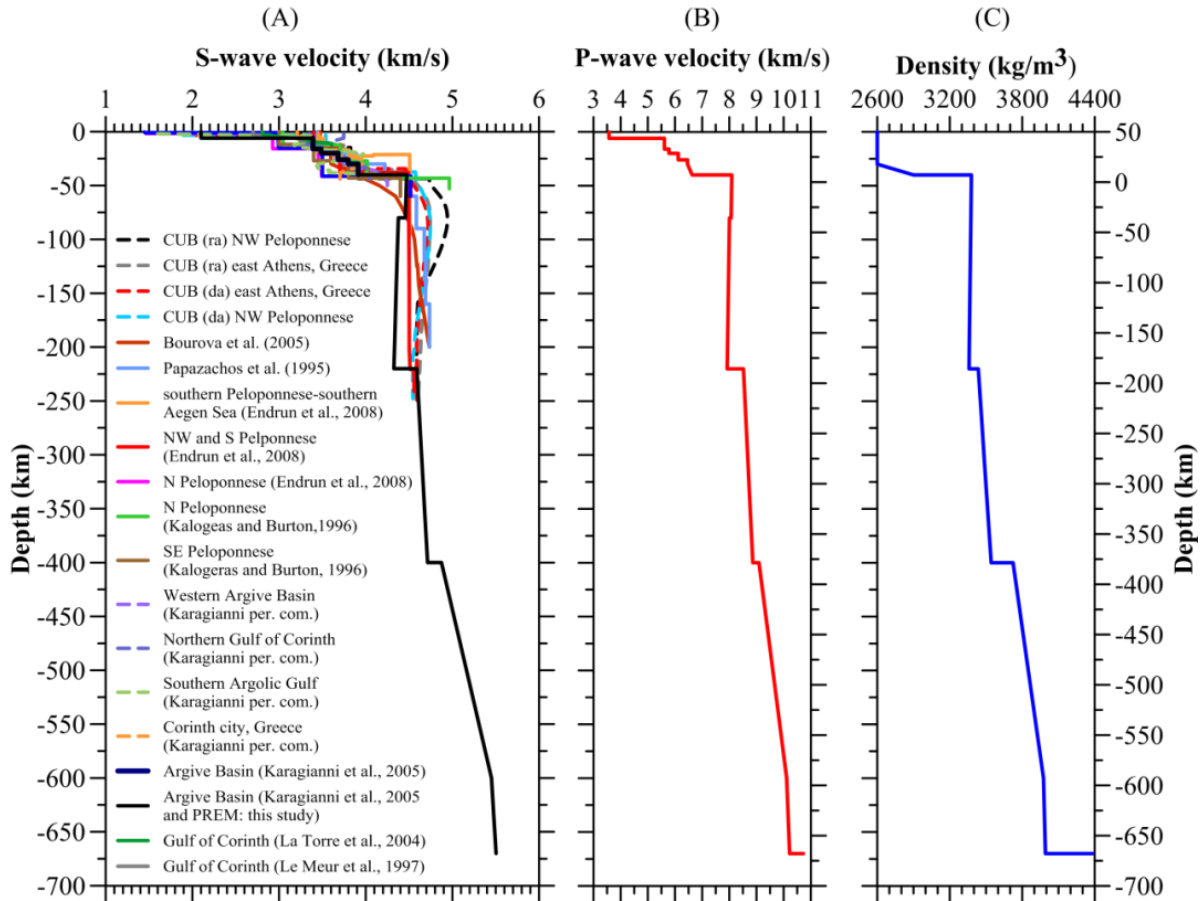


Figure 5.6: Models of (A) v_s , (B) v_p , and (C) density adopted in this study for the simulation of fault-segments. Various v_s models in (A) are shown for comparison.

5.2.2 Duration Model

The FINSIM code requires a subsource-radiation duration model, incorporating a linear increase of duration with distance, with slopes depending on the distance range. For the stochastic simulation of finite-faults, Boore and Thompson (2014) recently compiled a database of nearly 16,000 earthquakes ranging from $3 < M_w < 8$ to produce a new global duration model for earthquakes with $6 < M_w < 7$ (Figure 5.7). Details of the methodology and a comparison with previous global duration models are given in Boore and Thompson (2014). In this dissertation, two path duration models were utilized following the procedure of Boore and Thompson (2014): two separate duration models for earthquakes with $6 < M_w < 7$ and $7 < M_w < 8$ were used (Figure 5.7). The first duration model is a slight modification of the duration model proposed by the Boore and Thompson (2014). It is a fit to the data points corresponding to $6 < M_w < 7$ up to a distance of 175 km, as opposed to 300 km. This truncation was implemented to reflect the maximum epicentral distance to crustal earthquakes in the AB, PCCR, and IEST. The second duration model is a fit to the data points corresponding to $7 < M_w < 8$ interface and intraplate earthquakes in the HSZ. The distance range and corresponding slopes of the derived duration models are shown in Table 5.6.

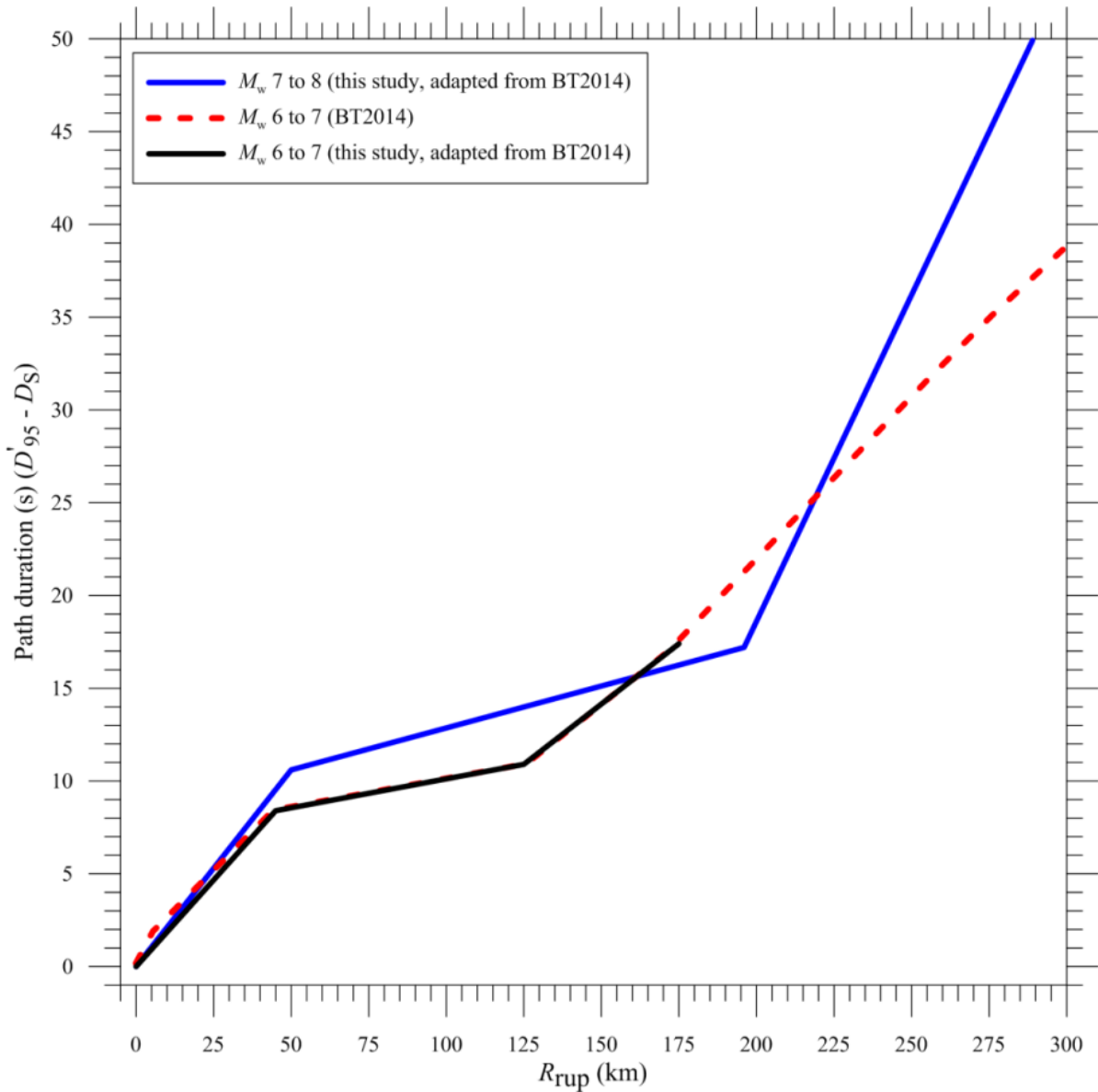


Figure 5.7: Path duration models used in this study.

Table 5.6: Path duration models in the stochastic simulation of finite-faults adopted in this study (data from Boore and Thompson, 2014).

Duration model for $6 < M_w < 7$ earthquakes				
distance (km)	duration (s)	slope 1 (0 to 45 km)	slope 2 (45 to 125 km)	slope 3 (125 to 175 km)
270	34.2	0.187	0.031	0.130
175	17.4			
125	10.9			
45	8.4			
7	2.4			
0	0			
Duration model for $7 < M_w < 8$ earthquakes				
distance (km)	duration (s)	slope 1 (0 to 50 km)	slope 2 (50 to 196 km)	slope 3 (196 to 289 km)
289	49.92	0.212	0.045	0.352
196	17.2			
50	10.6			
0	0			

5.2.3 The Kappa Parameter

The kappa (κ) parameter, in units of seconds, accounts for the near-surface attenuation (energy absorption) of upward propagating seismic waves in the uppermost 4 km of the earth's crust including the uppermost 30 m of the ground surface (Chandler et al., 2006). Values of κ can vary from as low as 0.011 s for very-hard rock sites to 0.06 s for very-soft to stiff soil sites under the National Earthquake Hazards Reduction Program (NEHRP) (2003) site class definition. The κ parameter is difficult to measure in regions of low and moderate seismicity, like the AB (Hatzfeld et al., 1993; Makris et al., 2004; Georgiou and Galanakis, 2010), because of magnitude or epicentral distance requirements related to the measurements where records of local moderate and large magnitude earthquakes in the near-field are either non-existent or scarce (Chandler et al., 2005a, 2006). Values of κ are available for several site classes from active tectonic regions in Greece (Table 5.7) (Hatzidimitrou et al., 1993; Margaris and Boore, 1998; Klimis et al., 1999) and other regions around the world (e.g., Atkinson, 1995; Boore and Joyner, 1997; Chandler et al., 2005a, 2005b, 2006). Chandler et al. (2005a) provide a global database of published κ values.

Chandler et al. (2005a, 2005b, 2006) established an empirical correlation between κ and crustal v_s (or v_{uc}) and the v_s of shallow reference depth of 30 m namely v_s^{30} in the engineering community, which are represented by equations (14) and (15), respectively,

$$\kappa = 0.145 - 0.12 \ln(v_{uc}) \geq 0 \quad [v_{uc} \geq 1.6 \text{ km/s}] \quad (14)$$

$$\kappa = \frac{0.057}{(v_s^{30})^{0.8}} - 0.02 \quad [0.5 \text{ km/s} \leq v_s^{30} \leq 3.0 \text{ km/s}] \quad (15)$$

The κ parameter is required in the stochastic simulation method (i.e., FINSIM code), but not in the Green's function method. Tiryns classifies as a rock site (class site B) (Hinojosa-Prieto and Hinzen, 2015) and Midea has very similar geologic conditions. This means that both archaeological sites straddle the limit between 'very-hard rock site' (class site A) and 'rock site' (class site B) under the NEHRP site classification scheme. The range of κ values listed in Table 5.7 was tested by a trial-and-error procedure in a validation model. Only values between 0.035–0.40 s yield good results, but 0.035 s gives the best results as proposed by Margaris and Boore (1998) for Greek sites. The criterion is based on achieving a good fit between the acceleration response spectra of both the simulated and the observed event. The use of a v_{uc} value of 2.5 km/s and a v_s^{30} value of 1.04 km/s in equations (14) and (15), respectively, predicts a κ value of 0.035 s. These v_s are in full agreement with published range of v_s values for the local bedrock in the AB (Karastathis et al., 2010a, 2010b; Hinojosa-Prieto and Hinzen, 2015) and for the Peloponnesian crust (discussed in section 5.2.1).

Table 5.7: Available κ values for Greece.

κ (s)	Class site	Reference
0.035	very-hard rock site (A)	Margaris and Boore (1998)
0.047 to 0.066	rock site (B)	Margaris and Boore (1998)
0.046 to 0.076	very stiff soil-soft rock (C)	Margaris and Boore (1998)
0.044	very stiff soil- soft rock (C)	Klimis et al. (1999)
0.066	stiff soil (D)	Klimis et al. (1999)
0.06	very-soft to stiff soil (D to F)	Hatzidimitrou et al. (1993)

5.2.4 Stress Drop ($\Delta\sigma$)

Mohammadioun and Serva (2001) investigated the theoretical relationships of earthquake stress drop ($\Delta\sigma$), M_w , surface wave magnitude (M_s), M_o , fault rupture length, and displacement on the fault using a composite earthquake database of strike-slip, normal, and reverse slip events. The database consists of twenty-one events selected by the authors from reduced portion (87 events) of the well-known global earthquake database of Wells and Coppersmith (1994). Mohammadioun and Serva (2001) found that $\Delta\sigma$ values increase versus DRW (depth) up to approximately the depth of the brittle-ductile transition boundary and beyond this depth high $\Delta\sigma$ levels vanish generally remaining ≤ 100 bars. Recently, Allmann and Shearer (2009) investigated the global variation of $\Delta\sigma$ for moderate to large earthquakes ($5.2 < M_w < 8.3$) using spectra of about 2000 earthquakes from different tectonic regimes and estimated $\Delta\sigma$ by tectonic region: 2.98 ± 0.21 MPa for subduction zone, 3.42 ± 0.56 MPa for oceanic collision, 2.63 ± 0.5 MPa for continental collision, 2.82 ± 0.48 MPa for oceanic ridge, 3.37 ± 0.47 MPa for continental ridge, 3.31 ± 0.18 MPa for interface, 6.03 ± 0.68 MPa for oceanic transform, 3.54 ± 0.64 MPa for continental transform, and 5.95 ± 1.01 MPa for intraplate. In this study, the implemented values of $\Delta\sigma$ are used according to seismic source type (Table 5.8) and were taken from Allmann and Shearer (2009).

Table 5.8: Stress drop values for different source zones (Allmann and Shearer, 2009).

Tectonic setting	Seismic source	For Stochastic method	For Green's function method
Subduction zone interplate	HSZ	30 bar	30 bar
Intraplate	HSZ and AB	60 bar	60 bar
Continental Transform	IEST	35 bar	35 bar
Continental Ridge	PCCR	34 bar	34 bar

5.2.5 Crustal Attenuation (Q -factor)

The attenuation of seismic waves, expressed by the inverse of the quality factor (Q^{-1}), is one of the most important seismological parameters that characterizes the earth material through which the seismic waves propagate (Hatzidimitriou, 1995). Nearly 90% of the total attenuation in bedrock occurs within the upper 4 km of the earth's upper crust (Abercrombie, 1997). Q is frequency dependent following the relation (Aki, 1980)

$$Q = Q_0 \cdot f^\eta \quad (16)$$

where Q_0 is the attenuation factor, f is the frequency, and η is a coefficient that can vary from 0.4 for tectonically stable regions to nearly 1.0 for tectonically active regions (Hatzidimitriou et al., 1993). The quality factor can be determined from P-phases (Q_p), S-phases (Q_s), or coda waves (Q_c). Values of Q_c and Q_s are available for different regions of Greece (Table 5.9) including southwestern Peloponnese (Tselentis et al., 1988), the whole of Peloponnese

(Martin, 1988), Northern Greece (Hatzidimitriou, 1993, 1995), large areas throughout Greece (Hashida et al., 1988; Papazachos et al., 1992; Hatzidimitriou et al., 1993), and the southern Aegean lithosphere (Kovachev et al., 1991).

In a stochastic strong ground-motion simulation of the 7 September 1999 Athens M_w 5.9 earthquake, Roumelioti et al. (2004a) used the $Q = 100 \cdot f^{0.8}$ for the Aegean Sea and surroundings derived by Hatzidimitriou (1993, 1995) from studies of Q_s and Q_c . Similarly, Karastathis et al. (2010a, 2010b) adopted the same Q model (i.e., $Q = 100 \cdot f^{0.8}$) to evaluate the liquefaction potential of cohesive soils in the southeastern AB (< 2 km south of Tiryns) in response to three earthquake scenarios selected on the basis of historical seismicity data: the Iria fault (M_w 6.4) and Epidaurus fault (M_w 6.3) located in the IEST and the Xylokaastro fault (M_w 6.7) located in the eastern Gulf of Corinth. A $Q_0 \leq 100$ implies a low crustal shear wave velocity and a high density of planar discontinuities in form of cracks, fractures, joints, shear zones, and faults (Aki, 1980; Hatzidimitriou, 1993). A $Q_0 \leq 100$ is more suitable for an area with moderate to high levels of seismicity such as the adjacent Messenian Gulf (Papazachos et al., 1988; Lyon-Caen et al., 1988; Tselentis et al., 1998) and the Thessaloniki area (Martin, 1998; Hatzidimitriou, 1993, 1995; Chávez-García et al., 2000). The present study considers the AB as a zone with much lower seismic activity compared to adjacent areas or basins, so the crustal Q_0 can extend beyond 100. Several crustal Q values (e.g., 30, 50, 100, 150, 210, 250, 300, 350, 380, 400, 450, 490, and 800 that fall within the range of values in Table 5.8) and η values (e.g., 0.75, 0.80, 0.85, 0.90, and 0.95) were tested by a trial-and-error procedure in a validation model (discussed in the following section). Q_0 values between 300 to 490 and $\eta = 0.80$ yield good results, but the combination of $Q_0 = 380$ with $\eta = 0.80$ provides the best match between the observed and simulated acceleration response spectra. Hence, the selected value for crustal Q_0 and η is 380 and 0.80, respectively, resulting in an anelastic attenuation model defined by $Q = 380 \cdot f^{0.8}$. This Q model is within the range of available upfront models for Greek territory and it supports the current tectonic understanding of the AB.

Table 5.9: Available crustal attenuation (Q) values for Greece derived with Coda-waves (Q_c) and S-waves (Q_s).

Q	Reference
$Q_c = 73 f^{0.95}$	Martin (1988)
$Q_c = 44 f^{0.81}$	Tselentis et al. (1988)
$Q_c = 32.6 \pm 3.28 f^{1.01 \pm 0.06}$	Hatzidimitriou (1993)
$Q_c = 60 \pm 0.83 f^{0.79 \pm 0.01}$	Hatzidimitriou (1993)
$Q_c = 89.1 \pm 2.67 f^{0.72 \pm 0.02}$	Hatzidimitriou (1993)
$Q_c = 94.4 \pm 4.13 f^{0.78 \pm 0.03}$	Hatzidimitriou (1993)
$Q_c = 128.5 \pm 5.09 f^{0.74 \pm 0.02}$	Hatzidimitriou (1993)
$200 < Q_s < 300$	Kovachev et al. (1991)
$50 < Q_s < 1000$	Hashida et al. (1988)
mean $Q_s = 350 \pm 140$	Papazachos et al. (1992)
$Q_s = 30$ to 360 (avg. 130)	Hatzidimitriou et al. (1993)
$Q_s = 115 \pm 18 f^{0.91}$	Hatzidimitriou (1995)
$Q_s = 244 \pm 36 f^{0.91}$	Hatzidimitriou (1995)
$Q_s = 477 \pm 96 f^{0.91}$	Hatzidimitriou (1995)
$Q_s = 755 \pm 83 f^{0.91}$	Hatzidimitriou (1995)

Recently, Chandler et al. (2005a, 2006) established an empirical correlation between the crustal Q -factor and v_s for the upper crust (v_{uc}) as well as Q -factor and v_s^{30} . Respectively, these relations are represented by equations (17) and (18),

$$Q = 100 + 2.5v_{uc}^{4.5} \quad [v_{uc} \geq 1.6 \text{ km/s}] \quad (17)$$

$$Q = 60 + 320(v_s^{30} - 0.5)^{0.8} \quad [0.5 \text{ km/s} \leq v_s^{30} \leq 3.0 \text{ km/s}] \quad (18)$$

Following equation (17) and equation (18), a Q -factor of 380 translates into a $v_s^{30} = 2.855$ km/s and a $v_{uc} = 1.500$ km/s, respectively. These resulting v_s are in full agreement with the published v_s values for the local bedrock in the AB (Karastathis et al., 2010a, 2010b; Hinojosa-Prieto and Hinzen, 2015) and for the Peloponnesian upper crust (e.g., Shapiro and Ritzwoller, 2002; Endrun et al., 2008; Karagianni, pers. comm.). In addition, these ranges of v_s are common in highly-jointed formations (Chandler et al., 2006) and the Peloponnese is highly fractured and jointed due to both the compressional stresses linked to the overthrusting of carbonates platforms during the Alpine orogeny (Molnar et al., 2007) and the regional extensional stress field associated to the ongoing orogenic collapse (Taymaz et al., 2007). The crustal attenuation model required in the FINSIM and Green's function computer codes is implemented down to the Mohorovičić (Moho) discontinuity. At the observation point(s), the Green's function method requires the Q_p and Q_s attenuation models from the ground surface down to the upper mantle (~670 km depth). So beyond the Moho, Q_p and Q_s values are taken from the Preliminary Reference Earth Model (PREM) of Dziewonski and Anderson (1981) (Figure 5.8).

The Moho discontinuity in the AB is detected at ~34 km (Karagianni et al., 2005) and at ~37 km (Endrun et al., 2008) with the used of group velocities of Rayleigh wave fundamental mode, and at ~38 km with P-and S-wave receiver functions from teleseismic earthquakes (Sodoudi et al., 2006). The data sets of Karagianni et al. (2005) and Sodoudi et al. (2006) have good seismic ray path coverage for the whole Argolis Peninsula including the AB. Figure 5.9 shows a map of Moho topography overlaid by isodepth contours of the subduction plate interface (Papazachos et al., 2000a). A ~10 km difference in the Moho depth for the region along the western and southern Hellenic oceanic trench is also seen in Figure 5.9. This region corresponds to the location of several offshore reverse faults (i.e., HSZ-3, HSZ-4, HSZ-5, HSZ-6, and HSZ-Crete; Figure 5.3) modeled in this study.

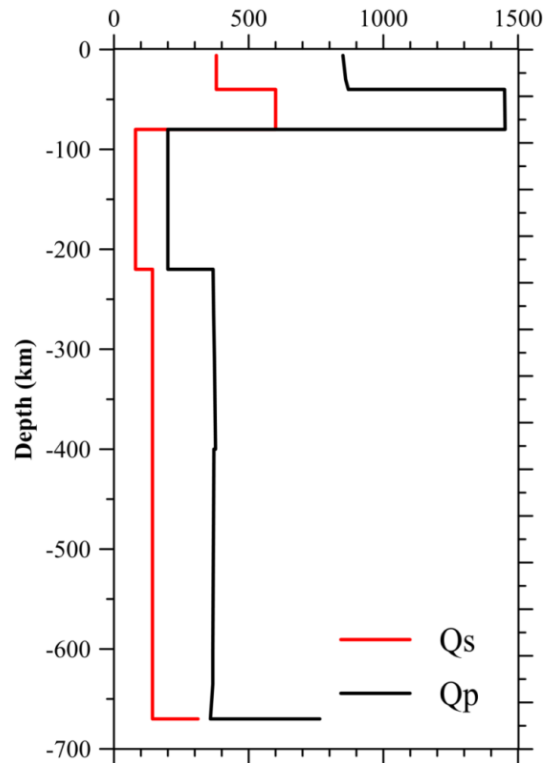


Figure 5.8: Q_s and Q_p 1D model for the multi-layered half-space used in the Green's function approach.

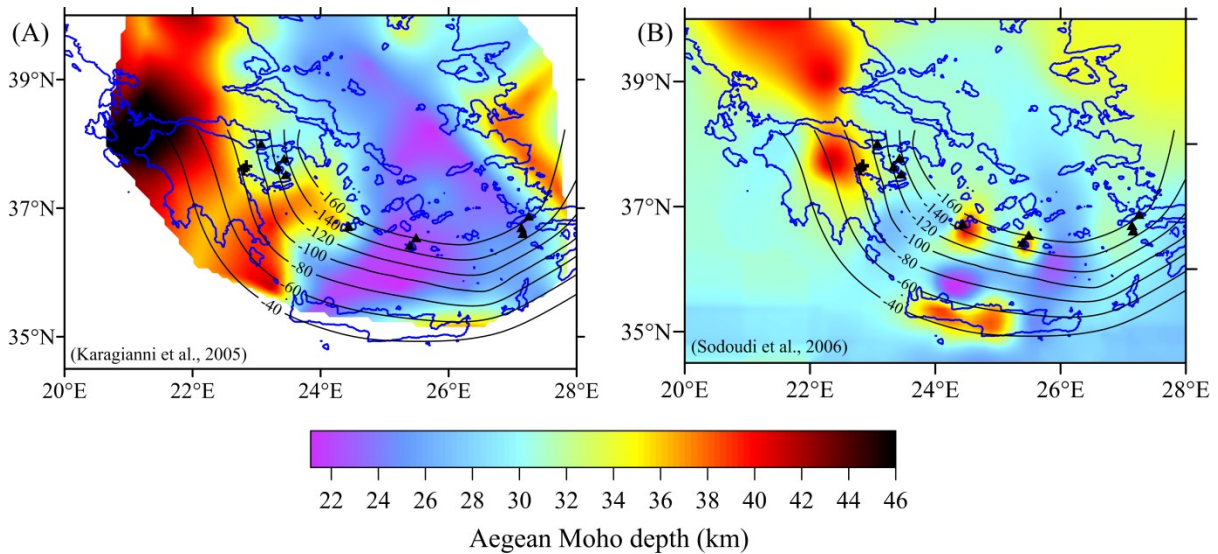


Figure 5.9: Map of the Moho after (A) Karagianni et al. (2005) and (B) Sodoudi et al. (2006). Isodepth lines (black) of the subduction-zone plate interface (Papazachos et al., 2000a) are superimposed on both Moho maps. Crosses correspond to the location of Tiryns and Midea, and triangles correspond to active volcanoes of the Hellenic arc. (Data sources: (A) courtesy of Lena Karagianni; (B) digitized from Sodoudi et al., 2006).

The Moho depth map of Tiberi et al. (2001) for a portion of the Peloponnese, generated by the inversion of gravity data, suggests that the Moho depth increases from ~ 26 km in the northern edge of the AB to as much as ~ 33 km in the Argolic Gulf. Makris (1978) detected the Moho depth between 26 to 46 km depth using deep seismic soundings along a NE-SW trending transect running from the Ionian Sea to the Saronic Gulf estimating the Moho at ~ 30

km under the AB. Also along a NE-SW trending profile running from the Ionian Sea into the Aegean Sea, Tsokas and Hansen (1997) collected gravity data and derived an undulating crustal thickness of 30–41 km under the Argolis Peninsula. The Moho map of Tirel et al. (2004), derived with satellite marine gravity data, suggests a Moho depth of 23–32 km offshore the AB. At a much larger scale and with the receiver function technique, van der Mijde et al. (2003) obtained the crustal structure and thickness beneath 17 broad-band stations in the Mediterranean region including northern Africa, and measured a Moho depth of 43 ± 1.7 km under the Pylos archaeological site (e.g., southwestern Peloponnese). Overall, these geophysical observations are in good agreement with each other in regards to the Moho depth under eastern Peloponnese.

5.3 Model Validation

Both the Stochastic and the Green's function model parameters were verified using recordings of a recent offshore M_w 4.3 earthquake (06/12/2012). The event occurred 78.5 and 82 km south of Tiryns and Midea, respectively. The Seismological Observatory of the University of Athens (SOUA) provides focal mechanism consistent with normal faulting in the southeastern Argolic Gulf, the hypocenter (9 km), strike/dip ($329^\circ/44E$), rake (-111°), and the aforementioned M_w 4.3 (http://dggsl.geol.uoa.gr/en_index.html). In the present study, the event was modeled stochastically with a fault plane of 1.7×0.5 km, a 9 km depth hypocenter, and strike/dip of $329^\circ/44E$. The same event was modeled with the Green's function approach with the source parameters reported by SOUA; though the fault plane was a bit larger than in the stochastic simulation (3×1.7 km). Figure 5.10 shows a comparison between the observed and simulated response spectra acceleration for this event. For the stochastic method, the acceleration seismograms were calculated from velocity proportional recordings at a station located on bedrock inside the Tiryns citadel. The station site was modeled as a hard-rock site also located inside Tiryns. The calculated peak ground acceleration (PGA) for the north, east, and vertical components is 1.74, 1.78, and 1.10 cm/s^2 , respectively. The stochastically simulated horizontal acceleration seismogram, modeled with $\kappa = 0.035$ for hard-rock site conditions, shows a PGA of 1.96 cm^2 . The north, east, and vertical acceleration seismograms modeled with the Green's function method show PGA of 0.870, 2.15, and 1.06 cm^2 , respectively.

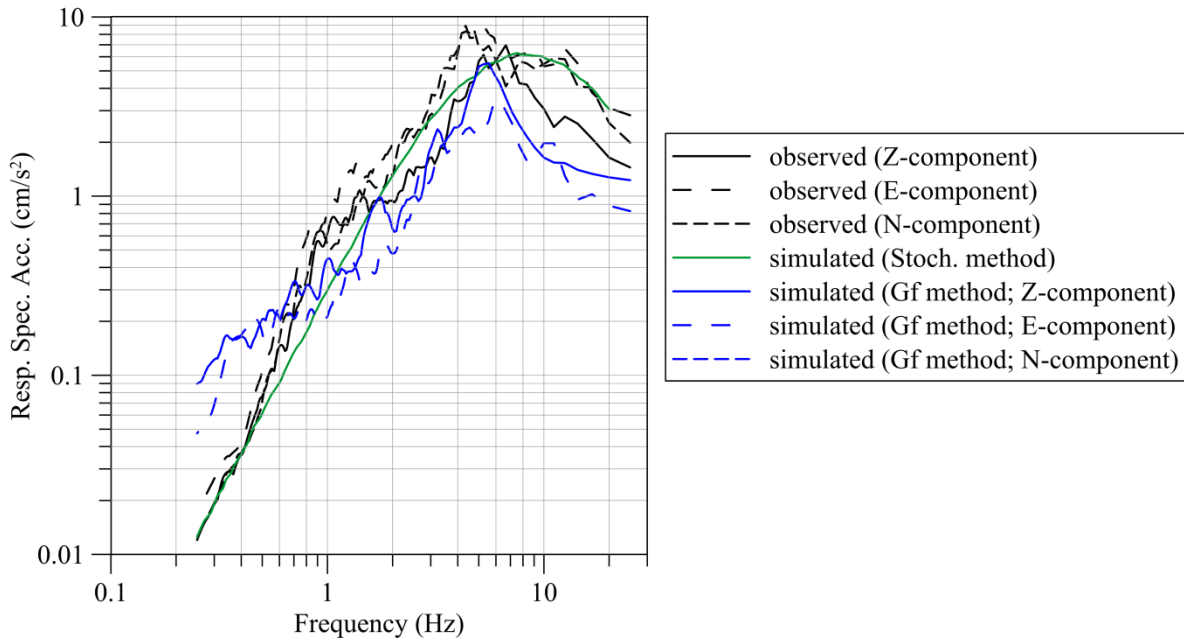


Figure 5.10: Observed and simulated response spectra acceleration versus frequency from the 06/12/2012 local earthquake M_w 4.3 that ruptured south of the Argive Basin. Simulation done with the stochastic (Stoch.) and Green's function (Gf) methods.

5.4 Application of the Stochastic and Green's Function Methods

This section presents the synthetic acceleration seismograms modeled with the widely applied stochastic method (Beresnev and Atkinson, 1998) and the synthetic acceleration, velocity, and displacement seismograms modeled with the Green's function method (Wang, 1999). The resulting maximum PGA (g) values of all seismogenic sources modeled with both methods are plotted against M_w , SRL (km), and DRW (km) in Figure 5.11 which shows that PGA values of all sources obtained with the stochastic method are lower compared to the PGA values obtained with the Green's function method. The PGA values of Tiryns and Midea, obtained with the stochastic method, range from 0.006 to 0.270 g and 0.006 to 0.213 g , respectively (Figure 5.11). Seismogenic sources in the HSZ yield PGA values between 0.006 to 0.055 g and 0.006 to 0.069 g for Tiryns and Midea, respectively. However, sources in the AB, which are the closest ones to the archaeological sites, yield both the highest variability and PGA values despite of their relatively lower M_w compared to the other seismogenic sources; however, marginal differences are observed between the PGA values of Tiryns (0.053–0.270 g) and Midea (0.062–0.213 g). The sources in the PCCR and IEST result in a narrow range of PGA values (0.020–0.100 g); thus intermediate between the PGA values of the AB and HSZ sources due to the source-to-site distance. Figure 5.11 also shows a wider range of PGA values of Tiryns and Midea when all seismogenic sources are modeled with the Green's function method. The PGA values of Tiryns and Midea vary from 0.016 to 0.993 g and from 0.013 to 0.815 g , respectively. In particular, the PGA values of all sources in the HSZ yield values both below 0.155 g and 0.160 g for Tiryns and Midea, respectively. Again, sources in the AB give both the highest variability and PGA values; however the range of PGA values for Tiryns (0.241–0.993 g) and Midea (0.199–0.815 g) are marginally different. The sources in the PCCR and IEST yield a narrow range of PGA values. For Tiryns these

values are 0.048–0.079 *g* and 0.045–0.161 *g*, respectively; for Midea 0.049–0.061 *g* and 0.037–0.196 *g*, respectively. Finally, Figure 5.11 clearly illustrates that all the seismogenic sources in the HSZ, PCCR, and IEST (except source IrEp1) modeled with either the stochastic or the Green’s function methods result in PGA values that are below the expected PGA value for both the AB (0.16 *g* low bound value of Tselentis and Danciu, 2008) and the whole Argolis Peninsula (~0.30 *g* value of Giardini et al. [2013] and 0.24 *g* value of USGS [2014]). However, only a few normal faults with the AB exceed the aforementioned expected PGA values when the sources are modeled with the stochastic method. These sources include ABNF2, ABNF4, ABNAF4, ABNF6, and ABNF7. On the other hand, a wide range of PGA values results when all the seismogenic sources in the AB are modeled with the Green’s function approach. These PGA values exceed the low bound of the expected PGA value of the AB. Some even exceed the upper bound PGA value of 0.500 *g* calculated by Tselentis and Danciu (2008). Clearly, this observation strongly suggests the hazardous nature of the understudied local normal faults in the AB, but in particular faults such as ABNF1, ABNF2, ABNF3, ABNF4, ABNAF4, ABNF7, and Mycenae which are responsible for exceeding a PGA value of 0.500 *g*. These local steeply dipping faults strike mainly NW-SE and N-S.

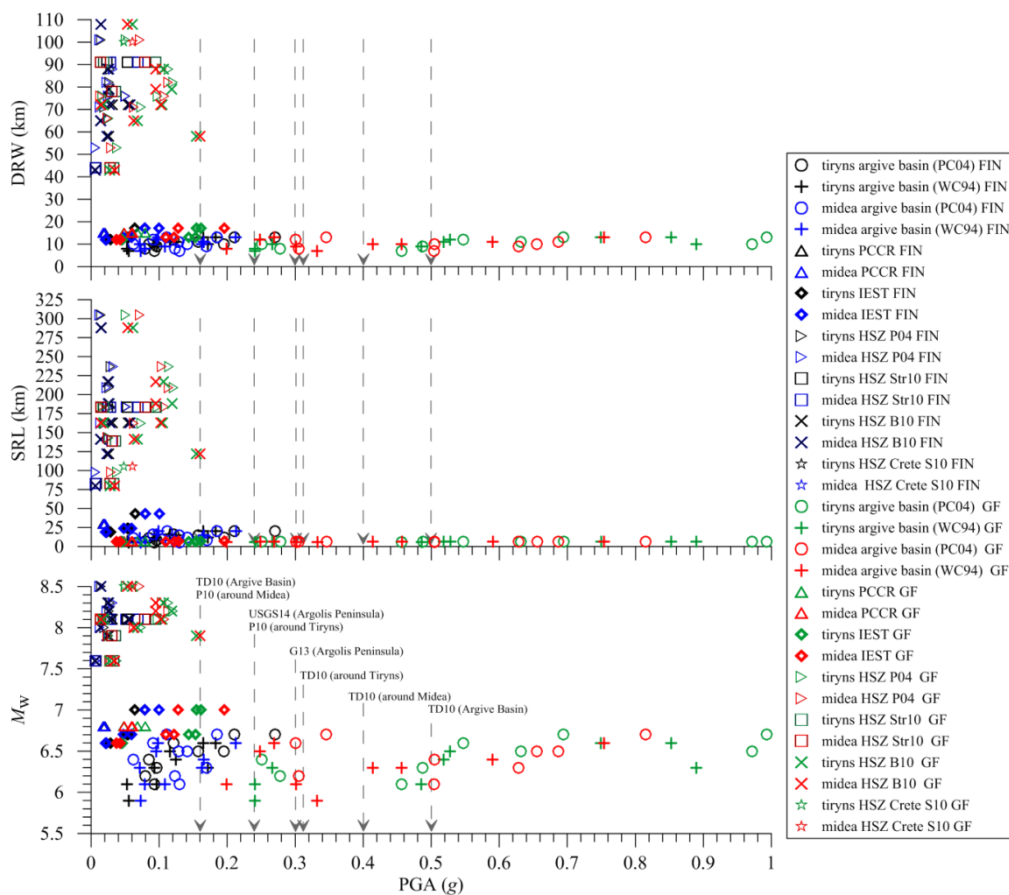


Figure 5.11: Summary of calculated maximum horizontal PGA values (in *g*) of all seismogenic sources modeled with the Stochastic (FIN: FINSIM computer code) and Green’s function (GF) methods plotted against M_w , SRL, and DRW. Expected PGA values (having a 10 % probability of being exceeded in 50 years) for different regions (dashed line) shown for reference (after Tselentis and Danciu (2010a) [TD10], Papathanassiou et al. (2010) [P10], Giardini et al. (2013) [G13], United States Geological Survey (2014) [USGS14]).

The empirical relations of Ambraseys (1974) and Tselentis and Danciu (2008) were used to compute MMI (Modified Mercalli Intensity) scale values from the resulting maximum PGA values. The empirical relations are represented by equations (19) and (20), respectively,

$$\text{MMI} = \frac{\log_{10}(\text{PGA}_{h_{max}}) + 0.16}{0.36} \quad (19)$$

$$\text{MMI} = -0.946 + (3.563 \cdot \log_{10}(\text{PGA}_{\bar{h}})) \quad (20)$$

where $\text{PGA}_{h_{max}}$ and $\text{PGA}_{\bar{h}}$ correspond to maximum horizontal PGA and the average of both horizontal components in cm/s^2 , respectively. Figure 5.12 shows the MMI values plotted against M_w , SRL (km), DRW (km), and the ‘‘Joyner-Boore source-to-site distance’’ (r_{JB}) (i.e., the closest horizontal distance to the vertical projection of the rupture). The resulting PGA values obtained with the Stochastic and Green’s function approaches yield MMI values between 4-7 and 4-8, respectively. In both cases, the normal faults in the AB yield the highest MMI values in comparison to the other seismogenic sources.

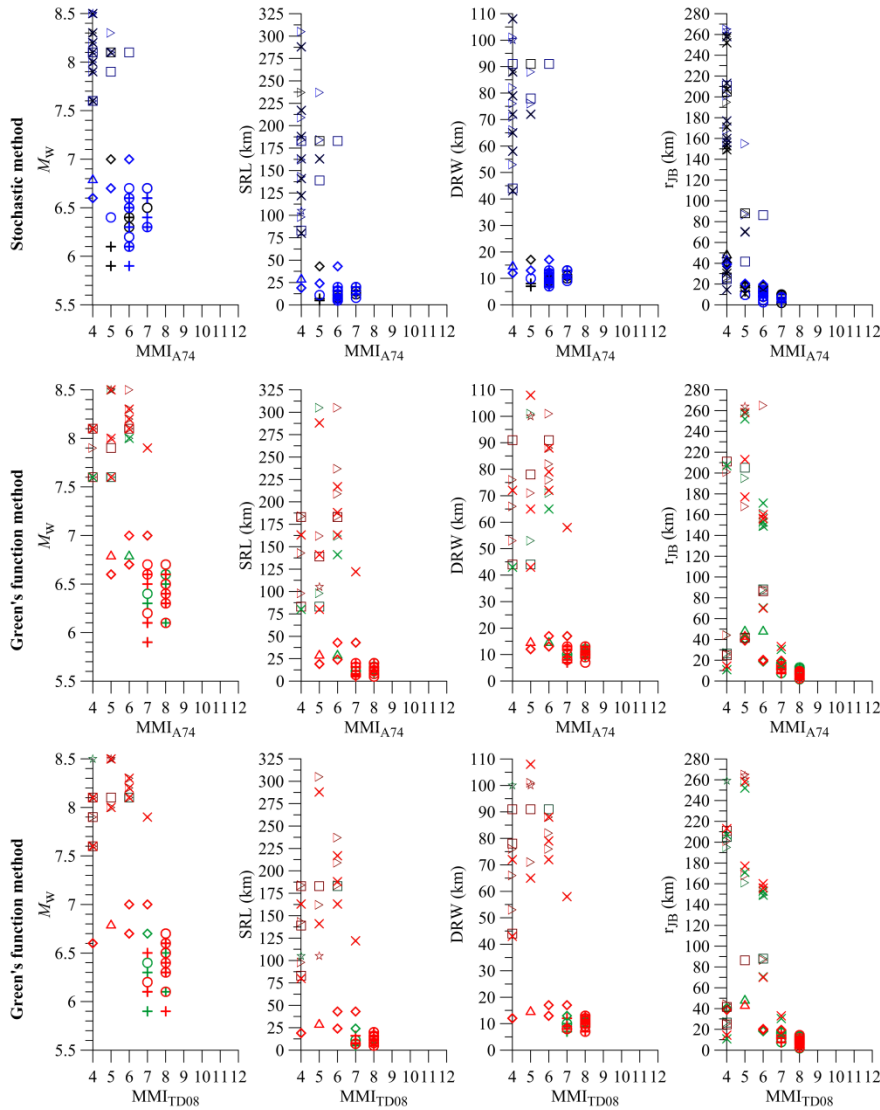


Figure 5.12: Summary of computed MMI scale values of all seismogenic sources modeled with the Stochastic and Green’s function methods plotted against M_w , SRL, DRW, and r_{JB} . A74 = Ambraseys (1974). TD08 = Tselentis and Danciu (2008). Symbols same as in Figure 5.11.

5.4.1 Normal Faulting Earthquakes in the Argive Basin

A minor difference in the computed M_w is obtained for some onshore normal faults when using the global empirical relations of Wells and Coppersmith (1994) and Pavlides and Caputo (2004). This noticeable difference is in the order of 0.1 to 0.2 units and is due to the different number of sub-faults required to reach the target M_w for a given fault. Tables 5.10 and 5.11 in Appendix C show the modeling parameters used to simulate normal faulting earthquakes within the Argive Basin using both the stochastic and the Green's function methods, respectively. Despite that the empirical relations of Wells and Coppersmith (1994) and Pavlides and Caputo (2004) required a slightly different number of sub-faults in the stochastic simulation, the resulting synthetic acceleration seismograms are in full agreement with each other. The most obvious difference occurs in the resulting PGA; however, the M_w , duration, and frequency content are comparable as seen in Figure 5.13. Figure 5.14 (upper left corner) shows the resulting acceleration response spectra of all modeled normal faults in the Argive Basin. An example of the resulting three components (e.g., East-West [X], North-South [Y], and vertical [Z]) synthetic acceleration seismograms based on the Green's function approach using the empirical relations of Wells and Coppersmith (1994) and Pavlides and Caputo (2004) are shown in Figure 5.15. This example corresponds to the normal faulting earthquake triggered by the reactivation of the ABNAF4 normal fault segment passing through the area between Tiryns and Midea. Figures 5.16 and 5.17 show the associated synthetic velocity and displacement seismograms, respectively, for the same event.

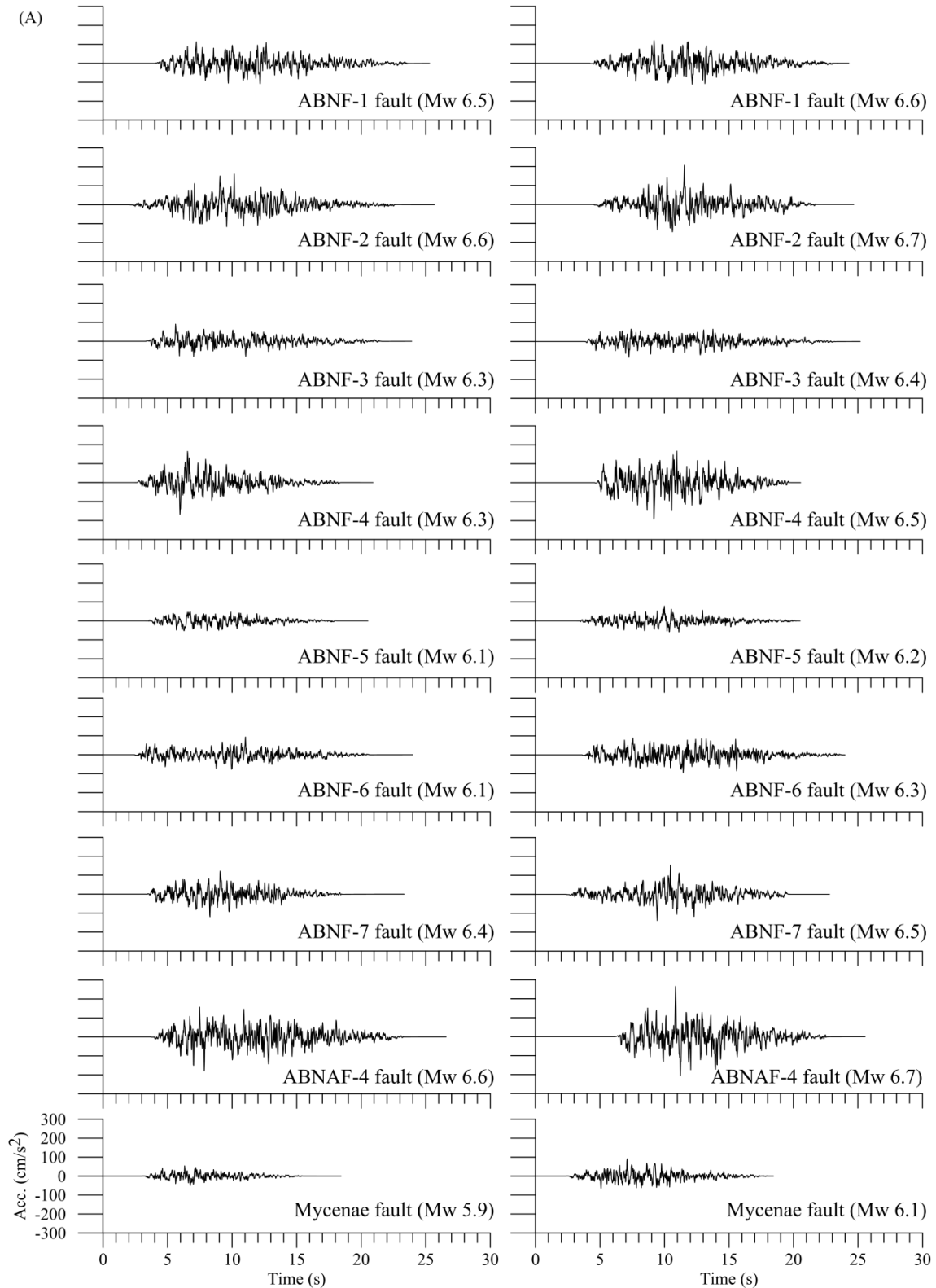


Figure 5.13: Stochastically simulated acceleration seismograms of the horizontal acceleration at (A) the Tiryns and (B) Midea citadels for 9 earthquakes at probably active normal faults in the Argive Basin (Peloponnese, Greece). Accelerograms of the left and right column are modeled using the global empirical relation of Wells and Coppersmith (1994) and the regional empirical relation for *Aegean-type* normal faults of Pavlides and Caputo (2004), respectively. Labels at the end of the accelerograms correspond to the fault segment and target M_w listed in Table 5.3. Vertical and horizontal scale is equal for all the accelerograms.

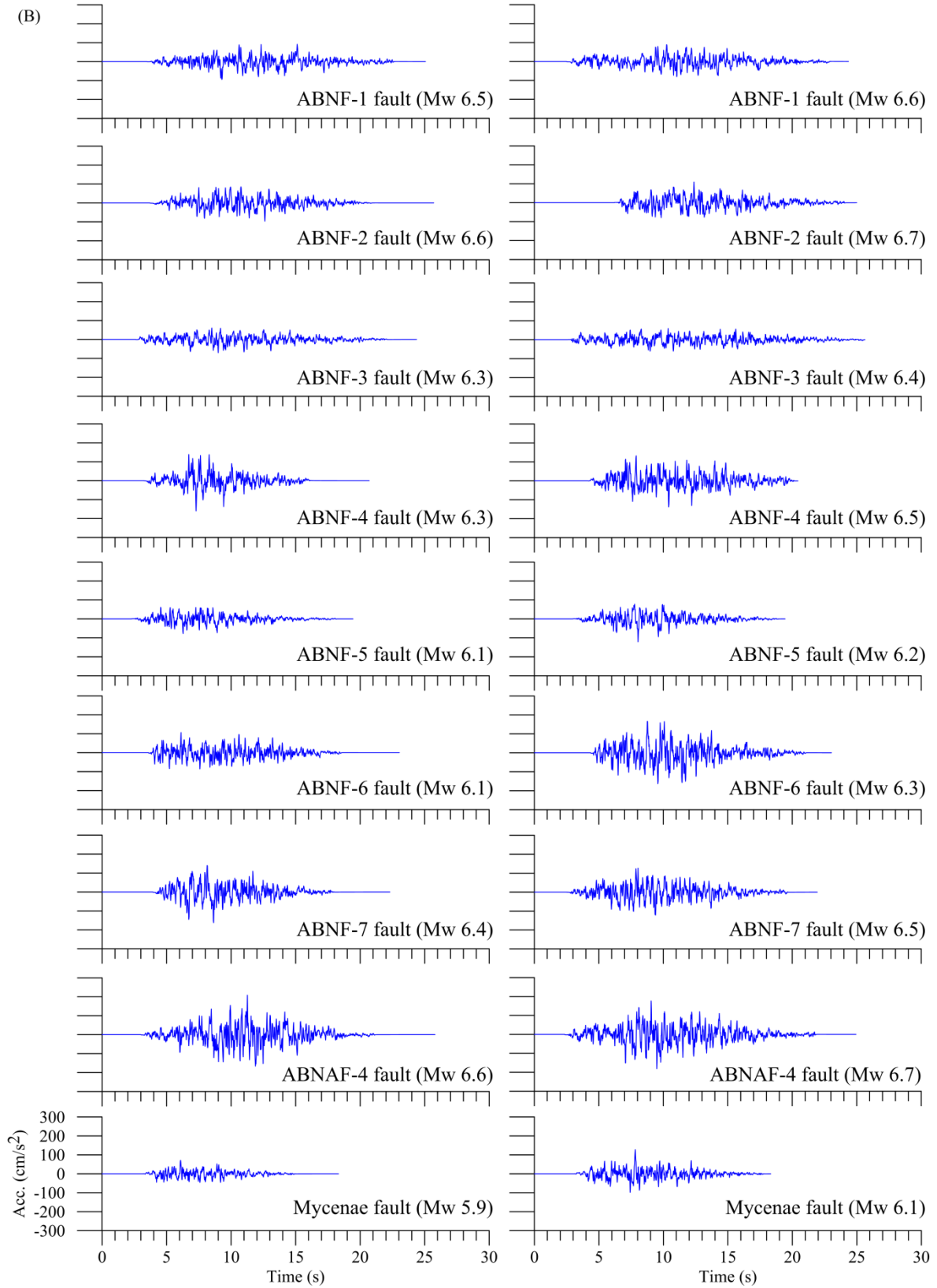


Figure 5.13: *continued.*

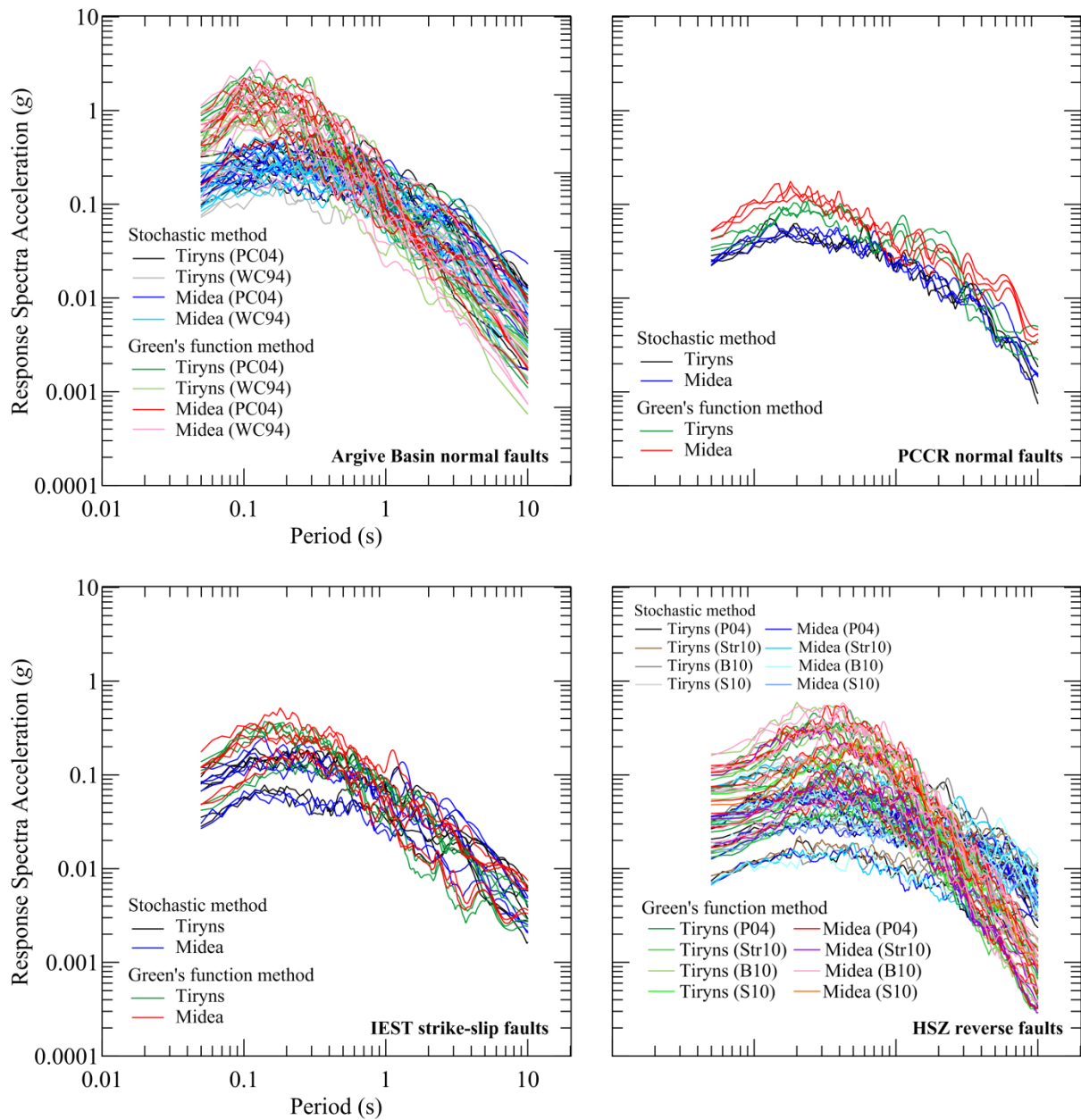


Figure 5.14: Calculated acceleration response spectra for all seismogenic sources modeled with both the Stochastic and Green's function methods with an observation point located at the citadels of Tiryns and Midea.

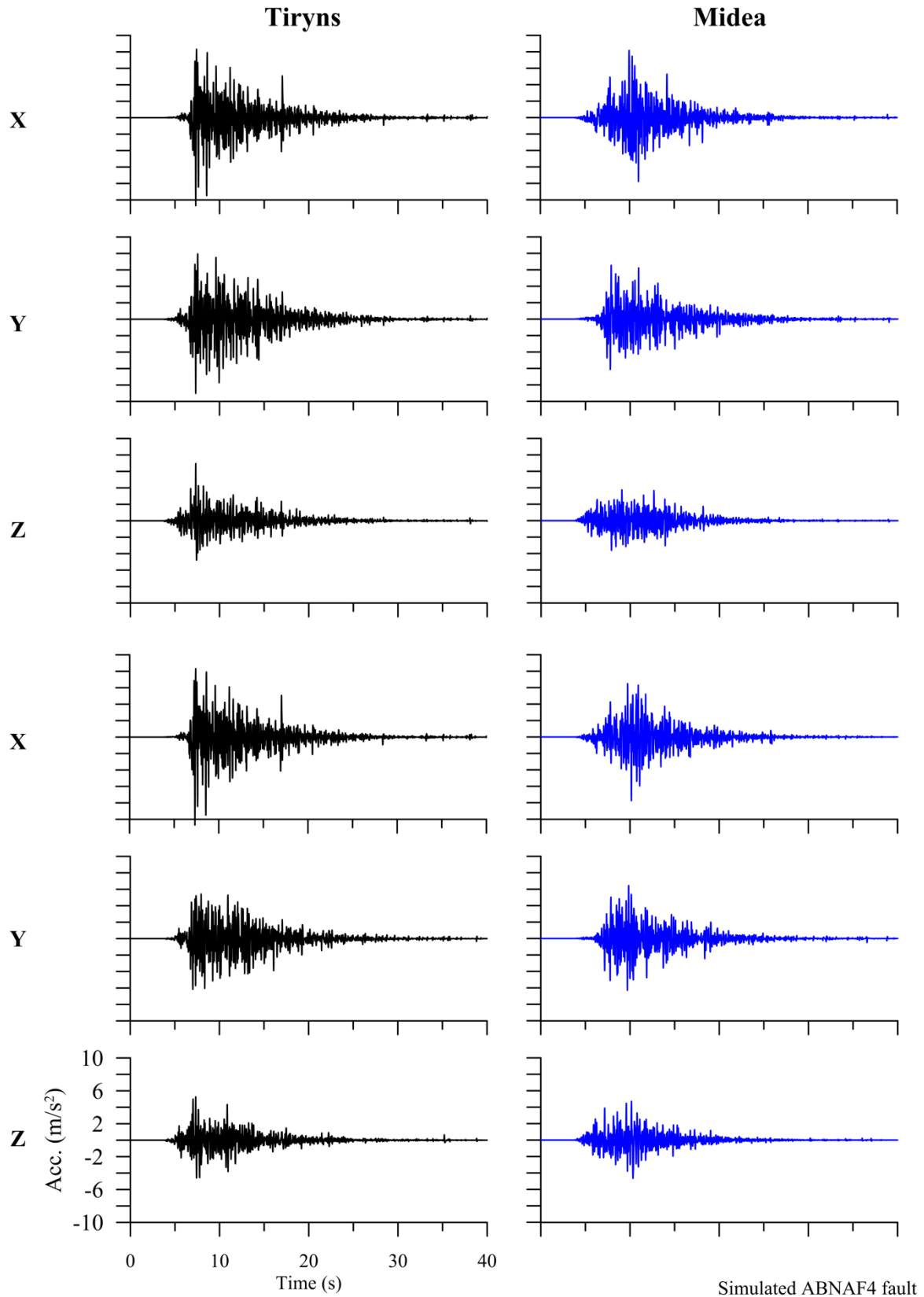


Figure 5.15: Simulated acceleration seismograms for the East-West (X), North-South (Y), and vertical (Z) components with observation point located at the Tiryns (*left-side*) and Midea (*right-side*) citadels. Accelerograms of the upper and lower three rows correspond to modeled M_w 6.7 and M_w 6.6 normal faulting earthquakes based on the empirical relation of Pavlides and Caputo (2004) and Wells and Coppersmith (1994), respectively, triggered by the ABNAF4 fault segment. Vertical and horizontal scale equal for all accelerograms.

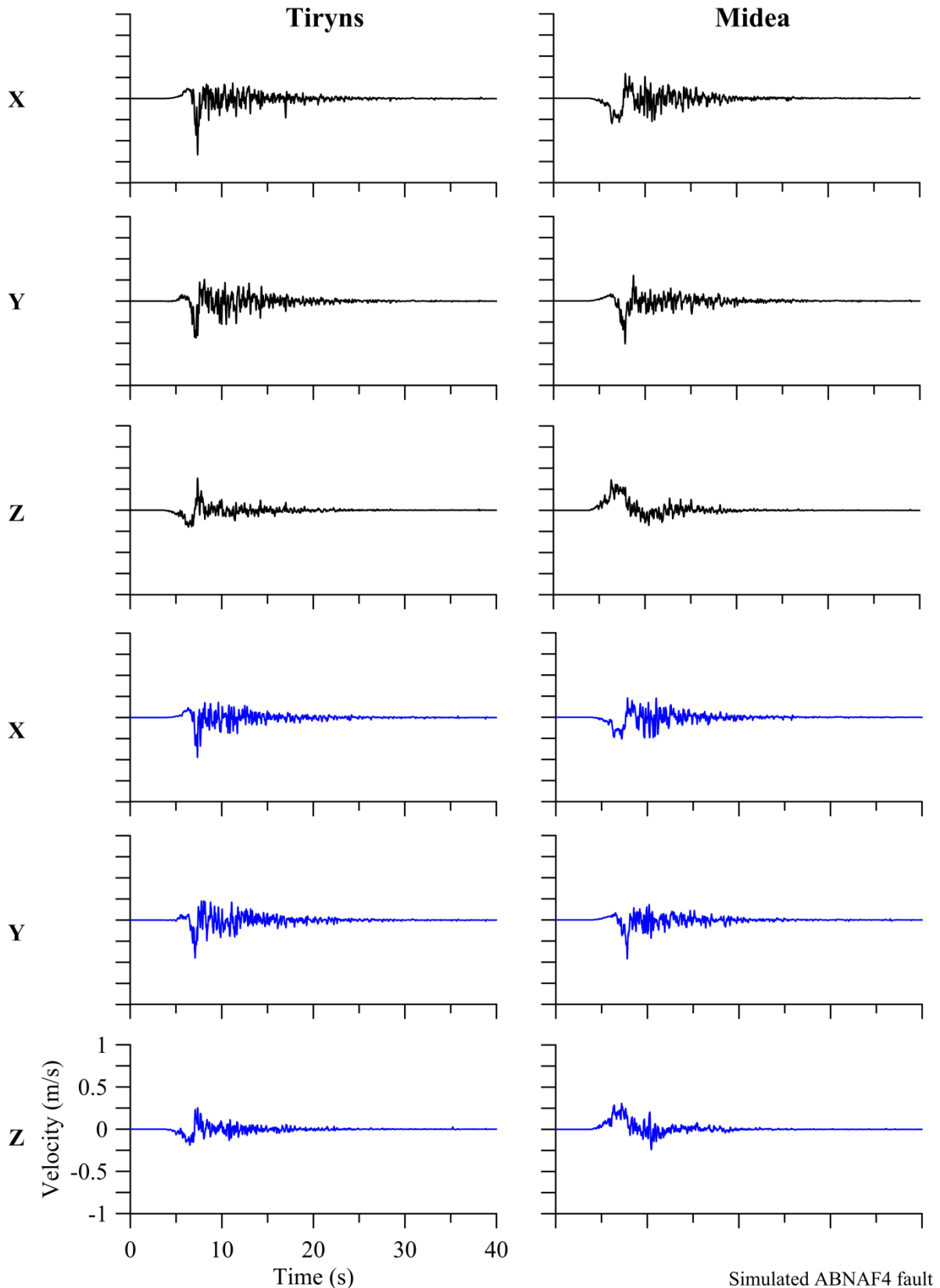


Figure 5.16: Simulated velocity seismograms for the East-West (X), North-South (Y), and vertical (Z) components with observation point located at the Tiryns (*left-side*) and Midea (*right-side*) citadels. Velocity seismograms of the upper and lower three rows correspond to modeled M_w 6.7 and M_w 6.6 normal faulting earthquakes based on the empirical relation of Pavlides and Caputo (2004) and Wells and Coppersmith (1994), respectively, triggered by the ABNAF4 fault segment. Vertical and horizontal scale equal for all seismograms.

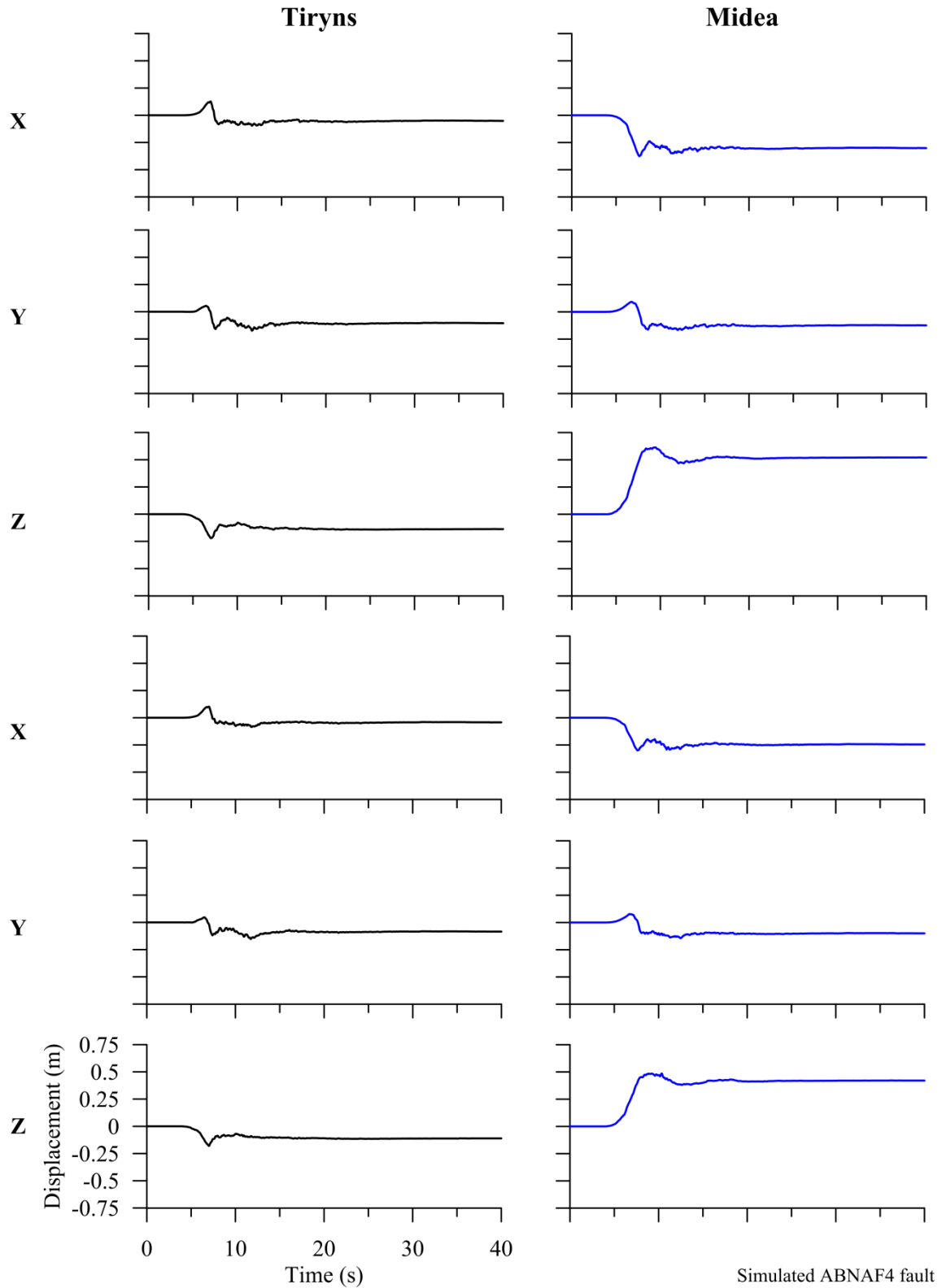


Figure 5.17: Simulated displacement seismograms for the East-West (X), North-South (Y), and vertical (Z) components with observation point located at the Tiryns (*left-side*) and Midea (*right-side*) citadels. Displacement seismograms of the upper and lower three rows correspond to modeled M_w 6.7 and M_w 6.6 normal faulting earthquakes based on the empirical relation of Pavlides and Caputo (2004) and Wells and Coppersmith (1994), respectively, triggered by the ABNAF4 fault segment. Vertical and horizontal scale equal for all seismograms.

5.4.2 Normal Faulting Earthquakes in the Patras–Corinth Continental Rift

The empirical relation of Wells and Coppersmith (1994) and Pavlides and Caputo (2004) are used to model the three scenarios of the Xylokastro normal fault. The fault geometries of the three fault scenarios are in Table 5.3. Both empirical relations yield the same moment magnitude (i.e., M_w 6.8) for all fault scenarios with the observation point located at Tiryns and Midea. The resulting synthetic horizontal acceleration seismograms of the fault scenarios modeled stochastically are shown in Figure 5.18. The resulting synthetic two horizontal and vertical component acceleration, velocity, and displacement seismograms computed for the fault scenarios using the Green's function method are shown in Figures 5.19, 5.20 and 5.21, respectively. In Figure 5.19, noticeable differences are observed when comparing the accelerations of Tiryns and Midea. Contrariwise, indiscernible differences occur when comparing the velocity and displacement seismograms. This is likely due the close proximity (7 km) between both sites (i.e., observation points). For direct comparison, Figure 5.14 (upper-right corner) shows the resulting acceleration response spectra of all the fault scenarios modeled with the Stochastic and Green's function methods.

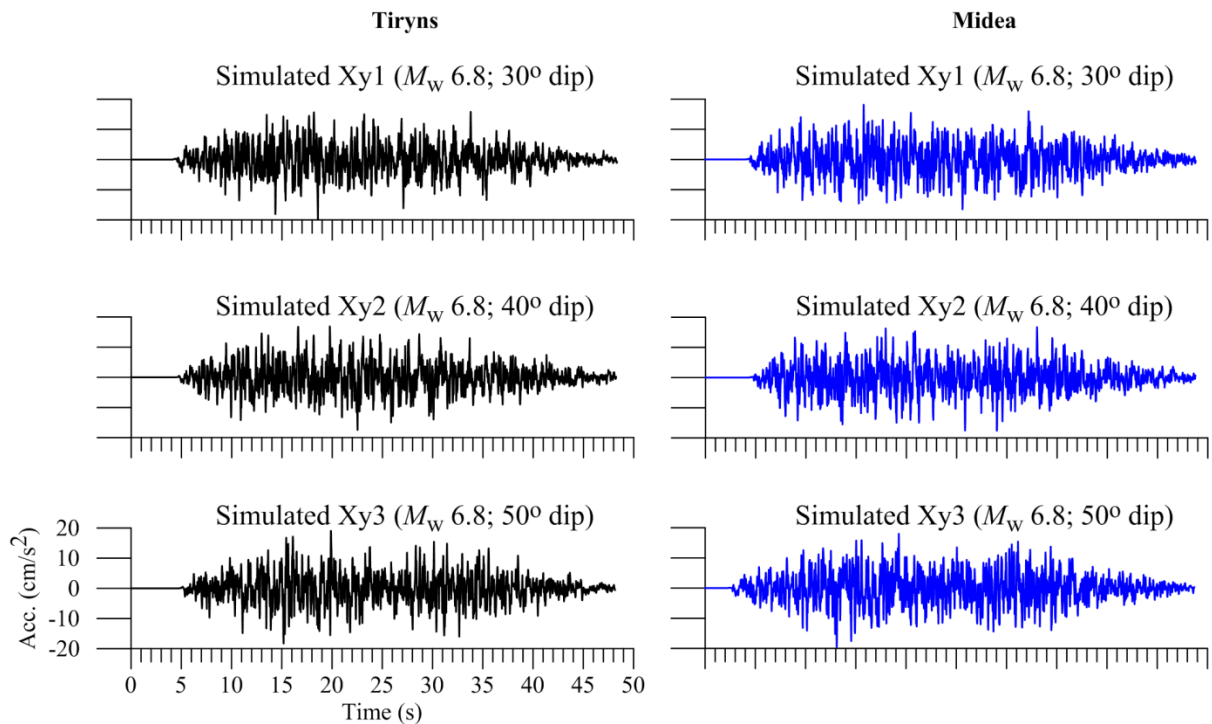


Figure 5.18: Stochastically simulated horizontal acceleration seismograms for three fault scenarios of the Xylokastro normal fault in the PCCR with observation points located at Tiryns (black) and Midea (blue). Vertical and horizontal scale is equal for all the accelerograms.

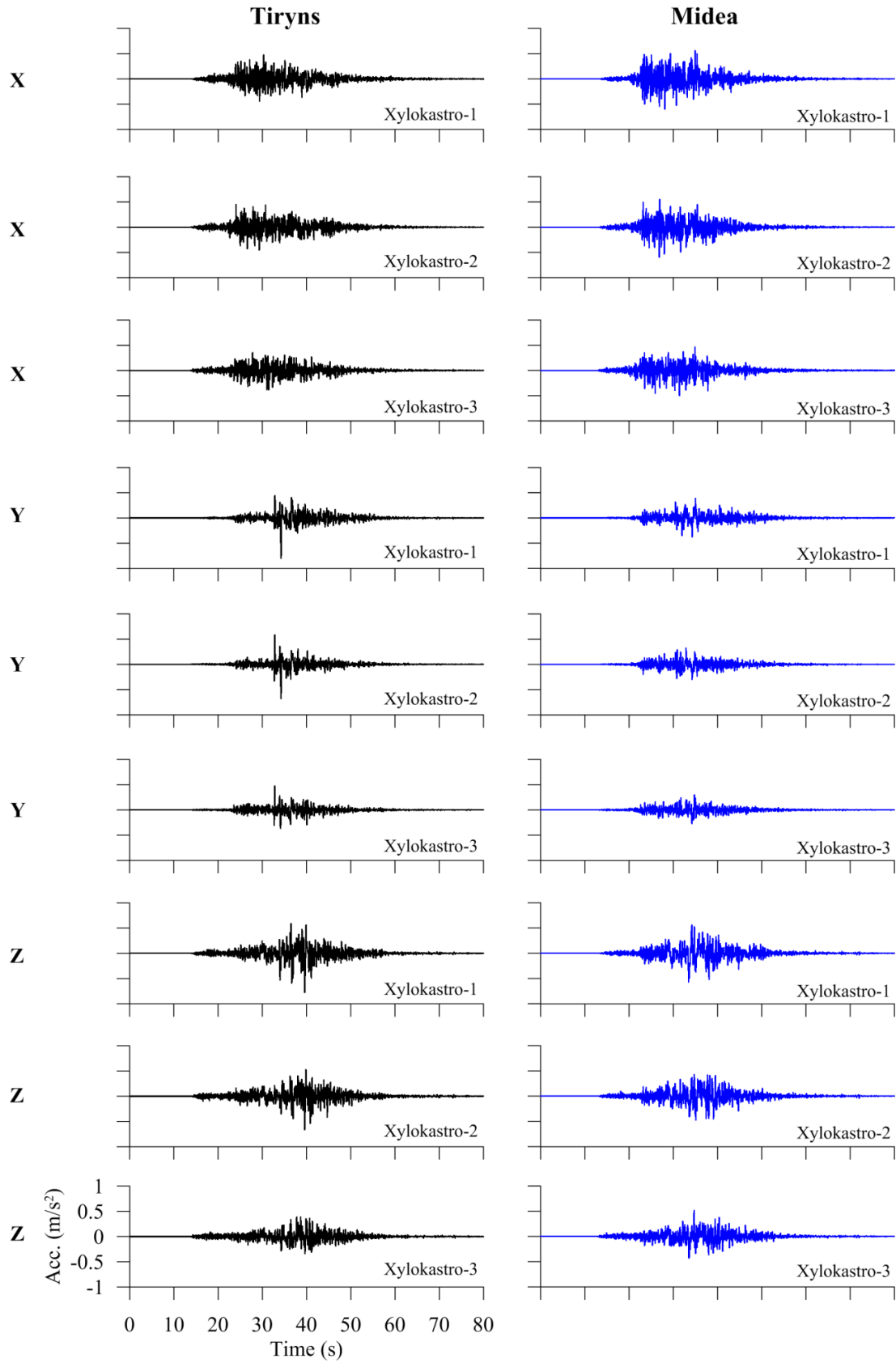


Figure 5.19: Simulated acceleration seismograms, with the Green’s function method, for the East-West (X), North-South (Y), and vertical (Z) components with observation point located at the Tiryns (*left-side*) and Midea (*right-side*) citadels. The accelerograms correspond to earthquakes triggered by the three scenarios of the Xylokaastro normal fault.

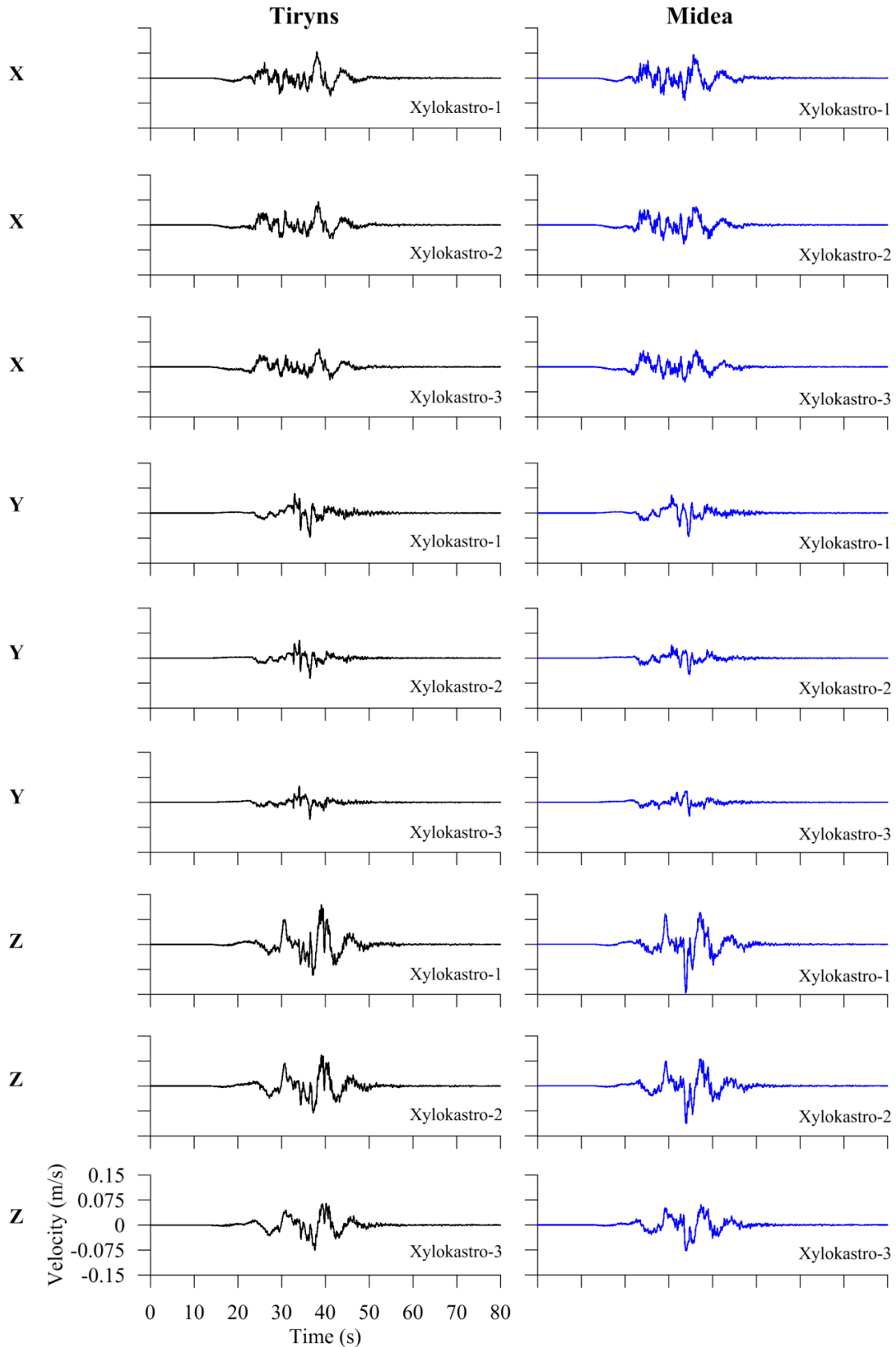


Figure 5.20: Simulated velocity seismograms, with the Green's function method, for the East-West (X), North-South (Y), and vertical (Z) components with observation point located at the Tiryns (*left-side*) and Midea (*right-side*) citadels. The velocity seismograms correspond to earthquakes triggered by the three scenarios of the Xylokastro normal fault.

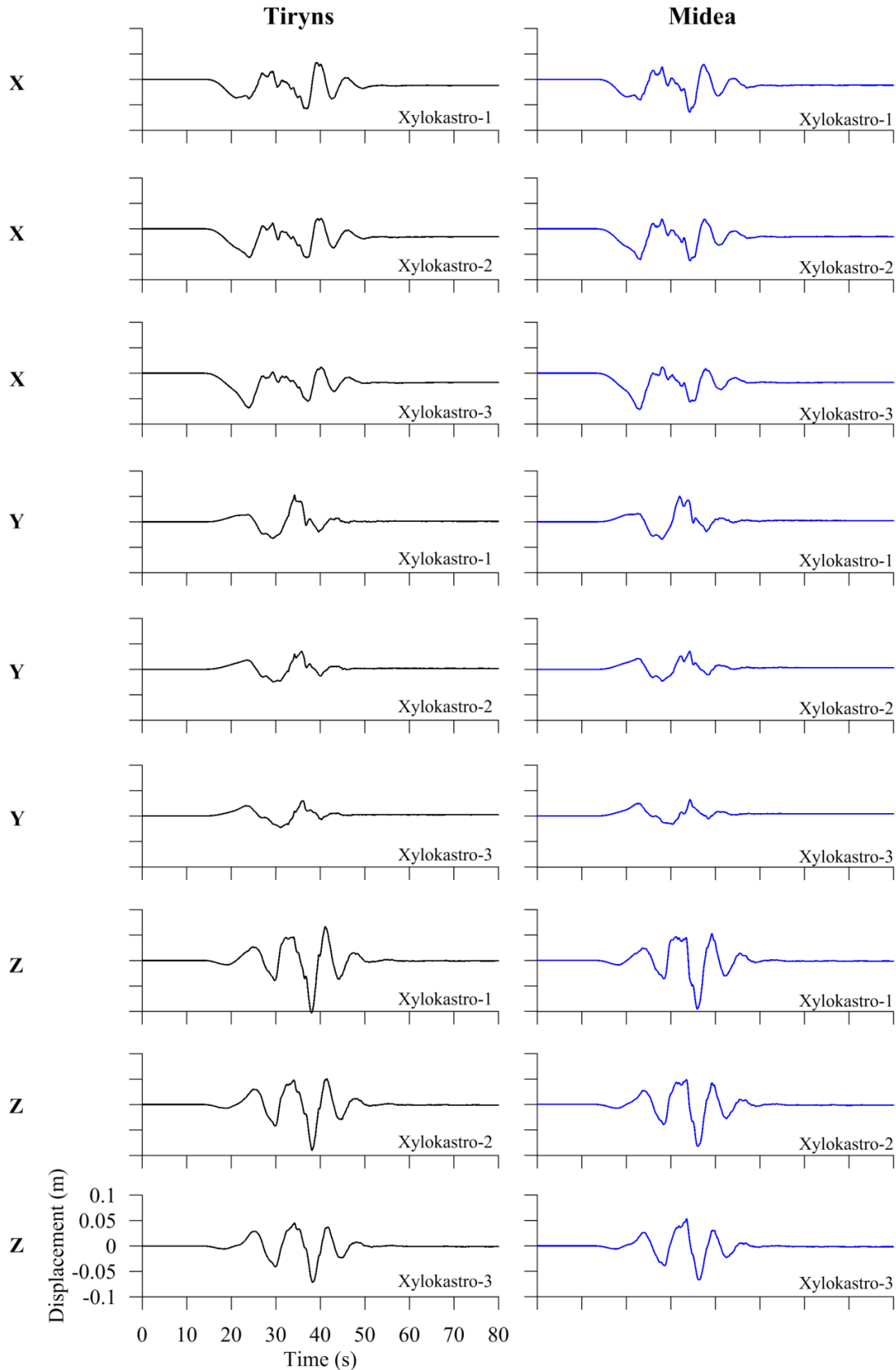


Figure 5.21: Simulated displacement seismograms, with the Green's function method, for the East-West (X), North-South (Y), and vertical (Z) components with observation point located at the Tiryns (*left-side*) and Midea (*right-side*) citadels. The displacement seismograms correspond to earthquakes triggered by the three scenarios of the Xylokastro normal fault.

5.4.3 Strike-Slip Faulting Earthquakes in the Iria–Epidaurus Sinistral Transform Fault System

Only the empirical relation of Wells and Coppersmith (1994) was used to compute M_w for the strike-slip faults in the IEST system. The geometry of these fault segments is given in Table 5.4. The stochastically modeled synthetic horizontal accelerograms of all the fault scenarios are shown in Figure 5.22. Figures 5.23, 5.24, and 5.25 show an example of the resulting X, Y, and Z component synthetic acceleration, velocity, and displacement seismograms, respectively, corresponding to the Iria-Epidaurus1 (IrEp1) strike-slip fault segment. Figure 5.14 (lower-left corner) displays the resulting computed acceleration response spectra of all the strike-slip faults modeled with both the stochastic and Green's function methods.

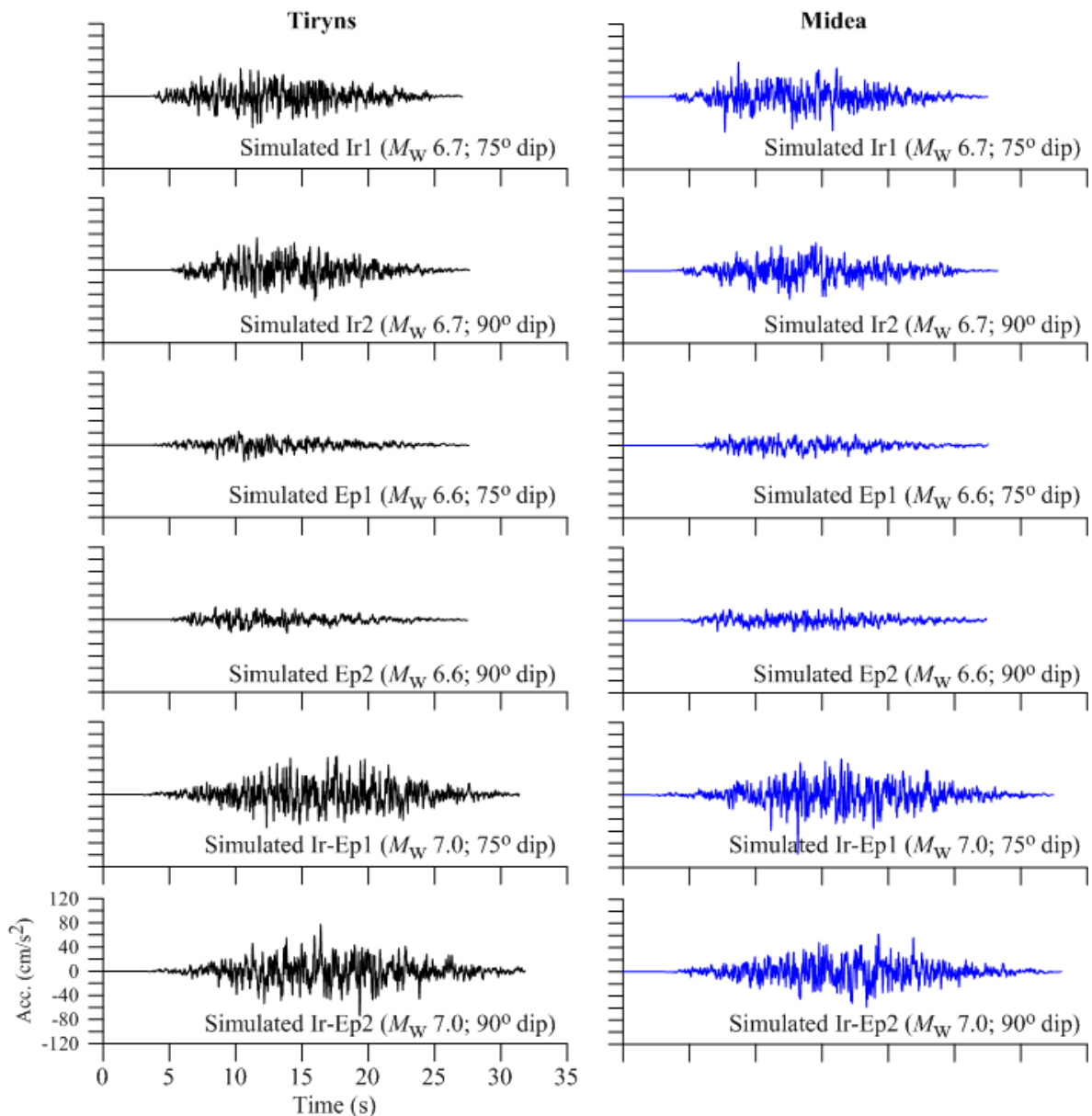


Figure 5.22: Stochastically simulated horizontal acceleration seismograms for all the strike-slip faults in the IEST fault system with observation point located at the Tiryns (*left-side*) and Midea (*right-side*) citadels.

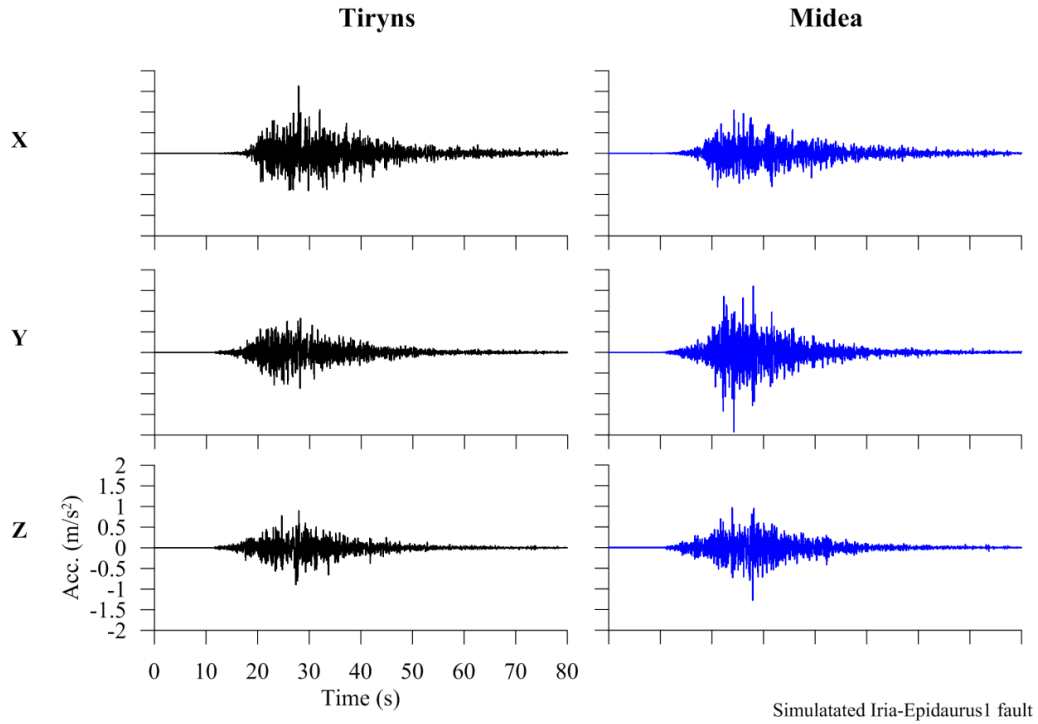


Figure 5.23: Simulated acceleration seismograms, with the Green’s function method, for the East-West (X), North-South (Y), and vertical (Z) components with observation point located at the Tiryns (*left-side*) and Midea (*right-side*) citadels. The accelerograms correspond to the earthquake triggered by the Iria-Epidauros1 strike-slip fault (IrEp1).

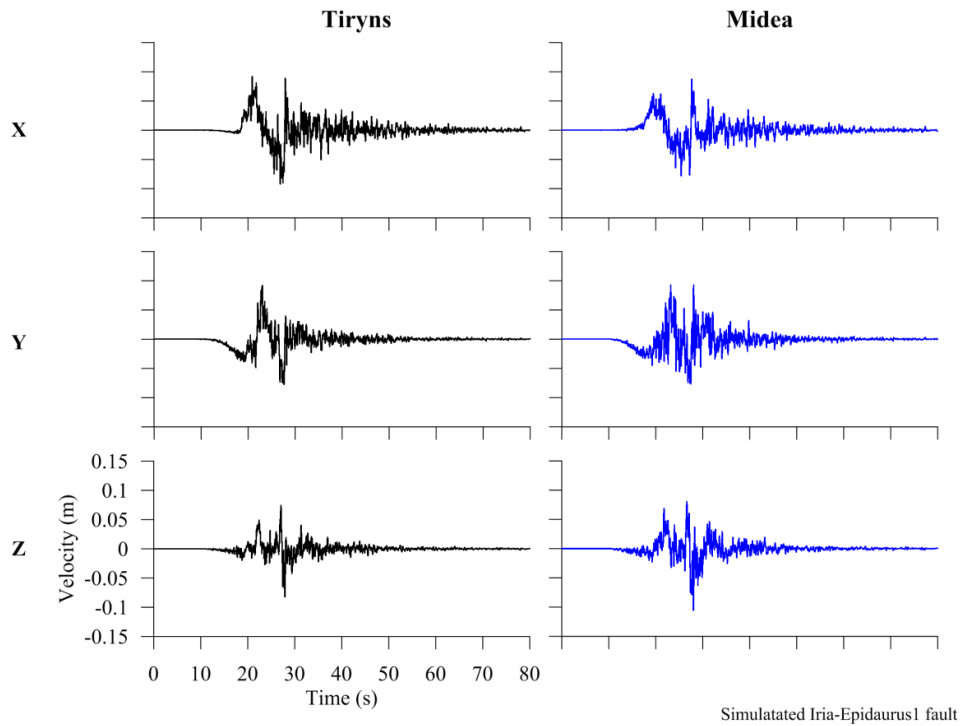


Figure 5.24: Simulated velocity seismograms, with the Green’s function method, for the East-West (X), North-South (Y), and vertical (Z) components with observation point located at the Tiryns (*left-side*) and Midea (*right-side*) citadels. The velocity seismograms correspond to the earthquake triggered by the Iria-Epidauros1 strike-slip fault (IrEp1).

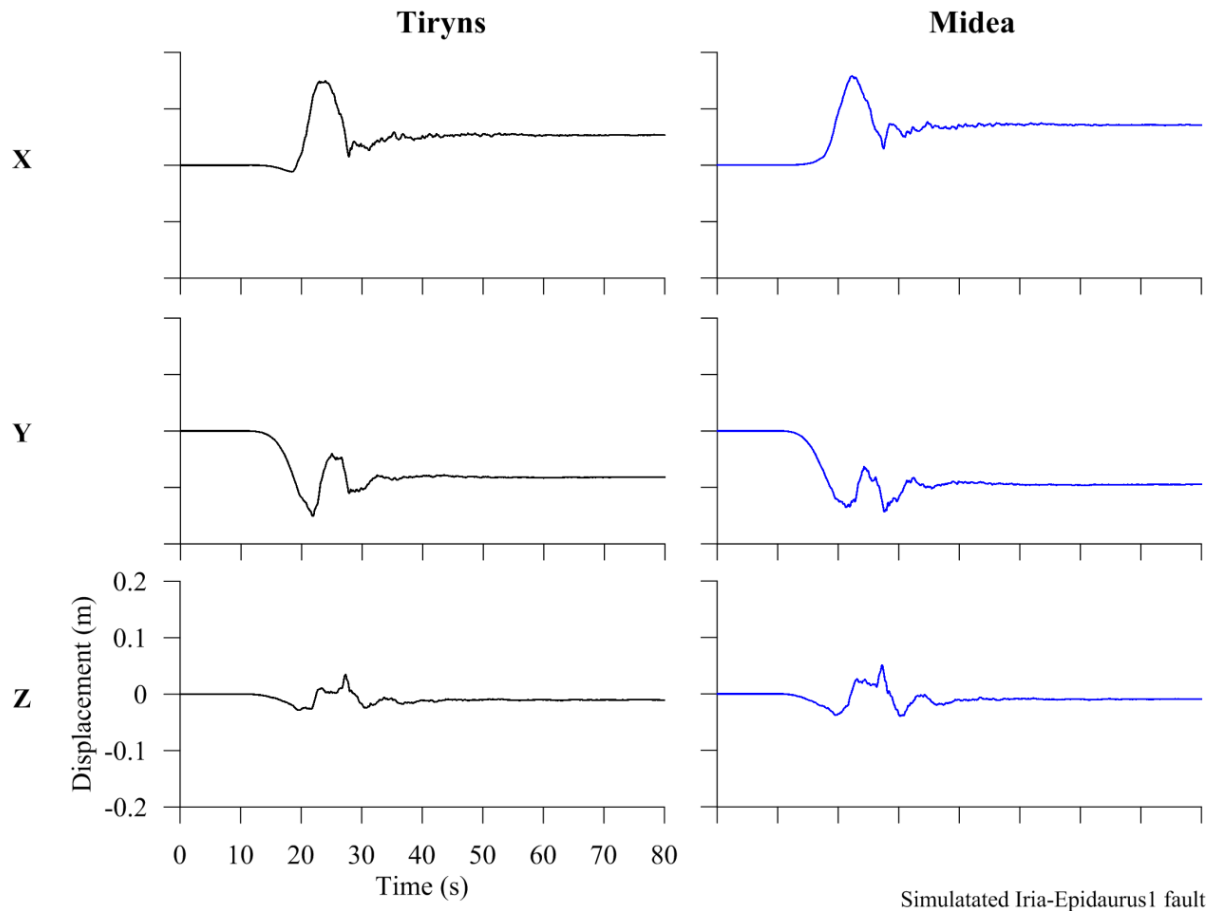


Figure 5.25: Simulated displacement seismograms, with the Green's function method, for the East-West (X), North-South (Y), and vertical (Z) components with observation point located at the Tiryns (*left-side*) and Midea (*right-side*) citadels. The displacement seismograms correspond to the earthquake triggered by the Iria-Epidauros1 strike-slip fault (IrEp1).

5.4.4 Reverse Faulting Earthquakes in the Hellenic Subduction Zone

The global scaling empirical relations of Papazachos et al. (2004), Blaser et al. (2010), and Strasser et al. (2010) were developed for subduction-related reverse faulting earthquakes using different data sets of M_w ; hence, they yield noticeably different source dimensions (i.e., SRL and DRW) and consequently different synthetic seismograms. Further, only the empirical equations of Strasser et al. (2010) differentiate between interface and intraplate earthquakes. Therefore, only a limited range of target or hypothetical earthquake M_w can be directly compared to one another (see Table 5.5). An example of stochastically modeled acceleration seismograms of an interface earthquake (event HSZ-2) and an intraplate earthquake (event HSZ-6) based on the empirical relations of Papazachos et al. (2004), Blaser et al. (2010), and Strasser et al. (2010) are shown in Figure 5.26. Figures 5.27, 5.28, and 5.29 show the acceleration, velocity, and displacement seismograms, respectively, for the same interface and intraplate events modeled with the Green's function method and the same empirical relations. Figure 5.14 (lower-right corner) shows the resulting acceleration response spectra of all interface and intraplate earthquakes modeled with both the stochastic and Green's functions methods.

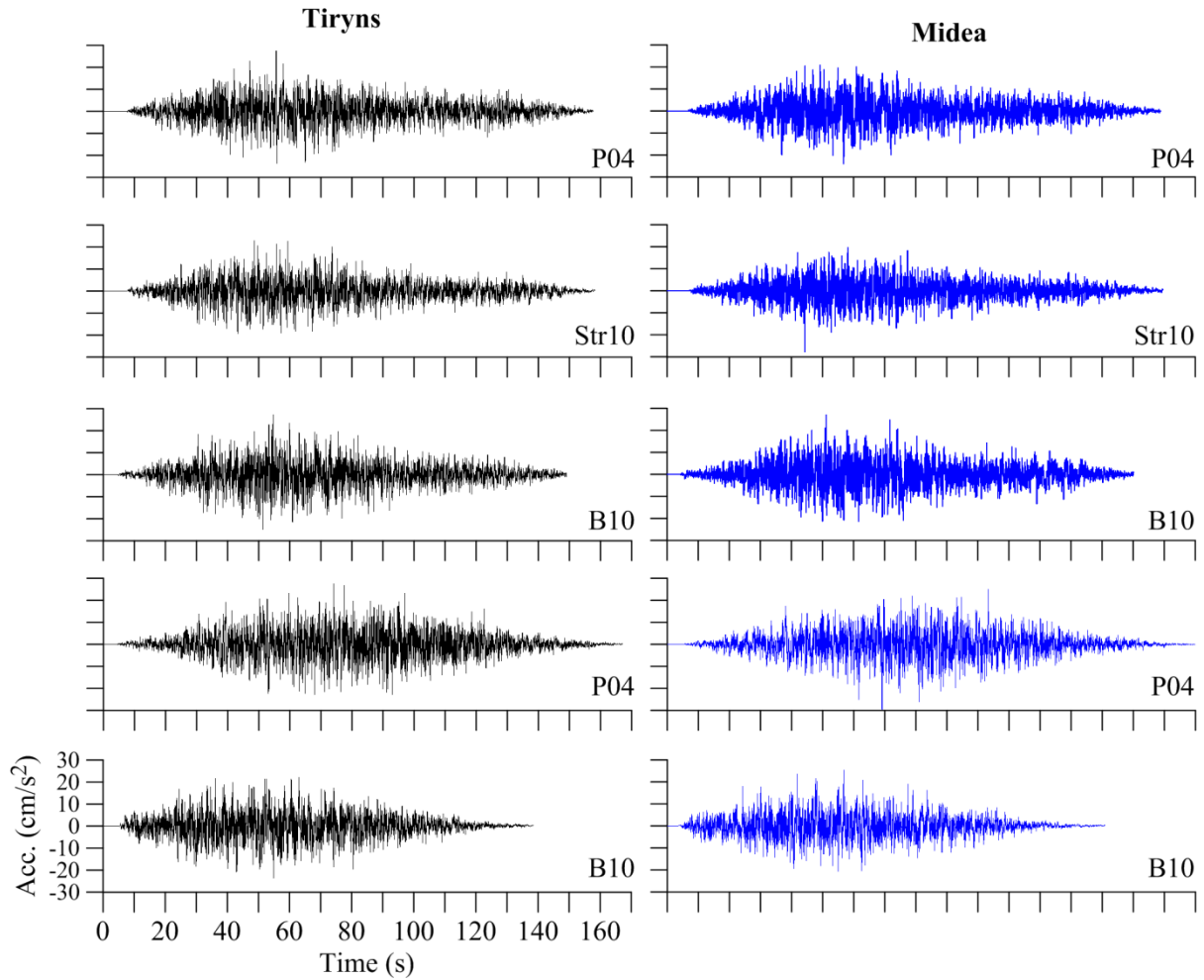


Figure 5.26: Stochastically simulated horizontal acceleration seismograms for interface M_w 8.1 event (HSZ-2, upper three rows) and intraplate M_w 8.3 event (HSZ-6, lower two rows) with observation point located at the Tiryns (*left-side*) and Midea (*right-side*) citadels. Event HSZ-2 is modeled using the empirical relation of Papazachos et al. (2004) [P04], Strasser et al. (2010) [Str10], and Blaser et al. (2010) [B10]. Event HSZ-6 is modeled with the empirical relation of P04 and B10.

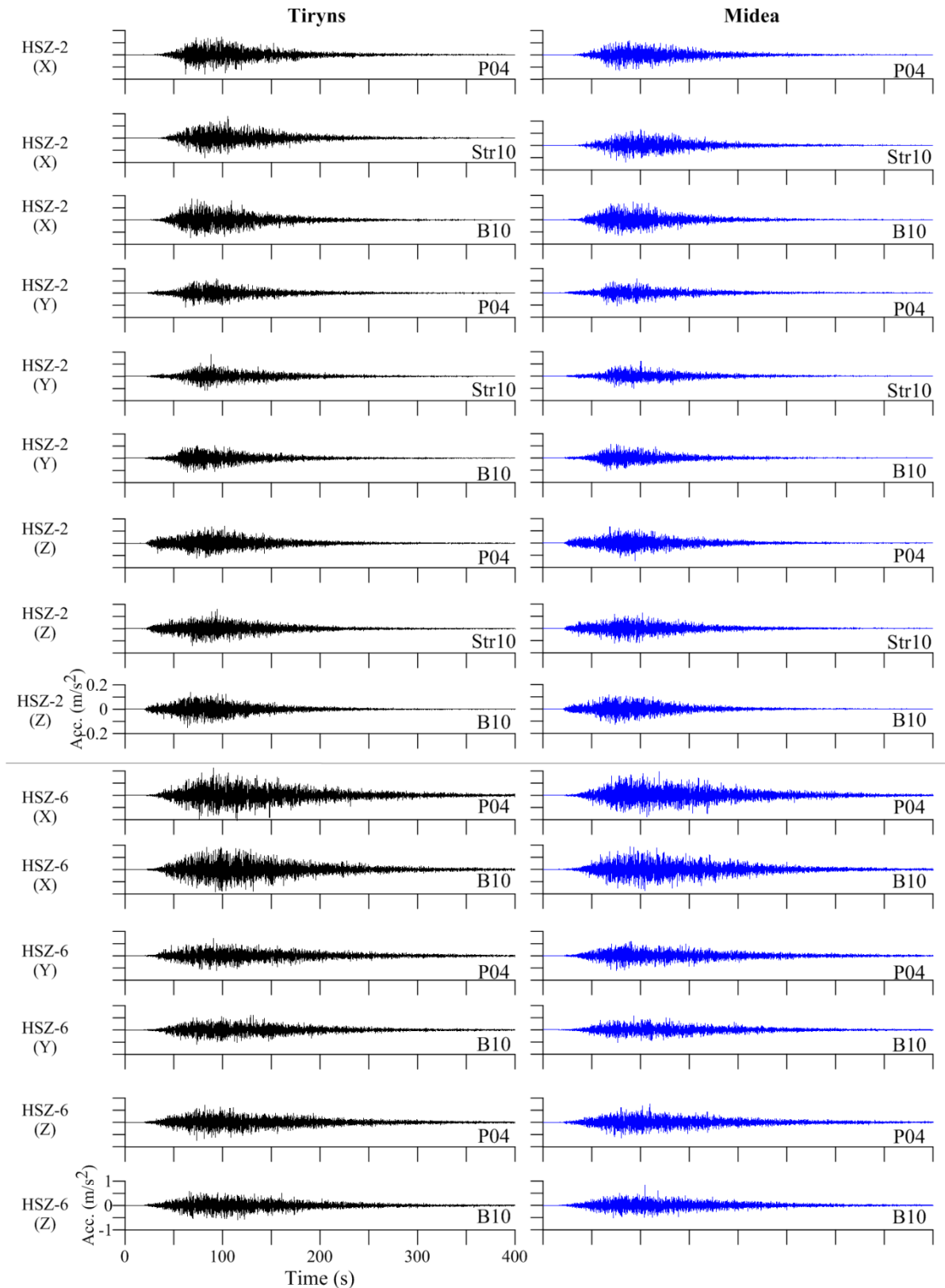


Figure 5.27: Synthetic East-West (X), North-South (Y), and vertical (Z) components accelerograms for interface M_w 8.1 event (HSZ-2, upper 9 rows) and intraplate M_w 8.3 event (HSZ-6, lower 6 rows) using the Green's function method with observation point located at the Tiryns (*left-side*) and Midea (*right-side*). Event HSZ-2 is modeled using the empirical relation of Papazachos et al. (2004) [P04], Strasser et al. (2010) [Str10], and Blaser et al. (2010) [B10]. Event HSZ-6 is modeled with the relation of P04 and B10.

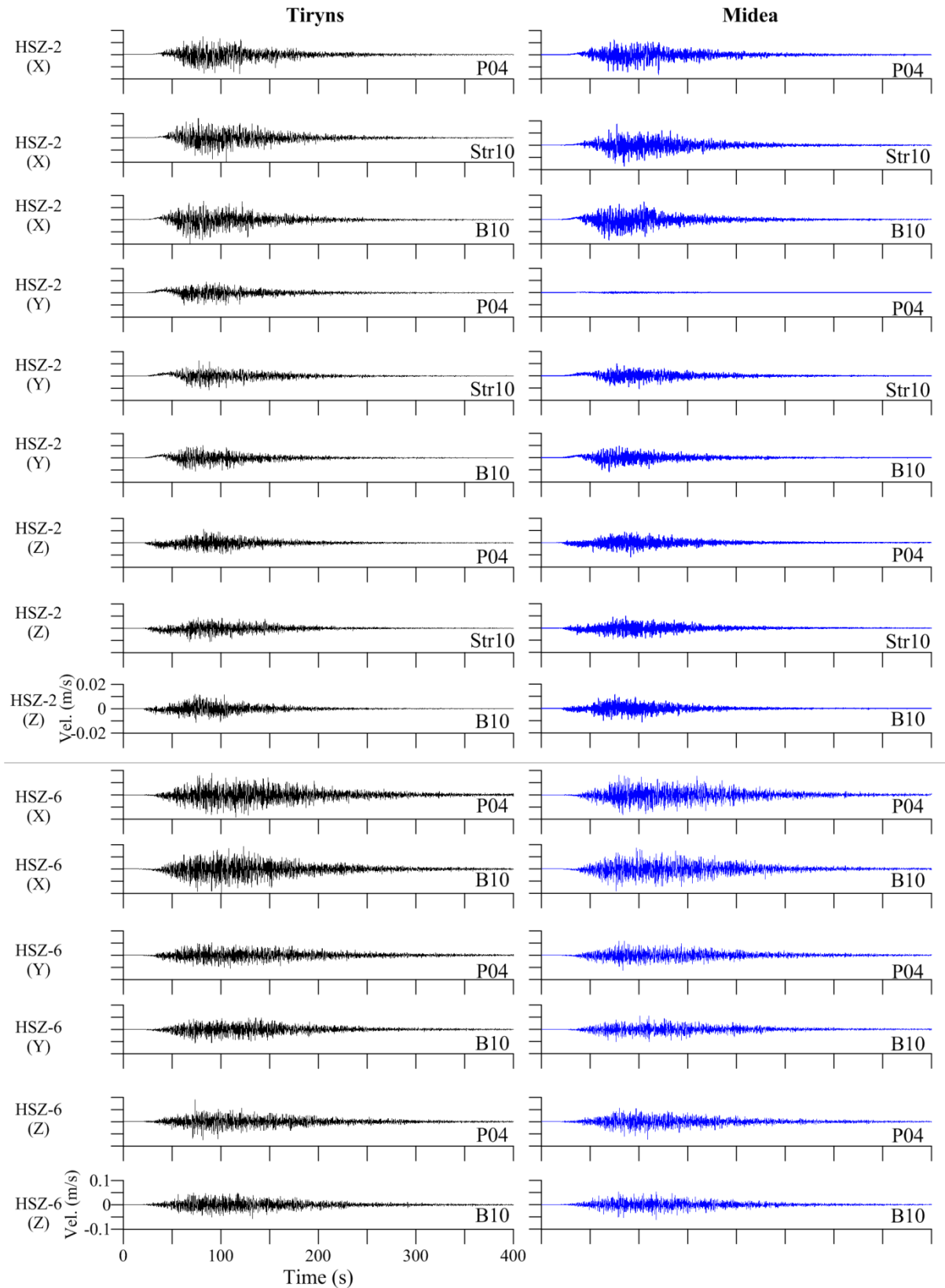


Figure 5.28: Synthetic velocity seismograms for the East-West (X), North-South (Y), and vertical (Z) components using the Green's function method with observation point located at the Tiryns (*left-side*) and Midea (*right-side*) citadels. The velocity seismograms correspond to the M_w 8.1 and M_w 8.3 events triggered by faults HSZ-2 (upper 9 rows) and HSZ-6 (lower 6 rows), respectively.

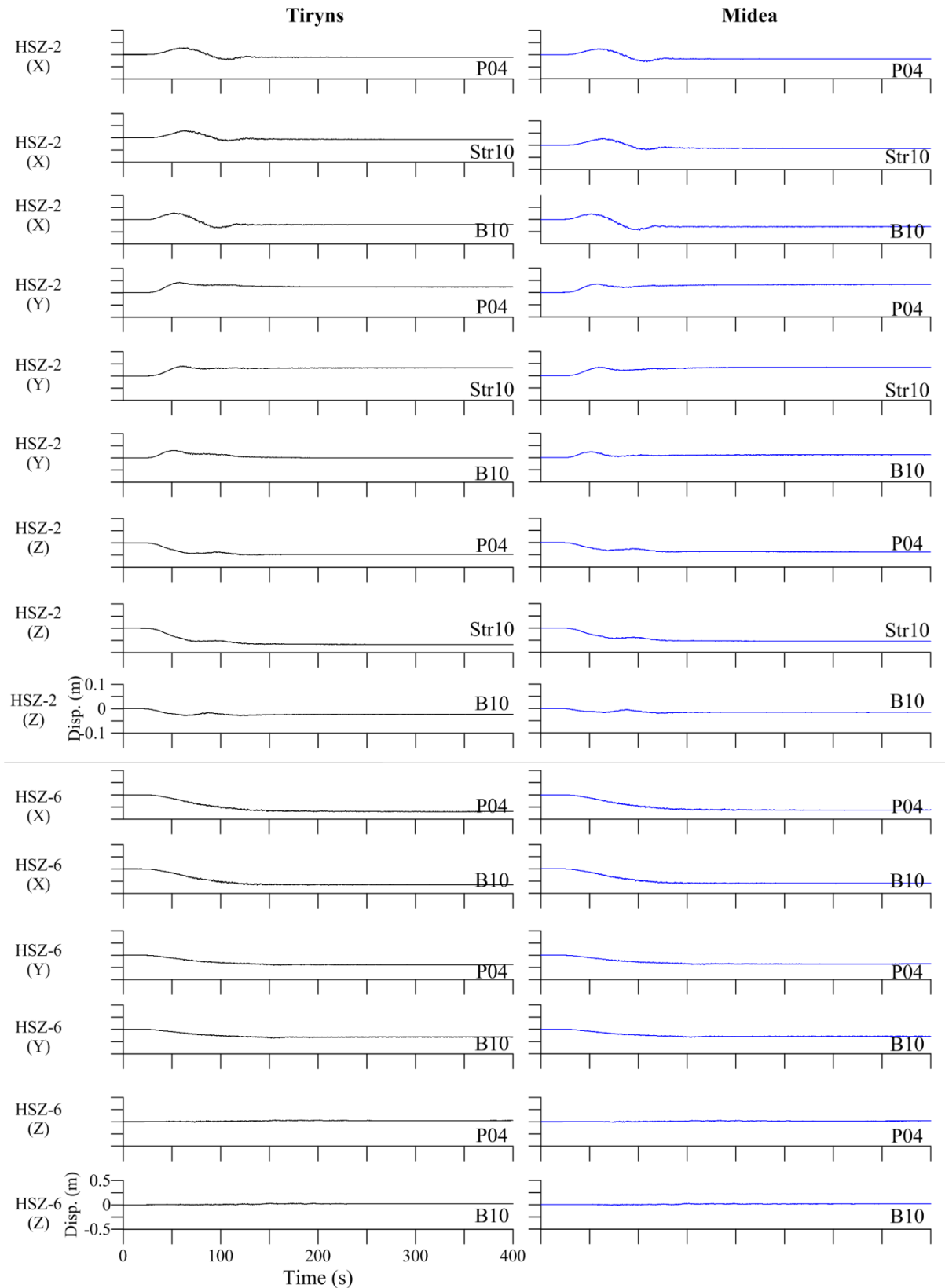


Figure 5.29: Simulated displacement seismograms for the East-West (X), North-South (Y), and vertical (Z) components using the Green's function method with observation point located at the Tiryns (*left-side*) and Midea (*right-side*) citadels. The displacement seismograms correspond to the M_w 8.1 and M_w 8.3 events triggered by faults HSZ-2 (upper 9 rows) and HSZ-6 (lower 6 rows), respectively.

6. FORWARD MODELING OF LOCAL SITE EFFECTS AT TIRYNS AND MIDEA

6.1 Dynamic Loading of Ground Surface

During earthquakes the ground surface undergoes multi-directional cyclic stresses with different frequencies and amplitudes that lead to cyclic deformations and fluctuations in stress–strain and strength properties (Kramer, 1996; Ansal et al., 2001). Near-surface materials typically comprise young soft-soils deposited on stiffer sediments underlain by weathered bedrock, a stratigraphic column commonly referred to as *regolith*. Regolith can amplify the level of surface ground-motion during an earthquake (Murphy et al., 1971; Borcherdt and Gibbs, 1976; Seed et al., 1976; Steidl et al., 1996; Robinson et al., 2006). Real surface ground-motion scenarios usually involve fine–grained to very coarse–grained layered soil deposits of varying stiffness and damping characteristics with interfaces at which elastic wave energy is reflected and/or transmitted (Kramer, 1996; Rodríguez-Marek et al., 2001; Thompson et al., 2012). The amplification of seismic waves is due to the impedance contrast between hard-rock (bedrock) and the overlying sediments and soils (Kramer, 1996; Şafak, 2001; Cornou and Bard, 2003). A site with relatively softer soils over bedrock, typically referred to as “soil-site”, will amplify low-frequency (long-period) bedrock motions more than a nearby site with relatively stiffer soils over the same bedrock (Kramer, 1996). These last two amplification scenarios are expected to occur in the Late Neogene–Quaternary Argive Basin because of the abundance of less stiff and stiffer soils deposited around the Tiryns and Midea archaeological sites, respectively, of which stiffness changes upsection due to their geologic age and heterogeneous textures, as shown in chapters 3 and 4.

The characteristics of surface ground-motion of soft-soil deposits are influenced by the magnitude of the earthquake and epicentral distance, the impedance contrast between the soil column and underlying bedrock, and attenuation of the soils encountered along the seismic wave propagation path (Seed and Idriss, 1969; Kramer, 1996; Şafak, 2001; Meng, 2007). The behavior of soils under seismic loading also depends on the number of loading cycles, amplitude of loading, in-situ confining pressure, soil plasticity index, soil density, soil void ratio, geologic age, particle shape (round to angular), and grain-size (gradation or texture) (Hashash and Park, 2001; Menq, 2003; Meng, 2007). The dynamic behavior of cohesive soils (e.g., clays, silts, muds, and fine-grained sands) has been investigated extensively (Ansal et al., 2001; Rodríguez-Marek et al., 2001; Stewart et al., 2003). However, the dynamic behavior of granular soils (e.g., coarse sands, gravels, and coarser material) and hard-rock (i.e., bedrock) remain moderately (Menq, 2003) and scarcely (Chandler et al., 2005a, 2005b) studied, respectively. Ansal et al. (2001), Menq (2003), and Chandler et al. (2005a, 2005b, 2006) summarize the dynamic behavior of cohesive soils, granular soils, and bedrock, respectively. Rodríguez-Marek et al. (2001) developed an empirical geotechnical seismic site response procedure that includes measures of the dynamic stiffness of the surficial materials and the depth to the soil–bedrock interface as primary parameters in assessing seismic site response. Their work highlights that sites traditionally grouped as “rock” should be subdivided as “competent rock sites” and “weathered soft rock/shallow stiff soil sites” leading to a significant reduction of uncertainty in defining site-dependent ground motions. Their work also subdivides stiff cohesive soils according to thickness and age; however, it

excludes granular soil deposits. Table 6.1 shows the proposed geotechnical site classification system of Rodríguez-Marek et al. (2001).

Table 6.1: Geotechnical seismic site class categories proposed by Rodríguez-Marek et al. (2001).

Site	Description	Comments
A	Hard Rock	Hard, strong, intact rock; $v_s \geq 1500$ m/s
B	Rock	Most “unweathered” California Rock cases ($v_s \geq 760$ m/s or < 6 m of soil).
C-1	Weathered/Soft Rock	Weathered zone > 6 m and < 30 m, ($v_s > 360$ m/s increasing to > 700 m/s).
C-2	Shallow Stiff Soil	Soil depth > 6 m and < 30 m
C-3	Intermediate Depth Stiff Soil	Soil depth > 30 m and < 60 m
D-1	Deep Stiff Holocene Soil (either Sand or Clay)	Soil Depth > 60 m and < 200 m. Sand has low fines content (< 15 %) or nonplastic fines (Plastic Index < 5). Clay has high fines content (> 15 %) and plastic fines (Plastic Index > 5).
D-2	Deep Stiff Pleistocene Soil (Sand or Clay)	Depth > 60 m and < 200 m
D-3	Very Deep Stiff Soil	Depth > 200 m
E-1	Medium Thickness Soft Clay	Thickness of soft clay layer 3-12 m
E-2	Deep Soft Clay	Thickness of soft clay layer > 12 m
F	Potentially Liquefiable Sand or Peat	Holocene loose sand with high water table ($z_w \leq 6$ m)

Geotechnical laboratory cyclic testing of cohesive soils (Seed and Idriss, 1970; Seed and Sun, 1989; Idriss, 1990; Ansal et al., 2001) and granular soils (Menq, 2003) indicates that soils go under cycles of increasing and decreasing levels of shear strain (γ) during earthquake shaking. Depending on the maximum amplitude of γ , soil behavior can change the soil rheology from linear to elastic–plastic to plastic. Soils behave elastically at low cyclic γ levels in the linear range (1×10^{-6} to $\sim 1.5 \times 10^{-4}$ %) because stress is directly proportional to γ and the constant of proportionality is the Young’s modulus. As cyclic γ amplitude increases, the soil enters the nonlinear–elastoplastic range ($\sim 1.5 \times 10^{-4}$ to 1×10^{-2} %), and with increasing γ amplitude the soil enters the nonlinear range (1×10^{-2} to ≥ 1.0 %) behaving plastically (Ansal et al., 2001; Menq, 2003). Laboratory measurements also reveal both a progressive decrease in normalized shear modulus (G/G_{max}) and a progressive increase in damping ratio (ξ) both with increasing cyclic γ amplitude during the duration of seismic loading. Such strain-dependent changes in material properties tend to reduce the amplitudes of short-period ground motions and to move the period of the resonance of the soil layer to longer periods (Somerville and Moriwaki, 2003). Further, hard-rock (bedrock) also presents a progressive decrease in G/G_{max} and a progressive increase in ξ both with increasing cyclic γ amplitude during earthquake shaking; however, at a much smaller amplitude (0.1 to ~ 5 %) compared to soil deposits (Chandler et al., 2005a, 200b, 2006). G/G_{max} and ξ curves for rocks with various degree of stiffness are available and have been verified successfully (Chandler et al., 2005a).

In the present study, the adopted G/G_{max} curves and ξ curves for cohesive soils, granular soils, and bedrock (i.e., weathered and unweathered) are taken from the literature and shown in Figure 6.1. The adopted G/G_{max} curves and ξ curves are used extensively for estimating

seismic site-response in deep soils deposits (≤ 200 m). The ξ curves for fine-grained sands and clays are essentially equal, but field data indicates that the strength (Zangger, 1993) and v_s (Hinojosa-Prieto and Hinzen, 2015) are different due to in-situ confining pressure and geologic age. The soil thickness in the Argive Basin can reach up to 200 m near the coastline and thins landwards to approximately 100 m (Karastathis et al., 2010a, 2010b; Karmis et al., 2010; Hinojosa-Prieto and Hinzen, 2015). The effect of increasing in-situ confining pressure in very deep soil deposits (≥ 200 m) results in lesser G/G_{max} degradation at a given cyclic shear strain and a decrease in the ξ due to sediment compaction (Hashash and Park, 2001). Therefore, the adopted G/G_{max} curves and ξ curves for the regolith layers in the Argive Basin are appropriate for the present study.

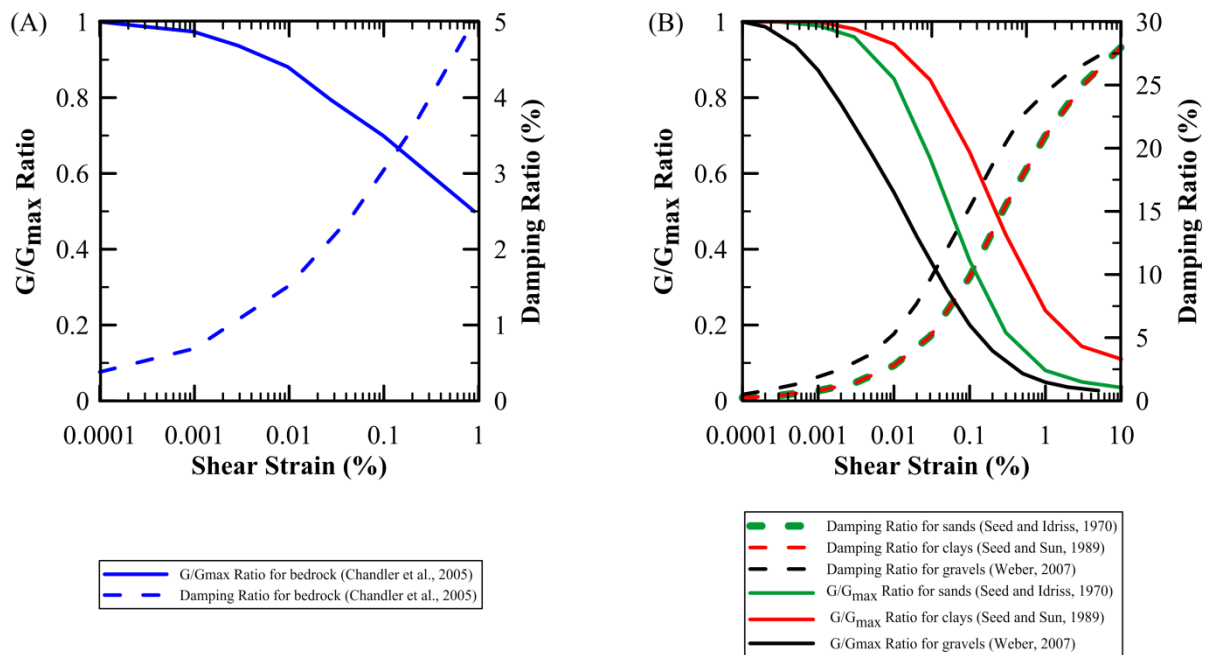


Figure 6.1: Shear modulus (G/G_{max}) curve and damping ratio (ξ) curve as a function of increasing shear strain (γ) for (A) bedrock and (B) soils adopted in the present Equivalent-Linear model.

6.2 1D Forward Modeling of Local Site Effects with the Equivalent-Linear Model

One-dimensional (1D) site-response analysis is a common practice in geotechnical earthquake engineering. The goal of a site-response analysis is to estimate nonlinear cyclic response of soils with either a nonlinear model or with an approximation using the widely accepted Equivalent-Linear model (Seed et al., 1969; Kramer, 1996; Zhang and Zhao, 2009; Hashash et al., 2010). A 1D site-response analysis solves the problem of horizontally polarized vertically propagating shear waves with planar wave fronts from the bedrock (i.e., elastic half-space) into horizontally layered soils with frequency independent damping (Seed et al., 1969; Satoh et al., 1995; Kramer, 1996; Hashash and Park, 2002; Park and Hashash, 2004; Chandler et al., 2006; Hashash, 2014). A 1D site-response analysis considers the wave modification properties of layered, damped soil deposits overlying weathered/unweathered elastic bedrock (Kramer, 1996; Meng, 2007). Seismic wave modifications that occur in weathered bedrock and weathered ridges are important for modeling seismic site effects (Steidl et al., 1996; Chandler et al., 2005a, 2005b, 2006; Robinson et al., 2006; Narayan and

Kumar, 2015). A 1D site-response analysis can capture most essential aspects of surface ground response (Kramer, 1996); however, it cannot model slopping, irregular ground surfaces, basin effects, topographic effects, and embedded geologic structures which are apt for two-dimensional (2D) or three-dimensional (3D) models. Hashash et al. (2010) provides an up to date summary of 1D nonlinear site-response analysis. The use of 1D models from sedimentary basins with a width/depth ratio (WDR) ≥ 6 are considered valid for a 1D seismic site-response analysis (Zhang and Zhao, 2009). The width and the depth of the Argive Basin varies from 12 to 17 km and ≤ 0.200 km, respectively, corresponding to a $60 < WDR < 85$. Under these criteria, the present 1D site-response analysis is appropriate with the use of 1D layered, damped soil models over heterogeneous elastic bedrock (e.g., half-space).

The nonlinear–elastic stress-strain behavior of regolith can be modeled numerically with the Equivalent–Linear site-response analysis method, which is an approximation of the cyclic nonlinear model (Robinson et al., 2006) and is referred herein as the EL model. The EL model was proposed by Seed and Idriss (1969) to perform seismic site response analysis in the frequency domain. Frequency domain methods solve the wave propagation equation and are widely used approaches to calculate local site effects due to their robustness, simplicity, and low computational cost (Kramer, 1996; Park and Hashash, 2004; Hashash et al., 2010). The EL model requires the v_s , density, G/G_{max} curve, ζ curve, and thickness of each layer comprising the 1D regolith column under consideration. The EL model provides satisfactory results when compared with both empirical field data (Robinson et al., 2006; Hashash and Park, 2002; Hashash et al., 2010; Hashash, 2014; Hinzen et al., submitted) and numerical modeling (Zhang and Zhao, 2009; Zhao et al., 2009; Zhao and Zhang, 2010; Hinzen et al., submitted). The EL model has been verified extensively through the comparison of recorded versus predicted ground surface acceleration time histories and acceleration response spectrum (Seed and Idriss, 1969; Idriss, 1993; Satoh et al., 1995; Robinson et al., 2006; Hashash et al., 2010). However, some restrictions of the EL model include the inability to capture the full range of cyclic behavior of soil, including modulus degradation due to number of loading cycles (limited accuracy to cyclic shear strains of up to $\sim 1\%$), soil failure, excess of pore water generation and dissipation, permanent displacements of soil, and changes in soil stiffness that occur during earthquake shaking. These important aspects of soil behavior can be captured by the true nonlinear model through hysteretic loading-unloading cycles in the soil model using equations of motion and equilibrium solved in discrete time increments in the time domain (Kramer, 1996; Hashash and Park, 2001; Stewart et al., 2008). Moreover, these aspects are necessary when a site response analysis is tailored to assess the likelihood of soil liquefaction; otherwise the EL model is a good approximation to model the nonlinear–elastic stress-strain behavior of a regolith column.

The computed strain level depends on the values of the EL model properties. An iterative procedure is implemented to ensure that the material properties used in the analysis are compatible with the computed strain levels in all layers of the 1D model (Kramer, 1996; Hashash et al., 2010). The iterative process proceeds as follows: (1) first it assigns an initial value for G/G_{max} and ζ in each material layer by reading the first value of their respective $G(\gamma)$ and $\zeta(\gamma)$ curves; (2) then, for the selected G/G_{max} and ζ , it calculates the strain time

histories for each layer for the given seismic rock-site motion; (3) next, it obtains the maximum strain values for each layer and calculates the corresponding effective shear strain (i.e., 65% of peak strain); (4) from the above calculated effective shear strain, new pair of G and ζ are selected for the next iteration using the degradation curves; however the G/G_{max} and ζ value remains constant while stepping through the entire earthquake record during that iteration; (5) steps 2 to 4 are repeated until the maximum difference between computed G/G_{max} and ζ values in two successive iterations are less than a user-specified threshold (5%); in other words, when convergence is reached. The term effective strain refers to 65% of the earthquake induced maximum shear strain in a soil layer undergoing seismic loading (Kramer, 1996).

Forward modeling of the Equivalent–Linear 1D seismic site-response is completed with the set of MATLAB routines called *SUA* (Robinson et al., 2006). *SUA* enables investigating how uncertainties in the input data (i.e., v_s , density, and layer thickness) affect the response functions (i.e., transfer function and frequency-dependent amplification). This part is handled by specifying a number of velocity models to be created (e.g., 50 in this case study) from a user-specified normal distribution (i.e., mean and standard deviation) of slopes, intercepts and unit thicknesses. *SUA* also allows the use of an average v_s or a vertical v_s gradient for each material layer. Robinson et al. (2006) demonstrate successfully *SUA*'s ability to estimate seismic site-response and associated uncertainty for a probabilistic seismic hazard analysis. The reader is referred to the work of Robinson et al. (2006) for a detailed description of the theoretical solution of the wave equation, development of the v_s models, and computation of the response functions implemented in the *SUA* code. *SUA*'s input data consists of an excitation record (i.e., acceleration time-history in units of g) and a modeling site under investigation. The acceleration record can be an empirical or synthetic earthquake record, or an analytic signal. This case study uses several synthetic earthquake records and one analytic signal, all previously discussed in chapter 5. Each modeling site is represented by a site-specific 1D geologic model (i.e., regolith). Each layer of the 1D model has an assigned thickness (in m), v_s (in m/s), density (in g/cm^3), G/G_{max} curve (ratio), and ζ curve (in %).

The forward modeling of the Equivalent–Linear 1D seismic site-response was made within a frequency band from 0.1 to 20 Hz and in two ways: the first case uses corresponding average v_s for each material layer in the regolith column while the second case uses the corresponding linear v_s gradient for the same material layer; however, both simulations keep the other input parameters unchanged. The first and second cases are referred herein as “model A” and “model B”, respectively. The adopted 1D v_s –depth models for each modeling soil-site and rock-site at Tiryns, Midea, and the area between them are shown Figures D1, D2, and D3 in Appendix D, respectively. Several modeling sites (total of 63) are located inside and outside Tiryns and Midea fortification walls, and the area between them, as shown in Figures 6.2, 6.3, and 6.4, respectively. In general, a total of 45 modeling sites outside Tiryns and Midea comprise a soil column underlain by weathered bedrock in turn underlying the elastic half-space (e.g., unweathered bedrock). A total of 18 modeling rock-sites on the hills of Tiryns and Midea comprise weathered/fractured bedrock underlain by unweathered bedrock (e.g., elastic half-space). The geologic descriptions of the soils and bedrock at Tiryns and Midea

were discussed in chapter 3, and the stratigraphy around Tiryns, Midea, and the area between them was shown in Figures 4.15-4.17.

Following the geotechnical site classification scheme of Rodríguez-Marek et al. (2001), the subsurface conditions outside both Tiryns and Midea citadels are dominated by “shallow stiff soils” (soil-site class C-2, total of 34) with a minor presence of both “intermediate depth stiff soils” (soil-site class C-3, total of 4) and “deep stiff Pleistocene soils” (soil-site class D-2, total of 7) (see Table 6.1). The geotechnical site category for all the rock-sites inside the fortification walls of Tiryns and Midea correspond to weathered rock (rock-site class C-1, total of 18) following the same site classification scheme. A list of the geotechnical site classes of individual modeling soil-sites and rock-sites is provided in Appendix E (Table E6.2). The general Equivalent–Linear modeling workflow is shown in Figure 6.5. Figure 6.6 shows examples of a soil-site and a rock-site simulated in the adopted four ways (i.e., with both the average v_s and a v_s gradient and with input signals calculated with both the Stochastic and the Green’s function methods).

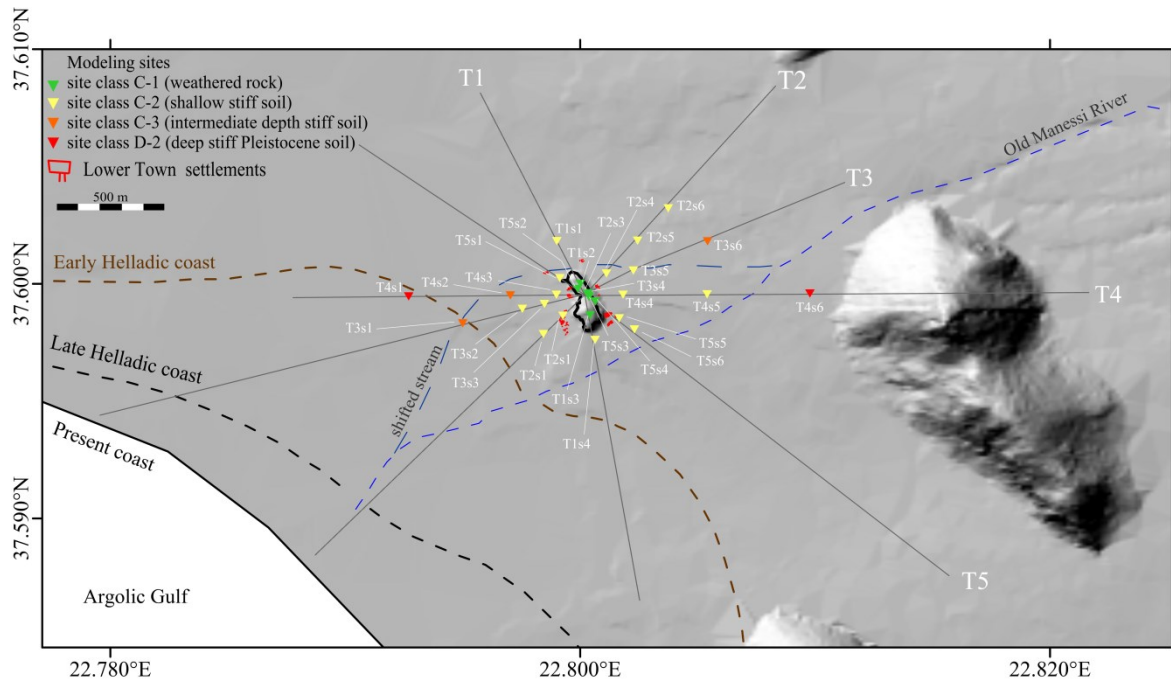


Figure 6.2: Distribution and class category of the modeling sites along corresponding profiles (black line) for Tiryns. Early and Late Helladic coastlines, shifted stream, and old Manessi River taken from Zangger (1993, 1994). Lower Town settlements and outline of Tiryns citadel taken from Maran (2004b).

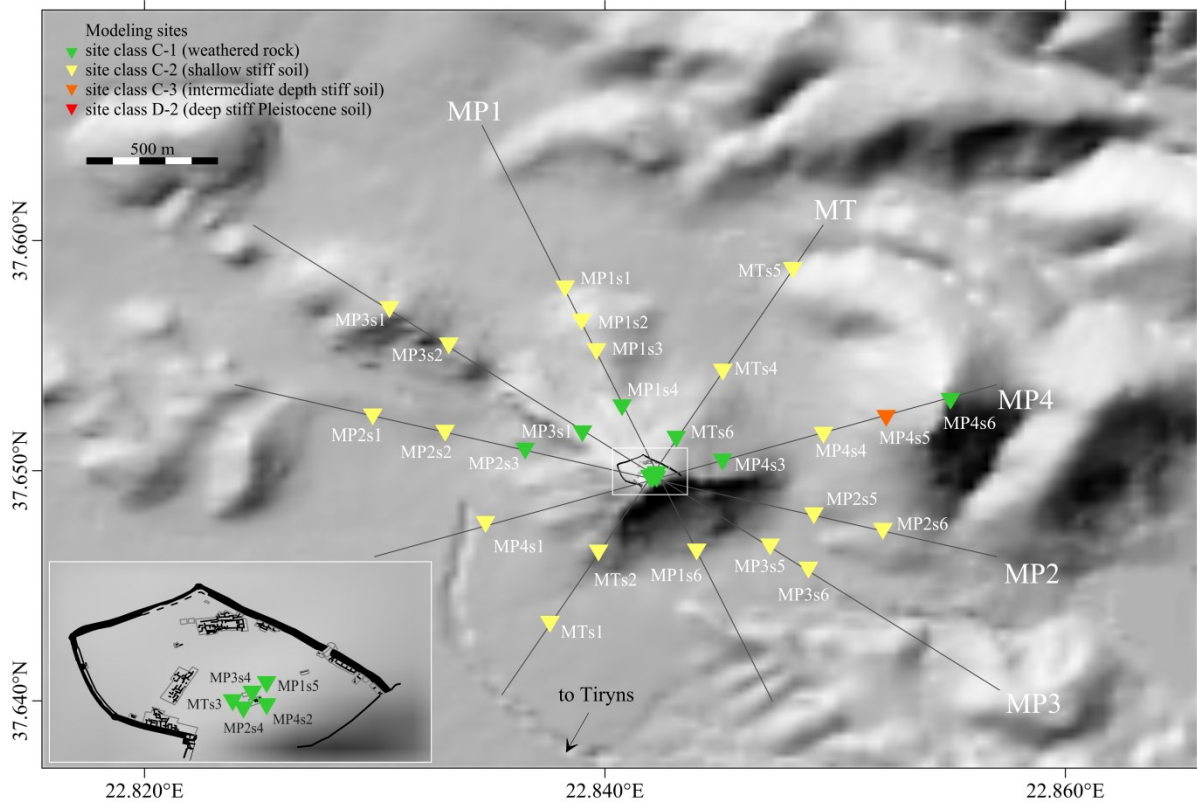


Figure 6.3: Distribution and class category of the modeling sites along corresponding profiles (black line) for Midea. Inset map corresponds to the archaeological plan of Midea taken from Demakopoulou (2012).

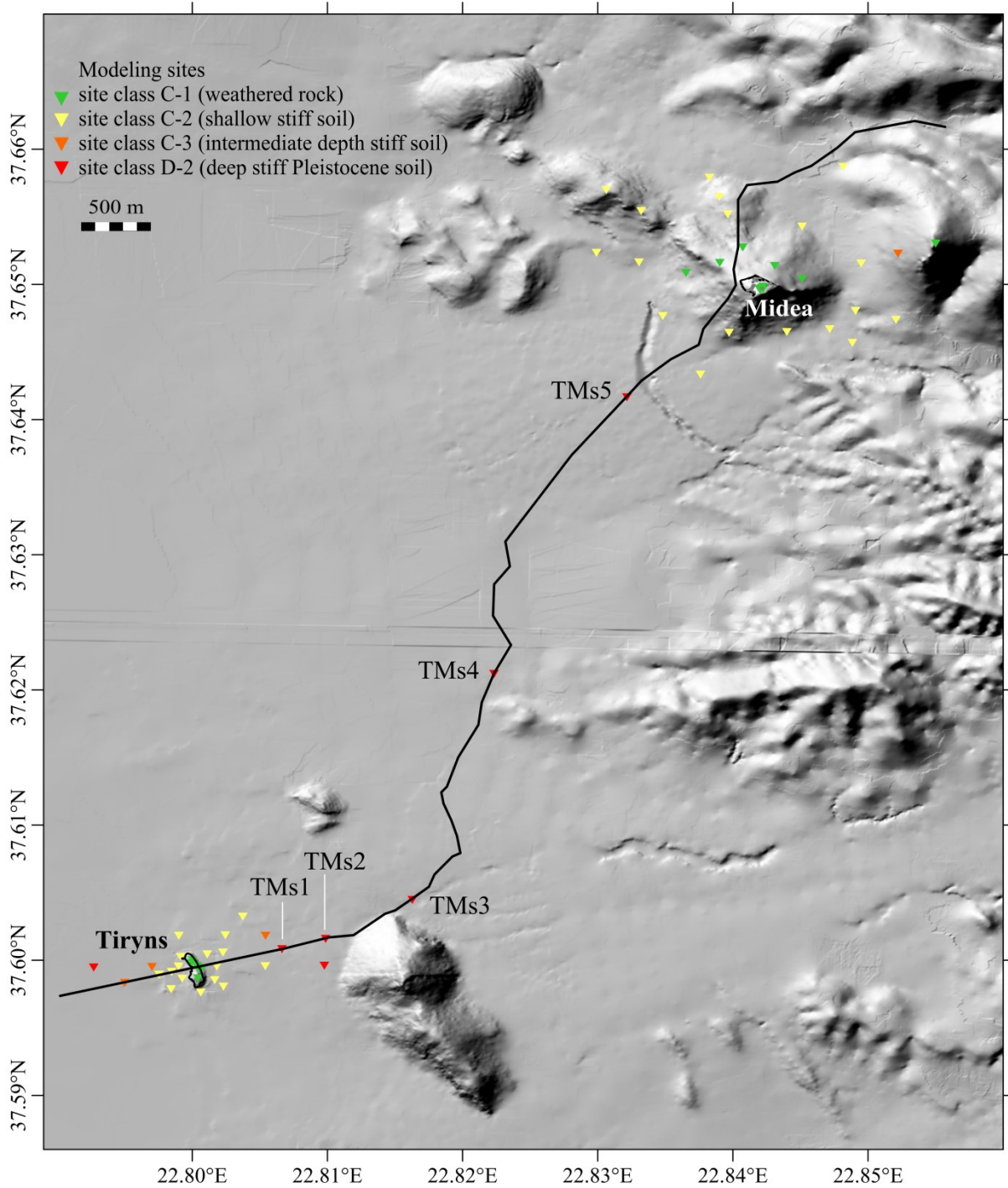


Figure 6.4: Distribution and class category of the modeling sites (labeled TMs1-TMs5) along the Tiryns-Midea profile (black line). Modeling sites from Tiryns and Midea shown for comparison.

Workflow of Forward Modeling of 1D Seismic Site Effects

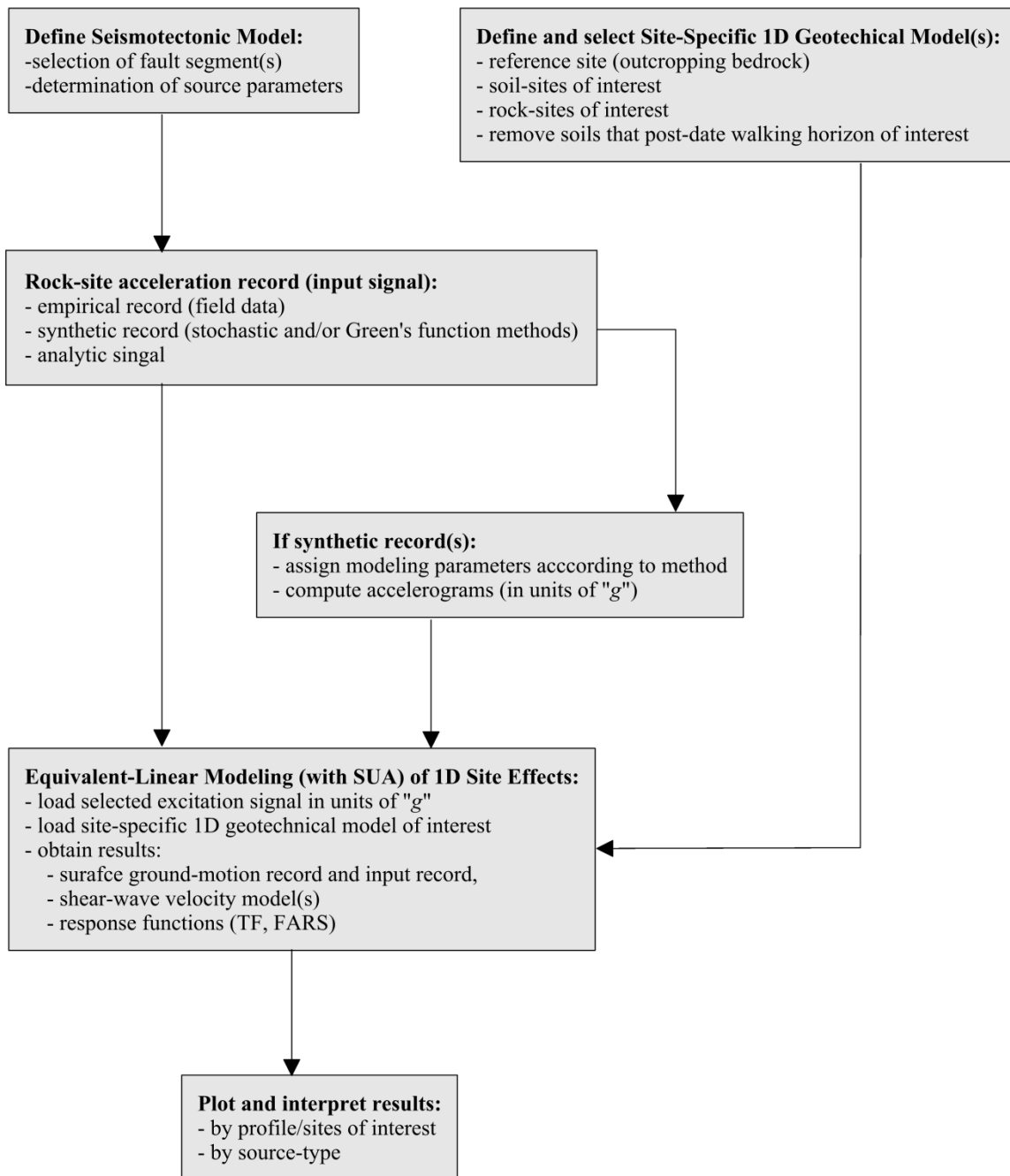


Figure 6.5: Schematized workflow of the forward modeling of 1D seismic site effects adopted in this study.

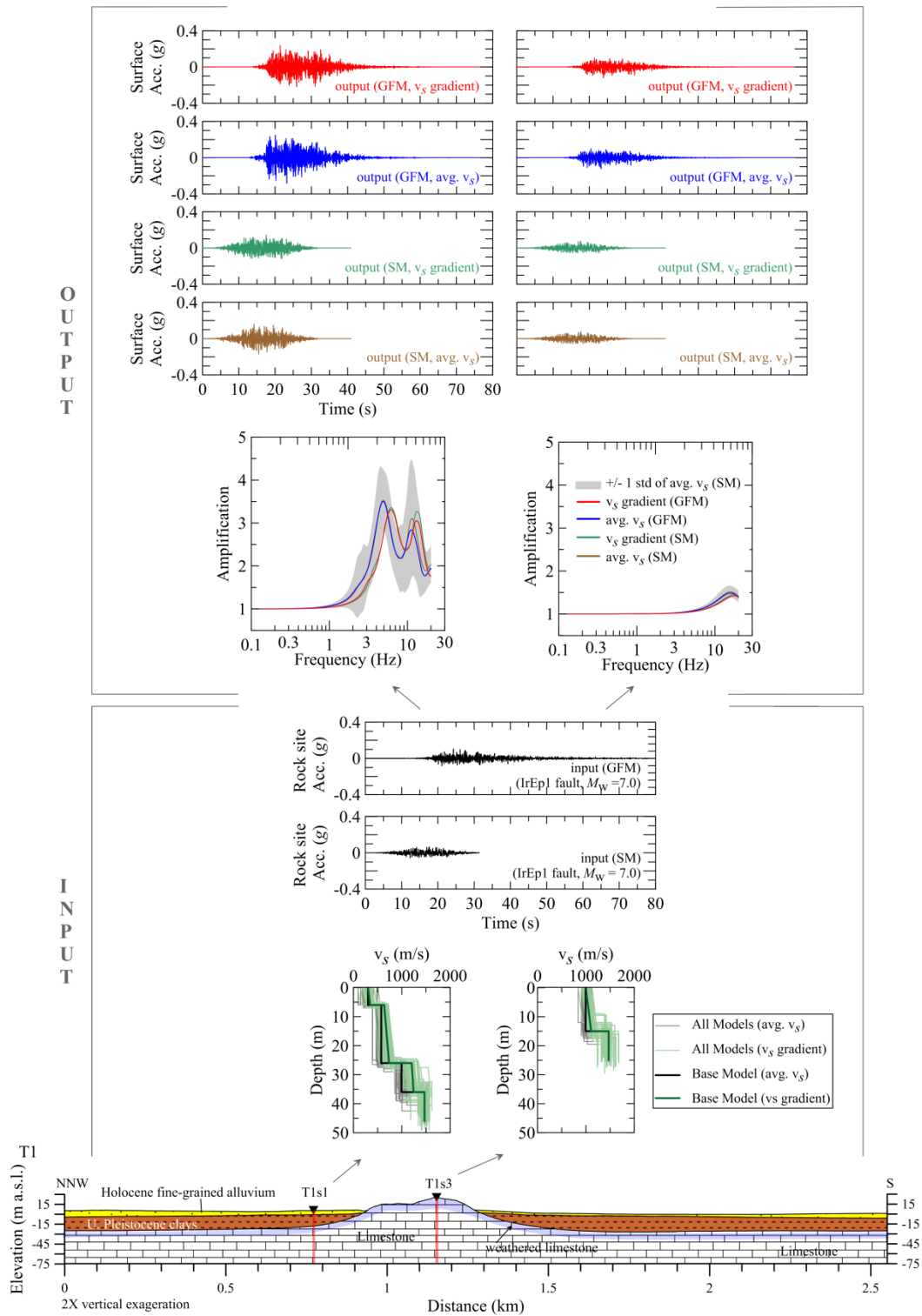


Figure 6.6: Example of four individual simulations using the Equivalent–Linear model for two 1D site-specific cases from Tiryns: a soil-site (T1s1, class C-2) and rock-site (T1s3, class C-1) highlighted by the vertical red bars located along the geologic profile. For one simulation, the input consists of one modeling site (e.g., T1s1 or T1s3) represented in two ways: by an average v_s model and a v_s gradient. Each case is accelerated twice: once with a synthetic accelerogram calculated with the Stochastic method (SM) and then with another synthetic accelerogram calculated with the Green’s function method (GFM). The output yields a computed site-specific surface acceleration record and an amplification function. The synthetic accelerograms correspond to a local strike-slip earthquake ($M_w = 7.0$) triggered by the Iria-Epidaurus1 fault segment (IrEp1) located in the IEST source region.

6.2.1 Results and Interpretation

The results concerning both the calculated amplification factors and surface accelerations at all modeling sites are grouped in four geotechnical site categories corresponding to site class C-1, C-2, C-3, and D-2 following the site classification scheme of Rodríguez-Marek et al. (2001). A side-by-side class comparison of amplification factors shows general trends and differences (Figures 6.7A-H). This is also the case for the estimated surface accelerations (Figures 6.8A-H).

6.2.1.1 Variability of Amplification Factors

For a given site the calculated amplification factor is virtually identical when using a synthetic accelerogram made with either the Stochastic or the Green's function method. This is shown in individual frequency-dependent amplification response function plots for an example profile for Tiryns, Midea, and the Tiryns-Midea profile (Figures E1 to E3 in Appendix E). Further, the use of the average v_s (model A) or the vertical v_s gradient (model B) for each material layer has a noticeable influence on the amplification level and the frequency in which it occurs, as it is expected. Particularly, the use of model A typically yields slightly higher amplification factors at a slightly lower frequency compared with amplification factors computed with the use of model B, as shown in the Tiryns example (Figure 6.6; see Figures E1 to E3 in Appendix E for additional examples).

The soil–bedrock interface deepens gradually outward relative to the Tiryns and Midea ridges. This translates into a systematic change in the geotechnical site class category (Figures 6.2-6.4 and Table 6.1); consequently the amplification peak shifts gradually towards lower frequencies as shown in Figures 6.7A-H. Class C-1 sites correspond exclusively to any modeling site located on outcropping weathered-unweathered bedrock of Tiryns and Midea. The C-1 class sites of Tiryns and Midea yield the lowest amplification factors (≤ 2) in the frequency range of ~8-20 Hz, as displayed in Figures 6.7A-B. Conversely, soil-sites of class C-2, C-3, and D-2 yield amplification factors between 2 to 4.4, but at systematically narrowing frequency bands, as illustrated in Figures 6.7C-H. For the case of the soil-sites, the seismic response is interpreted to be caused by the outward gradual thickening of the Late Neogene–Quaternary soil cover and its textural vertical and lateral heterogeneity. In general, the fine-grained soil-sites of Tiryns yield the highest levels of soil amplification (Figures 6.7C, E, and G) because they have a lower shear strength and are rich in clays/silts/muds compared to the stiffer granular (coarse-grained) soil-sites around Midea for which fine-grained detritus is only present in the matrix.

Sites of class C-1 (e.g., weathered rock-sites) from Tiryns and Midea are located inside the fortifications wall. The C-1 class rock-sites show the lowest amplification factors in comparison with soil-sites whether numerically modeled with model A or model B. Figure 6.7A depicts that the rock-sites from Tiryns define a tight cluster corresponding to amplification factors from 1.3 to 1.6 within a frequency band of 15.5-20 Hz. Conversely, the rock-sites from Midea show a marginally wider cluster with similar amplification factors (1.0 to 1.5), but within a noticeably wider frequency band (7.8-15.5 Hz) (Figure 6.7B). The difference in the shape of the clusters can be explained by the contrasting underground

geologic conditions that characterize each highly weathered and tectonically fractured hard-rock hill (e.g., only karstic limestone at Tiryns and karstic limestone thrust on continental flysch deposits at Midea). For class C-1 rock-sites, the most influencing parameter is the v_s structure of the hard-rock ridge, which is entirely controlled by the degree and thickness of the weathering horizon and the degree of bedrock heterogeneity. Particularly, less amplification occurs when the bedrock is composed of weathered-unweathered flysch and amplification commonly increases in areas where bedrock consists of both limestone and flysch (see Figure E2 in Appendix E for different examples).

Soil-sites of class C-2 from Tiryns and Midea define a remarkably distinctive amplification–frequency cluster of points, broader for Tiryns than for Midea (Figures 6.7C-D). The discrepancy in the clusters can be explained again by the contrasting site-specific geologic conditions outside the citadels, including the shear strength and texture of soils, the varying soil thickness (≤ 30 m), and the weathering profile and composition of the bedrock. For instance, the higher amplification factors observed in all the modeling sites of Tiryns are attributed to the dominant presence of fining-downwards and less stiff cohesive soils (e.g., fine-grained sand passing into chaotic mix of clays, silts, and muds) of Upper Pleistocene–Holocene age. Conversely, the lower amplification factors observed in all Midea sites are imposed by the coarser, stiffer, and marginally older (Upper Pliocene–Quaternary) soils that flank the Midea ridge. Figures 6.7C-D show that the range of amplification factors for Tiryns is noticeably greater than for Midea despite that they occur within a similar frequency range. Particularly, the results from model A and model B yield marginally different amplification peaks for both Tiryns (2.6 to 4.4 at 3.8-20 Hz and 2.8 to 4.4 at 5.1-20 Hz, respectively) and Midea (2 to 2.7 at 4.8-20 Hz and 2 to 2.5 at 6.3-20 Hz, respectively).

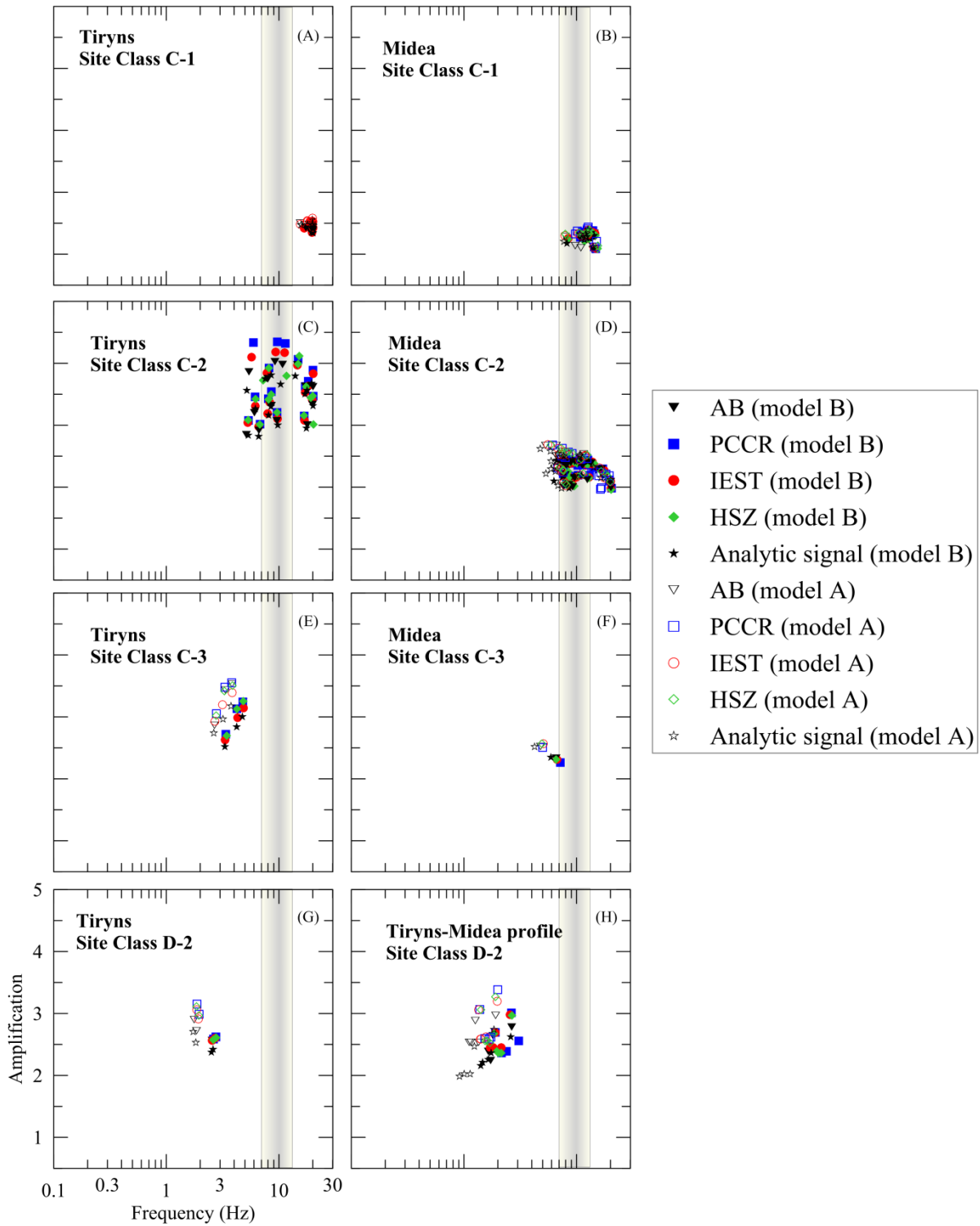


Figure 6.7: Summary of resulting amplification peaks plotted against frequency (Hz) for all modeling sites from Tiryns, Midea, and along the Tiryns-Midea profile using input accelerograms computed with the Green’s function approach. Results are grouped according to site category and sorted by v_s model (models A or B) and seismogenic sources: Argive Basin (AB) and Patras–Corinth Continental Rift (PCCR), Iria–Epidauros Sinistral Transform fault system (IEST), and Hellenic Subduction Zone (HSZ) are source regions with extensional, left-lateral strike-slip, and compressional faulting earthquakes, respectively. Labels in the upper left-hand corner indicate the archaeological site and the site class category. The vertical bar centered at 10 Hz (with a ± 3 Hz uncertainty) indicates the hypothesized fundamental frequency of a one-storey height Mycenaean building.

In terms of potential coseismic structural damage, all the Mycenaean structures (i.e., Cyclopean wall and rooms/buildings) that once stood on the outcropping bedrock formation were erected on highly to moderately weathered-unweathered and fractured hard-rock (Hinojosa-Prieto and Hinzen, 2015); therefore, any site within the hill of Tiryns and Midea classifies as class C-1 rock-site under the adopted classification scheme. On the other hand, the contemporaneous settlements of the Lower Town of Tiryns were founded on shallow young soils deposited on highly to moderately weathered-unweathered and fractured limestone bedrock (Hinojosa-Prieto and Hinzen, 2015). Current excavation data outside Tiryns is limited; therefore, the surface extent of the Lower Town and the soil conditions where it was developed yet remains poorly estimated. However, available upfront geoarchaeological (Zangger, 1993, 1994) and archaeological (Maran, 2004b, 2010) excavation data outside Tiryns show that the Lower Town settled in a small zone characterized by class C-2 soil-sites, as demonstrated in Figure 6.2. The geotechnically classified modeling sites coupled with both the computed amplification factors and the surface ground-motions have implications for the dynamic behavior of both the Cyclopean wall circuit of Tiryns and Midea and all Mycenaean structures inside and outside the citadels. For instance, the fundamental frequency of most Mycenaean rooms/buildings is estimated at 10 ± 3 Hz (e.g., assuming buildings were one-storey height). The one-storey height building assumption stems from two facts: (i) the preservation and (ii) current archaeological data of Mycenaean architecture fails to provide adequate architectural and structural information necessary to better estimate the fundamental period/frequency of specific structures. This fundamental frequency intersects the amplification–frequency cluster of class C-1 sites of the Tiryns and Midea ridges, which had buildings and fortification walls, as well as C-2 sites (Figures 6.7B-C) of the Lower Town of Tiryns which had the buildings of the peasants. This implies that some Mycenaean structures might have been in resonance during the dynamic loading of the ground surface at the corresponding sites. Conversely, this aspect is not observed at rock-sites (class C-1) from Tiryns. The lack of excavated Mycenaean structures outside the Midea hill (i.e., class C-2 soil-sites) hampers structural implications between the calculated amplification–frequency cluster and the assumed fundamental frequency of 10 ± 3 Hz. Soils-sites of class C-3 and D-2 are relatively rare near the citadels of Tiryns and Midea in comparison to class C-2 sites (see Table 6.1 and Figures 6.2-6.4). Nonetheless, class C-3 and D-2 sites become more abundant farther away from the citadels (see Figures 3.3 and 3.4); therefore, these soil-sites define zones of intermediate to deep soil conditions, respectively, relative to the location of the citadels and have implications for the Mycenaean chamber tombs scattered around the Argive Basin. The implications for the potential dynamic behavior of Mycenaean structures are further discussed in the next chapter.

The class C-3 soil-sites from both citadels have a distinguishing amplification–frequency cluster of points (Figures 6.7E-F). The amplification factors fluctuate more for sites at Tiryns (2.5 to 3.6) than for sites at Midea (2.3 to 2.6), but the frequency range in which they occur is wider for Midea (4.2-7.2 Hz) than it is for Tiryns (2.6-4.9 Hz). The amplification–frequency cluster for class C-3 sites from Tiryns and Midea are tighter compared to the clusters of class C-2 sites. This is due to the fact that class C-3 sites have a thicker soil column (30 to 50 m thick) relative to class C-2 sites (≤ 30 m) which is in turn due to the deepening of the local

bedrock formation, the Late Neogene–Quaternary depositional, and the tectonic history of the Argive Basin (cf. Hinojosa-Prieto and Hinzen, 2015). Alternatively, the observed amplification–frequency cluster for class C-3 sites could be linked to the smaller count of class C-3 sites (total of 4) relative to class C-2 sites (total of 34).

Soil-sites of class D-2 are also few outside Tiryns and along the Tiryns-Midea profile (see Table 6.1) and non-existing in the soils flanking the Midea hill, at least within the population of modeling sites under examination. The class D-2 sites from Tiryns define a tight cluster corresponding to amplification factors between 2.4 to 3.1 within a narrow frequency band of 1.8-2.8 Hz (Figure 6.7G). Conversely, class D-2 sites along the Tiryns-Midea profile depict a slightly broader cluster of points corresponding to amplification factors from 2 to 3.4 within a wider frequency band of 1-3 Hz. The differences in cluster patterns are attributed to the contrasting soil thickness west and east of Tiryns (~50 and ~100 m thick, respectively) and also to the changing nature of the soils beyond 1 km distance northeast of Tiryns (see Figures 3.1, 4.15, 4.17). At this location, less stiff cohesive soils pass rapidly into stiffer granular soils, a textural change simply related to the sedimentary architecture of the alluvial fan. Particularly, the cohesive soils are dominated by a ~10 m thick layer of Holocene alluvium composed of chaotically interbedded, poorly sorted sandy gravel, silts, sandy silts, sandy clays, minor pebbly gravel–silts, and lesser silty sands passing into a 55 to 90 m thick layer of well-consolidated Upper Pleistocene clays, silts, and muds all deposited unconformably on weathered-unweathered karstic limestone. On the contrary, the granular soils are dominated by ~100 m thick sequence of torrential very-coarse and pebbly to coarse conglomerates and lesser sands of Pleistocene–Holocene age deposited unconformably on weathered-unweathered continental flysch deposits (mainly) and limestone.

Soil-sites of class C-3 and D-2, when dynamically loaded by local extensional and transform faulting earthquakes, produce similar amplification factors that are noticeably higher than the amplification factors produced when dynamically loaded by subduction-related earthquakes. This is an effect of the ground-motion amplitude of the input signal, not of the earthquake type. This dynamic behavior is well expressed in the cohesive soils of Tiryns (Figures 6.7C-E) and is better seen in categories C-3 and D-2. This conclusion has also been reached by numerical modeling using the EL method and empirical strong motion data applied to a single-layer soft-soil (modeled as elastic) over a half-space (bedrock) (Zhao and Zhang, 2010). It is unclear if the stiffer and older granular soils exhibit the same dynamic behavior. The resulting amplification factors of weathered rock-sites (class C-1) and shallow stiff soil-sites (class C-2) seem less dependent on source-type, M_w , and source-to-site distance as shown by the constricted clusters of points (Figures 6.7A-B). In the case of the class C-1 site category, this stems in the fact that such rock-sites are comprised solely of hard-rock while the class C-2 sites are a combination of shallow weather and unweathered rock sealed by irregularly thick layered soils (≤ 30 m), as previously established by shallow and deep boreholes (see chapter 4) and shallow seismic field data (Karastathis et al., 2010a, 2010b; Hinojosa-Prieto and Hinzen, 2015).

6.2.1.2 Estimated Surface Ground-Motions and Intensity Values

The resulting surface ground-motions from each analyzed zone vary noticeably due to the nature of the site-specific regolith column (e.g., modeling site), the site-to-source distance, and the M_w . The estimated PGA (in g) plotted against M_w is shown in Figures 6.8A-B for all modeling sites and sorted by seismogenic source and v_s model (i.e., v_s models A and B). Figures 6.8A-B illustrate that seismic hazard for the vicinities of Tiryns and Midea mainly comes from nearby moderate to strong extensional crustal earthquakes on normal faults within the Argive Basin (i.e., closest seismogenic source to the modeling sites). The calculated PGA values exceed the mean PGA value for the zones of Tiryns and Midea, and the Argive Basin corresponding to 0.31, 0.40, and 0.50 g according to a recent probabilistic seismic hazard assessment (PSHA) for Greece (Tselentis and Danciu, 2010a) that includes a deaggregation of seismic sources (Tselentis and Danciu, 2010b). The deaggregation results for PGA indicate that the seismic hazard for the city of Nafplion (i.e., 3.5 km south of Tiryns) is from local (< 20 km) and moderate earthquakes ($M_w < 6.3$) (Tselentis and Danciu, 2010b). Moreover, this supports the idea that nearby (< 20 km) extensional crustal earthquakes within the Argive Basin are critical potential candidate sources for causing significant surface ground-motions, e.g., above the calculated mean PGA value around Tiryns (0.31 g) and Midea (0.40 g) as denoted in Figures 6.8A-B. Further, some seismic hazard for certain soil-sites around Tiryns and Midea can come from nearby strike-slip strong to major earthquakes and back-arc interface compressional major to great earthquakes from the IEST and HSZ, respectively, which can also induce PGA that exceed the aforementioned mean PGA of Tiryns and Midea at some sites. This is the effect of adopting the average v_s in the equivalent-linear modeling as illustrated in Figure 6.8A. Conversely, this trend is only observed for some soil-sites near Tiryns, but not for soil-sites around Midea when using the vertical v_s gradient as demonstrated in Figure 6.8B. Finally, extensional strong earthquakes from the PCCR produce surface acceleration values that remain below the aforementioned values for Tiryns, Midea, and the Argive Basin regardless of the adopted v_s model (Figures 6.8A-B). Overall, the use of v_s models A and B in the equivalent-linear modeling of local site effects yields comparable results. This is attributed to the used of the field-measured v_s structure, which reveals a < 15 m weathered horizon in the local bedrock formation (Hinojosa-Prieto and Hinzen, 2015).

The wide range of the estimated PGA values for all the modeling sites shown in Figures 6.8A-B must be examined in terms of the adopted geotechnical site class category. This is an important step because the site class changes laterally relative to citadels of Tiryns and Midea and most Mycenaean buildings developed on site class C-1 and C-2. To serve this purpose, Figure 6.9 depicts the range of resulting PGA values for all modeling sites sorted by both site class category and acceleration source. In descending order, Figure 6.9 shows that the extensional crustal earthquakes from the AB produce the highest range of PGA values, followed by the IEST, and the PCCR. Particularly, the HSZ yields a broad range of PGA values for all site classes, which encloses the range of PGA values of the IEST and PCCR (Figures 6.9A-H), and is attributed to the contribution of several along-arc intraplate compressional earthquakes that have a long site-to-source distance (> 150 km) and back-arc interface compressional earthquakes underneath the Argive Basin. The range of calculated

PGA values for each class site category and for each seismogenic source modeled with v_s model B overlaps the range of PGA values modeled with v_s model A; however, v_s model A typically yields a wider range of PGA values although v_s model B commonly yields slightly higher PGA values principally for soil-sites. The resulting range of PGA values produced by the analytic signal (non-tectonic source) with v_s model A and B are also shown in Figure 6.9. These are rather narrow mainly due to the selected amplitude of 0.1 g.

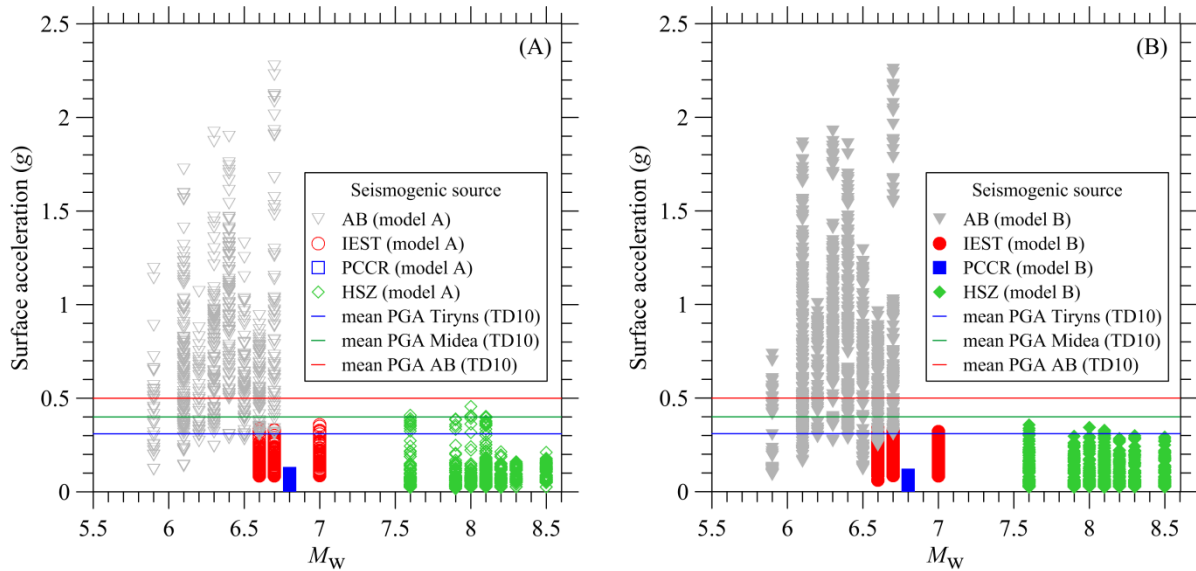


Figure 6.8: Summary of resulting maximum surface acceleration (in g) values plotted against M_w for all modeling sites using input accelerograms computed with the Green's function approach. Results are shown according to (A) average v_s (model A) and (B) vertical v_s gradient (model B), and seismogenic sources (AB, PCCR, IEST, and HSZ, as in Figure 6.7). The horizontal blue, green, and red lines correspond to the calculated mean PGA value around Tiryns, around Midea, and the Argive Basin, respectively, according to the results by Tselentis and Danciu (2010a) [TD10].

At class C-1 sites (e.g., weathered rock-sites), hypothetical moderate to strong local crustal extensional earthquakes ($5.9 < M_w < 6.7$) from the AB produce the highest range of PGA values for Tiryns and Midea relative to other seismogenic sources. The range of PGA values corresponds to ~0.2 to 1.0 and 0.1 to 1.2 g, respectively (Figures 6.9A-B). The discrepancy in the range of PGA values is due to the contrasting v_s structure within each hill. Some of the moderate to strong extensional crustal earthquakes produced PGA values, at certain modeling sites, that exceeded the mean PGA value for the vicinity of Tiryns (0.31 g) and Midea (0.40 g), and even that of the Argive Basin (0.50 g) (Figures 6.9A-B). This implies that, during the Mycenaean palatial period, such earthquakes (if they ever ruptured) were a hazard for the citadels of Tiryns and Midea and their fortification walls all erected on a class C-1 site zone. Moreover, strong to great extensional, strike-slip, and compressional earthquakes ($6.6 < M_w < 8.5$) outside the Argive Basin yield PGA values below the aforementioned 0.31 g and 0.40 g values (Figures 6.9A-B), therefore, it is unlikely they were a hazard for the citadels (if they ruptured). Indeed, distal sources within both the PCCR and HSZ (e.g., along-arc intraplate earthquakes) produce little seismic loading on weathered rock-sites from Tiryns (class C-1). Thus, only in such cases, the iterative procedure of the EL model does not converge. This is

because the applied shear strain is less than the minimum shear strain value (0.0001 %), hence, neither the first G/G_{max} nor the first ξ value can be calculated from the pre-assigned modulus reduction and damping curves, respectively. This explains the lack of data for the PCCR and the HSZ seismogenic sources in Figure 6.9A.

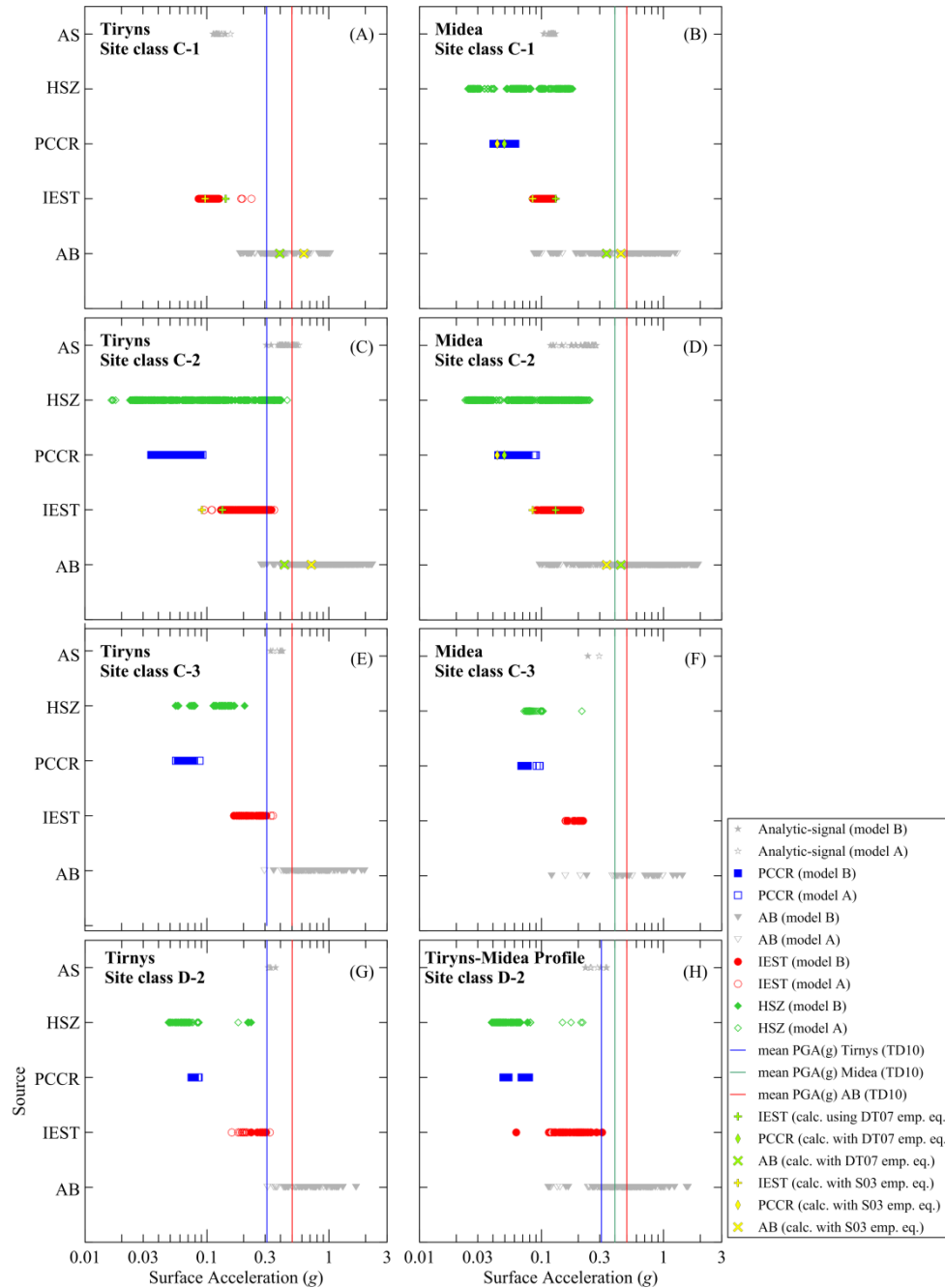


Figure 6.9: Summary of resulting surface ground-motions for all modeling sites from Tiryns, Midea, and along the Tiryns-Midea profile using input accelerograms computed with the Green’s function approach. Results are grouped according to site class category and sorted by v_s model (models A or B) and seismogenic sources (AB, PCCR, IEST, and HSZ), as in Figure 6.7). Labels in the upper left-hand corner indicate the archaeological site and the site class category. The blue, green, and red vertical lines correspond to the mean PGA values around Tiryns, Midea, and the Argive Basin, respectively, calculated by Tselentis and Danciu (2010a) [TD10]. The peak ground-motion values for crustal extensional and strike-slip earthquakes in A to D are calculated using the empirical equations of Skarlatoudis et al. (2003) [S03] and Danciu and Tselentis (2007) [DT07].

The resulting broad range of PGA values (0.30-2.30 g) for Tiryns' class C-2 sites exceed the mean PGA value (0.31 g) for the area of Tiryns, when the sites are dynamically loaded by moderate to strong extensional crustal earthquakes from the Argive Basin (Figures 6.8 and 6.9C). However, this pattern does not replicate entirely for class C-2 sites bordering Midea because of the wide range of PGA values (0.10-1.90 g) straddling the 0.40 g values (Figure 6.9D). More importantly, both the existence and fault-activity of these local normal faults is still uncertain, as discussed in chapter 5 (section 5.1.1), particularly the ones traversing the Late Neogene–Quaternary sediments of the Argive Basin which produce high accelerations (e.g., $PGA > 1.0$ g). Surface acceleration induced by certain major to great ($7.9 < M_w < 8.5$) interface and intraplate earthquakes (i.e., events HSZ-1 to HSZ-4) and by strong to major ($6.6 < M_w < 7.0$) strike-slip crustal earthquakes (Figure 6.9C) produces PGA values > 0.31 g for few class C-2 sites around Tiryns. Yet, the 0.40 g value of Midea is not surpassed in response to strong to great crustal earthquakes from Argive Basin, as shown in Figure 6.9D. This dynamic behavior is due to the stiffer and older nature of the granular soils around Midea. Strong extensional crustal earthquakes (M_w 6.8) from the PCCR yield PGA values significantly below the mean PGA value for the localities of Tiryns and Midea (Figures 6.8C-D). The results of this deterministic approach strongly suggest that local (< 20 km) moderate to strong extensional and strike-slip crustal earthquakes would have been a hazard for class C-2 sites during the Mycenaean palatial period. This is in full agreement with the PSHA for Greece (Tselentis and Danciu, 2010a, 2010b). The Lower Town settlement developed on class C-2 sites flanking the Tiryns hill. Consequently, such local earthquakes would have been a probable hazard for the Lower Town community contemporaneous with Mycenaean Tiryns.

Figures 6.9E-F illustrate that all class C-3 sites around Tiryns and some sites around Midea exceed their corresponding mean PGA values of 0.31 g and 0.40 g, respectively, when accelerated by hypothetical moderate to strong local crustal extensional earthquakes from the Argive Basin (Figures 6.8 and 6.9E-F). Under such seismogenic sources, the resulting range of PGA values corresponds to 0.30 to 2.0 and 0.16 to 0.98 g for Tiryns and Midea, respectively, as denoted in Figures 6.9E-F. Further, only a few class C-3 sites east of Tiryns surpass the 0.31 g value in the event of strong to major local crustal strike-slip earthquakes from the IEST fault system. Yet, the PGA values for the sites around Midea remain below the 0.40 g value (Figures 6.9E-F), due to the stiffer nature of the granular soils flanking the Midea hill. None of the class C-3 sites around Tiryns and Midea citadels exceed their corresponding mean PGA value when the ground surface is accelerated by strong extensional crustal earthquakes (e.g., M_w 6.8) from both the PCCR and major to great interface and intraplate earthquakes ($7.6 < M_w < 8.5$) from the HSZ (Figures 6.9E-F). Again, the results indicate that seismic hazard for class C-3 sites did or does not come from strong to great dip-slip earthquakes outside the Argive Basin, but more likely from nearby moderate to strong extensional and strike-slip crustal poorly understood and understudied faults.

Figures 6.9G-H demonstrate that all class D-2 sites around Tiryns and most sites along the Tiryns-Midea profile exceed the mean PGA value (0.31 g) for Tiryns, established by the PSHA for Greece (e.g., Tselentis and Danciu, 2010a, 2010b) when the ground surface is

seismically loaded by local crustal extensional earthquakes from the Argive Basin. The mean PGA values of both Midea (0.40 g) and the Argive Basin (0.50 g) are also exceeded at several sites. Hypothetical local strike-slip crustal earthquakes rarely yield surface ground-motions > 0.31 g. Neither strong extensional crustal earthquakes (M_w 6.8) from the PCCR, nor major to great interface and/or intraplate earthquakes ($7.6 < M_w < 8.5$) from the HSZ produce PGA greater than the mean PGA value for the vicinities of Tiryns, Midea, or the Argive Basin (Figures 6.9G-H). Thus, seismic hazard for all class D-2 sites is interpreted to be restricted to local (< 20 km) moderate to strong extensional crustal earthquakes, as for the other site classes.

Empirical peak ground-motion predictive relations for light to major ($4.5 < M_w < 7.0$) normal, strike-slip, and compressional shallow earthquakes are available for Greece (Skarlatoudis et al., 2003; Danciu and Tselentis, 2007). Recently, ground-motion predictive equations for intermediate-depth (45 to 300 km) subduction-related light to major ($4.5 < M_w < 6.7$) earthquakes became available for Greece (Skarlatoudis et al., 2013). For comparison purposes, the empirical relations for shallow earthquakes were used to calculate peak ground-motion values for both weathered-unweathered rock-sites (class C-1) and shallow stiff soil-sites (class C-2) located within the zones of Tiryns and Midea. Only such site classes were selected because Mycenaean buildings and structures were erected on such environments. The peak ground-motion values calculated with the empirical predictive relations of such site classes are plotted in Figures 6.9A-D and are in full agreement with the resulting peak ground-motions determined by the present study. The empirical relations for intermediate-depth subduction-related earthquakes were not used because of two reasons: (i) the earthquake database used to develop the predictive equations does not include earthquakes with $M_w > 7.0$; and (ii) the PGA values computed with the Equivalent-Linear model do not exceed the aforementioned critical mean PGA values established by the PSHA.

An example of the resulting surface ground-motion calculated for all the modeling sites of Tiryns, Midea, and the Tiryns-Midea profile using the EL model are shown in Figures 6.10A-C and Figures 6.11A-C for results based on v_s model A and v_s model B, respectively. The selected acceleration time histories for all sites correspond to a hypothetical local strong crustal extensional earthquake (M_w 6.6; event ABNF1). The surface accelerograms calculated with the v_s model A are noticeably different than those calculated with the v_s model B despite of using the same input signal. The later ones typically show higher PGA particularly in soil-sites. Table 5.2 and Figure 5.1 (in chapter 5) show the source parameters of this event and the trace of the normal fault, respectively.

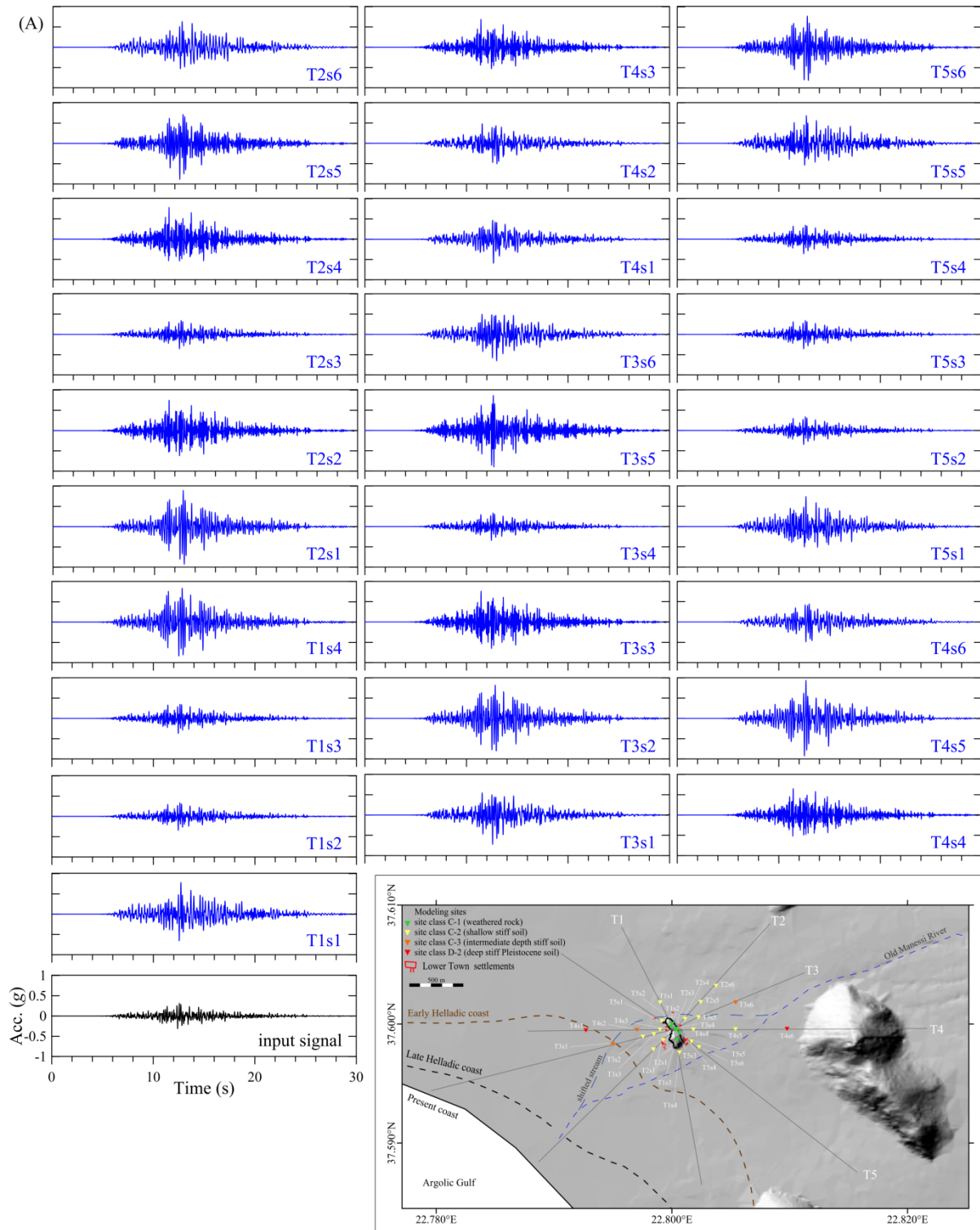


Figure 6.10: Calculated surface acceleration time histories (blue) resulting from the forward modeling of 1D local site effects using v_s model A. The results for Tiryns, Midea, and the Tiryns-Midea profiles are displayed in (A), (B), and (C), respectively. The calculated surface accelerations are in response to a local strong crustal earthquake (M_w 6.6) (event ABNF1) represented by the input signal (black accelerogram) modeled with the Green's function approach.

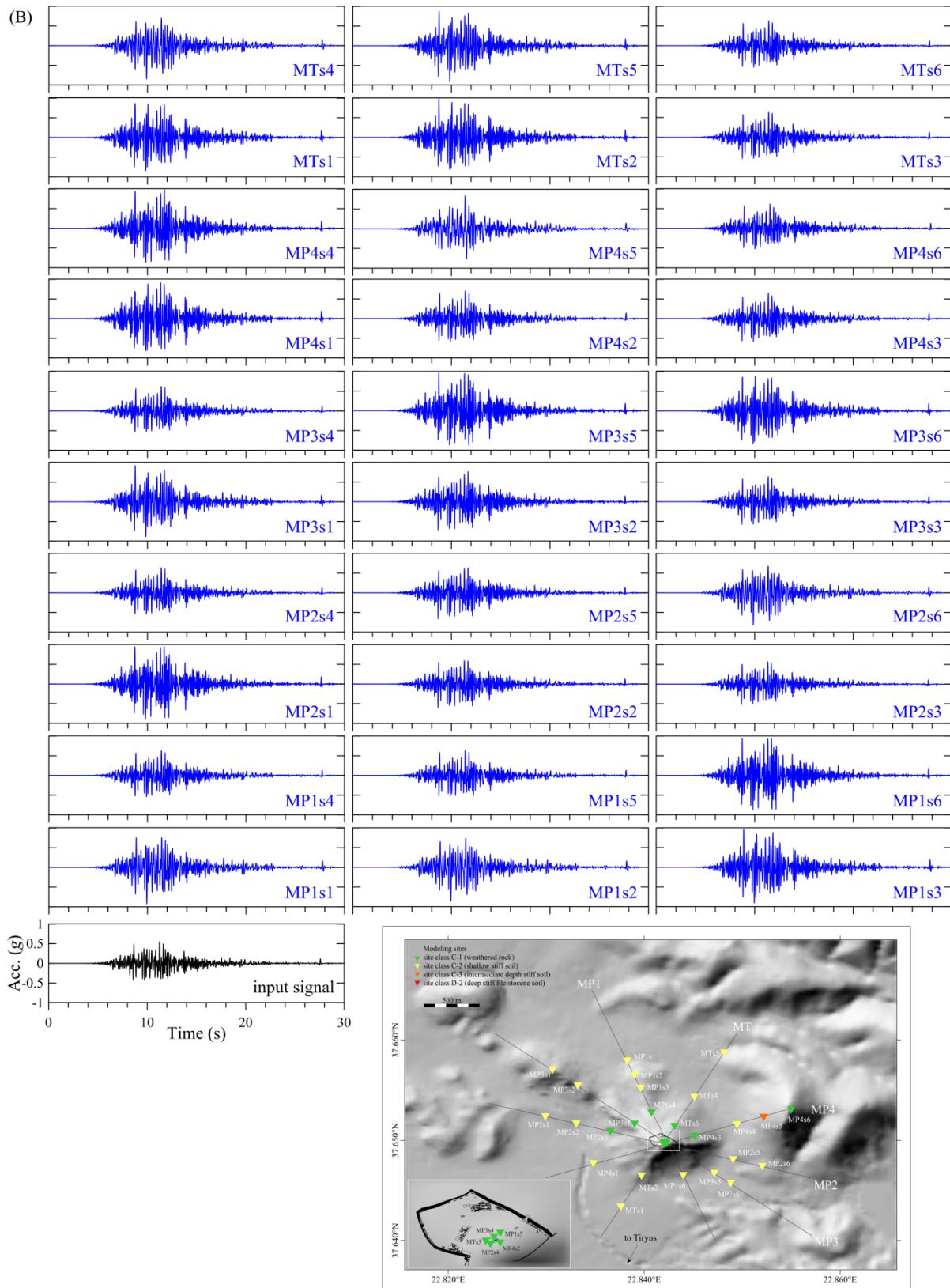


Figure 6.10: continued.

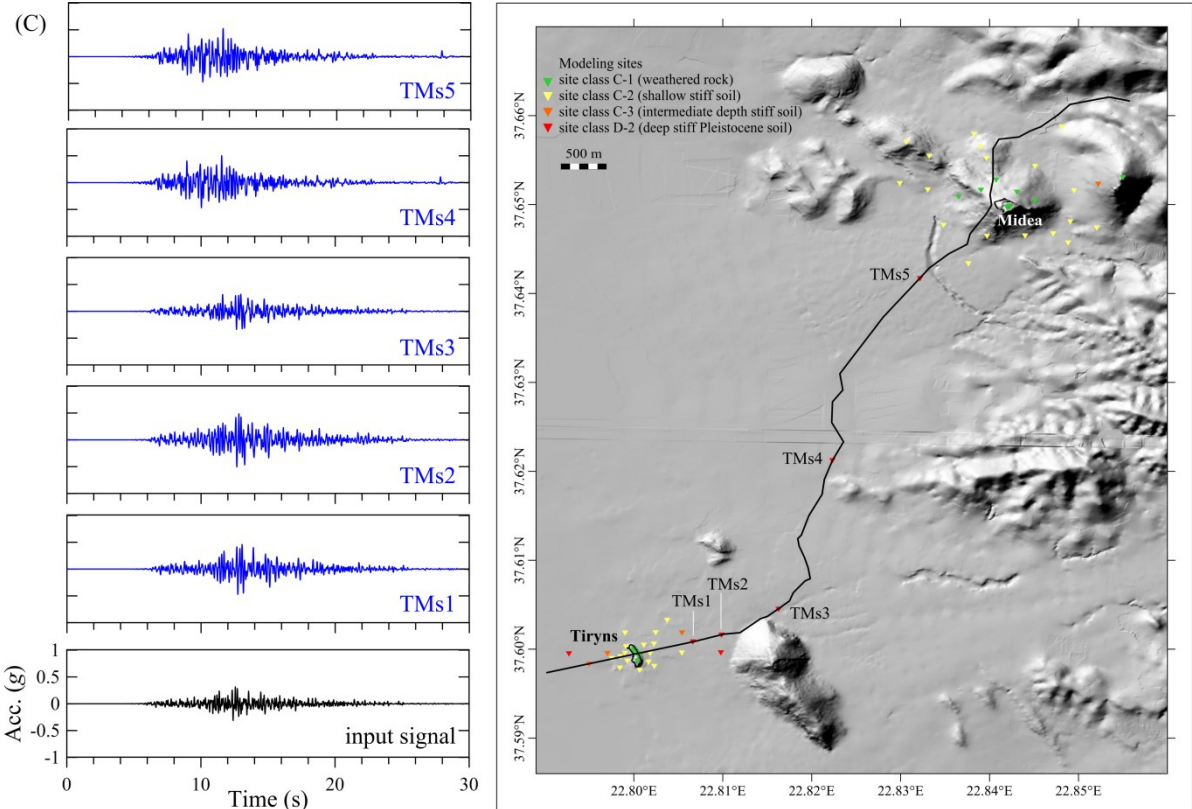


Figure 6.10: continued.

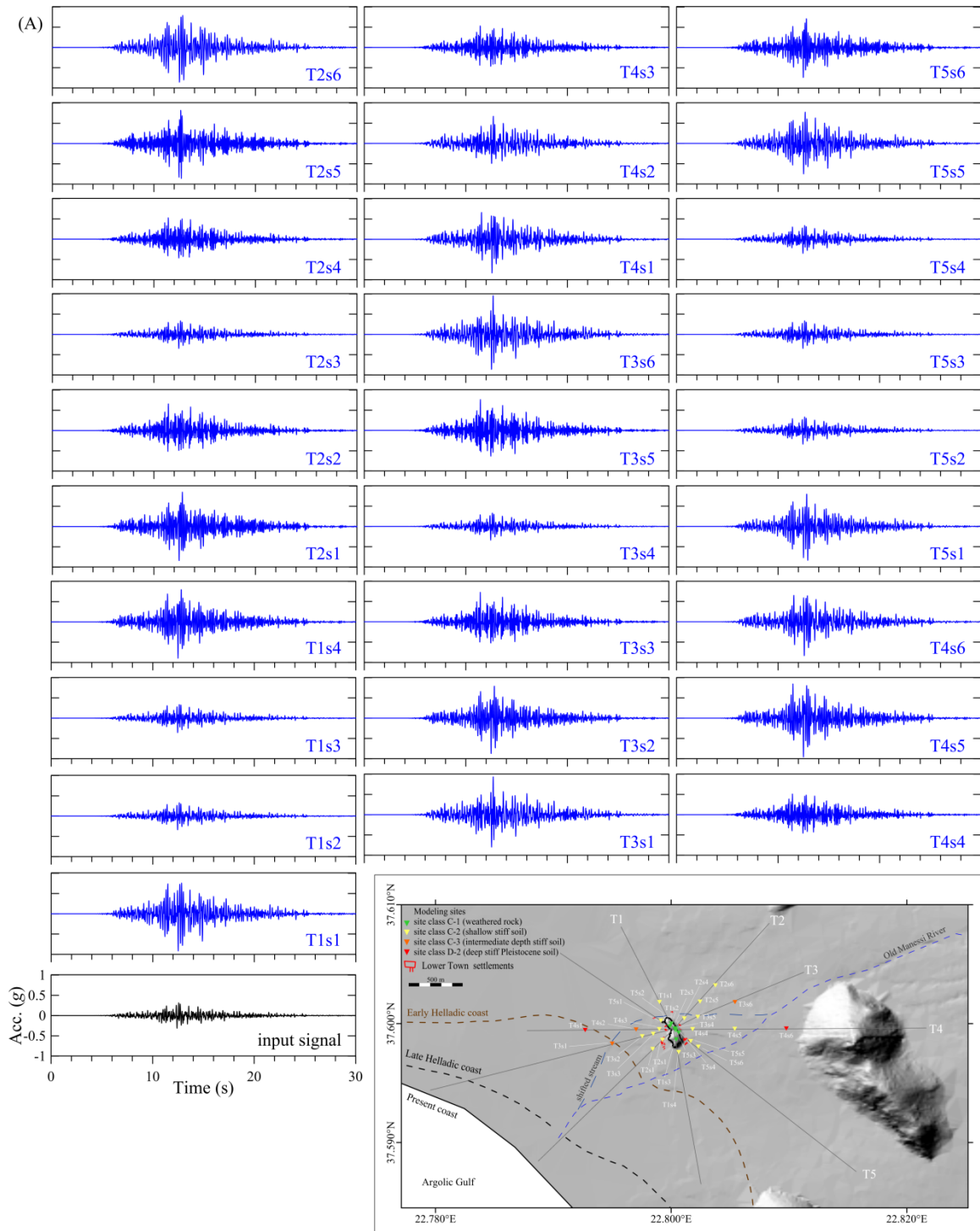


Figure 6.11: Calculated surface acceleration time histories (blue) resulting from the forward modeling of 1D local site effects using v_s model B. The results for Tiryns, Midea, and the Tiryns-Midea profiles are displayed in (A), (B), and (C), respectively. The calculated surface accelerations are in response to a local strong crustal earthquake (M_w 6.6) (event ABNF1) represented by the input signal (black accelerogram) modeled with the Green's function approach.

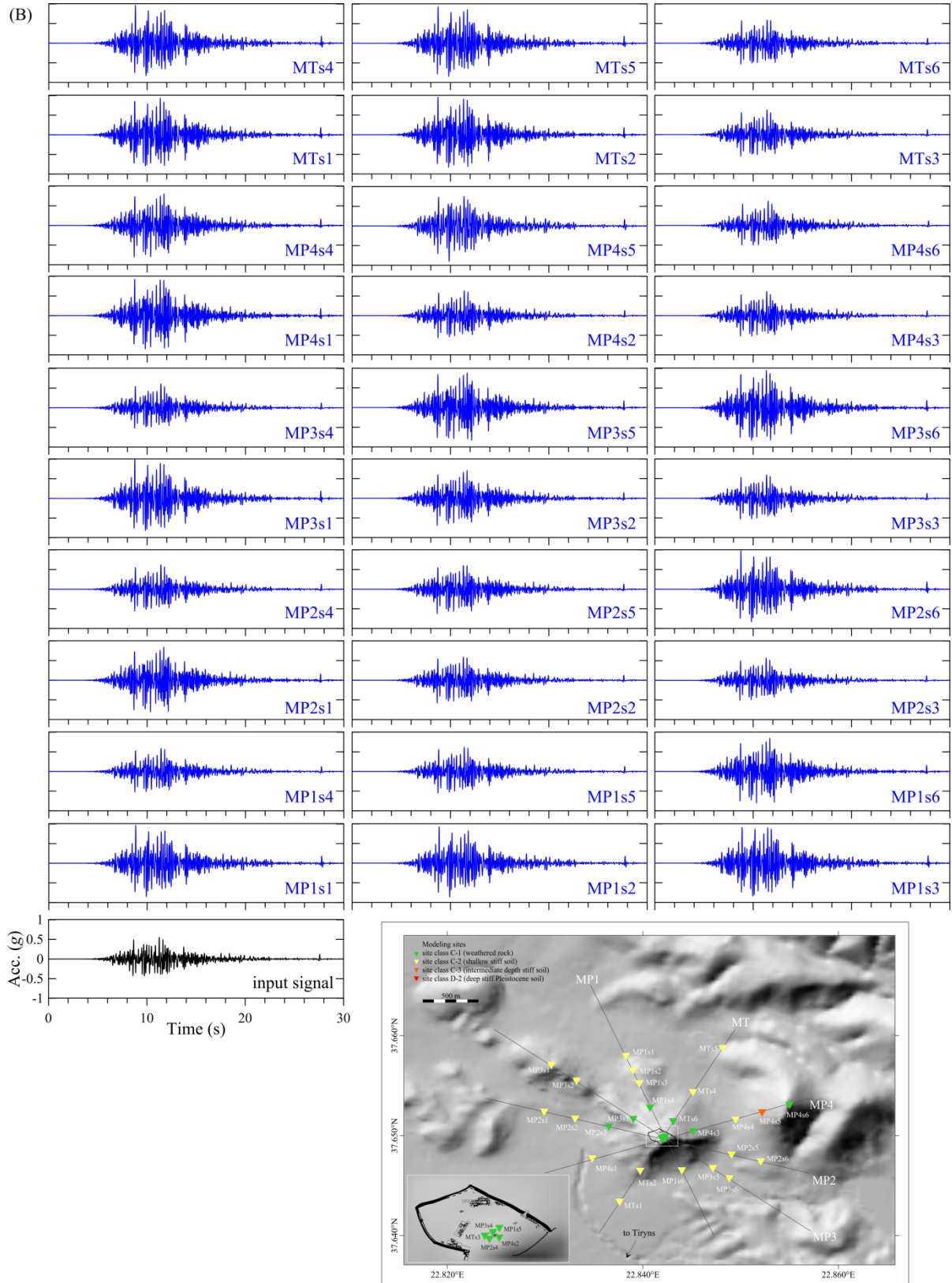


Figure 6.11: continued.

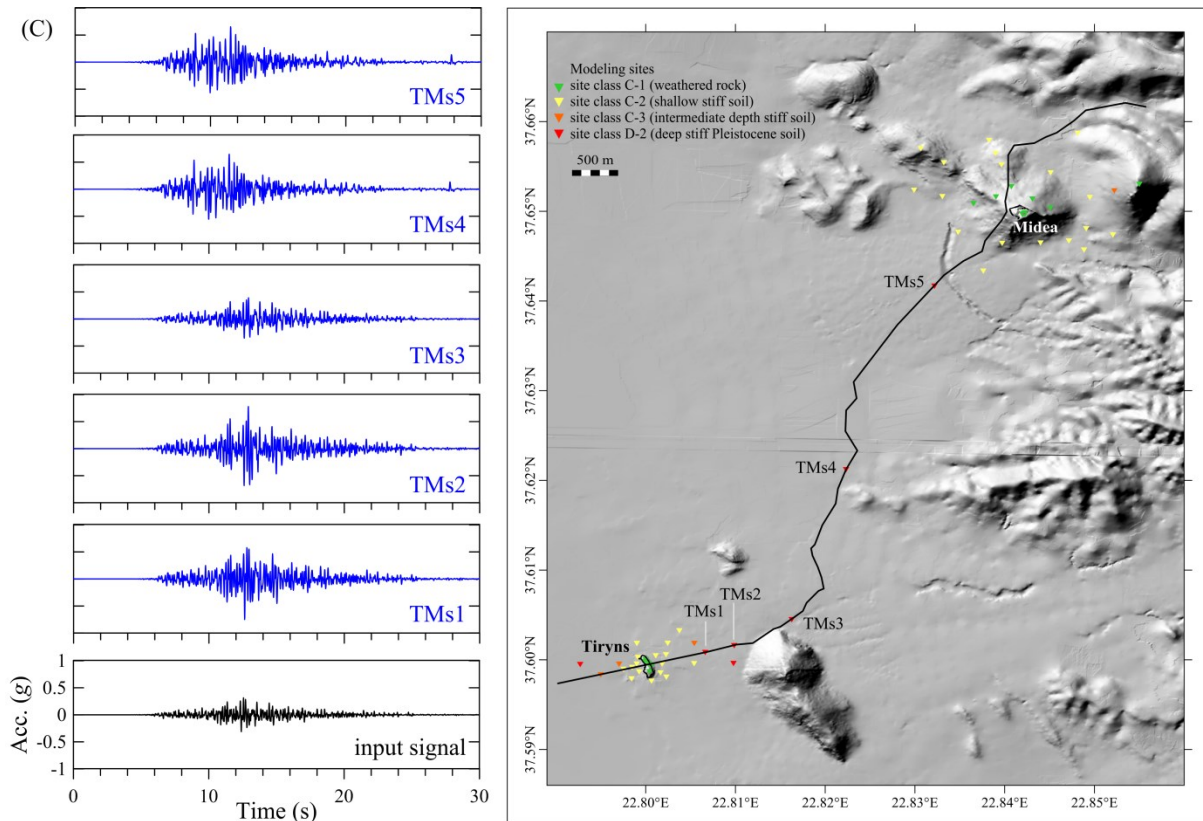


Figure 6.11: continued.

Finally, the resulting surface ground-motions were converted into intensity (e.g., Modified Mercalli Intensity, MMI) scale values using the empirical relations of Ambraseys (1974) and Tselentis and Danciu (2008), which from now on are referred to as A74 and TD08, respectively. The results of this study have implications for the testing of the Mycenaean earthquake hypothesis, and add knowledge to our ongoing understanding of both seismic site effects at Mycenaean Tiryns and Midea and the dynamic behavior of Mycenaean structures. The MMI scale quantifies the effects of earthquake shaking on the ground surface, objects of nature, humans, and man-made structures on a scale from 1 (not felt) to 12 (total destruction) (Sheriff, 2006). The computed intensity values for all the modeling sites and all the modeled earthquakes scenarios are shown in Figure 6.12. The obtained intensity values can provide an estimate of the size of the “affected area” (Michetti et al., 2015) in response to the hypothetical rupture of local extensional earthquakes from the Argive Basin. Both class C-1 sites (weathered rock) and class C-2 sites (shallow stiff soils) are critical sites for Mycenaean constructions because they can produce intensity values ≥ 8 corresponding to $PGA \geq 0.30 g$ (Sheriff, 2006). Intensity values of 8 to 11 are reached in response to all local shallow extensional earthquakes of the Argive Basin, as illustrated in Figure 6.12.

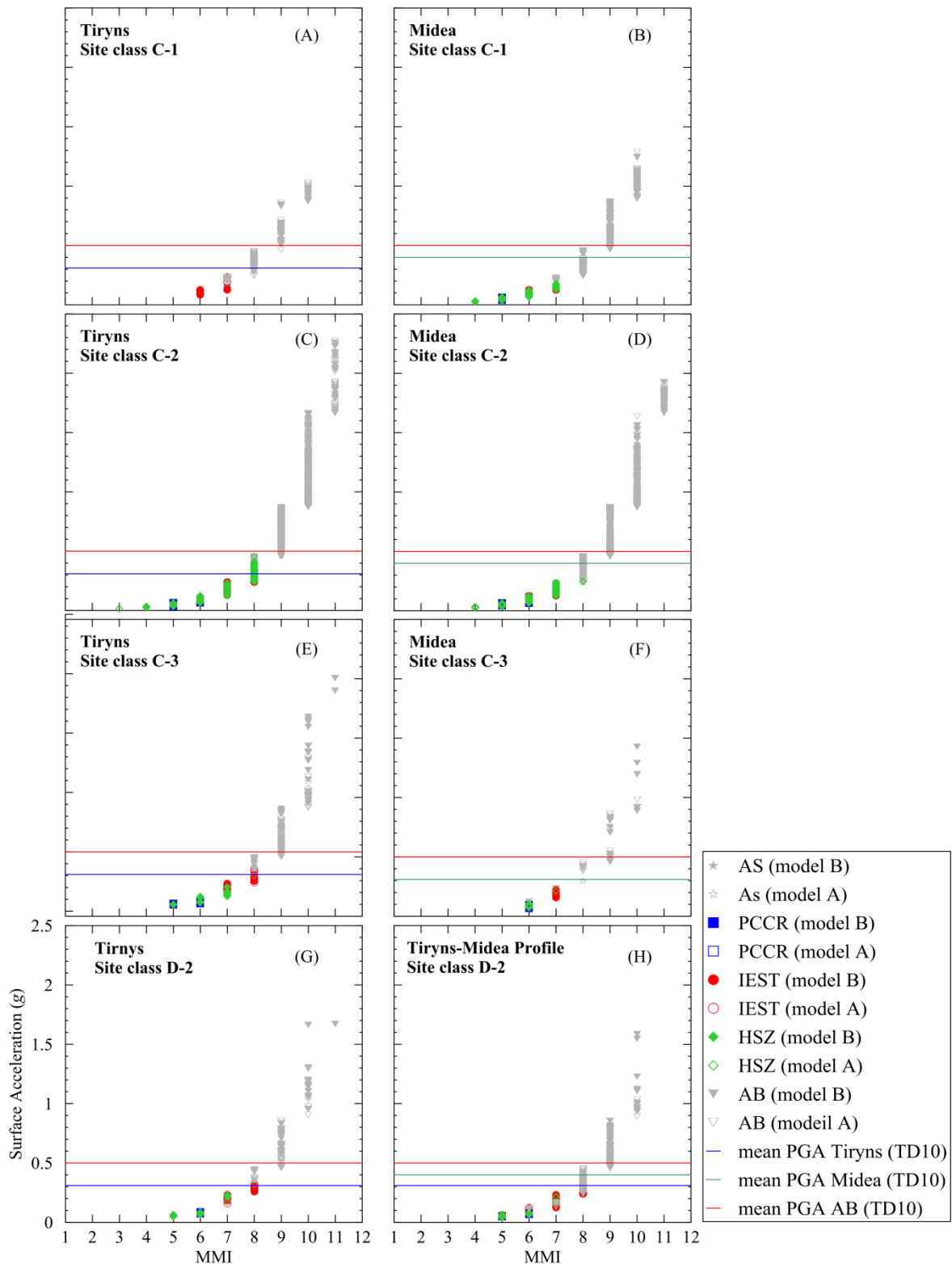


Figure 6.12: Summary of resulting intensity values (MMI) for all modeling sites from Tiryns, Midea, and along the Tiryns-Midea profile using input accelerograms computed with the Green's function approach. Results are grouped according to site class category and sorted by v_s model (models A or B), and seismogenic sources (AB, PCCR, IEST, and HSZ, as in Figure 6.7). Labels in the upper left-hand corner indicate the archaeological site and site class category. The blue, green, and red horizontal lines correspond to the calculated mean PGA value around Tiryns, around Midea, and the Argive Basin, respectively, according to Tselentis and Danciu (2010a) [TD10].

7. DISCUSSION

For decades, archaeologists have taken for granted that earthquakes during the LBA caused earthquake damage to Mycenaean buildings in the Argive Basin, Peloponnese, Greece. However, the hypothesis has lacked insights from archaeoseismologists. Prior to the present study, no data existed concerning site-specific surface amplifications and surface ground-motions at Mycenaean Tiryns and Midea. The synthetic seismograms calculated in this study correspond to extensional, strike-slip, and compressional earthquake faulting from seismogenic sources affecting the Argive Basin and include the influence of local site effects.

7.1 The Role of Local Site Effects in the Mycenaean Earthquake Hypothesis Testing

Local seismic site effects link the earthquake source and surface ground-motion. Archaeoseismic observations often contain a small portion of the mesoseismal area (Hinzen et al., submitted) and the correlation of structural damage across several nearby sites is frequently hindered by uncertainties in dating the damaging events (Galadini et al., 2006; Jusseret et al., 2013). These factors might lead to inaccurate estimates of the strength of past earthquakes if local site effects are over- or undervalued or even overlooked (Hinzen et al., submitted). Therefore, the consideration of local site effects is crucial in archaeoseismology. Quantitative estimates of local site effects point that the Late Neogene–Quaternary cohesive soils around Mycenaean Tiryns and the central Argive Basin had a higher seismic hazard than the granular soils around Midea; while the citadels themselves had the smallest hazard. Seismic hazard for Mycenaean constructions likely came from local (≤ 20 km) shallow extensional earthquakes from the Argive Basin rather than from more distant extensional, strike-slip, or compressional earthquakes, if these earthquakes ever happened (e.g., evidence does not exist).

7.1.1 Site Amplification and Surface Ground-Motions

The results from recent quantitative seismic site effects studies (Karastathis et al., 2010a, 2010b; Hinzen et al., submitted) and numerical modeling of earthquake-induced toppling of Mycenaean ceramic objects (Hinzen et al., 2015) coupled with the results of the present study contribute to a holistic examination of the Mycenaean earthquake hypothesis. The reliability of the computed surface amplification factors and surface ground-motions of the present study relies on site-specific soil-and-rock models instead of attenuation models derived from empirical predictive relations.

At ~ 1 km southwest of Tiryns, Karastathis et al. (2010a, 2010b) estimate a 70% probability of soil-liquefaction and a PGA of 0.20 g at a depth interval of 4.0 to 6.0 m in response to a nearby shallow strike-slip earthquake (M_w 6.4) on the Iria fault. Other predicted PGA values in a zone between Tiryns and Nafplion, which classifies as a class D-2 site area, are between 0.124 to 0.217 g; still below the mean PGA of 0.31 g estimated by Tselentis and Danciou (2010a) for the same area. This result is also reached by the present study for the same earthquake/fault (see chapter 6). The modeling procedure of Karastathis et al. (2010a, 2010b) excludes the hills of Tiryns and Midea and takes into account the current water table depth

and surficial geologic conditions. For the examined zone, they report only PGA values for depth intervals between 4.0 to 16.0 m (depending on the site) instead of the surface PGA, but do not report surface amplification factors. The present study reports both estimates and removes post-Mycenaean soils as an attempt to reconstruct the Mycenaean walking horizon during ca. 1200 BCE. Hypothetically, if soil-liquefaction happened during Mycenaean times, it could have affected the soils around Tiryns; but evidence of soil-liquefaction or earthquake damage to ancient structures have not been found yet in archaeological (Maran, personal communication, 2015) or geoarchaeological (Zangger, 1993) excavations. The conclusive remark from these studies is that, during ca. 1200 BCE, the soils around Tiryns could have reached high levels of surface ground-motion and caused earthquake damage and soil-liquefaction due to local earthquakes.

Recently, Hinzen et al. (submitted) deduced small-to-moderate seismic site effects at Mycenaean Tiryns and Midea using the combined results of local earthquakes ($1.6 < M_w < 4.9$), ambient noise data, and 1D forward modeling. They show small site amplifications < 2 on the Tiryns hill and amplifications of 4.0 to 6.0 at frequencies between 2.0 and 10.0 Hz in the surroundings class C-2 soft-soils sites, where the Lower Town settlements were located. At Midea, the topography of the hill induces ground-motion amplifications between a factor of 2.0 and 3.0 at frequencies between 1.0 and 3.0 Hz. The ambient noise measurements taken at the top and base of the current Cyclopean walls (10.0 m high and ~ 7.0 m wide) at Tiryns indicate high eigenfrequencies of ~ 15.0 Hz; though, the current wall height is not the exact original. They concluded that fortified citadels of Tiryns and Midea, built on class C-1 sites (weathered rock), were at a lower hazard level than the surroundings soils. This is in full agreement with the interpretation derived from the geotechnical classification of the sites and the 1D forward modeling of local site effects of the present study.

Moreover, Hinzen et al. (2015) used seismological engineering models to topple Mycenaean terracotta figures and clay vessels found in a room within the Lower castle of Tiryns, which according to Kilian (1980, 1996) were toppled by an earthquake during ca. 1200 BCE. In their numerical simulations the objects stood on a bench and were excited by 11 horizontal strong ground motion records of instrumentally recorded Greek earthquakes ($3.4 < M_w < 6.4$). Although these ground motions are not site-specific for the Tiryns citadel, the 11 recordings cover a broad range of horizontal motions (e.g., PGA from ~ 0.02 to 1.0 g) and ground motion variability (e.g., horizontal components rotated between 0° and 327°). They concluded that the simulated thrown position of the toppled objects do not match the original find spots found by the excavators; therefore, refuting the earthquake hypothesis of Kilian (1980, 1996) based on the toppled objects.

Finally, the earthquake storm idea of Nur and Cline (2000) relates the partial structural coseismic collapse of numerous LBA man-made structures (including Mycenaeans) from Aegean and Eastern Mediterranean regions with several earthquakes rupturing during ca. 1200 BCE. At least for Mycenaean constructions in the Argive Basin, this hypothesis is

challenged by insights from the aforementioned local site effects studies. For instance, source-to-site distances (> 45 km) induce surface accelerations below strong surface ground-motions (< 0.30 g), hence, nearby earthquakes were more likely to be the hazard for Mycenaean structures.

7.1.2 Seismic Response of Mycenaean Structures

The frequency range considered in the present study is between 0.1 to 20.0 Hz. Both surface amplification and related surface ground-motion are dependent on site category. The natural frequency of Mycenaean structures in the Argive Basin is difficult to estimate because of scarce archaeological information. The hypothesized natural frequency of a Mycenaean building is here estimated at 10 ± 3 Hz. The seismic response of the established class C-1, C-2, C-3, and D-2 sites is defined by their range of natural frequencies corresponding to 8.0-20.0, 4.0-20.5, 2.6-7.2, and 1.0-3.0 Hz, respectively; therefore, the buildings inside and outside the citadels of Tiryns and Midea were likely sensitive to surface ground-motions containing frequencies between 5.0 to 20.0 Hz. Consequently, some Mycenaean structures might have been in resonance with the site they were built on.

The constructions inside the citadels of Tiryns and Midea and the Cyclopean walls were all built on weathered-and-fractured rock (e.g., class C-1 sites). The archaeological floor plan of Tiryns (Maran, 2010) and Midea (Demakopoulou, 2012) indicate that the citadels had buildings of different dimensions because they had different uses. Some buildings were erected on elevated rocky spots while others on smoother ground. As pointed out by Hinzen et al. (submitted), current archaeological information suggests that there were no tall buildings or structures at Bronze Age Tiryns and Midea (Fields, 2004) and that most structures were likely one storey and some two storey constructions (Maran, 2010). Therefore, the buildings of the citadels were subtle to surface ground-motions in the frequency range from 5.0 to 20.0 Hz. An empirical model for the basic eigenmovements of a Cyclopean wall has been established (Hinzen et al., submitted). The model comprises ambient noise measurements taken at three locations on top and at the base of the 10 m high and 6.7 m wide Cyclopean wall of Tiryns showing high eigenfrequencies in the range of 15.0 Hz. The measuring spots were on the western wall, which was restored in the 1970s without enough documentation. The authors express that the exact original height of the walls remains unknown so the current height might not necessarily reach the original one; however, the width is original so the readings provide a rough estimate of the main resonance frequencies of a Cyclopean wall. They conclude that the Cyclopean walls of Tiryns were probably sensitive to natural frequencies in the range of 15.0 Hz. Current archaeological information about the Cyclopean wall of Midea indicates that the height of the wall is partially preserved up to 7.0 m and the width varies from 5.0 to 7.0 m (Fischer, 1986; Walberg, 2001; Demakopoulou, 2012); therefore, the eigenfrequency of the Cyclopean walls of Midea might deviate from 15.0 Hz likely due the ground–structure interaction. Several of the site-specific surface ground-motions estimated in the present study yield PGA above 0.30 g in the

frequency range between 5.0 to 20.0 Hz. Particularly, this is the case for moderate-to-strong local shallow extensional earthquakes of the Argive Basin.

The constructions outside the citadels of Tiryns and Midea include all the buildings of the Lower Town of Tiryns, the massive Mycenaean Dam of Megalo Rema located ~4.0 km east of Tiryns, and several Mycenaean chamber tombs scattered throughout the Argive Basin. The dam and the tombs were operational during the Mycenaean palatial period (ca. 1200-1300 BCE) and were important structures to the Mycenaeans.

The constructions of the Lower Town were most likely one storey buildings with a hypothesized natural frequency of 10 ± 3 Hz. The buildings were erected on class C-2 soils whose natural frequency ranges between 4.0 to 20.0 Hz due to the systematic rapid deepening of the soil–bedrock interface. Therefore, the buildings were also sensitive to strong surface ground-motions in the frequency range of 5.0 to 15.0 Hz. Again, the critical surface ground-motions that might have contained such frequency content could have been those triggered by the nearby earthquakes of the Argive Basin.

The Mycenaean dam is between 80 to 100 m long, has a total height of ~10 m, and a mean base width of ~60 m (Balcer, 1974). Its core comprises rock and clay fill while the exterior walls are built with Cyclopean blocks of limestone. The dam is partially destroyed due to intense erosion caused mostly by torrential floods and the removal of blocks in recent times (Maroukian et al., 2004); however, coseismic damage has not been considered. The site class for the area encompassing the dam is unknown. The eigenfrequency range of the dam remains unestimated due to insufficient archaeological information and lack of ambient noise measurements on its top and at its base. Therefore, it is difficult to define seismic response of the dam and to assess if it is sensitive to the frequency content of the same local earthquakes that may affect other Mycenaean constructions.

Numerous Mycenaean chamber tombs were already functioning during the Mycenaean palatial period in the Argive Basin, throughout the Peloponnese, and mainland ancient Greece (Mee and Cavanagh, 1984, 1990). Their architectural design is constant and complex, but their dimensions vary (Dirlik, 2012). The number of Mycenaean tombs exceeds the number of fortified Mycenaean citadels (Mee and Cavanagh, 1984, 1990). These factors suggest that tombs are valuable structures for archaeoseismic research. Numerous tombs exist around the Argive Basin (Mee and Cavanagh, 1984, 1990; Dirlik, 2012). Tombs frequently show signs of structural collapsed with occasional deposition of sediment in the interior space (Karkanis et al., 2012). This is the case for several tombs in the Cemetery of Dendra located near Midea. The lack of stratigraphic analysis in the tombs hampers the identification of the cause of the collapse (Karkanis et al., 2012; Dirlik, 2012). The tomb of Aegisthus, next to the Mycenae citadel, is another example of a collapsed tomb (Spathari, 2001; Dirlik, 2012). Galanakis (2007) links its collapse to the same earthquake that supposedly damaged Mycenae during ca.

1200 BCE (French, 1996); however, structural damaged is no longer visible due to the recent restauration.

Conversely, while archaeologists suggests that the citadels of Tiryns (Kilian, 1996), Midea (Åström and Demakopoulou, 1996), and Mycenae (French, 1996) contain coseismic structural damage, the Mycenaean tombs of Tiryns and Atreus, located ~1100 and ~500 m southeast and southwest from Tiryns and Mycenae, respectively, lack evidence of structural collapse or destruction (Dirlik, 2012). This raises two questions: how can the citadels of Tiryns, Midea, and Mycenae show synchronized earthquake damage while some adjacent tombs do not? Can Mycenaean tombs resonate with the sites they were built on during seismic loading? The first question stems from synthesizing archaeological interpretations and is problematic because it contradicts insights from local site effects studies. The tombs were built on coarse-grained class C-2 to D-2 soil-sites which undergo soil amplification while citadels were prone to undergo less amplification. It is plausible that if a local strong earthquake caused structural damage to the citadels, the nearby tombs would also have been damaged by the same earthquake. The absence of earthquake damage in the tombs challenges the Mycenaean earthquake hypothesis. The second question is difficult to answer because the eigenfrequencies and dynamic response of Mycenaean chamber tombs remain unknown and unestimated, respectively. Therefore, it is difficult to estimate if tombs are sensitive to strong motions in the frequency range considered in this study. This calls for a dynamic response analysis and numerical simulations of the collapse process of Mycenaean structures including tombs, buildings, Cyclopean walls, and the dam.

7.2 Can Earthquake Environmental and Archaeological Effects be Assessed in the Argive Basin?

Earthquake intensity is established on a classification of earthquake-induced effects caused on man-made structures and on natural environments (Michetti et al., 2015). The evaluation of epicentral intensity (I_0) relies on the observation of primary effects (i.e., m-scale surface rupture, tectonic uplift/subsidence) and on the total area affected by secondary earthquake environmental effects (i.e., ground cracks, slope movements, soil-liquefaction deposits, and tsunamiites). Tentatively, even if we consider the Mycenae normal fault scarp (Papanastassiou et al., 1993) and other normal faults scarps near Nafplion (Georgiou and Galanakis, 2010) as ‘causative’ faults, the I_0 approach still becomes inapplicable because the time of their last rupture remains undated. Moreover, evidence for earthquake archaeological effects at Tiryns and Midea presented by archaeologists is still considered a matter of debate. Even if we considered that Aegean-type morphogenic normal faulting ($M_w \geq 5.5$: Pavlides and Caputo, 2004) has affected the soils of the Argive Basin during the Late Helladic IIIB period at ca. 1200 BCE, the expected primary environmental effects would be undetectable in the present topographic conditions due to natural and anthropogenic adverse forces acting on the ground surface for the past ca. 3200 years. Such features were likely erased by subsequent erosion, by thousands of years of land use, or buried by post-Mycenaean alluviation affecting the Argolis, processes that are well understood for the Argolid Peninsula (e.g., Pope and van Andel, 1984;

van Andel et al., 1986, 1990a, 1993). Therefore, at Mycenaean Tiryns and Midea, the available information precludes both the assessment of I_0 (Michetti et al., 2015) and the usage of the earthquake archeological effects approach (Rodríguez-Pascua et al., 2011).

In contrast, the resulting intensity values from 8 to 11 (see Figure 6.12) are consistent with an affected surface area between 100 to 5000 km². These dimensions encompass the area of the Argive Basin (~300 km²). From the territorial point of view, this analysis favors the idea that Tiryns, Midea, and Mycenae could have experienced synchronized coseismic-related structural damage (e.g., Gaki-Papanastassiou et al., 1996; Maroukian et al., 1996; French, 1996; Kilian, 1996; Åström and Demakopoulou, 1996; Nur and Cline, 2000) due to the rupture of a local earthquake during ca. 1200 BCE; for instance, the Mycenae normal fault (Papanastassiou et al., 1993), or other normal faults in the area, coupled with the influence of the local site effects.

7.3 Criteria for Modeling Local Site Effects in Archaeoseismology

The 1D forward modeling of seismic local site effects requires the proper knowledge of the model parameters, including the conditions of the ‘ancient ground surface and subsurface’, values for the material properties (e.g., density, shear-wave velocity, and Q), and the source parameters of the hypothetical causative earthquake(s). Archaeological-and-geoarchaeological excavations, geophysical surveys, and both geological and geotechnical studies provide essential site-specific information to estimate the local site effects and to define the seismic response of a site. The choice of computer codes to compute synthetic seismograms and to forward model the equivalent-linear 1D site-response is also important.

Archaeological and geoarchaeological excavations provide information about the texture, density, type, age, and thickness of the shallow soils and sediments that pre- and-postdate the stratigraphic horizon of interest; however, they rarely reach the soil–bedrock interface. The removal of the overburden (i.e., material that postdates the horizon of interest) and the depth to the soil–bedrock interface are required parameters for a realistic and accurate estimation of local site effects. Deeper boreholes and geophysical surveys should be pursued to detect the soil–bedrock contact and to gain information about possible heterogeneities in the soils and bedrock. In general, seismic methods (reflection or refraction) provide an in situ measurement of the P and S wave velocities; while geoelectrical and/or electromagnetic methods can detect and discriminate between fine-grained soils (cohesive) from coarse-grained soils (granular). Inaccurate knowledge of the ‘actual’ composition, thickness, and dynamic properties of the subsurface materials can lead to the misrepresentation of the regolith column and the inaccurate selection of strain-dependent shear modulus and damping values for individual material, and to uncertainties in the forward calculation of frequency-dependent surface amplifications, surface ground-motions, and the estimation of the seismic site response (cf. Rodríguez-Marek et al., 2001). The site class is important for a seismic site-specific response analysis. The geotechnical site classification scheme of Rodríguez-Marek et al. (2001) is the most adequate for an archaeoseismic research because it allows an accurate representation of

the regolith column in comparison with the geologic and geophysical site classification schemes. Therefore, the dynamic response of ancient structures is estimated with a better degree of accuracy. The geotechnical site classification system is based on several measurable parameters: the type of deposit (i.e., hard-rock, competent rock, weathered rock, stiff-soil, soft-soil, and potentially liquefiable sand) which automatically introduces a measure of the dynamic stiffness (v_s^{30}) to the classification system; depth to bedrock defined by $v_s > 760$ m/s or to a significant seismic impedance contrast between surficial soil deposits and geologic material with a $v_s \approx 760$ m/s; the depositional age of the soil(s) (i.e., Holocene or Pleistocene), and soil-type (i.e., cohesive or granular). The geotechnical site classification system breaks down sites traditionally grouped as “rock” into competent rock sites and weathered soft-rock/shallow stiff soil sites. This subdivision leads to a significant reduction of uncertainty in defining site-dependent surface ground-motions, and allows assigning proper model parameters and dynamic properties to individual material layers more accurately. Conversely, the geologic site classification scheme is based on one or more parameters obtained from surficial geologic observations, namely geologic age-only, age-and-depositional environment, or age-and-sediment texture (Stewart et al., 2003) (Table E7.1 in Appendix E). This classification system does not provide information about the depth and/or the integrity of bedrock, which is a discriminating factor for a seismic site response analysis (Rodríguez-Marek et al., 2001). Moreover, the geophysical site classification scheme is solely based on the uppermost 30 m of the surface, namely v_s^{30} (Borcherdt, 1994; NERHP, 2003) (Table E7.2 in Appendix E). Although the use of the v_s^{30} has the advantage of uniformity within the 30 m depth range and correlates well with detailed surface geology (i.e., age-and-soil texture and age-and-weathering/fracture spacing for rock) (Wald and Allen, 2007; Stewart et al., 2014), it is still an oversimplification of most natural site conditions, and therefore, an indirect approach to define the true composition of the near-surface materials and to estimate the soil–bedrock interface.

Nowadays, high-frequency synthetic seismograms are computed for modeling local site effects (Friederich and Dalkolmo, 1995; Wang, 1999). Most high-frequency motions might be caused by direct P and S waves (Spudich and Frazer, 1984). For modeling purposes, the computed synthetic seismogram should contain such body waves. However, not all algorithms can compute synthetic seismograms with distinct body (P and S), surface waves, and high-frequencies. This is the case for the FINSIM code (Beresnev and Atkinson, 1998) used in this study; however, the algorithm of Wang (1999), also used in this study, allows the computation of high-frequency synthetic seismograms (i.e., near-field motions) with recognizable body and surface waves. Several computer codes can model the nonlinear–elastic stress-strain behavior of a realistic 1D regolith column (Seed and Idriss, 1969; Hashash and Park, 2001; Stewart et al., 2008; Robinson et al., 2006; Hashash et al., 2010). The *SUA* computer code (Robinson et al., 2006), used in this study to forward model the equivalent-linear 1D site-response, is an adequate code to forward model 1D local site effects in archaeoseismology. The code has the ability to incorporate uncertainties in the model parameters including density, shear-wave velocities, and layer thickness. It also allows

defining thin material layers (< 1 m thick), assigning strain-dependent shear modulus and damping curves to each material layer, and the use of either an average or a gradient shear-wave velocity model.

The shear-wave velocity of the material layers is a fundamental model parameter for an equivalent-linear 1D site-specific response analysis. The use of an average shear-wave velocity (model A) for each material layer is an acceptable approach in the absence of depth-dependent (gradient) shear-wave velocities (model B). This study shows that the implementation of model A and model B yield similar results: model A typically produces a slightly higher amplification peak at a slightly lower frequency value in comparison to model B. The use of model B should be the first choice if available information (geologic and/or seismic) shows that there is an increase of geologic age, density, consolidation, and shear strength with increasing depth. In this way, the stiffness of the near-surface materials would be accurately represented. Conversely, model A should be adopted when the presence of “homogenous” material layers is demonstrated by data from geologic logs and archaeological-and-geoarchaeological excavations, or when a gradient velocity model cannot be constrained for the depth interval of interest.

8. CONCLUSION AND RECOMMENDATIONS

Qualitative studies of damage by ancient earthquakes to man-made constructions are widely documented in the archaeoseismological literature but research on local site effects is still rare in archaeoseismology. Archaeoseismic observations are often based on a limited mesoseismal area and poorly constrained dated events and damage by ancient earthquakes. Besides, damage by ancient earthquake to constructions is sometimes ambiguous. The combination of these factors can hamper the correlation of ancient earthquake damage to constructions across nearby sites and might lead to inaccurate estimates of the strength of past earthquakes if local site effects are ignored or over/undervalued. It is important not to rely on intensities based on archaeologically documented earthquake damage without the consideration of the near-surface geologic conditions of the site(s) and the estimation of earthquake site effects.

The present multidisciplinary study is an important contribution to archaeoseismology because it lays out a quantitative and deterministic approach for estimating local site effects. Explicitly, the proposed approach allows the calculation of site-specific surface amplification and associated surface ground-motions at multiple sites due to potential ancient earthquake ground shaking; thus, elucidating the level of seismic hazard. The resulting site-specific surface accelerations can be converted into MMI (Modified Mercalli Intensity) values, if empirical relations are available for the region under investigation. The approach requires input from archaeological, geoarchaeological, geophysical, geological, geotechnical, and historical (if available) investigations relevant to the site(s) of interest. The premise is that such sources of information must facilitate the reconstruction of the ancient ground surface conditions at the time of the (postulated) ancient earthquake. This requires the identification and removal of accrued soils younger than the archaeological horizon of interest; resulting in a realistic estimation of the “ancient walking horizon” and modeling sites. This key step avoids an over-or-underestimation of local site effects. The approach is applicable to archaeological sites worldwide that have unambiguous or ambiguous evidence of damage by ancient earthquake(s) to man-made constructions. The approach is scalable to any area size provided there is accurate and ample information about the archaeological site(s) and surroundings. Hence, the area of study can overlap and/or exceed the dimension of an existing archeologically documented earthquake damage zone; or else can guide the location of future archaeological excavations targeting damage by ancient earthquakes to constructions.

Particularly, the present study is important because it contributes to the archaeoseismic knowledge and our understanding of the seismicity of the Argive Basin and allows the testing of the Mycenaean earthquake hypothesis –*repeated coseismic structural damage to Tiryns, Midea, and Mycenae during the end of the Late Bronze Age (ca. 1200 BCE)* – using site-specific one-dimensional (1D) forward modeling of local site effects due to hypothetical earthquake scenarios that affect the Argive Basin. The potential earthquake sources relevant for the Mycenaean citadels of Tiryns and Midea were identified. These include nearby (≤ 40 km) moderate-to-major normal-faulting and strike-slip earthquakes in the Argive Basin and the Iria–Epidaurus Sinistral Transform fault system, respectively, as well as distant (40-

150 km) strong-to-great normal and reverse faulting earthquakes in the eastern Gulf of Corinth and the Hellenic Subduction Zone, respectively. Synthetic acceleration seismograms of these earthquake sources were calculated, for the first time, with an observation point located in the Mycenaean citadels of Tiryns and Midea. The resulting acceleration seismograms were used as input signals to accelerate site-specific 1D geotechnical models for sites distributed inside and outside the citadels. This procedure allowed a first-time estimation of site-specific surface amplifications and related surface ground-motions due to potential earthquake shaking during ca. 1200 BCE.

The geological survey and geophysical methods applied in the field coupled with information from available upfront archaeological, geoarchaeological, geophysical, geological, and geotechnical studies within the Argive Basin produced results important for estimating site-specific regolith models of both archaeological sites required for the 1D forward modeling of earthquake site effects. These results include:

- mapping the Argive Basin's irregularly thick Late Neogene to Quaternary sedimentary package that reaches up to 200 m thickness near the coastline;
- the reconstruction of the Mycenaean walking horizon;
- the estimation of the thickness and geometry of the soils around the Tiryns and Midea hills, which thicken rapidly away from the hills and the mapping of the soil–bedrock interface;
- the measuring of the near-surface seismic velocity structure (v_p and v_s) which permitted the identification of a high v_p and v_s impedance contrast between the soils and the underlying bedrock;
- the transition from weathered (10-15 m thick) to unweathered limestone bedrock, which is a common geomorphological feature in the karstic terrain that dominates southern and central Greece;
- the identification of water-saturated and undersaturated clays-and-silts sealing the soil–bedrock boundary around Tiryns suggesting lower shear strength for the clay-rich and soft soils compared to the clay-poor and hard soils around Midea;
- the classification of the citadels' rock mass quality index (fair–very poor);
- a comprehensive geotechnical model of each citadel;
- and a microzonation of seismic site class distribution within the vicinity of both archaeological sites following the geotechnical site classification scheme.

The seismic microzonation permitted a site classification of both unexcavated and excavated sites within the ancient urban zones of both Tiryns and Midea. The bedrock of the Mycenaean citadels of Tiryns and Midea classified as site class C-1 (weathered rock-site). Conversely, the rapid deepening of the soils induces a quick and systematic natural transition of soil-site class categories varying from C-2 to C-3 to D-2 sites, being the first one closest to the citadels. This indicates that the citadels had (and still have) a low seismic hazard compared to the buildings of the peasants and other Mycenaean structures built on the sedimentary plain which had (and

still have) a higher seismic hazard. The general rule is that all Mycenaean acropolises occur in karstic landscape and rise above a sedimentary plain; therefore, the near-surface geologic-and-geotechnical conditions and seismic hazard levels identified by the present study may well occur at other or in all Mycenaean acropolises; though, this natural pattern is hard to demonstrate without a seismic microzonation at each Mycenaean citadel.

In particular, it was found that cohesive and granular soils dominate the inner and outer parts of the Argive Basin, respectively, with weathered and tectonically fractured limestone and flysch outcropping bedrock rising above these soils. The cohesive soils, which surround the Tiryns knoll, consist of unconsolidated Holocene alluvial deposits at the surface passing into consolidated Upper Pleistocene clays-and-silts and together overlay the weathered-to-unweathered hard limestone bedrock of lower Late Cretaceous age that comprises the Tiryns knoll. In contrast, medium to coarse-grained, consolidated, hard granular soils characterized by a rather homogenous sequence of Upper Pliocene to Holocene sandy marls, very-coarse sands and gravels, and conglomerates are deposited against the Midea knoll, which comprises a weathered-to-unweathered assemblage of Upper Triassic to Early Eocene hard rocks composed of limestone thrust over flysch. Overall, the soils of the Argive Basin, where the buildings of the peasants and the tombs settled, have variable shear strength, geometry, depositional environment, texture, and consequently, seismic site class categories. The Mycenaean dam rises above Quaternary fluvio-torrential deposits and appears to be erected on the local flysch formation that dominates the eastern Argive Basin. It is hard to say if the Mycenaean were aware of the near-surface geologic and geotechnical conditions. Fact is that the Mycenaean were aware of the wide spacing between the joints and the bedding planes in the local limestone formation, which created naturally equidimensional blocks that allowed them quarrying of large blocks suitable for the construction of the Cyclopean walls and the nearby dam. Likewise, the Mycenaean were mindful of the topographic conditions and their rule of construction used that as an advantage for the development of their massive infrastructure on ground surface with a slope angle $< 40^\circ$.

From the seismic hazard point of view, the seismic site response analysis indicates that rock-sites (class C-1) and soil-sites (class C-2, C-3, and D-2) produce low and high level surface ground-motions, respectively. The highest surface ground-motions in the soil-sites occur in the frequency band between 5 to 20 Hz; suggesting that most Mycenaean structures were most likely sensitive to surface ground-motions containing such frequencies. The soft soils flanking Tiryns were found to amplify earthquake surface ground-motion and were hence more prone to earthquake damage relative to the hard soils flanking Midea. Moreover, both the nearby extensional and strike-slip faults in the Argive Basin and the Iria–Epidaurus Sinistral Transform fault system, respectively, do not show fault-activity within the last 1 Ma. Besides, their subsurface fault geometry and seismic hazard are still uncertain and poorly constrained, respectively. Therefore, these previously proposed finite-fault segments are considered improbable seismic hazards for the Mycenaean constructions in the Argive Basin. Likewise, seismic hazard unlikely came from (the hypothetical) distal earthquakes ($6.8 \leq M_w \leq 8.5$) on

normal or reverse faults from the Gulf of Corinth and the Hellenic Subduction Zone, respectively, due to their large source-to-site distances; even though they are well-known and highly investigated active seismogenic sources of the Aegean microplate that have caused earthquake environmental effects elsewhere during historic and present times.

In summary, the archaeological community may still be unaware of the significance of local site effects and its implications for the dynamic response of (ancient) man-made structures. Since the late 1970s, some Aegean archaeologists have cultivated the Mycenaean earthquake hypothesis without considering the influence of local geologic and soil conditions. The Mycenaean earthquake hypothesis has also left unexplained the size of the probable causative earthquake(s) and related fault(s) and implicitly suggests that the postulated earthquakes during the end of the Late Bronze Age produced partial damage to Mycenaean buildings within the citadels and, consequently, an even higher intensity for the adjacent buildings of the peasants settled on soft grounds. If this is true, evidence of a town-wide devastation pattern would have come to light in previous archaeological excavations. Indeed, the seismic microzonation, the results of the 1D forward modeling of seismic site effects, and the fact that evidence of earthquake damage has never been found in the excavated buildings within the sedimentary plain collectively demonstrate an opposing reality: the citadels had the lower seismic hazard and the constructions settled on the adjacent soft soils had the higher hazard. Therefore, the insights gained from the quantification of ancient earthquake site effects weaken the plausibility of the Mycenaean earthquake hypothesis. The previously archaeologically documented structural damage to buildings inside the citadels of Tiryns and Midea and corresponding partially collapsed Cyclopean walls may not represent physical evidence of ancient earthquake damage. Additionally, evidence of tsunamis and volcanic eruptions within the Aegean microplate, dating back to the end of the Late Bronze Age, is absent in the geological and archaeological record. Therefore, these events are ruled out as possible causes of synchronous structural damage to Mycenaean constructions.

As a final remark, several unexplored topics came to light throughout the duration of the HERACLES project. The realization of these topics would enrich both our archaeoseismic knowledge of the region and allow further quantitative testing of the Mycenaean earthquake hypothesis. These topics are as follow:

- Paleoseismological investigations coupled with detailed geologic and geomorphologic mapping and geophysical prospecting are needed to investigate previously postulated normal faults in the Argive Basin, particularly the ones near Tiryns and Midea and the sedimentary deposits of Lake Lerna. These studies should also target evidence of soil-liquefaction. This multidisciplinary step would shed light into the possible coseismic deformation of Quaternary soils in the Argive Basin.
- An airborne LiDAR (Light Detection And Ranging) survey over the Argive Basin is necessary to detect potential small elevation changes that may be linked to potential morphogenic normal faulting during the Holocene. (This was already proposed as part of the HERACLES project, but hindered by budget limitations.)

- Future archaeological excavations outside Mycenaean Tiryns and Midea should implement the recently proposed innovative excavation-parallel laser scanning methodology of Schreiber et al. (2012) that permits the quantitative documentation of structural damage.
- The eigenfrequencies of still-standing massive Mycenaean structures such as the Cyclopean walls, tombs, and dam should be measured in the field with seismological engineering techniques in order to estimate the frequency range they were/are sensitive to during earthquake ground shaking.
- The tombs and dam in the Argive Basin were essential structures during the Mycenaean palatial period. Field observations should be made for exploring potential evidence of earthquake damage, which can be used for further testing of the Mycenaean earthquake hypothesis.

REFERENCES

- Abbaszadeh-Shahri, A., Esfandiyari, B., and Hamzeloo, H. (2011). Evaluation of a nonlinear seismic geotechnical site response analysis method subjected to earthquake vibrations (case study: Kerman province, Iran), *Arabian Journal of Geosciences*. 4, 1103-1116. doi: 10.1007/s12517-009-0120-7.
- Abercrombie, R. E. (1997). Near-surface attenuation and site effects from comparison of surface and deep borehole recordings, *Bulletin of the Seismological Society of America*. 87, 731-744.
- Aki, K. (1980). Attenuation of shear-waves in the lithosphere for frequencies from 0.05 to 25 Hz, *Physics of the Earth and Planetary Interiors*. 21, 50-60.
- Aki, K. (1993). Local site effects on weak and strong ground motion, *Tectonophysics*. 218, 93-111.
- Allmann, B. P., and Shearer, P. M. (2009). Global variations of stress drop for moderate to large earthquakes, *Journal of Geophysical Research*. 114, B01310, doi:10.1029/2008JB005821.
- Ambraseys, N. N. (1971). Value of historic records of earthquakes, *Nature*. 232, 375-379.
- Ambraseys, N. N. (1974). The correlation of intensity with ground motions, in *Advancements in Engineering Seismology in Europe*, Trieste.
- Ambraseys, N. N., and Jackson, J. A. (1990). Seismicity and associated strain of central Greece between 1890 and 1988, *Geophysical Journal International*. 101, 663-708.
- Ambraseys, N. N. (1996). Material for the investigation of the seismicity of central Greece, in *Archaeoseismology* (eds. Stiros, S., and Jones, R. E.), pp. 23-36. Fitch Laboratory Occasional Paper No. 7, Athens. Exeter: Short Run Press.
- Ambraseys, N. N. (2005). Archaeoseismology and neocatastrophism, *Seismological Research Letters*. 76, 560-564.
- Ambraseys, N. N. (2006). Earthquakes and archaeology, *Journal of Archaeological Science*. 33, 1008-1016.
- American Society for Testing and Materials (ASTM). (1985). Classification of soils for engineering purposes: Annual Book of ASTM Standards, D 2487-83, pp. 395-408.
- Ansal, A., İyisan, R., and Yildirim, H. (2001). The cyclic behavior of soil and effects of geotechnical factors in microzonation, *Soil Dynamics and Earthquake Engineering*. 21, 445-452.
- Apostolidis, E., and Koutsouveli, A. (2010). Engineering geological mapping in the urban and suburban region of Nafplion city (Argolis, Greece). *Bulletin of the Geological Society of Greece*. 43, 1418-1427.
- Armijo, R., Meyer, B., King, G. C. P., Rigo, A., and Papanastassiou, D. (1996). Quaternary evolution of the Corinth rift and its implications for the late Cenozoic evolution of the Aegean, *Geophysics Journal International*. 126, 11-53.
- Åström, P., and Demakopoulou, K. (1986). New excavations in the citadel of Midea 1983-1984, *Opuscula Atheniensia*. XV, 19-25.
- Åström, P., Demakopoulou, K., and Walberg, G. (1988). Excavations in Midea 1985, *Opuscula Atheniensia*. XIX, 7-11.

- Åström, P., Demakopoulou, K., Divari-Valakou, N., Fisher, P., and Walberg, G. (1990). Excavations in Midea 1987, *Opuscula Atheniensia*. XVIII, 9-22.
- Åström, P., Demakopoulou, K., Divari-Valakou, N., and Fisher, P. (1992). Excavations in Midea 1989-1990. *Opuscula Atheniensia*. XIX, 11-22.
- Åström, P., and Demakopoulou, K. (1996). Signs of an earthquake at Midea? , in *Archaeoseismology* (eds. Stiros, S., and Jones, R. E.), pp. 37-40. Fitch Laboratory Occasional Paper No. 7, Athens. Exeter: Short Run Press.
- Atkinson, G. M. (1995). Attenuation and source parameters of earthquakes in the Cascadia region, *Bulletin of the Seismological Society of America*. 85, 1327-1342.
- Atkinson, G. M., and Boore, D. M. (1995). Ground-motion relations for eastern North America, *Bulletin of the Seismological Society of America*. 85, 17-30.
- Avallone, A., Briole, P., Agatza-Balodimou, A. M., Billiris, H., Charade, O., Mitsakaki, C., Necessian, A., Papazissi, K., Paradissis, D., Veis, G. (2004). Analysis of eleven years of deformation measured by GPS in the Corinth rift laboratory area, *Tectonics*. 336, 304-311.
- Bachmann, G. H., and Risch, H. (1979). Die geologische Entwicklung der Argolis-Halbinsel (Peloponnes, Griechenland) (in German). *Geologisches Jahrbuch. Reihe B, Heft 32*, 1-177.
- Balcer, J. M. (1974). The Mycenaean dam at Tiryns, *American Journal of Archaeology*. 78, 141-149.
- Bard, P.-Y., and Bouchon, M. (1985). The two-dimensional resonance of sediment-filled valleys, *Bulletin of the Seismological Society of America*. 75, 519-541.
- Barton, N. (2007). *Rock Quality, Seismic Velocity, Attenuation and Anisotropy*, Taylor & Francis Group, London, UK, 729 pages.
- Beaufils, K. (2000). *Beyond the Argos-Polis: A Social Archaeology of the Argolid in the 6th and Early 5th Centuries BCE*. Ph.D. Thesis. University College London, 340 pages.
- Becker, D., Meier, T., Bohnhoff, M., and Harjes, H.-P. (2010). Seismicity at the convergent plate boundary offshore Crete, Greece, observed by an amphibian network, *Journal of Seismology*. 14, 369-392. doi 10.1007/s10950-009-9170-2.
- Bensalem, R., Chatelain, J.-L., Mechane, D., Oubaiche, E. H., Hellel, M., Guiller, B., Djeddi, M., and Djadia, L. (2010). Ambient vibration techniques applied to explain heavy damages caused in Corso (Algeria) by the 2003 Boumerdes earthquake: understanding seismic amplification due to gentle slopes, *Seismological Research Letters*. 81, 928-940.
- Beresnev, I. A., and Atkinson, G. M. (1997). Modeling finite-fault radiation from the ω^n spectrum, *Bulletin of the Seismological Society of America*. 87, 67-84.
- Beresnev, I. A., and Atkinson, G. M. (1998). FINSIM—a FORTRAN program for simulating stochastic acceleration time histories from finite faults, *Seismological Research Letters*. 69, 27-32.
- Berilgen, M. M. (2007). Evaluation of local site effects on earthquake damages of Fatih mosque, *Engineering Geology*. 91, 240-253.
- Bernard, P., Briole, P., Meyer, B., Lyon-Caen, H., Gomez, J.-M., Tiberi, C., Berge, C., Cattin, R., Hatzfeld, D., Lachet, C., Lebrun, B., Deschamps, A., Courboux, F., Larroque, C., Rigo, A., Massonnet, D., Papadimitriou, P., Kassaras, J., Diagourtas, D., Makropoulos, K., Veis, G., Papazisi, E., Mitsakaki, C., Karakostas, V., Papadimitriou, E., Papanastassiou, D., Chouliaras, M., and Stavrakakis, G. (1997). A low angle normal fault earthquake: the $M_s = 6.2$, June 1995 Aigion earthquake (Greece), *Journal of Seismology*. 1, 131-150.

- Bilham, R. (2015). Raising Kathmandu, *Nature Geoscience*. 8, 582-584.
- Blaser, L., Krüger, F., Ohrnberger, M., and Scherbaum, F. (2010). Scaling relations of earthquake source parameter estimates with special focus on subduction environment, *Bulletin of the Seismological Society of America*. 100, 2914-2926.
doi: 10.1785/0120100111.
- Boggs, S. Jr. (2001). *Principles of Sedimentology and Stratigraphy*. Prentice Hall, Inc., Upper Saddle River, New Jersey. pp. 267-320.
- Bohnhoff, M., Rische, M., Meier, T., Endrun, B., Becker, D., Harjes, H.-P., and Stavrakakis, G. (2004). CYC-NET: A temporary seismic network on the Cyclades (Aegean Sea, Greece), *Seismological Research Letters*. 75, 352-359.
- Boore, D. M. (1972). A note on the effect of simple topography on seismic SH waves, *Bulletin of the Seismological Society of America*. 62, 275-284.
- Boore, D. M. (1983). Stochastic simulation of high-frequency ground motions based on seismological models of radiated spectra, *Bulletin of the Seismological Society of America*. 73, 1865-1894.
- Boore, D. M., and Atkinson, G. M. (1987). Stochastic prediction of ground motion and spectral response parameters at hard-rock sites in eastern North America, *Bulletin of the Seismological Society of America*. 77, 440-467.
- Boore, D. M., and Joyner, W. B. (1997). Site amplification for generic rock sites, *Bulletin of the Seismological Society of America*. 87, 327-341.
- Boore, D. M. (2003). SMSIM–Fortran programs for simulating ground motions from earthquakes: version 2.0—a revision of OFR 96-80-A, SMSIM–Fortran programs for simulating ground motions from earthquakes, U.S. Geological Survey, 56 pages.
- Boore, D. M. (2004). Can site response be predicted?, *Journal of Earthquake Engineering*. 8, 1-41.
- Boore, D. M., and Thompson, E. M. (2014). Path durations for use in the stochastic-method simulation of ground motions, *Bulletin of the Seismological Society of America*. 104, 2541-2552, doi: 10.1785/0120140058.
- Borcherdt, R. D., and Gibbs, J. F. (1976). Effects of local geological conditions in the San Francisco bay region on ground motions and the intensities of the 1906 earthquake, *Bulletin of the Seismological Society of America*. 66, 467-500.
- Borcherdt, R. D. (1994). Estimates of site-dependent response spectra for design (methodology and justification), *Earthquake Spectra*. 10, 617-653.
- Bottari, C., Bottari, A., Carveni, P., Saccà, C., Spigo, U., and Teramo, A. (2008). Evidence of seismic deformation of the paved floor of the decumanus at Tindari (SE, Sicily), *Geophysical Journal International*. 174, 213-222.
doi: 10.1111/j.1365-246X.2008.03772.x.
- Bottari, C., Stiros, S. C., and Teramo, A. (2009). Archaeological evidence for destructive earthquakes in Sicily between 400 B.C. and A.D. 600, *Geoarchaeology*. 24, 147-175.
- Bourova, E., Kassaras, I., Pedersen, H. A., Yanovskaya, T., Hatzfeld, D., and Kiratzi, A. (2005). Constraints on absolute S velocities beneath the Aegean Sea from surface wave analysis, *Geophysical Journal International*. 160, 1006-1019.
doi: 10.1111/j.1365-246X.2005.02565.x

- Bryson, R. A., Lamb, H. H., and Donley, D. L. (1974). Drought and the decline of Mycenae, *Antiquity*. 467, 46-50.
- Buck, V. (2006). *Archaeoseismology in the Atalanti Region, Central Mainland Greece: Theories, methods and practice*. Archaeopress, Oxford, England, BAR International Series 1552, 110 pages.
- Campillo, M., Gariel, J.C., Aki, J., and Sánchez-Sesma, F. J. (1989). Destructive strong ground motion in Mexico city: source, path, and site effects during great 1985 Michoacán Earthquake, *Bulletin of the Seismological Society of America*. 79, 1718-1735.
- Caputo, R., and Helly, B. (2008). The use of distinct disciplines to investigate past earthquakes, *Tectonophysics*. 453, 7-19.
- Caputo, R., Hinzen, K.-G., Liberatore, D., Schreiber, S., Helly, B., and Tziafalias, A. (2010). Quantitative archaeoseismological investigation of the Great Theatre of Larissa, Greece, *Bulletin of Earthquake Engineering*. doi 10.1007/s10518-010-9206-6.
- Castro, R. R., Rovelli, A., Cocco, M., Di Bona, M., and Pacor, F. (2001). Stochastic simulation of strong-motion records from the 26 September 1997 (Mw 6) Umbria-Marche (central Italy) earthquake, *Bulletin of the Seismological Society of America*. 91, 27-39.
- Cavanagh, W. G., and Laxton, R. R. (1981). The structural mechanics of the Mycenaean Tholos tombs, *The Annual of the British School of Athens*. 76, 109-140.
- Chandler, A. M., Lam, N. T. K., Tsang, H. H., and Sheikh, M. N. (2005a). Estimation of near-surface attenuation in bedrock for analysis of intraplate seismic hazard, *Journal of Seismology and Earthquake Engineering*. 7, 159-173.
- Chandler, A. M., Lam, N. T. K., and Tsang, H. H. (2005b). Shear wave velocity modeling in crustal rock for seismic hazard analysis, *Soil Dynamics and Earthquake Engineering*. 25, 167-185.
- Chandler, A. M., Lam, N. T. K., and Tsang, H. H. (2006). Near-surface attenuation modeling based on rock shear-wave velocity profile, *Soil Dynamics and Earthquake Engineering*. 26, 1004-1014.
- Chávez-García, F. J., and Cuenca, J. (1996). Site effects in Mexico city urban zone. A complementary study, *Soil Dynamics and Earthquake Engineering*. 15, 141-146.
- Chávez-García, F. J., Sánchez, R., and Hatzfeld, D. (1996). Topographic site effects and HVSR. A comparison between observations and theory, *Bulletin of the Seismological Society of America*. 86, 1559-1573.
- Chávez-García, F. J., Rodríguez, M., Field, E. H., and Hatzfeld, D. (1997). Topographic site effects. A comparison of two non-reference methods, *Bulletin of the Seismological Society of America*. 87, 1667-1673.
- Chávez-García, F. J., Raptakis, D., Makrab, K., and Pitilakis, M. (2000). Site effects at Euroseistest-II. Results from 2D numerical modeling and comparison with observations, *Soil Dynamics and Earthquake Engineering*. 19, 23-39.
- Chen, Q. S., Gao, G. Y., and Yang, J. (2011). Dynamic response of deep soft soil deposits under multidirectional earthquake loading, *Engineering Geology*. 121, 55-65.
- Chin, B-H., and Aki, K. (1991). Simultaneous study of the source, path, and site effects on strong ground motion during the 1989 Loma Prieta earthquake: A preliminary result on pervasive nonlinear site effects, *Bulletin of the Seismological Society of America*. 81, 1859-1884.

- Clarke, P. J., Davies, R. R., England, P. C., Parsons, B. E., Billiris, H., Paradissis, D., Veis, G., Denys, P. H., Cross, P. A., Ashkenazi, V., and Bingley, R. (1997). Geodetic estimate of seismic hazard in the gulf of Korinthos, *Geophysical Research Letters*. 24, 1303-1306.
- Clément, C., Sachpazi, M., Charvis, P., Graindorge, D., Laigle, M., Hirn, A., and Zafiroopoulos, G. (2004). Reflection–refraction seismics in the Gulf of Corinth: hints at deep structure and control of the deep marine basin, *Tectonophysics*. 391, 97-108.
- Clift, P. D., and Robertson, A. H. F. (1990). Deep-water basins within the Mesozoic carbonate platform of Argolis, Greece, *Journal of the Geological Society, London*. 147, 825-836. doi: 10.1144/gsjgs.147.5.0825.
- Clift, P. D. (1996). Accretion tectonics of the Neotethyan Ermioni complex, Peloponnese, Greece, *Journal of the Geological Society, London*. 153, 745-757.
- Comniakis, P. E., and Papazachos, B. C. (1980). Space and time distribution of the intermediate focal depth earthquakes in the Hellenic arc, *Tectonophysics*. 70, 35-47.
- Constable, S. C., Parker, R. L., and Constable, C. G., (1987). Occam's inversion: A practical algorithm for generating smooth models for electromagnetic sounding data, *Geophysics*. 52, 289-300.
- Cornou, C., and Bard, P.-Y. (2003). Site-to-bedrock over 1D transfer function ratio: An indicator of the proportion of edge-generated surface waves?, *Geophysical Research Letters*. 30, 1453. doi:10.1029/2002GL016593.
- Crouch, D. P. (1996). Environmental geology of ancient Greek cities, *Environmental Geology*. 27, 233-245.
- Damm-Meinhardt, U. in press. Baubefunde und stratigraphie der unterburg (kampagnen 1976 bis 1983) Die mykenische palastzeit (SH III B2) und beginnende nachpalastzeit (beginn SH III C). Tiryns 17.1, Forschungen und Berichte. Wiesbaden: Reichert.
- Danciu, L., and Tselentis, G-A. (2007). Engineering ground-motion parameters attenuation relationships for Greece, *Bulletin of the Seismological Society of America*. 97, 162-183. doi: 10.1785/0120040087.
- Dao, P. (2011). Marine geophysical and geomorphic survey of submerged Bronze Age shorelines and anchorage sites at Kalamianos (Korphos, Greece). Open Access Dissertations and Theses. Master Thesis, McMaster University, 141 pages. <http://digitalcommons.mcmaster.ca/opendissertations/6310>
- Davies, L. T., and West, L. R. (1973). Observed effects of topography on ground motion, *Bulletin of the Seismological Society of America*. 63, 283-298.
- Demakopoulou, K., Divari-Valakou, N., and Walberg, G. (1994). Excavations and restoration work in Midea 1990-1992, *Opuscula Atheniensia*. 20, 19-41.
- Demakopoulou, K. (1995). Mycenaean citadels: recent excavations on the acropolis of Midea in the Argolid, *Bulletin of the Institute of Classical Studies*. 40, 151-176.
- Demakopoulou, K., Divari-Valakou, N., Åström, P., and Walberg, G. (1996). Excavations in Midea 1994, *Opuscula Atheniensia*. 21, 13-32.
- Demakopoulou, K. (2012). *The Mycenaean acropolis of Midea*. Archaeological Receipts Fund Publications Department, Athens, 1-44.
- Drake, B. L. (2012). The influence of climatic change on the Late Bronze Age collapse and the Greek dark ages, *Journal of Archaeological Science*. 39, 1862-1870.

- Drakatos, T. G., Karastathis, V., Makris, J., Papoulia, J., and Stavrakakis, G. (2005). 3D crustal structure in the neotectonic basin of the gulf of Saronikos (Greece), *Tectonophysics*. 400, 55-65.
- Drakopoulos, J. C., and Srivastava, H. N. (1970). Investigations of the aftershocks of July 4, 1968 earthquake in Epidavros, *Annals of Geophysics*. 23, 1-20. doi: 10.4401/ag-5139.
- Dirlik, N. (2012). The Tholos tombs of Mycenaean Greece. Master Thesis, Uppsala University, 131 pages.
- Di Vita, A. (1995). Archaeologist and earthquakes: the case of 365 A.D., *Annali Di Geofisica*. XXXVIII, 971-976.
- Dziewonski, A. M., and Anderson, D. L. (1981). Preliminary Reference Earth Model, *Physics of the Earth and Planetary Interiors*. 24, 297-356.
- Dziewonski, B., Meier, T., Lebedev, S., Bohnhoff, M., Stavrakakis, G., and Harjes, H.-P. (2008). S velocity structure and radial anisotropy in the Aegean region from surface wave dispersion, *Geophysical Journal International*. 174, 593-616. doi: 10.1111/j.1365-246X.2008.03802.x.
- Endrun, B., Meier, T., Lebedev, S., Bohnhoff, M., Stavrakakis, G., and Harjes, H.-P. (2008). S velocity structure and radial anisotropy in the Aegean region from surface wave dispersion, *Geophysical Journal International*. 174, 593-616. doi: 10.1111/j.1365-246X.2008.03802.x.
- European Center on Prevention and Forecasting of Earthquakes and Protection Organization (ECPFEO), Tectonic Committee of the Geological Society of Greece. (1996). Neotectonic Map of Greece (Korinthos sheet, scale 1:1000000).
- Evans, A. (1928). *The palace of Minos, Part II*, McMillan: London, 844 pages.
- Fäh, D., Steimen, S., Oprsal, I., Ripperger, J., Wössner, J., Schatzmann, R., Kästil, P., Spottke, I., and Huggenberger, P. (2006). The earthquake of 250 A.D. in Augusta Raurica, a real event with a 3D effect?, *Journal of Seismology*. 10, 459-477.
- Falter, S. (2012). Erstellung und geologisch/morphologische Interpretation eines digitalen gelänemodells von Tiryns und Umgebung. Bachelor Thesis, Universität zu Köln (in German), 40 pages.
- Fields, N. (2004). *Mycenaean citadels ca. 1350-1200 BC*, Osprey Publishing, Oxford, 63 pages.
- Finke, E. A. W. (1988). Landscape evolution of the Argive plain, Greece: paleoecology, Holocene depositional history and coastline changes. Ph.D. Thesis, Stanford University. Ann Arbor: University Microfilms.
- Fischer, P. M. (1986). The Cyclopean-built wall of the Mycenaean citadel of Midea: a survey using electronic distance measuring equipment, *Journal of Field Archaeology (News and Short Contributions)*. 13, 499-503.
- Fletcher, J. B., and Boatwright, J. (2013). Site response and basin waves in the Sacramento-San Joaquin delta, California, *Bulletin of the Seismological Society of America*. 103, 196-210.
- Flotté, N., Sorel, D., Müller, C., and Tensi, J. (2005). Along strike changes in the structural evolution over a brittle detachment fault: example of the Pleistocene Corinth-Patras rift (Greece), *Tectonophysics*. 403, 77-94. doi:10.1016/j.tecto.2005.03.015.

- Force, E. R. (2008). Tectonic environments of ancient civilizations in the eastern hemisphere, *Geoarchaeology*. 23, 644-653.
- French, E. B. (1996). Evidence for an earthquake at Mycenae, in *Archaeoseismology* (eds. Stiros, S., and Jones, R. E.), pp. 51-54. Fitch Laboratory Occasional Paper No. 7, Athens. Exeter: Short Run Press.
- Friederich, W., and Dalkolmo, J. (1995). Complete synthetic seismograms for a spherically symmetric earth by a numerical computation of the Green's function in the frequency domain, *Geophysical Journal International*. 122, 537-550.
- Friedrich, W. L., Kromer, B., Friedrich, M., Heinemeier, J., Pfeiffer, T., and Talamo, S. (2006). Santorini eruption radiocarbon dated to 1627-1600 B.C., *Science*. 312, 548.
- Fritsche, S., and Fäh, D. (2009). The 1946 magnitude 6.1 earthquake in the Valais: site-effects as contributor to the damage, *Swiss Journal of Geosciences*. 102, 423-439. doi 10.1007/s00015-009-1340-2.
- Fytikas, M., Giuliani, O., Innocenti, F., Marinelli, G., and Mazzuoli, R. (1976). Geochronological data on recent magmatism of the Aegean Sea, *Tectonophysics*. 31, 29-34.
- Galadini, F., Hinzen, K. G., and Stiros, S. (2006). Archaeoseismology: methodological issues and procedure, *Journal of Seismology*. 10, 395-414. doi: 10.1007/s10950-006-9027-x.
- Galanakis, Y. (2007). The construction of the Aegisthus Tholos tomb at Mycenae and the 'Helladic Heresy', *The Annual of the British School at Athens*. 102, 239-256.
- Galanakis, Y. (2012). Mycenaean society and culture, in *The Encyclopedia of Ancient History* (eds. Bagnall, R. S., Brodersen, K., Champion, C. B., Erskine, A., and Huebner, S. R.), First Edition. Blackwell Publishing Ltd., 4653-4658. doi: 10.1002/9781444338386.wbeah02133.
- Gaki-Papanastassiou, K., Papanastassiou, D., and Maroukian, H. (1996). Geomorphic and archaeological-historical evidence for past earthquakes in Greece, *Annali di Geofisica*. XXXIX, 589-601.
- Gariel, J.C., Bard, P.-Y., and Pitilalds, K. (1991). A theoretical investigation of source, path and site effects during the 1986 Kalamata earthquake (Greece), *Geophysical Journal International*. 104, 165-177.
- Geli, L., Bard, P.-Y., and Jullien, B. (1988). The effect of topography on earthquake ground motion: A review and new results, *Bulletin of the Seismological Society of America*. 78, 42-63.
- Georgiou, Ch., and Galanakis, D. (2010). Neotectonic study of urban and suburban Nafplion area (Argolida-Greece), *Bulletin of the Geological Society of Greece*. XLIII, 1428-1437.
- Goldsworthy, M., Jackson, J., and Haines, J. (2002). The continuity of active faults systems in Greece, *Geophysical Journal International*. 148, 596-618.
- Garduño-Monroy, V. H., Macías, J. L., Oliveros, A., Hernández-Madrigal, V. M. (2012a). Progress in seismic and archaeoseismic studies in the zone of Mitla, Oaxaca. Earthquake Geology and Archaeology: science, society and seismic hazard. Abstract vol. 3 pp. 43-46. Proceedings of the 3rd INQUA-IGCP 567 International Workshop on Earthquake Geology, Palaeoseismology and Archaeoseismology. 19-24 November, Morelia, México.
- Garduño-Monroy, V. H., Benavente-Escóbar, C., Oliveros, A., Rodríguez-Pascua, M. A., Pérez-López- R., and Giner, J. L. (2012b). Evidence of past seisms in Cusco (Peru) and

- Tzintzuntzan (Mexico): cultural Relations. Earthquake Geology and Archaeology: Science, society and Seismic hazard. Abstract vol. 3 pp. 47-50. Proceedings of the 3rd INQUA-IGCP 567 International Workshop on Earthquake Geology, Palaeoseismology and Archaeoseismology. 19-24 November, Morelia México.
- Giardini, D., Woessner, J., Danciu, L., Valensise, G., Grünthal, G., Cotton, F., Akkar, S., Basili, R., Stucchi, M., Rovida, A., Stromeyer, D., Arvidsson, R., Meletti, F., Musson, R., Sesetyan, K., Demircioglu, M. B., Crowley, H., Pinho, R., Pitilakis, K., Douglas, J., Fonseca, J., Erdik, M., Campos-Costa, A., Glavatovic, B., Makropoulos, K., Lindholm, C., and Cameelbeeck, T. (2013). Seismic Hazard Harmonization in Europe (SHARE): Online Data Resource. doi: 10.12686/SED-00000001-SHARE.
- Guidoboni, E., and Bianchi, S. S. (1995). Collapse and seismic collapses in archaeology: proposal for a thematic atlas, *Annali Di Geofisica*. XXXVIII, 1013-1017.
- Haaf, N. (2015). Transient electromagnetic (TEM) measurements for exploring sedimentary structures in Tiryns and Midea, Greece. Master Thesis, University of Cologne, 204 pages.
- Harbi, A., Maouchea, S., Vaccari, F., Aoudia, A., Oussadou, F., Panza, G. F., and Benouar, D. (2007). Seismicity, seismic input and site effects in the Sahel—Algiers region (North Algeria), *Soil Dynamics and Earthquake Engineering*. 27, 427-447.
- Haroon, A., Adrian, J., Bergers, R., Gurk, M., Tezkan, B., Mammadov, A. L., and Novruzov, A. G. (2014). Joint inversion of long-offset and central-loop transient electromagnetic data: Application to a mud volcano exploration in Perekishkul, Azerbaijan, *Geophysical Prospecting*. 1-17. doi: 10.1111/1365-2478.12157.
- Hashash, Y. M. A., and Park, D. (2001). Non-linear one-dimensional seismic ground motion propagation in the Mississippi embayment, *Engineering Geology*. 62, 185-206.
- Hashash, Y. M. A., and Park, D. (2002). Viscous damping formulations and high frequency motion propagation in non-linear site response analysis, *Soil Dynamics and Earthquake Engineering*. 22, 611-624.
- Hashash, Y. A., Groholski, D. R., and Phillips, C. (2010). Recent advances in non-linear site response analysis. Fifth International Conference in Recent Advances in Geotechnical Earthquake Engineering and Soil Dynamics and Symposium in Honor of Professor I. M. Idriss. May 24-29, San Diego, California. Paper No. OSP 4, pp. 1-22.
- Hashash, Y. A. (2014). Current issues in evaluation of seismic site effects. The 18th Great Lakes Geotechnical and Geoenvironmental Conference (GLGGC), and The 2014 Chicago Geotechnical Lecture Series Geotechnical Earthquake Engineering. 02 May, 2014.
- Hashida, T., Stavrakakis, G., and Shimazaki, K. (1988). Three-dimensional seismic attenuation structure beneath the Aegean region and its tectonic implication, *Tectonophysics*. 145, 43-54.
- Hatzfeld, D., Pedotti, G., Hatzidimitriou, P., Panagiotopoulos, D., Scordilis, M., Drakopoulos, I., Makropoulos, K., Delibasis, N., Latousakis, I., Baskoutas, J., and Frogneux, M. (1989). The Hellenic subduction zone beneath the Peloponnesus: first results of a microearthquake study, *Earth and Planetary Science Letters*. 93, 283-291.
- Hatzfeld, D., and Martin, C. (1992). Intermediate depth seismicity in the Aegean defined by teleseismic data, *Earth and Planetary Science Letters*. 113, 267-275.
- Hatzfeld, D., Besnard, M., Markopoulos, K., Voulgaris, N., Kosuskouna, V., Hatzidimitriou, P., Panagiotopoulos, D., Karakaisis, G., Deschamps, A., and Lyon-Caen, H. (1993a).

- Subcrustal microearthquake seismicity and fault plane solutions beneath the Hellenic arc, *Journal of Geophysical Research*. 98, 9861-9870.
- Hatzfeld, D., Besnard, M., Markopoulos, K., and Hatzidimitriou, P. (1993b). Microearthquake seismicity and fault-plane solutions in the southern Aegean and its geodynamic implications, *Geophysical Journal International*. 115, 799-818.
- Hatzfeld, D. (1994). On the shape of the subducting slab beneath the Peloponnese, Greece, *Geophysical Research Letters*. 21, 173-176.
- Hatzfeld, D., Karakostas, V., Ziazia, M., Kassaras, I., Papadimitriou, E., Makropoulos, K., Voulgaris, N., and Papaioannou, C. (2000). Microseismicity and faulting geometry in the Gulf of Corinth (Greece), *Geophysics Journal International*. 141, 438-456.
- Hatzidimitriou, P. M. (1993). Attenuation of coda wave in northern Greece, *Pure Applied Geophysics*. 140, 63-78.
- Hatzidimitriou, P. M. (1995). S-wave attenuation in the crust in northern Greece, *Bulletin of the Seismological Society of America*. 85, 1381-1387.
- Hellenic Military Geographical Service (HMGS). (1951). Nafplion topographic charts 6386/1, 6385/2, 6385/4, 6386/3, 6386/5, 6385/6, 6395/1, 6395/2, 6396/3, 6395/4, 6386/7, and 6385/8 (in Greek), Scale 1:5,000.
- Hemingway, C., and Hemingway, S. (2000). "Mycenaean civilization". In Heilbrunn timeline of art history. New York: The Metropolitan Museum of Art. http://www.metmuseum.org/toah/hd/myce/hd_myce.htm (October 2003)
- Hinojosa-Prieto, H. R., and Hinzen, K.-G. (2015). Seismic velocity model and near-surface geology at Mycenaean Tiryns, Argive basin, Peloponnese, Greece, *Near Surface Geophysics*. 13, 103-113. doi: 10.3997/1873-0604.2015002.
- Hinzen, K.-G. (2005). The use of engineering seismological models to interpret archaeoseismological findings in Tolbiacum, Germany: A case study, *Bulletin of the Seismological Society of America*. 95, 521-539.
- Hinzen, K.-G., and Weiner, J. (2009). Testing a seismic scenario for the damage of the Neolithic wooden well of Erkelenz-Kückhoven, Germany, *Geological Society, London, Special Publications*. 316, 189-205.
- Hinzen, K.-G. (2009). Simulation of toppling columns in archaeoseismology, *Bulletin of the Seismological Society of America*. 99, 2855-2875.
- Hinzen, K.-G., Schreiber, S., and Yerli, B. (2010). The Lycian sarcophagus of Arttumpara, Turkey: testing seismogenic and anthropogenic damage scenarios, *Bulletin of the Seismological Society of America*. 100, 3148-3164.
- Hinzen, K.-G. (2011). Archaeoseismology, in *Encyclopedia of Solid Earth Geophysics* (ed. Gupta, H. K.), Springer, Heidelberg, 11-15. doi: 10.1007/978-90-481-8702-7.
- Hinzen, K.-G., Fleischer, C., Reamer, S. K., Schreiber, S., Schütte, S., and Yeril, B. (2011). Quantitative methods in archaeoseismology, *Quaternary International*. 242, 31-41.
- Hinzen, K.-G. (2012). Sensitivity of earthquake toppled columns to small changes in ground motion and geometry, *Israel Journal of Earth Sciences*. 58, 309-326. doi: 10.1560/IJES.58.3-4.309.
- Hinzen, K.-G., Schreiber, S., Fleischer, C., Reamer, S. K., and Wisona, I. (2012). Archaeoseismic study of damage in Roman and Medieval structures in the center of Cologne, Germany, *Journal of Seismology*. doi: 10.1007/s10950-012-9327-2.

- Hinzen, K.-G., Kehmeier, H., and Schreiber, S. (2013a). Quantitative archaeoseismological study of a Roman Mausoleum in Pinara (Turkey)-testing seismogenic and rockfall damage scenarios, *Bulletin of the Seismological Society of America*. 103, 1008-1021.
- Hinzen, K.-G., Fleischer, C., Hinojosa, H., Maran, J., Meinhardt, U., Reamer, S. K., Schweppe, G., and Tzislakis, J. (2013b). The Mycenaean palace of Tiryns, elements of a comprehensive archaeoseismic study, *Seismological Research Letters*. 84, 350.
- Hinzen, K.-G., Veters, M., Kalytta, T., Reamer, S. K., and Damm-Meinhardt, U. (2015). Testing the response of Mycenaean terracotta figures and vessels to earthquake ground motions, *Geoarchaeology*. 30, 1-18. doi: 10.1002/gea.21499.
- Hinzen, K.-G., Hinojosa-Prieto, H. R., and Kalytta, T. (Submitted). Earthquake site effects at Mycenaean Tiryns and Midea. *Seismological Research Letters*.
- Hough, S. E., Friberg, P. A., Busby, R., Field, E. F., Jacob, K. H., and Borchardt, R. D. (1990). Sediment induced amplification and the collapse of the Mimitz freeway, *Nature*. 344, 853-855.
- Hübner, C., and Giese, S. (2006). Bericht zur geophysikalischen prospektion im stadtgebiet von Tiryns. In: Deutsches Archäologisches Institut Archäologischer Anzeiger Vol. 1 Halbband, pp. 163-169. Verlag Philipp von Zabern.
- Idriss, I. M. (1990). Response of soft soil sites during earthquakes. *Proceedings of the Symposium to Honor Professor H. B. Seed*, Berkely, May, 273-289.
- Idriss, I. M. (1993). *Procedure for selecting earthquake ground motions at rock sites*. A Report to the U.S. Department of Commerce, 42 pages. <http://fire.nist.gov/bfrlpubs/fire91/PDF/f91026.pdf>
- Iakovidis, Sp. E. (1986). Destruction horizons at Late Bronze Age Mycenae, in *Philia Epi eis Gergion E. Mylonan, v. A.*, 233-260. Athens: Library of the Archaeological Society of Athens.
- Innocenti, F., Manetti, P., Peccerillo, A., and Poli, G. (1981). South Aegean volcanic arc: geochemical variations and geotectonic Implications, *Bulletin Volcanologique*. 44, 377-391.
- Jacobshagen, V. (1986). *Geologie von Griechenland*. Gebrüder Borntrager, Berlin, 363 pages.
- Jusseret, S., and Sintubin, M. (2013). The origins of an old myth: Sir Arthur Evans, Claude Schaeffer and the seismic destruction of Late Bronze Age eastern Mediterranean civilizations, *Seismological Research Letters, Historical Seismologist*. 84, 94-100.
- Jusseret, S., Langohr, C., and Sintubin, M. (2013). Tracking earthquake archaeological evidence in Late Minoan IIIB (~1300-1200 B.C.) Crete (Greece): A proof of concept, *Bulletin of the Seismological Society of America*. 103, 3026-3043. doi: 10.1785/0120130070.
- Jusseret, S. (2014). Contextualizing the birth of Mediterranean archaeology, *Antiquity*. 88, 964-974.
- Kalogeras, I. S., and Burton, P. W. (1996). Shear-wave velocity models from Rayleigh-wave dispersion in the broader Aegean area, *Geophysical Journal International*. 125, 679-695.
- Kalytta, T. (2014). Site effects determined from local earthquake records at the Mycenaean citadels of Tiryns and Midea, Greece. Master Thesis, Rheinische Friedrich-Wilhelms-Universität Bonn, 73 pages.
- Kaniewski, D., Paulissen, E., Van Campo, E., Weiss, H., Otto, T., Bretschneider, J., and Van

- Lerberghe, K. (2010). Late second-early first millennium BC abrupt climate changes in coastal Syria and their possible significance for the history of the eastern Mediterranean, *Quaternary Research*. 74, 207-215.
- Kanta, A., Soupios, P., Barsukov, P., Kouli, M., and Vallianatos, F. (2013). Aquifer characterization using shallow geophysics in the Keritis basin of western Crete, Greece, *Environmental Earth Sciences* (Springer). doi: 10.1007/s12665-013-2503-z.
- Karagianni, E. E., Panagiotopoulos, D. G., Panza, G. F., Suhadolc, P., Papazachos, C. B., Papazachos, B. C., Kiratzi, A., Hatzfeld, D., Makropoulos, K., Priestley, K., and Vuan, A. (2002). Rayleigh wave group velocity tomography in the Aegean area, *Tectonophysics*. 358, 187-209.
- Karagianni, E.E., Papazachos, C. B., Panagiotopoulos, D. G., Suhadolc, P., Vuan, A., and Panza, G. F. (2005). Shear velocity structure in the Aegean area obtained by inversion of Rayleigh waves, *Geophysical Journal International*. 160, 127-143.
- Karagianni, A., Karoutzos, G., Ktena, S., Vagenas, N., Vlachopoulos, I., Sabatakis, N., and Koukis, G. (2010). Elastic properties of rocks, *Bulletin of the Geological Society of Greece*. 43, 1165-1168.
- Karastathis, V. K., Karmis, P., Novikova, T., Roumelioti, Z., Gerolymatou, E., Papanastassiou, D., Lakopoulos, S., Tsombos, P., and Papadopoulos, G. A. (2010a). The contribution to geophysical techniques to site characterization and liquefaction risk assessment: case study of Nafplion city, Greece, *Journal of Applied Geophysics*. 72, 194-211.
- Karastathis, V. K., Papadopoulos, G. A., Novikova, T., Roumelioti, Z., Karmis, P., and Tsombos, P. (2010b). Prediction and evaluation of nonlinear site response with potentially liquefiable layers in the area of Nafplion (Peloponnesus, Greece) for a repeat of historical earthquakes, *Natural Hazards and Earth System Sciences*. 10, 2281-2304.
- Karcz, I., and Kafri, U. (1978). Evaluation of supposed archaeoseismic damage in Israel, *Journal of Archaeological Science*. 5, 237-253.
- Karmis, P. (2008). Electrical-electromagnetical survey at the urban area of Nafplion, Argolis prefecture. Technical report, Institute of Geology and Mineral Exploration of (I.G.M.E.), Athens, Greece.
- Karmis, P. D., Giannoupoulos, P., and Tsombos, P. (2010). Geophysical investigations at Nafplion city, Greece: hydrogeological implications, *Bulletin of the Geological Society of Greece*. 43, 1447-1456.
- Karkanis, P., Dabney, M .K., Smith, R. A, K., and Wright, J. C. (2012). The geoarchaeology of Mycenaean chamber tombs, *Journal of Archaeological Science*. 39, 2722-2732.
- Karo, G. (1934). "Die Perseia von Mykenai," *American Journal of Archaeology*. 38, 123-127.
- Kawase, H. (1996). The cause of the damage belt in Kobe: "The basin-edge effect," constructive interference of the direct S-wave with the basin-induced diffraction/Rayleigh waves, *Seismological Research Letters*. 67, 25-34.
- Kawase, H. (2003). Site effects on strong ground motions, in *International Handbook of Earthquake & Engineering Seismology: Part B*. William H.K. Lee, Hiro Kanamori, Paul c. Jennings, and Carl Kisslinger (Editors), International Association of Seismology and Physics of the Earth's Interior (IASPEI), 1013-1030.

- Kiratzi, A., and Louvari, E. (2003). Focal mechanisms of shallow earthquakes in the Aegean Sea and the surrounding lands determined by waveform modeling: a new database, *Journal of Geodynamics*. 36, 251-274.
- Kilian, K. (1978). Ausgrabungen in Tiryns 1976. *Bericht zu den Grabungen, Archäologischer Anzeiger*. 1978, 449-470.
- Kilian, K. (1980). Zum Ende der mykenischen Epoche in der Argolis. *Jarbuch des Römisch-Germanischen Zentralmuseums Mainz*. 27, 166-195.
- Kilian, K. (1983). Ausgrabungen in Tiryns 1981. *Bericht zu den Grabungen, Archäologisches Anzeiger*. 97, 392-430.
- Kilian, K. (1988). Mycenaean up to date, trends and changes in recent research, in *Problems in Greek Prehistory* (eds. French, E. B., and Wardle, K. A.). 115-112. Bristol Classical Press, 609 pages.
- Kilian, K. (1996). Earthquakes and archaeological context at 13th century BC Tiryns, in *Archaeoseismology* (eds. Stiros, S., and Jones, R. E.), pp. 63-68. Fitch Laboratory Occasional Paper No. 7, Athens. Exeter: Short Run Press.
- King, G., and Bailey, G. (2006). Tectonics and human evolution, *Antiquity*. 80, 265-286.
- Klein, N. L. (1997). Excavation of the Greek temples at Mycenae by the British School at Athens. *The Annual of the British School at Athens*. 92, 247-322.
- Klimis, N. S., Margaritis, B. N., and Koliopoulos, B. N. (1999). Site-dependent amplification functions and response spectra in Greece, *Journal of Earthquake Engineering*. 3, 237-270.
- Koçkar, M. K., and Akgün, H. (2012). Evaluation of the site effects of the Ankara basin, Turkey, *Journal of Applied Geophysics*. 83, 120-134.
- Konstantinou, K. I., Melis, N. S., Lee, S.-J., Evangelidis, C. P., and Boukouras, K. (2009). Rupture process and aftershocks relocation of the 8 June 2008 Mw 6.4 earthquake in northwestern Peloponnese, western Greece, *Bulletin of the Seismological Society of America*. 99, 3374-3389.
- Koukouvelas, I., Mpresiakas, A., Sokos, E., and Doutsos, T. (1996). The tectonic setting and earthquake ground hazards of the 1993 Pyrgos earthquake, Peloponnese, Greece, *Journal of the Geological Society*. 153, 39-49. doi: 10.1144/gsjgs.153.1.0039.
- Kouskouna, V., and Makropoulos, K. (2004). Historical earthquakes investigations in Greece, *Annals of Geophysics*. 47, 723-731.
- Kovachev, S. A., Kuzin, I. P., Shoda, O. Yu, and Soloviev, S. L. (1991), Attenuation of S waves in the lithosphere of the Sea of Crete according to OBS observations, *Physics of the Earth and Planetary Interiors*. 69,101-111.
- Kraft, J. C., Aschenbrenner, S. E., and Rapp, G. J. (1977). Paleogeographic reconstructions of coastal Aegean archaeological sites, *Science*. 195, 941-947.
- Kramer, S. L. (1996). *Geotechnical earthquake engineering*. Prentice-Hall International Series in Civil Engineering and Engineering Mechanics. New Jersey, USA, 653 pages.
- Lachet, C., Hatzfeld, D., Bard, P.-Y., Theodulidis, N., Papaioannou, C., and Savvaidis, A. (1996). Site effects and microzonation in the city of Thessaloniki (Greece) comparison of different approaches, *Bulletin of the Seismological Society of America*. 86, 1692-1703.
- Latorre, D., Virieux, J., Monfret, T., Monteiller, V., Vanorio, T., Got, J.-L., and Lyon-Caen, H. (2004). A new seismic tomography of Aigion area (Gulf of Corinth, Greece) from the 1991 data set, *Geophysical Journal International*. 159, 1013-1031.

- Lazaridou-Varotsou, M., and Papanikolaou, D. (1987). Tectonoelectric zonation in the Hellenic Arc, *Tectonophysics*. 143, 337-342.
- Le Meur, H., Virieux, J., and Podvin, P. (1997). Seismic tomography of the gulf of Corinth: a comparison of methods, *Annali di Geofisica*. XL, 1-24.
- Lermo, J., and Chávez-García, F. J. (1994). Site effect evaluation at Mexico city: dominant period and relative amplification from strong motion and microtremor records, *Soil Dynamics and Earthquake Engineering*. 13, 413-423.
- Lyon-Caen, H., Armijo, R., Drakopoulos, J., Baskoutass, J., Delibassis, N., Gaulon, R., Kouslouna, V., Latoussakis, J., Makropoulos, K., Papadimitriou, P., Papanastassiou, D., and Pedotti, G. (1988). The 1986 Kalamata (south Peloponnesus) earthquake: detailed study of a normal fault, evidences for east-west extension in the Hellenic arc, *Journal of Geophysical Research*. 93, 14,967-15,000.
- Machette, M. N. (2000). Active, capable, and potentially active faults—a paleoseismic perspective, *Journal of Geodynamics*. 29, 387-392.
- Makris, J. (1978). The crust and upper mantle of the Aegean region from deep seismic soundings, *Tectonophysics*. 46, 269-284.
- Makris, J., Papoulia, J., and Drakatos, G. (2004). Tectonic deformation and microseismicity of the Saronikos gulf, Greece, *Bulletin of the Seismological Society of America*. 94, 920-929.
- Makropoulos, K. C., and Burton, P. W. (1984). Greek tectonics and seismicity, *Tectonophysics*. 106, 275-304.
- Makropoulos, K. C., Kaviris, G., and Kouskouna, V. (2012). An updated and extended earthquake catalog for Greece and adjacent areas since 1900, *Natural Hazards and Earth System Sciences*. 12, 1425-1430. doi:10.5194/nhess-12-1425-2012.
- Manning, S.W., Ramsey, C. B., Kutschera, W., Higham, T., Kromer, B., Steier, P., and Wild, E. M. (2006). Chronology for the Aegean Late Bronze Age 1700–1400 B.C., *Science*. 312, 565-569.
- Maran, J. (2004a). The spreading of objects and ideas in the Late Bronze Age eastern Mediterranean: two case examples from the Argolid of the 13th and 12th Centuries B.C.E., *Bulletin of the American School of Oriental Research*. 336, 11-30.
- Maran, J. (2004b). Architektonische innovation im spätmykenischen Tiryns—Lokale bauprogramme und fremde kultureinflüsse, in *Althellenische Technologie und Technik*, Conference (ed. Kyriatsoulis, A.). Proceedings Ohlstadt 21.-23.03.2003, Weilheim, 261-286.
- Maran, J. (2006). ‘Coming to terms with the past: ideology and power in Late Helladic IIIC’, in *Ancient Greece: from the Mycenaean palaces to the age of Homer* (eds. Deger-Jalkotzy, S., and Lemos, I.), 123-150 pp. Edinburgh: Edinburgh University Press,.
- Maran, J. (2010). Tiryns, in *The Oxford Handbook of the Bronze Age Aegean* (ca. 3000-1000 BC) (ed. Cline, E. H.), pp. 722-736. Oxford University Press, Inc.
- Marco, S. (2008). Recognition of earthquake-related damage in archaeological sites: examples from the Dead Sea fault zone, *Tectonophysics*. 453, 148-156.
- Margaris, B. N., and Boore, D. M. (1998). Determination of $\Delta\sigma$ and κ_0 from response spectra earthquakes in Greece, *Bulletin of the Seismological Society of America*. 88, 170-182.

- Marinos, P., and Hoek, E. (2001). Estimating the geotechnical properties of heterogeneous rock masses such as flysch, *Bulletin of Engineering Geology and the Environment*. 60, 85-92.
- Marinos, V. Fortsakis, P., and Prountzopoulos, G. (2006). Estimation of rock mass properties of heavily sheared flysch using data from tunneling construction. *The Geological Society of London*. IAEG2006 Paper number 314, 1-12.
- Marinos, P. V., and Tsiambaos, G. (2010). Strength and deformability of specific sedimentary and ophiolitic rocks, *Bulletin of the Geological Society of Greece*. 43, 1259-1266.
- Martin, C. (1988). Geometrie et cinématique de la subduction Egéenne structure en vitesse et en atténuation sous le Peloponnes. Thèse, Université Joseph Fourier, Grenoble, 262 pages.
- Maroukian, H., Gaki-Papanastassiou, K., and Papanastassiou, D. (1996). Geomorphologic-seismotectonic observations in relation to the catastrophes at Mycenae, in *Archaeoseismology* (eds. Stiros, S., and Jones, R. E.), pp. 189-194. Fitch Laboratory Occasional Paper No. 7, Athens. Exeter: Short Run Press.
- Maroukian, H., Gaki-Papanastassiou, K., and Piteros, Ch. (2004). Geomorphological and archaeological study of the broader area of the Mycenaean dam of Megalo Rema and ancient Tiryns, southeastern Argive plain, Peloponnesus, *Bulletin of the Geological Society of Greece*. 36, 1154-1163.
- Maufroy, E., Chaljub, E., Hollender, F., Kristek, J., Moczo, P., Klin, P., Priolo, E., Iwaki, A., Iwata, T., Etienne, V., De Martin, F., Theodoulidis, N. P., Manakou, M., Guyonenet-Benaize, C., Pitilakis, K., and Bard, P.-Y. (2015). Earthquake ground motion in the Mydgonian basin, Greece: The E2VP verification and validation of 3D numerical simulation up to 4 Hz, *Bulletin of the Seismological Society of America*. 105, 1398-1418. doi: 10.1785/0120140228.
- McClusky, S., Balassanian, S., Barka, A., Demir, C., Ergintav, S., Georgiev, I., Gurkan, O., Hamburger, M., Hurst, K., Kahle, H., Kastens, K., Kekelidze, G., King, R., Kotzev, V., Lenk, O., Mahmoud, S., Mishin, A., Nadariya, M., Ouzounis, A., Paradissis, D., Peter, Y., Prilepin, M., Reilinger, R., Sanli, I., Seeger, H., Tealeb, A., Toksöz, M. N., and Veis, G. (2000). Global positioning system constraints on plate kinematics and dynamics in the eastern Mediterranean and Caucasus, *Journal of Geophysical Research*. 105, 5695-5719.
- McCoy, F. W., and Heiken, G. (2000). Tsunami generated by the Late Bronze Age eruption of Thera (Santorini), Greece, *Pure and Applied Geophysics*. 157, 1227-1256.
- McKenzie, D. P. (1972). Active tectonics of the Mediterranean region, *Geophysical Journal International*. 30, 109-185.
- McKenzie, D. P. (1978). Active tectonics of the Alpine-Himalayan belt: the Aegean Sea and surrounding regions, *Geophysical Journal International*. 55, 217-254.
- Mee, C. B., and Cavanagh, W. G. (1984). Mycenaean tombs as evidence of social and political organization, *Oxford Journal of Archaeology*. 3, 45-64.
- Mee, C. B., and Cavanagh, W. G. (1990). The spatial distribution of Mycenaean tombs. *The Annual of the British School of Athens*. 85, 225-243.
- Meier, T., Rische, M., Endrun, B., Vafidis, A., and Harjes, H.-P. (2004). Seismicity of the Hellenic subduction zone in the area of western and central Crete observed by temporary local seismic networks, *Tectonophysics*. 383, 149-169.

- Menq, F.-Y. (2003). Dynamic properties of sandy and gravelly soils. Ph.D. Thesis, The University of Texas at Austin, 390 pages.
- Meng, J. (2007). Earthquake ground motion simulation with frequency-dependent soil properties, *Soil Dynamics and Earthquake Engineering*. 27, 234-241.
- Michetti, A. M., Esposito, E., Guerrieri, L., Porfido, S., Serva, L., Taatevossian, R., Vittori, E., Audemard, F., Azuma, T., Clague, J., Comercia, V., Gürppinar, A., McCalpin, J., Mohammadioun, B., Morner, N. A., Ota, Y., and Roghozin, E. (2015). Earthquake Environmental Effect for seismic hazard assessment: the ESI intensity scale and the EEE Catalogue, in *Memorie Descrittive della Carta Geologica d'Italia* (eds. Audemard, F., Azuma, T., Baiocco, F., Baize, S., Blumetti, A. M., Brustia, E., Clague, J., Commerci, V., Esposito, E., Guerrieri, L., Gurppinar, A., Grützner, C., Jin, K., Kim, Y. S., Kopsachilis, V., Lucarini, M., McCalpin, J., Michetti, A. M., Mohammadioun, B., Morner, N. A., Okumura, K., Ota, Y., Papathanassiou, G., Pavlides, S., Perez López, R., Porfido, S., Rreicheter, K., Rodríguez Pascua, M. A., Roghozin, E., Scaramella, A., Serva, L., Silva, P. G., Sintubin, M., Tatevossian, R., and Vittori, E.). XCVII, 11-20.
- Middleton, G. D. (2008). The collapse of palatial society in LBA Greece and the post-palatial period. Ph.D. Thesis, Durham University, 433 pages. Available at Durham E-Theses Online: <http://etheses.dur.ac.uk/2900/>
- Middleton, G. D. (2012). Nothing lasts forever: environmental discourses on the collapse of past societies, *Journal of Archaeological Research*. 20, 257-307.
doi:10.1007/s10814-011-9054-1.
- Mitropoulos, D., and Zananiri, I. (2010). Upper Quaternary evolution of the northern Argolis gulf, Nafplion area, *Bulletin of the Geological Society of Greece*. 43, 1474-1485.
- Mohammadioun, B., and Serva, L. (2001). Stress drop, slip type, earthquake magnitude, and seismic hazard, *Bulletin of the Seismological Society of America*. 91, 694-707.
- Mohraz, B. (1976). A study of earthquake response spectra for different geological conditions, *Bulletin of the Seismological Society of America*. 66, 915-935.
- Molnar, P., Anderson, R. S., and Anderson, S. P. (2007). Tectonics, fracturing of rock, and erosion, *Journal of Geophysical Research*. 112, 1-12. F03014, doi:10.1029/2005JF000433
- Mollidor, L., Tezkan, B., Bergers, R., and Löhken, J. (2013). Float-TEM: in-loop transient electromagnetic measurements on lake Holzmaar, Germany, *Geophysical Prospecting*. 61, 1056-1065.
- Moretti, I., Sakellariou, D., Lykousis, V., Micarelli, L. (2003). The gulf of Corinth: an active half Graben?, *Journal of Geodynamics*. 36, 323-340.
- Mühlenbruch, T. (2013). Baubefunde und stratigraphie der unterburg und des nordwestlichen stadtgebiets (campagnen 1976 bis 1983). Die mykenische nachpalastzeit (SH III C). Text, Tiryns 17.2, Forschungen und Berichte. Wiesbaden: Reichert.
- Murphy, J. R., Davis, A. H., and Weaver, N. L. (1971). Amplification of seismic body waves by low-velocity surface layers, *Bulletin of the Seismological Society of America*. 61, 109-145.
- Narayan, J. P., and Kumar, V. (2015). A numerical study of effects of ridge-weathering and ridge-shape-ratio on the ground motion characteristics, *Journal of Seismology*. 19, 83-104.

- NEHRP (National Earthquake Hazard Reduction Program). (2003). NEHRP recommended provisions for seismic regulations for new buildings and other structures (FEMA 450) part 1 (provisions).
- Nguyen, F., Van Rompaey, G., Teerlynck, H., Van Camp, M., Jongmans, D., and Camelbeeck, T. (2004). Use of microtremor measurement for assessing site effects in northern Belgium—interpretation of the observed intensity during the $M_S = 5.0$ June 11 1938 earthquake, *Journal of Seismology*. 8, 41-56.
- Nikonov, A. A. (1988). Reconstruction of the main parameters of old large earthquakes in Soviet central Asia using the palaeoseismological method, *Tectonophysics*. 147, 297-312.
- Ntageretzis, K. (2014). Paleotsunami imprints in the near-coast sedimentary records of the gulfs of Lakonia and Argolis (Peloponnese, Greece). Ph.D. Thesis. Johannes Gutenberg-Universität Mainz, 179 pages.
- Nur, A., and Cline, E. H. (2000). Poseidon's Horses: plate tectonics and earthquake storms in the Late Bronze Age Aegean and eastern Mediterranean, *Journal of Archaeological Science*. 27, 43-63.
- Nur, A., and Burges, D. (2008). *Apocalypse: earthquakes, archaeology, and the wrath of God*. Princeton University Press, 304 pages.
- Pacchiani, F., and Lyon-Caen. H. (2010). Geometry and spatio-temporal evolution of the 2001 Agios Ioanis earthquake swarm (Corinth Rift, Greece), *Geophysics Journal International*. 180, 59-72.
- Pham, V. N., Bernard, P., Boyer, D., Chouliaras, G., Le Mouél, J. L., and Stavrakakis, G. N. (2000). Electrical conductivity and crustal structure beneath the central Hellenides around the gulf of Corinth (Greece) and their relationship with the seismotectonics, *Geophysical Journal International*. 142, 948-969.
- Papadimitriou, A. (2001). *Tiryns: A guide to its history and archaeology*. Hesperos editions, Athens, 1-72.
- Papadopoulos, G. A., and Kijko, A. (1991). Maximum likelihood estimation of earthquake hazard parameters in the Aegean area from mixed data, *Tectonophysics*. 185, 277-294.
- Papadopoulos, G. A. (1996). An earthquake engineering approach to the collapse of the Mycenaean palace civilization of the Greek mainland, in *Archaeoseismology* (eds. Stiros, S., and Jones, R. E.), pp. 205-209. Fitch Laboratory Occasional Paper No. 7, Athens. Exeter: Short Run Press.
- Papadopoulos, G. A., Vassilopoulou, A., and Plessa, A. (2000). A catalogue of historical earthquakes for central Greece: 480 B.C.–A.D. 1910, Institute of Geodynamics, National Observatory of Athens, Publ. no. 11.
- Papadopoulos, G. A. (2011). A seismic history of Crete: earthquakes and tsunamis, 2000 B.C.–A.D. 2010. Ocelotos Publications, Athens, 415 pages.
- Papadopoulos, G. A., Grácia, E., Urgeles, R., Sallares, V., De Martini, P. M., Pantosti, D., González, M., Yalciner, A. C., Mascle, J., Sakellariou, D., Salamon, A., Tinti, S., Karastathis, V., Fokaefs, A., Camerlenghi, A., Novikova, T., and Papageorgiou, A. (2014). Historical and pre-historical tsunamis in the Mediterranean and its connected seas: geological signatures, generation mechanisms and coastal impacts, *Marine Geology*. 354, 81-109.

- Papaioannou, C. A., and Papazachos, B. C. (2000). Time-independent and time-dependent seismic hazard in Greece based on seismogenic sources, *Bulletin of the Seismological Society of America*. 90, 22-33.
- Papanastassiou, D., Maroukian, D. H., and Gaki-Papanastassiou, K. (1993). Morphotectonic and archaeological observations in the eastern Argive plain (eastern Peloponnese, Greece), and their palaeoseismological implications, *Zeitschrift für Geomorphologie Supplement Volumes*. 94, 95-105.
- Papanikolaou, D., Chronis, G., and Metaxas, C. (1994). Neotectonic structure of the Argolic gulf, *Bulletin of the Geological Society of Greece*. 30, 305-316.
- Papanikolaou, D. J., and Royden, L. H. (2007). Disruption of the Hellenic arc: late Miocene extensional detachment faults and steep Pliocene-Quaternary normal faults-or what happened at Corinth?, *Tectonics*. 26, 1-16, TC5003, doi:10.1029/2006TC002007.
- Papastamatiou, J., Vetoulis, D., Tataris, A., Christodoulou, G., Bornova, J., Lalechos, N., and Kounis, G. (1960). Argos sheet in scale 1:50,000, geological map of Greece. Institute for Geology and Subsurface Research, Athens, Greece.
- Papathanassiou, G., Valkaniotis, S., Chztipetros, Al., and Pavlides, S. (2010). Liquefaction susceptibility map of Greece, *Bulletin of the Geological Society of Greece*. 43, 1383-1392.
- Papoulia, J., Nocolich, R., Makris, J., Slejko, D., Mascle, J., Papadopoulos, G., Anagnostou, Ch., Camera, L., Daskalaki, E., Fasoulaka, Ch., Fokaefs, A., Fountoulis, I., Garcia, J., Gülkan, P., Mariolakos, I., Pomonis, A., Santulin, M., Tsambas, A., Wardell, N., and Yalçiner, A. (2014). A new seismogenic model for the Kyparissiakos gulf and western Peloponnese (SW Hellenic Arc), *Bolletino di Geofisica Teorica ed Applicata*. 55, 405-432. doi: 10.4430/bgta0217.
- Papazachos, B. C. (1980). Seismicity rates and long-term earthquake prediction in the Aegean area, *Quaterniones Geod.* 3, 171-190.
- Papazachos, B., Kiratzi, A., Karacostas, B., Panagiotopoulos, D., Scordilis, E., and Mountrakis, D. M. (1988). Surface fault traces, fault plane solution and spatial distribution of the aftershocks of the September 13, 1986 earthquake of Kalamata (southern Greece), *Pure and Applied Geophysics*. 126, 55-68.
- Papazachos, C. B. (1992). Anisotropic radiation modelling of macroseismic intensities for estimation of the attenuation structure of the upper crust in Greece, *Pure and Applied Geophysics*. 138, 445-469.
- Papazachos, B. C., and Papaioannou, A. (1993). Long-term earthquake prediction in the Aegean area based on a time and magnitude predictable model, *Pure and Applied Geophysics*. 140, 593-612.
- Papazachos, C. B., Hatzidimitriou, P. M., Panagiotopoulos, D. G., and Tsokas, G. N. (1995). Tomography of the crust and upper mantle in southeast Europe, *Journal of Geophysical Research*. 100, 12405-12422.
- Papazachos, B. C. (1996). Large seismic faults in the Hellenic arc, *Annali di Geofisica*. XXXIX, 891-903.
- Papazachos, C., and Nolet, G. (1997). *P* and *S* deep velocity structure of the Hellenic area obtained by robust nonlinear inversion of travel times, *Journal of Geophysical Research*. 102, 8349-8367.

- Papazachos, B. C., Karakostas, V. G., Papazachos, C. B., and Scordilis, E. M. (2000a). The geometry of the Wadati-Benioff zone and lithospheric kinematics in the Hellenic arc, *Tectonophysics*. 319, 275-300.
- Papazachos, B. C., Comninakis, P. E., Karakaisis, G. F., Karakostas, B. G., Papaioannou, Ch. A., Papazachos, C. B., and Scordilis, E. M. (2000b). A catalogue of earthquakes in Greece and surrounding area for the period 550 BC-1999, Publ. Geoph. Lab., University of Thessaloniki, 1, 333 pages.
- Papazachos, B. C., and Papazachou, C. B. (2003). *The earthquakes of Greece*. Ziti Publications, 317 pages. (in Greek).
- Papazachos, B. C., Panagiotopoulos, E. M., Papazachos C. B., and Karakaisis, G. F. (2004). Global relations between seismic fault parameters and moment magnitude of earthquakes, *Bulletin of the Geological Society of Greece*. XXXVI, 1482-1489.
- Panzer, F., Lombardo, G., D'Amico, S., and Galea, P. (2013). Speedy techniques to evaluate seismic site effects in particular geomorphologic conditions: faults, cavities, landslides and topographic irregularities, in *Engineering Seismology, Geotechnical and Structural Earthquake Engineering* (ed. D'Amico, S.). doi: 10.5772/3361.
- Park, D., and Hashash, Y. M. A. (2004). Soil damping formulation in nonlinear time domain site response analysis, *Journal of Earthquake Engineering*. 8, 249-274.
- Pavlidis, S., and Caputo, R. (2004). Magnitudes versus faults' surface parameters: quantitative relationships from the Aegean region, *Tectonophysics*. 380, 159-188.
- Pavlidis, S., Caputo, R., Koukouvelas, S., Kokkalas, S., and Chatzipetros, A. (2006). Paleoseismological investigations of Aegean-type active faults in mainland Greece and their implications, in *Post-collisional tectonics and magmatism in the Mediterranean region and Asia* (eds. Dilek, Y., and Pavlidis, S.), *Geological Society of America Special Paper 409*, 175-188. doi: 10.1130/2006.2409(10).
- Pitarka, A., and Irikura, K. (1996). Basin structure effects on long-period strong motions in the San Fernando valley and the Los Angeles basin from the 1994 Northridge earthquake and an aftershock, *Bulletin of the Seismological Society of America*. 86, 126-137.
- Pitilakis, K., Margaris, B., Lekidis, V., Theodulidis, N., and Anastasiadis, A. (1992). The Griva, northern Greece, earthquake of December 21, 1990 (seismological, structural and geotechnical aspects), *European Earthquake Engineering*. 29, 20-35.
- Pedersen, H. A., Le Brun, B., Hatzfeld, D., Campillo, M., and Bard, P.-Y. (1994). Ground-motion amplitude across ridges, *Bulletin of the Seismological Society of America*. 84, 1169-1183.
- Persson, A. W. (1931). The royal tombs at Dendra near Midea, *Acta Regiae Societatis Humaniorum Litterarum Lundensis 15*. Lund, C. W. K. Gleerup, 151 pages.
- Pe-Piper, G., Piper, D. J. W., Reynolds, P. H. (1983). Paleomagnetic stratigraphy and radiometric dating of the Pliocene volcanic rocks of Aegina, Greece, *Bulletin Volcanologique*. 46, 1-7.
- Pe-Piper, G., and Piper, J. W. (2013). The effect of changing regional tectonics on an arc volcano: Methana, Greece, *Journal of Volcanology and Geothermal Research*. 260, 146-163.

- Photiades, A., and Skourtsis-Coroneou, V. (1994). Stratigraphic and paleogeographic evolution of the northern Argolis (Greece) during the Cretaceous–Paleogene, *Bulletin of the Geological Society of Greece*, XXX, 135-146.
- Photiades, A. (2010). Geological contributions to the tectono-stratigraphy of the Nafplion area (NW Argolis, Greece), *Bulletin of the Geological Society of Greece*. XLIII, 1495-1507.
- Piper, D. J. W., Panagos, A. G., and PE, G. C. (1978). Conglomeratic Miocene flysch, western Greece, *Journal of Sedimentary Petrology*. 48, 117-126.
- Pope, K. O., and van Andel, T. H. (1984). Late Quaternary alluviation and soil formation in the southern Argolid: its history, causes, and archaeological implications, *Journal of Archaeological Science*. 11, 281-306.
- Rapp, G. Jr. (1986). Assessing archaeological evidence for seismic catastrophes, *Geoarchaeology*. 1, 365-379.
- Raptakis, D., Chávez-García, F. J., Pitolakis, K. (2000). Site effects at Euroseistest–I. Determination of the valley structure and confrontation of observations with 1D analysis, *Soil Dynamics and Earthquake Engineering*. 19, 1-22.
- Rathje, E. M., Stokoe, K. H., and Rosenblad, B. (2003). Strong motion station characterization and site effects during the 1999 earthquake in Turkey, *Earthquake Spectra*. 19, 653-675.
- Reid, H. F. (1910). The mechanics of the earthquake, v. II of Lawson, A.C., chairman, The California earthquake of April 18, 1906: Report of the State Earthquake Investigation Commission: Carnegie Institution of Washington Publication 87, 192 pages.
- Rigo, A., Lyon-Caen, H., Armijo, R., Deschamps, A., Hatzfeld, D., Makropoulos, K., Papadimitriou, P., and Kassaras, I. (1996). A microseismic study in the western part of the gulf of Corinth (Greece): Implications for large-scale normal faulting mechanisms, *Geophysics Journal International*. 126, 663-688.
- Roumelioti, Z., Kiratzi, A., and Thodulidis, N. (2004). Stochastic strong ground-motion simulation of the 7 September 1999 Athens (Greece) earthquake, *Bulletin of the Seismological Society of America*. 94, 1036-1052.
- Roumelioti, Z., Benetatos, C., and Kiratzi, A. (2009). The 14 February 2008 earthquake (M6.7) sequence offshore south Peloponnese (Greece): Source models of the three strongest events, *Tectonophysics*. 471, 272-284.
- Robinson, D., Dhu, T., and Schneider, J. (2006). SUA: a computer program to compute regolith site-response and estimate uncertainty for probabilistic seismic hazard analyses, *Computers & Geosciences*. 32, 109-123.
- Rodríguez-Marek, A., Bray, J. D., and Abrahamson, N. A. (2001). An empirical geotechnical seismic site response procedure, *Earthquake Spectra*. 17, 65-87.
- Rodríguez-Pascua, M. A., Pérez-López, R., Giner-Robles, J. L., Silva, P. G., Garduño-Monroy, V. H., and Reicherter, K. (2011). A comprehensive classification of earthquake archaeological effects (EAE) in archaeoseismology: Application to ancient remains of Roman and Mesoamerican cultures, *Quaternary International*. 242, 20-30.
doi: 10.1016/j.quaint.2011.04.044.
- Royden, L. H., and Papanikolaou, D. J. (2011). Slab segmentation and late Cenozoic disruption of the Hellenic arc, *Geochemistry Geophysics Geosystems*. 12, 1-24, Q03010.
doi:10.1029/2010GC003280.

- Rusnak, J. A., and Mark, C. (1999). Using the point load test to determine the uniaxial compressive strength of coal measure rock. Proc. 19th Int. Conference on Ground Control in Mining, pp. 362-371.
- Sabatakakis, N., Koukis, G., Tsimbaos, G., and Papanakli, S. (2008). Index properties and strength variation controlled by microstructure for sedimentary rocks, *Engineering Geology*. 97, 80-90.
- Saccani, E., Padoa, E., and Photiades, A. (2003). Triassic mid-ocean ridge basalts from the Argolis Peninsula (Greece): new constraints for the early oceanization phases of the Neotethyan Pindos basin, in *Ophiolites in Earth History* (eds. Dilek, Y., and Robinson, P. T.), *Geological Society of London Special Publication*. 218, 109-127.
- Sachpazi, M., Hirn, A., Clement, C., Haslinger, M., Laigle, M., Kissling, E., Charvis, P., Hello, Y., Lépine, J.-C., Sapin, M., and Asorge, J. (2000). Western Hellenic and Cephalonia Transform: local earthquakes and plate transport and strain, *Tectonophysics*. 319, 301-319.
- Sachpazi, M., Clement, C., Laigle, M., Hirn, A., and Roussos, N. (2003). Rift structure, evolution and earthquakes in the gulf of Corinth, from reflection seismic images, *Earth Planetary Science Letters*. 216, 243-257.
- Şafak, E. (2001). Local site effects and dynamic soil behavior, *Soil Dynamics and Earthquake Engineering*. 21, 453-458.
- Satoh, T., Kawase, H., and Sato, T. (1995). Evaluation of local site effects and their removal from borehole records observed in the Sendai region, Japan, *Bulletin of the Seismological Society of America*. 85, 1770-1789.
- Sampson, A. (1996). Cases of earthquakes at Mycenaean and pre-Mycenaean Thebes, in *Archaeoseismology* (eds. Stiros, S., and Jones, R. E.), pp. 113-117. Fitch Laboratory Occasional Paper No. 7, Athens. Exeter: Short Run Press.
- Schliemann, H. (1886). *Tiryns: Der prähistorische Palast der Könige von Tiryns*. F. A. Brockhaus, Leipzig, 487 pages.
- Scholl, C. (2005). The influence of multidimensional structures on the interpretation of LOTEM data with one-dimensional models and the application to data from Israel. Ph.D. Thesis, Cologne University, 814 pages.
- Schreiber, S., Hinzen, K.-G., Fleischer, C., and Schütte, S. (2012). Excavation-parallel laser scanning of a medieval cesspit in the archaeological zone Cologne, Germany, *ACM Journal of Computing and Cultural Heritage*. 5, Article 12, 22 pages. doi: 10.1145/2362402.2362406.
- Seed, H. B., and Idriss, I. M. (1969). Influence of soil conditions on ground motions during earthquakes, *ASCE Journal of the Soil Mechanics and Foundations Division*. 95, 99-137.
- Seed, H. B., and Idriss, I. M. (1970). Soil moduli and damping factors for dynamic response analyses, Report EERC 70-10, Earthquake Engineering Research Center, University of California, Berkeley.
- Seed, H. B., Ugas, C., and Lysmer, J. (1976). Site-dependent spectra for earthquake-resistant design, *Bulletin of the Seismological Society of America*. 66, 221-243.
- Seed, H. B., and Sun, J. H. (1989). Implication of site effects in the Mexico city earthquake of September 19, 1985 for earthquake-resistant design criteria in the San Francisco bay area

- of California, Report No. UCB/EERC-89/03, Earthquake Engineering Research Center, University of California, Berkeley.
- Sekiguchi, H., and Iwata, T. (2002). Rupture process of the 1999 Kocaeli, Turkey, earthquake estimated from strong-motion waveforms, *Bulletin of the Seismological Society of America*. 91, 300-311.
- Shapiro, N. M., and Ritzwoller, M. H. (2002). Monte-Carlo inversion for a global shear-velocity model of the crust and upper mantle, *Geophysical Journal International*. 151, 88-105.
- Shaw, B. Ambraseys, N. N., England, P. C., Floyd, M. A., Gorman, G. J., Higham, T. F. G., Jackson, J. A., Nocquet, J.-M., Pain, C. C., and Piggott, M. D. (2008). Eastern Mediterranean tectonics and tsunami hazard inferred from the AD 365 earthquake, *Nature Geosciences*. 1, 268-276.
- Sheriff, R. E. (2006). *Encyclopedic Dictionary of Applied Geophysics*, Society of Exploration Geophysics, USA, 429 pages.
- Sintubin, M. (2011). Archaeoseismology: past, present and future, *Quaternary International*. 242, 4-10.
- Skarlatoudis, A. A., Papazachos, C. B., Margaris, B. N., Theodulidis, N., Papaioannou, Ch., Kalogeras, I., Scordilis, E. M., and Karakostas, V. (2003). Empirical peak ground-motion predictive relations for shallow earthquakes in Greece, *Bulletin of the Seismological society of America*. 93, 2591-2603.
- Skarlatoudis, A. A., Papazachos, C. B. Margaris, B. N., Ventouzi, C., Kalogeras, I., and the EGGLEADOS Group. (2013). Ground-motion prediction equations of intermediate-depth earthquakes in the Hellenic Arc, southern Aegean subduction area, *Bulletin of the Seismological society of America*. 103, 1952-1968.
- Somerville, P., and Moriwaki, Y. (2003). Seismic hazard and risk assessment in engineering practice, in *International Handbook of Earthquake & Engineering Seismology: Part B*. (eds. William, H.K. L., Kanamori, H., Jennings, P. C., and Kisslinger, C.), International Association of Seismology and Physics of the Earth's Interior (IASPEI), 1065-1080.
- Sørensen, M. B., Oprsal, I., Bonnefoy-Claudet, S., Atakan, K., Mai, P. M., Pulido, N., and Yalciner, K. (2006). Local site effects in Ataköy, Istanbul, Turkey, due to a future large earthquake in the Marmara Sea, *Geophysical Journal International*. 167, 1413-1424.
- Soupios, P., Barsukov, P., Gurk, M., and Savvaidis, A. (2013). Regional tectonic model of Volvi Lake in northern Greece by applying 3D TEM modeling. 20th International Geophysical Congress and Exhibition of Turkey, 25-27 November, Antalya, Turkey.
- Soupios, P., Hinojosa-Prieto, H. R., and Hinzen, K.-G. (2014). Mapping the soil-bedrock interface in the alluvial Argive basin (Greece) with TEM Soundings. 20th European Meeting of Environmental & Engineering Geophysics, Athens, Greece, 14-18 September, Extended Abstract.
- Spathari, E. (2001). *Mycenae: A guide to the history and archaeology*. Hesperos Editions, Athens, 96 pages.
- Spudich, P., and Frazer, L. N. (1984). Use of ray theory to calculate high-frequency radiation from earthquake source having spatially variable rupture velocity and stress drop, *Bulletin of the Seismological Society of America*. 74, 2061-2082.

- Soudoudi, F., Kind, R., Hatzfeld, D., Priestley, K., Hanka, W., Wylegalla, K., Stavrakakis, G., Vafidis, A., Harjes, H.-P., and Bohnhoff, M. (2006). Lithospheric structure of the Aegean obtained from P and S receiver functions, *Journal of Geophysical Research*. 111, 1-23. B12307, doi:10.1029/2005JB003932.
- Steidl, J. H., Tumarkin, A. G., and Archuleta, R. J. (1996). What is a reference site?, *Bulletin of the Seismological Society of America*. 86, 1733-1748.
- Stewart, J. P., Liu, A. H., and Choi, Y. (2003). Amplification factors for spectral acceleration in tectonically active regions, *Bulletin of the Seismological Society of America*. 93, 332-352.
- Stewart, J. P., On-Lei Kwok, A. Hashash, Y. M. A., Matasovic, N., Pyke, R., Wang, Z., and Yang, Z. (2008). Benchmarking of nonlinear geotechnical ground response analysis procedures. *PEER Report 2008/04 Pacific Earthquake Engineering Research Center*, College of Engineering University of California, Berkeley, 205 pages.
- Stewart, J. P., Klimis, N., Savvaidis, A., Theodoulidis, N., Zargli, E., Athanasopoulos, G., Pelekis, P., Mylonakis, G., and Margaris, B. (2014). Compilation of a local v_s profile database and its application for interface of v_{s30} from geologic- and terrain-based proxies, *Bulletin of the Seismological Society of America*. 104, 2827-2841. doi: 10.1785/0120130331.
- Stiros, S., and Jones, R. E. (1996). *Archaeoseismology*. Fitch Laboratory Occasional Paper No. 7, Athens. Exeter: Short Run Press.
- Stiros, S. (1996). Identification of earthquakes from archaeological data: methodology, criteria and limitations, in *Archaeoseismology* (eds. Stiros, S., and Jones, R. E.), pp. 129-152. Fitch Laboratory Occasional Paper No. 7, Athens. Exeter: Short Run Press.
- Stiros, S. (2010). The 8.5+ magnitude, AD 365 earthquake in Crete: coastal uplift, topography changes, archaeological and historical signature, *Quaternary International*. 216, 54-63.
- Stiros, S. C., and Pytharouli, S. I. (2014). Archaeological evidence for a destructive earthquake in Patras, Greece, *Journal of Seismology*. 18, 687-693.
- Stockhammer, Ph., and French, E. B. (2009). Mycenae and Tiryns: the pottery of the second half of the thirteenth century BC—contexts and definition, *Annual of the British School at Athens*. 104, 175-232.
- Stos-Gale, Z. A., and Gale, N. H. (1982). The sources of Mycenaean silver and lead, *Journal of Field Archaeology*. 9, 467-485.
- Strasser, F. O., Arango, M. C., and Bommer, J. J. (2010). Scaling of the source dimensions of interface and intraslab subduction-zone earthquakes with moment magnitude, *Seismological Research Letters*. 8, 941-950.
- Tartaron, T. F., Puller, D., Dunn, R., Tzortzopoulou-Gregory, L., Dill, A., and Boyce, J. L. (2011). The Saronic harbors archaeological research project (SHARP): Investigations at Mycenaean Kalamianos, 2007-2009. *Hesperia*. 80, 559-634.
- Tataris, A., Kallergis, G., Kounis, G., Bizon, G., and Christodoulou, G. (1970). Nafplion sheet in scale 1:50,000, Geological map of Greece. Institute for Geology and Subsurface Research, Athens, Greece.
- Taymaz, T., Jackson, J., and McKenzie, D. (1990). Earthquake mechanisms in the Hellenic trench near Crete, *Geophysics Journal International*. 102, 695-731.
- Taymaz, T., Yilmaz, Y., and Dilek, Y. (2007). The geodynamics of the Aegean and Anatolia:

- Introduction, in *The Geodynamics of the Aegean and Anatolia* (eds. Taymaz, T., Yilmaz, Y., and Dilek, Y.), *Geological Society of London, Special Publications*. 291, pp. 1-16.
- Tendürüs, M., van Wijngaarden, G. J., and Kars, H. (2010). Long-term effect of seismic activities on archaeological remains: A test study from Zakynthos, Greece, in *Ancient Earthquakes* (eds. Sintubin, M., Stewart, I. S., Niemi, T. M., and Altunel, E.), *Geological Society of America Special Paper 471*, The Geological Society of America, Boulder, Colorado, 145-156.
- Thompson, E. M., Baise, L. G., Tanaka, Y., and Kayen, R. E. (2012). A taxonomy of site response complexity, *Soil Dynamics and Earthquake Engineering*. 41, 32-43.
- Tiberi, C., Lyon-Caen, H., Hatzfeld, D., Achauer, U., Karagianni, E., Kiratzi, A., Louvari, E., Panagiotopoulos, D., Kassarars, I., Kaviris, G., Makropoulos, K., and Papadimitriou, P. (2001). Crustal and upper mantle structure beneath the Corinth rift (Greece) from a teleseismic tomography study, *Journal of Geophysical Research*. 105, 28159-28171.
- Tiberi, C., Diament, M., Lyon-Caen, H., and King, T. (2001). Moho topography beneath the Corinth rift area (Greece) from inversion of gravity data, *Geophysical Journal International*. 145, 797-808.
- Tirel, C., Gueydan, F., Tiberi, C., and Bruna, J.-P. (2004). Aegean crustal thickness inferred from gravity inversion. Geodynamical implications, *Earth and Planetary Science Letters*. 228, 267-280.
- Tselentis, G.-A., Drakopoulos, J., and Makropoulos, C. (1988). On the frequency dependence of Q in the Kalamata (south Greece) region as obtained from the analysis of the coda of the aftershocks of the Kalamata 1986 earthquake, *Tectonophysics*. 152, 157-159.
- Tselentis, G.-A., Serpetsidaki, A., Martakis, N., Sokos, E., Paraskevopoulos, P., and Kapotas, S. (2007). Local high-resolution passive seismic tomography and Kohonen neural networks—Application at the Rio-Antirio Strait, central Greece, *Geophysics*. 72, 93-106.
- Tselentis, G.-A., and Danciu, L. (2008). Empirical relationships between Modified Mercalli Intensity and engineering ground-motion parameters in Greece, *Bulletin of the Seismological Society of America*. 98, 1863-1875. doi: 10.1785/0120070172.
- Tselentis, G.-A., and Danciu, L. (2010a). Probabilistic seismic hazard assessment in Greece – Part 1: Engineering ground motion parameters, *Natural Hazards and Earth System Sciences*. 10, 1-15.
- Tselentis, G.-A., and Danciu, L. (2010b). Probabilistic seismic hazard assessment in Greece – Part 3: Deaggregation, *Natural Hazards and Earth System Sciences*. 10, 51-59.
- Tsokas, G., N., and Hansen, R. (1997). Study of the crustal thickness and the subducting lithosphere in Greece from gravity data, *Journal of Geophysical Research*. 102, 20585-20597.
- Tourloukis, V., and Karkanis, P. (2012). Geoarchaeology in Greece: A Review, *Journal of the Virtual Explorer*. 42, paper 4. doi: 10.3809/jvirtex.2012.00304.
- Tziallas, G. P., Saroglou, H., and Tsiambaos, G. (2013). Determination of mechanical properties of flysch using laboratory methods, *Engineering Geology*. 166, 81-89.
- Varti-Matarangas, M., Matarangas, D., and Panagidis, G. (2000). Study of the lithofacies of the building stones of the Tiryns acropolis monuments (Greece). ASMOSIA VI Proceedings of the Sixth International Conference of The Association for the Study of Marble and Other Stones in Antiquity. Venice, June 15-18.

- Varti-Matarangas, M., and Matarangas, D. (2000). Microfacies analysis and endogenic decay causes of carbonate building stones at the Asklepieion Epidaurus monuments of Peloponnese, Greece, *Journal of Cultural Heritage*. 1, 165-177.
- Vassilopoulou, S. (2010). Morphotectonic analysis of southern Argolis peninsula (Greece) based on ground and satellite data by GIS development, *Bulletin of the Geological Society of Greece*. XLIII, 516-526.
- van Andel, T. H., and Lianos, N. (1984). High-resolution seismic reflection profiles for the reconstruction of postglacial transgressive shorelines: An example from Greece, *Quaternary Research*. 22, 31-45.
- van Andel, T. H., Runnels, C. N., and Pope, K. O. (1986). Five thousand years of land use and abuse in the southern Argolid, Greece, *Hesperia: The Journal of the American School of Classical Studies at Athens*. 55, 103-128.
- van Andel, T. H., Zangger, E., and Demitrack, A. (1990a). Land use and soil erosion in prehistoric and historical Greece, *Journal of Field Archaeology*. 17, 379-396.
- van Andel, T. H., Zangger, E., and Perissoratis, C. (1990b). Quaternary transgressive/regressive cycles in the gulf of Argos, Greece, *Quaternary Research*. 34, 317-329.
- van Andel, T. H., Perissoratis, C., and Rondoyanni, T. (1993). Quaternary tectonics of the Argolikos gulf and adjacent basins, Greece, *Journal of Geological Society, London*. 150, 529-539.
- van der Meijde, M., van der Lee, S., and Giardini, D. (2003). Crustal structure beneath broadband seismic stations in the Mediterranean region, *Geophysical Journal International*. 152, 729-739.
- Voigt, S. (2013). Bodenbewegungsparameter von erdbeben in Griechenland an temporären stationen des HERACLES Projektes. Bachelor Thesis, Cologne University, 60 pages.
- von Papen, M., Tezkan, B., and Israil, M. (2013). Characterization of an aquifer in Roorkee, India using the spatially constrained inversion of in-loop TEM data, *Near Surface Geophysics*. 11, 85-94. doi:10.3997/1873-0604.2012011.
- Wald, D. J. (1995). A preliminary dislocation model for the 1995 Kobe (Hyogo-ken Nanbu), Japan earthquake determined from strong motion and teleseismic waveforms, *Seismological Research Letters*. 66, 22-28.
- Wald, D. J., and Allen, T. I. (2007). Topographic slope as a proxy for seismic site conditions and amplification, *Bulletin of the Seismological Society of America*. 97, 1379-1395. doi: 10.1785/0120060267.
- Walberg, G. (1998). Midea: the Megaron complex and shrine area: excavations on the lower terraces 1994-1997. Prehistory Monographs 20. Institute for Aegean Prehistory (INSTAP). Academic Press Philadelphia, Pennsylvania.
- Walberg, G. (2001). Midea excavations on the acropolis of Midea. Results of the Greek-Swedish excavations, *The Classical Review, New Series*. 51, 355-357.
- Wang, R. (1999). A simple orthonormalization method for stable and efficient computation of Green's functions, *Bulletin of the Seismological Society of America*. 89, 733-741.
- Weber, B. (2007). Bodenverstärkung in der südlichen Niederrheinischen bucht. Ph.D. Thesis, Cologne University, 142 pages.

- Wells, D. L., and Coppersmith, K. J. (1994). New empirical relationships among magnitude, rupture length, rupture width, rupture area, and surface displacement, *Bulletin of the Seismological Society of America*. 84, 974-1002.
- Weiss, B. (1982). The decline of Bronze Age civilization as a possible response to climate change, *Climatic Change*. 4, 173-198.
- Wen, R., Ren, Y., Zhou, Z., Shi, D. (2010). Preliminary site classification of free-field strong motion stations based on Wenchuan earthquake records, *Earthquake Science*. 23, 101-110.
- Yogeshwar, P., Tezkan, B. and Haroon, A. (2013). Investigation of the Azraq sedimentary basin, Jordan using integrated geoelectrical and electromagnetic techniques, *Near Surface Geophysics*. 11, 381-389.
- Yogeshwar, P. (2014). A resistivity-depth model of the central Azraq basin area, Jordan: 2D forward and inverse modeling of time domain electromagnetic data. Ph.D. Thesis, Cologne University, 210 pages.
- Zachos, K. (1996). Tracing a destructive earthquake in the southwestern Peloponnese (Greece) during the Early Bronze Age, in *Archaeoseismology* (eds. Stiros, S., and Jones, R. E.), pp. 169-185. Fitch Laboratory Occasional Paper No. 7, Athens. Exeter: Short Run Press.
- Zananiri, I., Chiotis, E., Tsombos, P., Hademonos, V., and Zervakou, A. (2010a). Geoarchaeological studies in urban and suburban areas of the Argolis prefecture, *Bulletin of the Geological Society of Greece*. XLIII, 1539-1548.
- Zananiri, I., Hademenos, V., and Piteros, C. (2010b). Geophysical investigations near the ancient Agora at the city of Argos, Greece, *Journal of Geophysics and Engineering*. 7, 171-182.
- Zangger, E. (1993). The geoarchaeology of the Argolid. Deutsches Archäologisches Institut Athens: Gebr. Mann Verlag Berlin, 153 pages.
- Zangger, E. (1994). Landscape changes around Tiryns during the Bronze Age, *American Journal of Archaeology*. 98, 189-212.
- Zelt, B. C., Taylor, B., Weiss, J., Goodliffe, A. M., Sachpazi, M., and Hirn, A. (2004). Streamer tomography velocity models for the gulf of Corinth and gulf of Itea, Greece, *Geophysical Journal International*. 159, 333-346.
- Zelt, B. C., Taylor, B., Sachpazi, M., and Hirn, A. (2005). Crustal velocity and moho structure beneath the gulf of Corinth, Greece, *Geophysical Journal International*. 162, 257-268.
- Zhang, J., and Zhao, J. X. (2009). Response spectral amplification ratios from 1- and 2-dimensional nonlinear soil site models, *Soil Dynamics and Earthquake Engineering*. 29, 563-573.
- Zhao, J. X., Zhang, J., and Irikura, K. (2009). Side effect of using response spectral amplification ratios for soil sites—variability and earthquake-magnitude and source-distance dependent amplification ratios for soil sites, *Soil Dynamics and Earthquake Engineering*. 29, 1262-1273.
- Zhao, J. X., and Zhang, J. (2010). Side-effect using response spectral amplification ratios for soft soil sites—earthquake source-type dependent amplification ratios, *Soil Dynamics and Earthquake Engineering*. 30, 258-269.
- Zoback, M. L. (2006). The 1906 earthquake and a century of progress in understanding earthquakes and their hazards, *GSA Today*. 16, 4-11. doi: 10.1130/GSAT01604.1.

ONLINE RESOURCES

<http://geophysics.geo.auth.gr>

www.geophysics.geol.uoa.gr

<http://www.gein.noa.gr/en/general>

<http://ciei.colorado.edu/~nshapiro/MODEL/>

http://en.wikipedia.org/wiki/Linear_B

http://www.sia.gr/en/research/field_projects/dendra_midea

<http://www.archaiologia.gr/en/blog/2013/09/05/the-mycenaean-acropolis-of-midea/>

http://www.metmuseum.org/toah/hd/myce/hd_myce.htm (October 2003)

<http://earthquake.usgs.gov/hazards/apps/vs30/>

earthquakes.usgs.gov/earthquakes/map/

APPENDIX A: Structural Geologic Field Data

Table 3.1: Summary of planar geologic structures and sedimentary features of the Tiryns bedrock.

Bedding	Joints	Karstic features	Fossils
Outcrop No. 1: light gray mudstone			
wavy parallel bedding planes w/smooth to rough surfaces; strike NW-SE and dip moderately towards the SW; very-thickly bedded (~2 m); forms equidimensional blocks	few widely spaced (~700 mm) ordinary joints; strike EW to NW-SE, dip N-NW moderately; joint face varies from wavy smooth-surface to rough-surface	pressure dissolution seams (15-25 cm long, 1-2 cm wide, sub-parallel to joints), diameter of potholes and vugs from 0.5-15 cm; some intersect each other	absent or not observed
Outcrop No. 2: light gray mudstone			
smooth surfaces define wavy-parallel bedding planes; very-thickly bedded (~2.5 m); moderately S-dipping beds strike E-W; forms tabular blocks	various widely spaced (~750 mm) parallel joints dip N-NE at high-to-moderate angles and trend EW to NW-SE; joint faces are mainly rough w/some wavy smooth-surfaces	very common in joint and bedding planes; include pressure dissolution seams (10-45 cm long, 1-3 cm wide, perpendicular and sub-parallel to joints), vugs diameter of 1-2 cm, and up to 5-cm for potholes. Most features intersect each other	absent or not observed
Outcrop No. 3: light gray mudstones-wackestones			
well-defined by sharp planar-parallel bedding planes; have smooth-to-rough surfaces; strike NW-SE and dip towards the S-SW at shallow-to-moderate angles; thickly to very-thickly bedded; generates tabular and equidimensional blocks	planar joints are laterally persistent, widely to very-widely spaced (0.60-2 m); strike EW to NW-SE and dip N-NW at moderate-to-steep angles; conjugate joint sets are parallel to the ordinary ones, but they dip north and south at steep angles; wavy-rough surfaces w/lesser planar-smooth surfaces	potholes, vugs, lapis and pressure dissolution seams are parallel and perpendicular to bedding planes. Thin (1-5 mm thick) white calcite veinlets are common suggesting tensional stresses	uppermost bed has high density of disarticulated, calcified bivalves depicting a both a pavement and a nested arrangement when seen on both bedding and bedding cross-section planes, respectively
Outcrop No. 4: gray, thickening upwards wackestones			
wavy non-parallel bedding planes w/wavy-smooth surfaces; strike NW-SE, dip SW shallowly; thickly to very-thickly (~3 m) bedded; 10 cm by 21 cm geopetal structure occurs at 29° with respect to lower bed, made up of yellowish-light brown fibrous calcite crystals indicating that beds are not overturned	extremely to very-closely spaced (<20-60 mm) parallel joints create thin (1-4 cm thick) tabular slabs; only some joint planes are measurable, striking E-W to NW-SE and dipping at steep angles towards the N and SW, respectively; smooth and wavy-rough joint faces	vugs, potholes (6-20 cm diameter) and few vertical pressure dissolution seams (25-30 cm long by 0.5-3 cm wide) which intersect large potholes when seen on bedding cross-section planes	some cm-scale broken, disarticulated, calcified bivalves and algae at bottom of lower and upper beds; nested-type arrangement only on bedding cross-section planes
Outcrop No. 5: light gray wackestones			
very-thickly bedded separated by wavy-to-planar parallel bedding planes w/wavy-smooth to rough surfaces; beds strike EW to SW-NE and dip shallowly towards the south-southeast; geopetal structure (16 by 34 cm) occurs at 13° w/respect to bedding planes, composed of five coarsening-upwards layers of yellowish-brown calcite crystals (0.5-2 cm-long) suggesting that beds are not overturned	ubiquitous medium-to-widely spaced parallel joints; mainly wavy-smooth w/fewer rough faces; strike EW, SW-NE, and NW-SE dipping at moderate-to-steep angles towards the N and S, NW, and NE, respectively; a conjugate joint set cuts a very thick bed striking EW and dipping at very steep angles towards the SSW and N. The N-dipping joint is mineralized w/a white coarse-grained calcite vein (7 cm thick) adjacent to 5-60 mm thick white-brownish wavy calcite veinlet w/few 5 mm thick ramifications; white, 1-60 mm thick calcite veinlets suggest tensional stresses	vugs, potholes (up to meter scale), small lapis, pressure dissolution seams interrupt bedding at right and oblique angles and some intersect potholes of 10-30 cm in diameter	few disarticulated, calcified bivalves (1-4 cm) and algae occur in the bottom of some beds w/a nested arrangement
Outcrop No. 6: gray, thickening upwards wackestones			
sharp bedding contacts characterized by planar-parallel to wavy-parallel bedding planes w/wavy-smooth and rough surfaces; very thickly bedded (~2.2 m thick); trend SW-NE and dip shallowly to the SE	widely-very widely spaced parallel joints strike EW to SW-NE, dip steeply to NNW; planar joint-walls w/wavy-smooth surfaces; intersection w/bedding planes creates equidimensional blocks	lapis, vugs, potholes, and pressure dissolution seams at different orientations w/respect to the bedding planes	disarticulated, calcified bivalves and algae at bottom of all beds; fossil arrangement is nested to concordant on bedding cross-section planes

APPENDIX B: TEM Soundings and Summary of Geotechnical Laboratory tests

Table 4.2: Geographic coordinates of TEM stations in the Argive Basin (Peloponnese, Greece). The selected TEM sounding measurement (out of three) is indicated by the suffix A, B, or C.

Longitude (°)	Latitude (°)	TEM sounding	Longitude (°)	Latitude (°)	TEM sounding	Longitude (°)	Latitude (°)	TEM sounding
22.679661	37.692265	A038B	22.789521	37.627423	079B	22.774167	37.598239	A017C
22.692	37.689822	A039B	22.789766	37.619082	080B	22.776763	37.598124	A018B
22.702059	37.687546	A040B	22.79032	37.613836	081B	22.779248	37.598024	A019B
22.718273	37.685491	A041C	22.792403	37.607088	082B	22.782186	37.597296	A020B
22.727762	37.684685	A042C	22.80037	37.589721	084B	22.784826	37.597307	A021C
22.731425	37.685658	123B	22.804128	37.584775	085C	22.787453	37.597693	A022B
22.739223	37.685915	A043B	22.690759	37.618591	128B	22.789539	37.598841	A026A
22.750486	37.684497	A044B	22.698977	37.616965	129B	22.792358	37.600393	A024F
22.762145	37.685271	A045B	22.708076	37.61463	130B	22.794089	37.600701	A027B
22.774318	37.68579	A046C	22.714273	37.613679	131B	22.797374	37.600515	A028C
22.791513	37.68693	A047B	22.718674	37.610838	132B	22.775712	37.607036	A011B
22.80182	37.685545	A048C	22.726022	37.609317	133B	22.777663	37.606037	A012B
22.813484	37.681641	A049B	22.733993	37.609773	134B	22.779545	37.604407	A013B
22.825659	37.678736	A050B	22.741543	37.611157	135B	22.781029	37.603464	A014B
22.840632	37.679924	A051B	22.747305	37.608209	136B	22.78268	37.602079	A015C
22.837573	37.665876	A052B	22.75428	37.605903	137B	22.784939	37.600975	A016A
22.826268	37.663308	A053B	22.761257	37.606313	138B	22.785948	37.600151	A025C
22.815649	37.665346	A054B	22.767935	37.604736	139B	22.787453	37.597693	A022C
22.803666	37.66357	A055B	22.771557	37.602661	140B	22.788775	37.596191	A023C
22.792129	37.664817	A056B	22.795182	37.598497	143C	22.679661	37.692265	A038B
22.787678	37.660008	115B	22.814363	37.59332	144D	22.692	37.689822	A039B
22.779989	37.662596	116B	22.789606	37.586437	A086B	22.702059	37.687546	A040B
22.773749	37.662553	117B	22.790624	37.591187	A087B	22.718273	37.685491	A041C
22.770003	37.664945	074C	22.795681	37.595344	A088B	22.727762	37.684685	A042B
22.763298	37.665709	118B	22.799819	37.59617	A083B	22.739223	37.685915	A043B
22.759734	37.667127	119B	22.804948	37.597949	A010C	22.750486	37.684497	A044A
22.756237	37.670491	A059B	22.804746	37.600468	089B	22.762145	37.685271	A045B
22.748665	37.673354	120C	22.812757	37.605035	090C	22.774318	37.68579	A046C
22.740639	37.669933	A060B	22.818776	37.613062	091B	22.791513	37.68693	A047B
22.72892	37.6699	A061C	22.824684	37.618035	092C	22.80182	37.685545	A048C
22.715187	37.671977	A062B	22.826325	37.623505	093B	22.813484	37.681641	A049A
22.702582	37.674173	A063C	22.827393	37.627877	094B	22.825659	37.678736	A050B
22.690125	37.672562	A064C	22.830781	37.632647	095B	22.840632	37.679924	A051B
22.708685	37.6995	126B	22.836159	37.640278	096B	22.690125	37.672562	A064B
22.718132	37.69231	125B	22.840058	37.644746	097C	22.702582	37.674173	A063B
22.726228	37.689623	124B	22.84477	37.644732	098B	22.715187	37.671977	A062B
22.731425	37.685658	123B	22.848476	37.650319	099B	22.72892	37.6699	A061C
22.738657	37.682134	122B	22.847403	37.652558	100A	22.740639	37.669933	A060B
22.744095	37.679795	121B	22.846383	37.657773	101B	22.756237	37.670491	A059B
22.748665	37.673354	120B	22.753077	37.629661	148B	22.767169	37.670931	A058A
22.794626	37.659508	114B	22.76281	37.630818	147B	22.779609	37.66864	A057C
22.800338	37.655453	113B	22.776025	37.635734	146B	22.792129	37.664817	A056B
22.805204	37.650481	112C	22.783636	37.637181	078B	22.803666	37.66357	A055B
22.81465	37.64811	111B	22.792144	37.63638	149B	22.815649	37.665346	A054A
22.826006	37.647006	110B	22.80322	37.634568	150B	22.826268	37.663308	A053B
22.833167	37.645201	109B	22.774167	37.598239	A017C	22.837573	37.665876	A052B
22.840058	37.644746	097C	22.776763	37.598124	A018C			
22.84477	37.644732	098B	22.779248	37.598024	A019C			
22.851837	37.645001	108B	22.782186	37.597296	A020C			
22.855625	37.646322	107B	22.784826	37.597307	A021C			
22.868223	37.642952	105B	22.798845	37.600181	A031E			
22.74801	37.718314	066B	22.79904	37.599671	A033D			
22.751292	37.712624	067B	22.799151	37.599204	A034B			
22.753385	37.706413	068B	22.799819	37.59617	A083B			
22.751979	37.699614	069B	22.804942	37.59492	A009C			
22.758836	37.693566	070B	22.805243	37.592719	A008C			
22.759652	37.686392	071B	22.806473	37.592053	A029D			
22.76581	37.679617	072B	22.808244	37.589997	A030C			
22.7645	37.676701	073B	22.808765	37.588956	A006C			
22.767169	37.670931	A058B	22.810154	37.587069	A005C			
22.774336	37.657974	075B	22.81133	37.585279	A000C			
22.776751	37.65177	076B	22.813164	37.586178	A001C			
22.776026	37.644151	077B	22.815596	37.586768	A002A			
22.783636	37.637181	078B	22.816689	37.588223	A003B			

APPENDIX B: TEM Soundings and Summary of Geotechnical Laboratory tests

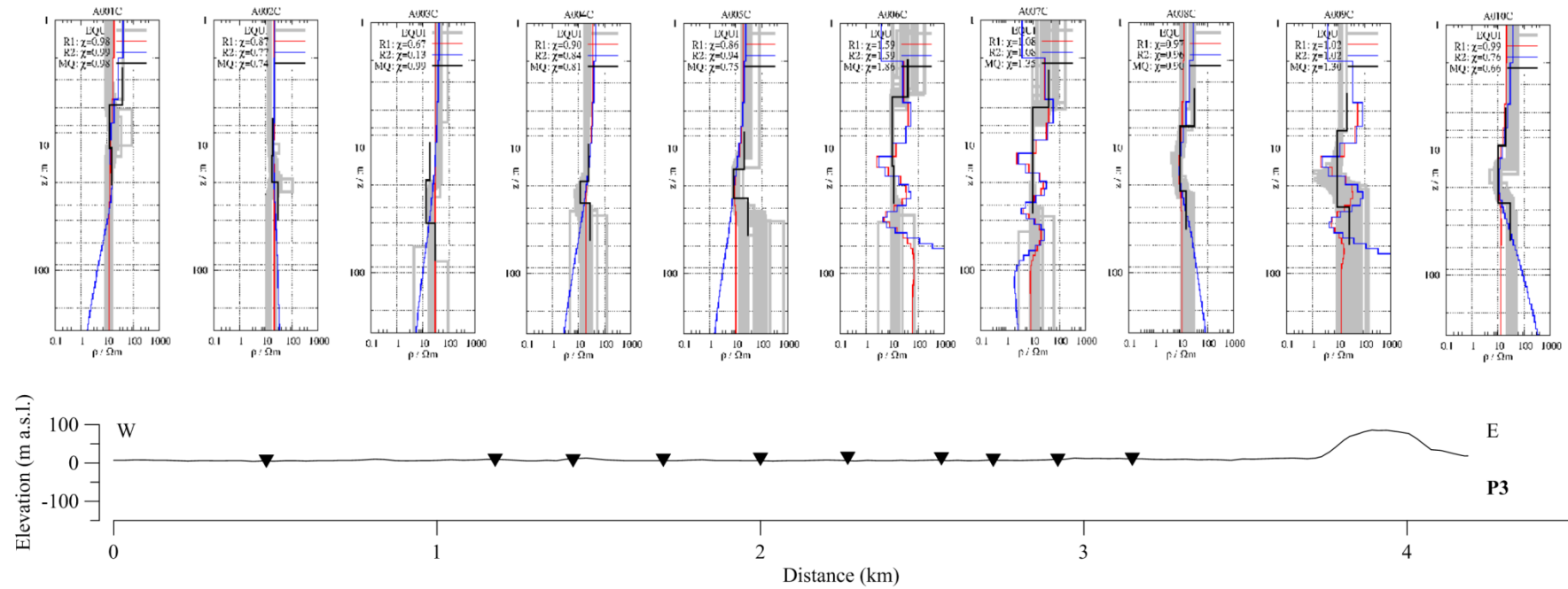


Figure B1: Final 1D TEM inverted models for with the Occam's R1 (red line) and R2 (blue line), Marquardt–Levenberg (black line), and Monte–Carlo (grey line) techniques (from Haaf, 2015) plotted along corresponding topographic profiles P3 to P10.

APPENDIX B: TEM Soundings and Summary of Geotechnical Laboratory tests

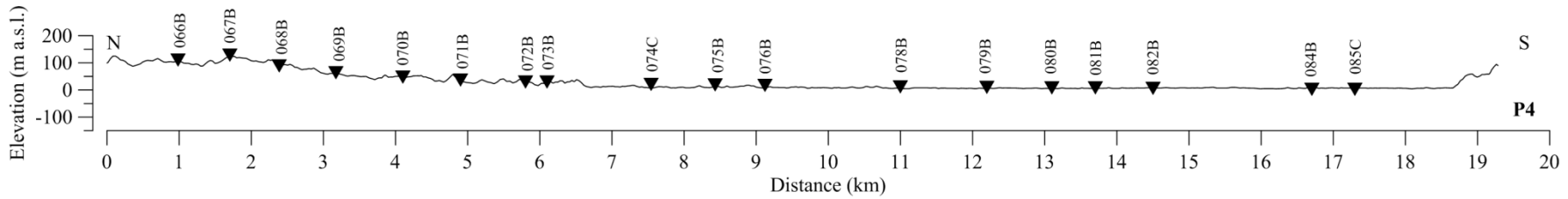
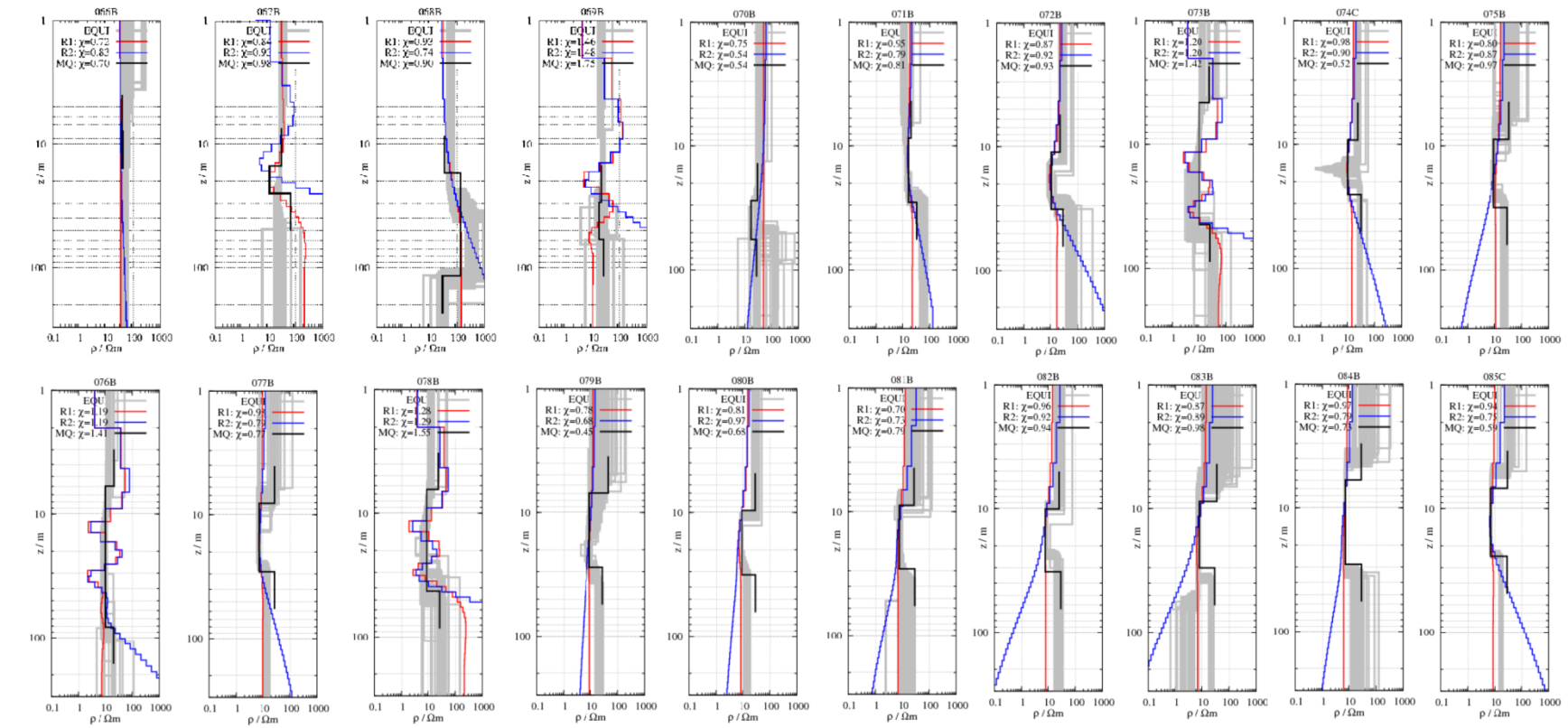


Figure B1: Continued.

APPENDIX B: TEM Soundings and Summary of Geotechnical Laboratory tests

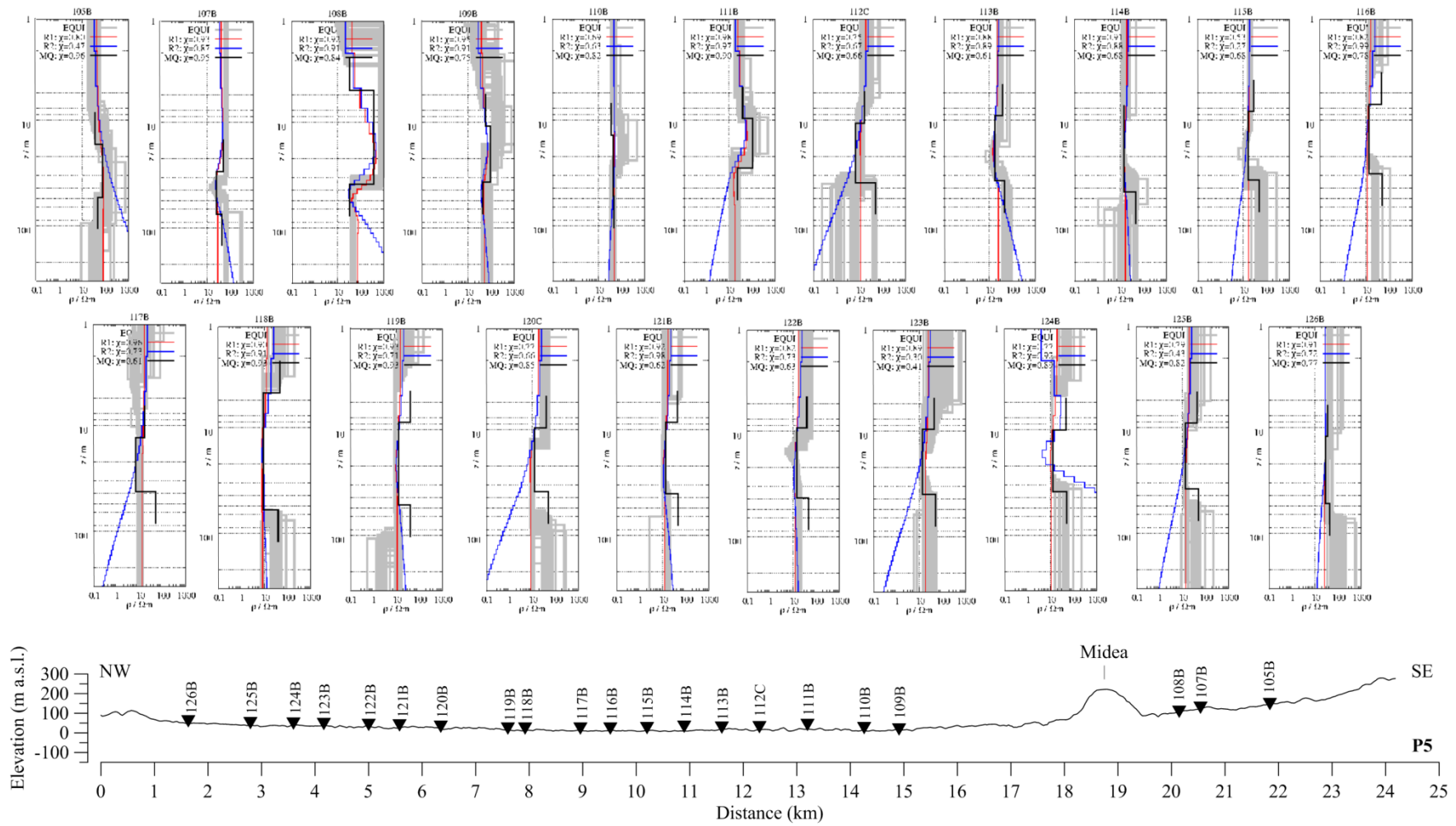


Figure B1: Continued.

APPENDIX B: TEM Soundings and Summary of Geotechnical Laboratory tests

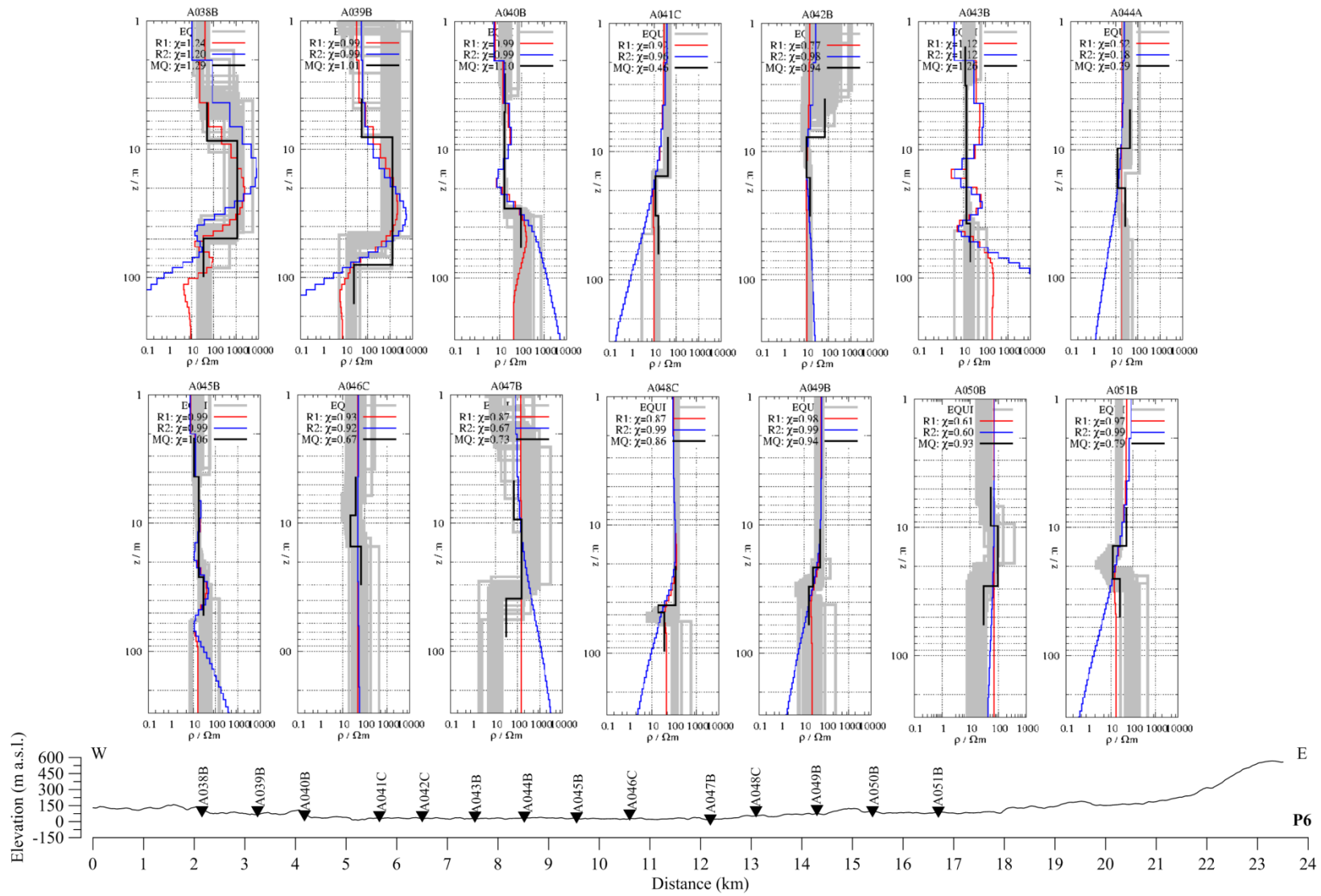


Figure B1: Continued.

APPENDIX B: TEM Soundings and Summary of Geotechnical Laboratory tests

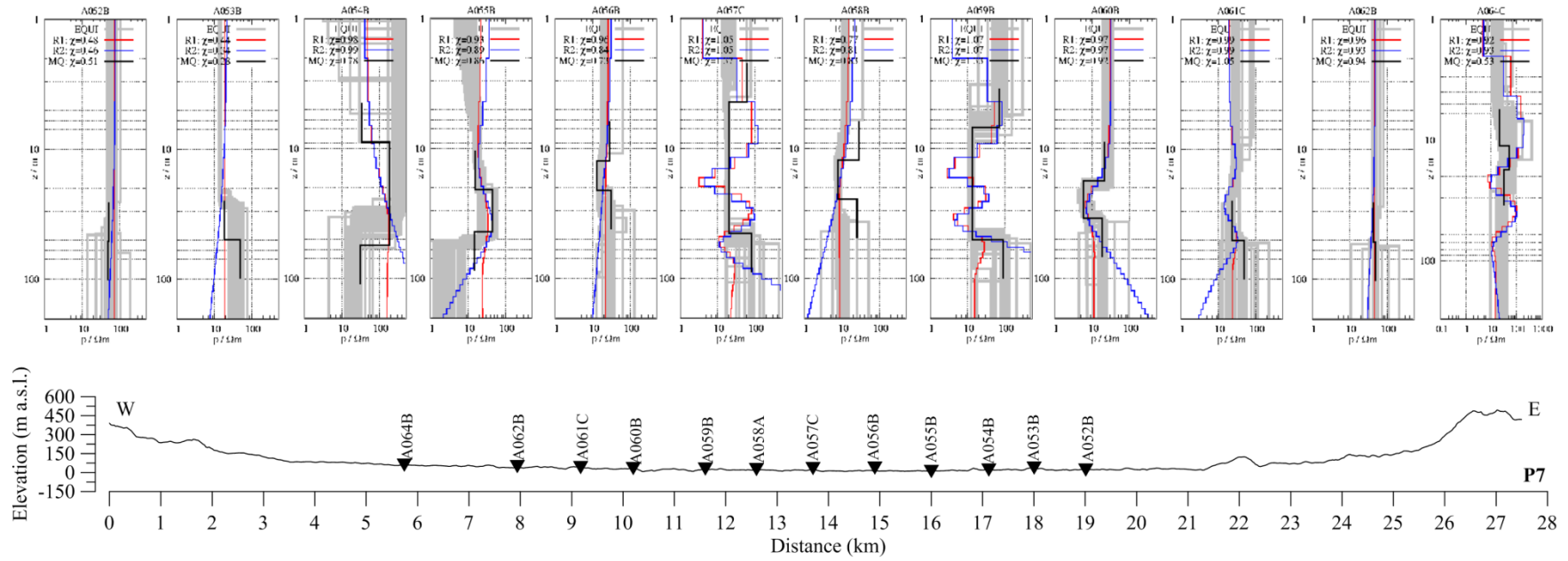


Figure B1: Continued.

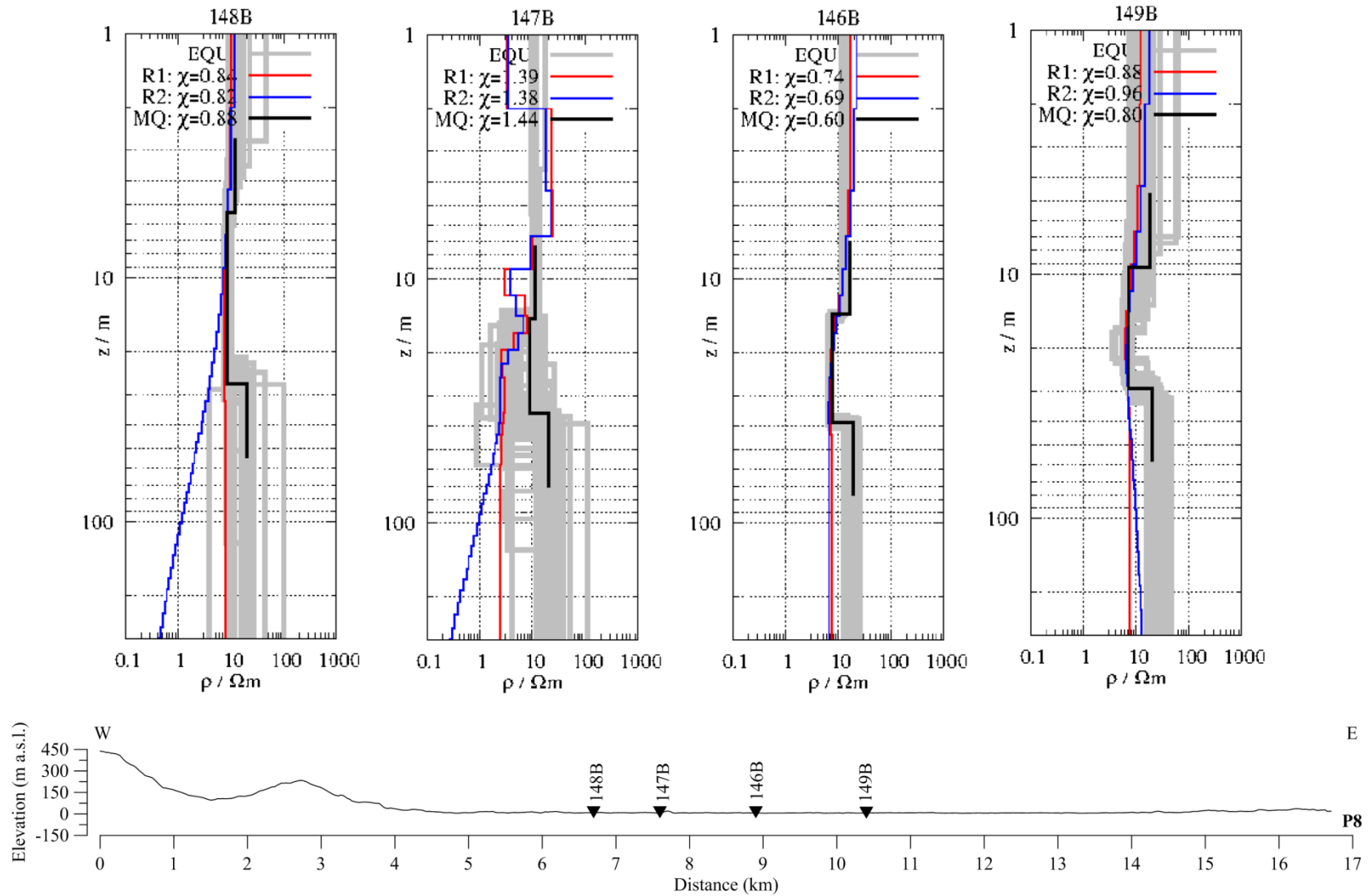


Figure B1: Continued.

APPENDIX B: TEM Soundings and Summary of Geotechnical Laboratory tests

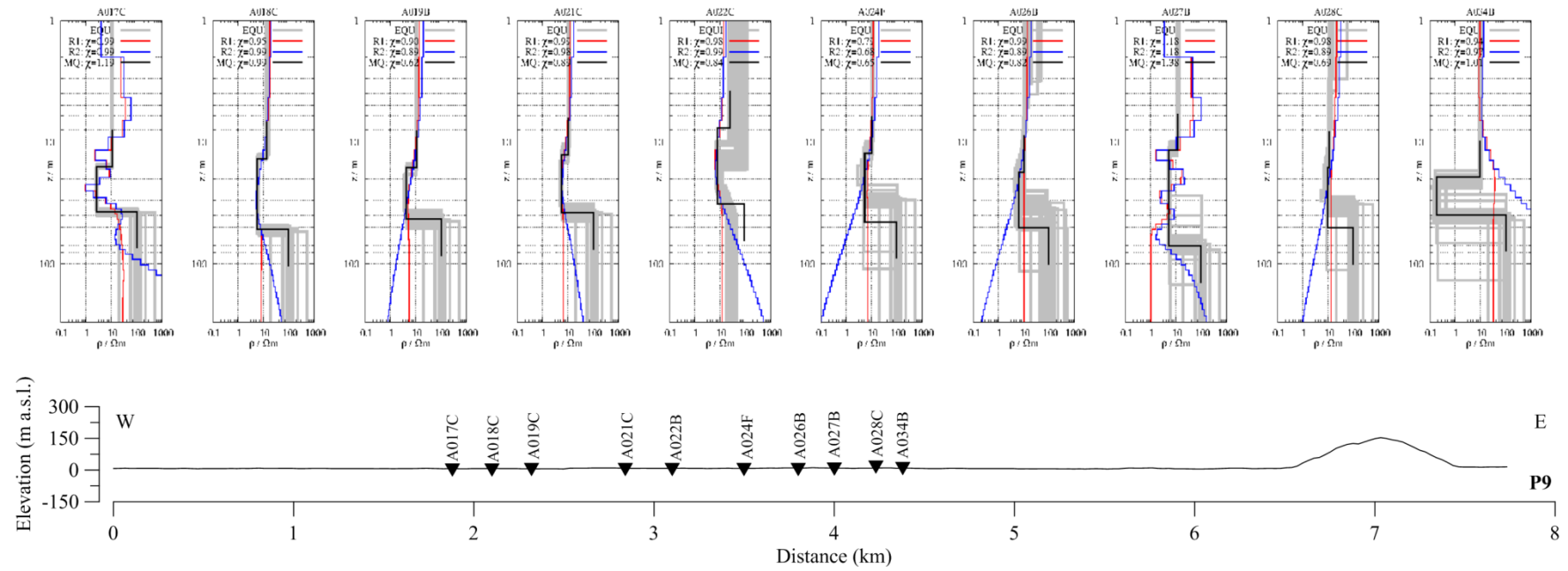


Figure B1: Continued.

APPENDIX B: TEM Soundings and Summary of Geotechnical Laboratory tests

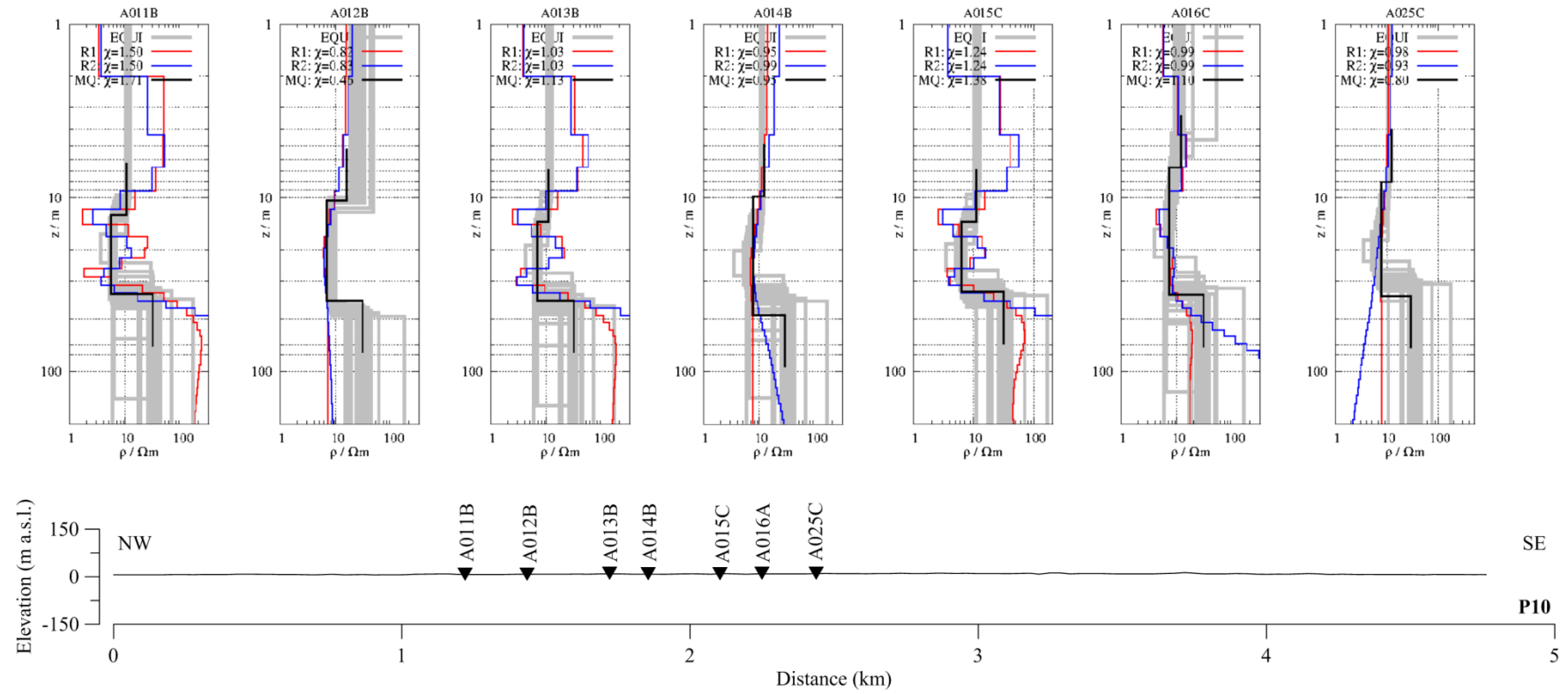
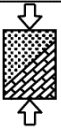


Figure B1: Continued.

Summary of Geotechnical Laboratory tests

				RHEINISCH- WESTFÄLISCHE TECHNISCHE HOCHSCHULE AACHEN		Anlage-Nr.: 5						
Ergebnisübersicht												
Projekt-Nr.: 1224 Hinzen		Projekt: Felsuntersuchungen			Sachbearbeiter: Wi							
Einaxiale Druckfestigkeit mit DMS												
Probe-Nr.:	Anlage-Nr.:	Gesamtprobe			DMS 1			DMS 2			Trockendichte [g/m ³]	Bodenart
		E _{ges} [MN/m ²]	q _u [MN/m ²]	ε _u [%]	E _{ver} [%]	ν [1]	Spannungsbereich [MN/m ²]	E _{ver} [%]	ν [1]	Spannungsbereich [MN/m ²]		
8684.1	3.1	22000	59,71	0,49	27628	0,101	10,9 - 21,1	116861	0,080	10,9 - 21,1	2,663	Fels grau
8684.2	3.2	33500	131,06	0,49	71349	0,292	21,3 - 60,3	65501	0,346	21,3 - 60,3	2,659	Fels grau
8684.3	3.3	26000	68,67	0,39	26057	0,244	21,7 - 50,3	35883	0,210	21,7 - 50,3	2,664	Fels grau
8685.1.1	3.4	21000	53,21	0,45	26251	0,255*	20,3 - 35,2	90027	0,081*	20,3 - 35,2	2,621	Fels rot
8685.1.2	3.5	19000	53,58	0,50	33485	0,083*	22,5 - 39,2	68310	0,725**	22,5 - 39,2	2,574	Fels rot
8685.1.3	3.6	10000	33,91	0,51	35896	0,211*	5,4 - 16,7	22058	0,059**	5,4 - 16,7	2,638	Fels rot
Spaltzugversuche												
Probe-Nr.:	Anlage-Nr.:	Trockendichte ρ _d		Zugfestigkeit σ _t		Prüfrichtung		Bodenart	Bemerkungen:			
		[g/cm ³]		[MN/m ²]		-						
8684.1	4.1	2,636		8,398		parallel		Fels grau	*= Probe war sehr rissig **= Probe war sehr rissig und die DMS mussten auf Risse geklebt werden. Die DMS (10x6 mm) wurden mittig angebracht. Da während der Belastung die Stauchung der Proben nicht homogen erfolgte, ergeben sich andere E-Module als aus der Gesamtprobe berechnet.			
8684.2	4.2	2,639		7,828		parallel		Fels grau				
8684.3	4.3	2,650		13,148		senkrecht		Fels grau				
8685.2.1	4.4	2,605		4,368		parallel		Fels rot				
8685.2.2	4.5	2,606		7,754		senkrecht		Fels rot				

										RHEINISCH- WESTFALISCHE TECHNISCHE HOCHSCHULE AACHEN		Anlage-Nr.: 5	
Ergebnisübersicht													
Projekt-Nr.: 1224 Hinzen				Projekt: Felsuntersuchungen				Sachbearbeiter: Wi					
Einaxiale Druckfestigkeit mit DMS													
Probe-Nr.:	Anlage-Nr.:	Gesamtprobe			DMS 1			DMS 2			Trockendichte [g/m ³]	Bodenart	
		E _{ges} [MN/m ²]	q _u [MN/m ²]	ε _u [%]	E _{ver} [%]	ν [1]	Spannungsbereich [MN/m ²]	E _{ver} [%]	ν [1]	Spannungsbereich [MN/m ²]			
8684.1	3.1	22000	59,71	0,49	27628	0,101	10,9 - 21,1	116861	0,080	10,9 - 21,1	2,663	Fels grau	
8684.2	3.2	33500	131,06	0,49	71349	0,292	21,3 - 60,3	65501	0,346	21,3 - 60,3	2,659	Fels grau	
8684.3	3.3	26000	68,67	0,39	26057	0,244	21,7 - 50,3	35883	0,210	21,7 - 50,3	2,664	Fels grau	
8685.1.1	3.4	21000	53,21	0,45	26251	0,255*	20,3 - 35,2	90027	0,081*	20,3 - 35,2	2,621	Fels rot	
8685.1.2	3.5	19000	53,58	0,50	33485	0,083*	22,5 - 39,2	68310	0,725**	22,5 - 39,2	2,574	Fels rot	
8685.1.3	3.6	10000	33,91	0,51	35896	0,211*	5,4 - 16,7	22058	0,059**	5,4 - 16,7	2,638	Fels rot	
Spaltzugversuche													
Probe-Nr.:	Anlage-Nr.:	Trockendichte ρ _d		Zugfestigkeit σ _t		Prüfrichtung		Bodenart	Bemerkungen:				
		[g/cm ³]		[MN/m ²]		-							
8684.1	4.1	2,636		8,398		parallel		Fels grau	Bemerkungen: *= Probe war sehr rissig **= Probe war sehr rissig und die DMS mussten auf Risse geklebt werden. Die DMS (10x6 mm) wurden mittig angebracht. Da während der Belastung die Stauchung der Proben nicht homogen erfolgte, ergeben sich andere E-Module als aus der Gesamtprobe berechnet.				
8684.2	4.2	2,639		7,828		parallel		Fels grau					
8684.3	4.3	2,650		13,148		senkrecht		Fels grau					
8685.2.1	4.4	2,605		4,368		parallel		Fels rot					
8685.2.2	4.5	2,606		7,754		senkrecht		Fels rot					

APPENDIX C: Modeling Parameters for Computed Synthetic Earthquakes

The modeling parameters required to compute synthetic earthquakes, with the stochastic and Green’s Function methods, are presented in this appendix. The modeling parameters are tabulated by seismic source [i.e., normal faulting in the Argive Basin (AB) and Patras–Corinth Continental Rift system (PCCR); strike-slip faulting in the Iria–Epidauros Sinistral Transform fault system (IEST); and intraplate and interface reverse faulting in the Hellenic Subduction Zone (HSZ)]. The observation point or reference station for all computed synthetic seismograms is positioned on outcropping bedrock inside the Tiryns and Midea citadels.

Table 5.10: Modeling parameters to stochastically simulate extensional earthquakes in the Argive Basin.

Modeling Parameter	Fault segment								
	ABNAF4	ABNF1	ABNF2	ABNF3	ABNF4	ABNF5	ABNF6	ABNF7	Mycenae fault
Fault strike (deg)	323	329	342	286	325	261	250	285	245
Fault dip (deg)	75	75	75	75	75	75	75	75	42
Fault length (km)	20	16	20	11	12	7	8	15	5
Fault width (km)	13	12	13	10	10	8	9	11	7
Depth (km) to upper edge of fault	5.0	5.0	5.0	5.0	5.0	5.0	5.0	5.0	5.0
Hypocenter location: i_0, j_0	1,2	1,2	1,2	1,2	1,2	3,2	2,1	3,2 ^a 2,2 ^b	1,2
No. of subfaults: $N_i \times N_w$	3x2 ^a 2x2 ^b	3x2 ^a 2x2 ^b	4x2 ^a 2x2 ^b	2x2 ^a 3x2 ^b	3x2 ^a 2x2 ^b	3x2	2x2	3x2 ^a 2x2 ^b	2x2
Stress drop ($\Delta\sigma$) (bars)	60	60	60	60	60	60	60	60	60
Crustal shear wave velocity (km/s): β	2.1	2.1	2.1	2.1	2.1	2.1	2.1	2.1	2.1
Crustal density (g/cm ³): ρ	2.6	2.6	2.6	2.6	2.6	2.6	2.6	2.6	2.6
High frequency level: s_{fact}	1	1	1	1	1	1	1	1	1
Parameter κ (kappa)	0.035	0.035	0.035	0.035	0.035	0.035	0.035	0.035	0.035
Attenuation factor: Q_0	380	380	380	380	380	380	380	380	380
$Q(f) = Q_0 \cdot f^\eta$: η (eta)	0.80	0.80	0.80	0.80	0.80	0.80	0.80	0.80	0.80
Geometric spreading: $igeom$ (1/R model)	0	0	0	0	0	0	0	0	0
Rmin*	0	0	0	0	0	0	0	0	0
Rdl*	45	45	45	45	45	45	45	45	45
rdl2*	125	125	125	125	125	125	125	125	125
Durmin*	5.0	5.0	5.0	5.0	5.0	5.0	5.0	5.0	5.0
b1*	0.187	0.187	0.187	0.187	0.187	0.187	0.187	0.187	0.187
b2*	0.031	0.031	0.031	0.031	0.031	0.031	0.031	0.031	0.031
b3*	0.130	0.130	0.130	0.130	0.130	0.130	0.130	0.130	0.130
Windowing function: $iwind$ (Hz) (Saragoni-Hart window)	1	1	1	1	1	1	1	1	1
Slip distribution model: $islip$	0	0	0	0	0	0	0	0	0

a: Wells and Coppersmith, 1994; b: Pavlides and Caputo, 2004; *: Distance-dependent duration (s) parameters

APPENDIX C: Modeling Parameters for Computed Synthetic Earthquakes

Table 5.11: Modeling parameters to simulate extensional earthquakes in the Argive Basin using the Green's Function approach.

Modeling Parameter	Fault segment								
	ABNAF4	ABNF1	ABNF2	ABNF3	ABNF4	ABNF5	ABNF6	ABNF7	Mycenae fault
Seismic moment (N*m)	9.63E18 ^a 1.19E19 ^b	6.53E18 ^a 8.82E18 ^b	9.63E18 ^a 1.19E19 ^b	3.40E18 ^a 5.32E18 ^b	3.96E18 ^a 5.98E18 ^b	1.55E18 ^a 2.89E18 ^b	1.96E18 ^a 3.46E18 ^b	5.84E18 ^a 8.09E18 ^b	8.63E17 ^a 1.83E18 ^b
Geographic coordinates of fault segment (ref_lat, ref_lon) (deg)	37.533, 22.898	37.508, 22.749	37.434, 22.765	37.644, 22.734	37.523, 22.885	37.749, 22.807	37.667, 22.799	37.671, 22.846	37.715, 22.800
Reference depth (m) (to upper edge of fault)	5000	5000	5000	5000	5000	5000	5000	5000	5000
Fault length (m)	20000	16000	20000	11000	12000	7000	8000	15000	5000
Fault width (m)	13000	12000	13000	10000	10000	8000	9000	11000	7000
Fault strike (deg)	323	329	342	286	325	261	250	285	245
Fault dip (deg)	75	75	75	75	75	75	75	75	42
Fault rake (deg)	-120	-30	-30	-30	-30	-160	-120	-120	-30
max. extension of composite events subject to Gutenberg-Richter law (lsubmax) (m)	2000	1000	1000	1000	1000	1000	1000	1000	500
max. extension of composite events subject to Gutenberg-Richter law (lsubmin) (m)	100	100	100	100	100	100	100	100	100
Hypocenter location from reference point: distance (m) along strike (xstar) and along dip (ystart)	4000, 10000	4500, 9000	5000, 9500	3000, 7500	3000, 7500	5800, 6000	3000, 7000	12500, 8250	3750, 5250
Moment distribution option (mdis)	0	0	0	0	0	0	0	0	0
Discretization step (m) (dstep)	500	500	500	500	500	500	500	500	250
No. of fault segments	1								
Stress drop ($\Delta\sigma$) (Pa)	6E06								
High-cut frequency (Hz)	20								
max. fluctuations strike (deg) (dstmax)	5								
max. fluctuations dip (deg) (ddimax)	5								
max. fluctuations rake (deg) (dramax)	10								
Rupture time (s) begin of the segment (tstart)	0.0								
Rupture velocity (m/s)	2680								
Selection (1/0) for geographical coordinate system	1								
If 1: x = latitude, y = longitude (deg)	37.620, 22.770								
Selection for irregular positions (= 0) or a 1D profile (= 1) or a rectangular 2D observation array (= 2): ixy	0								
Number of positions (n)	2								
Latitude/Longitude (deg) of observation point(s): (i.e., Tiryns and Midea)	(37.600, 22.799), (37.649, 22.841)								
Selection for inputting the soft cover parameters: 0 = uniform soft cover for all locations, 1 = via listing, 2 = via an external data file, others (3 for this study) = no site effect	3								

a: Wells and Coppersmith, 1994; b: Pavlides and Caputo, 2004

Table 5.12: Modeling parameters to stochastically simulate extensional earthquakes in the Patras–Corinth Continental Rift.

Modeling Parameter	Fault segment		
	Xylokaastro-1	Xylokaastro-2	Xylokaastro-3
Fault strike (deg)	295	295	295
Fault dip (deg)	30	40	50
Fault length (km)	30	30	30
Fault width (km)	15	15	15
Depth (km) to upper edge of fault	5.0	5.0	5.0
Hypocenter location: i_0/f_0	4,3	4,3	4,3
No. of subfaults: $N_l \times N_w$	6x3	6x3	6x3
Stress drop ($\Delta\sigma$) (bars)	34	34	34
Crustal shear wave velocity (km/s): β	2.1	2.1	2.1
Crustal density (g/cm^3): ρ	2.6	2.6	2.6
High frequency level: sfact	1	1	1
Parameter κ (kappa)	0.035	0.035	0.035
Attenuation factor: Q_0	380	380	380
$Q(f) = Q_0 f^\eta$: η (eta)	0.80	0.80	0.80
Geometric spreading: igeom (1/R model)	0	0	0
Rmin*	0	0	0
Rd1*	45	45	45
rdl2*	125	125	125
Durmin*	5.0	5.0	5.0
b1*	0.187	0.187	0.187
b2*	0.031	0.031	0.031
b3*	0.130	0.130	0.130
Windowing function: iwind (Hz) (Saragoni-Hart window)	1	1	1
Slip distribution model: islip	0	0	0

a: Wells and Coppersmith, 1994; b: Pavlides and Caputo, 2004; *: Distance-dependent duration (s) parameters

APPENDIX C: Modeling Parameters for Computed Synthetic Earthquakes

Table 5.13: Modeling parameters to simulate extensional earthquakes in the eastern Patras–Corinth Continental Rift using the Green’s Function approach.

Modeling Parameter	Fault segment		
	Xylokaastro-1	Xylokaastro-2	Xylokaastro-3
Fault dip (deg)	30	40	50
Fault length (m)		30000	
Fault width (m)		15000	
Fault strike (deg)		295	
No. of fault segments		1	
Stress drop ($\Delta\sigma$) (Pa)		3.4E06	
High-cut frequency (Hz)		20	
Seismic moment (N*m)		2.06E19	
Geographic coordinates of fault segment (ref_lat, ref_lon) (deg)		38.039, 22.756	
Reference depth (m) (to upper edge of fault)		5000	
Fault rake (deg)		-88	
max. fluctuations strike (deg) (dstmax)		5	
max. fluctuations dip (deg) (ddimax)		5	
max. fluctuations rake (deg) (dramax)		10	
max. extension of composite events subject to Gutenberg-Richter law (lsubmax) (m)		2000	
max. extension of composite events subject to Gutenberg-Richter law (lsubmin) (m)		100	
Hypocenter location from reference point: distance (m) along strike (xstar) and along dip (ystart)		20000, 15000	
Rupture time (s) begin of the segment (tstart)		0.0	
Rupture velocity (m/s)		2680	
Moment distribution option (mdis)		0	
Discretization step (m) (dstep)		500	
Selection (1/0) for geographical coordinate system		1	
If 1: x = latitude, y = longitude (deg)		37.620, 22.770	
Selection for irregular positions (= 0) or a 1D profile (= 1) or a rectangular 2D observation array (= 2): ixy		0	
Number of positions (n)		2	
Latitude/Longitude (deg) of observation point(s): (i.e., Tiryns and Midea)		(37.600, 22.799), (37.649, 22.841)	
Selection for inputting the soft cover parameters: 0 = uniform soft cover for all locations, 1 = via listing, 2 = via an external data file, others (3 for this study) = no site effect		3	

Table 5.14: Modeling parameters to stochastically simulate strike-slip earthquakes in the Iria–Epidaurus Sinistral Transform fault system.

Modeling Parameter	Fault segment					
	Iria1	Iria2	Epidaurus1	Epidaurus2	Iria-Epidaurus1	Iria-Epidaurus2
Fault strike (deg)	266	266	275	275	270	270
Fault dip (deg)	75	90	75	90	75	90
Fault length (km)	24	24	19	19	43	43
Fault width (km)	13	13	12	12	17	17
Depth (km) to upper edge of fault	5.0	5.0	5.0	5.0	5.0	5.0
Hypocenter location: i_0/f_0	1,2	1,2	1,2	1,2	1,3 and 7,3	1,3 and 7,3
No. of subfaults: $N_l \times N_w$	3x3	3x3	3x2	3x2	7x3	7x3
Stress drop ($\Delta\sigma$) (bars)	35	35	35	35	35	35
Crustal shear wave velocity (km/s): β	2.1	2.1	2.1	2.1	2.1	2.1
Crustal density (g/cm ³): ρ	2.6	2.6	2.6	2.6	2.6	2.6
High frequency level: sfact	1	1	1	1	1	1
Parameter κ (kappa)	0.035	0.035	0.035	0.035	0.035	0.035
Attenuation factor: Q_0	380	380	380	380	380	380
$Q(f) = Q_0 f^\eta$: η (eta)	0.80	0.80	0.80	0.80	0.80	0.80
Geometric spreading: igeom (1/R model)	0	0	0	0	0	0
Rmin*	0	0	0	0	0	0
Rd1*	45	45	45	45	45	45
rdl2*	125	125	125	125	125	125
Durmin*	5.0	5.0	5.0	5.0	5.0	5.0
b1*	0.187	0.187	0.187	0.187	0.187	0.187
b2*	0.031	0.031	0.031	0.031	0.031	0.031
b3*	0.130	0.130	0.130	0.130	0.130	0.130
Windowing function: iwind (Hz) (Saragoni-Hart window)	1	1	1	1	1	1
Slip distribution model: islip	0	0	0	0	0	0

a: Wells and Coppersmith, 1994; b: Pavlides and Caputo, 2004; *: Distance-dependent duration (s) parameters

APPENDIX C: Modeling Parameters for Computed Synthetic Earthquakes

Table 5.15: Modeling parameters to simulate strike-slip earthquakes in the Iria–Epidaurus Sinistral Transform fault system using the Green’s Function approach.

Modeling Parameter	Fault segment					
	Ir1	Ir2	Ep1	Ep2	IrEp1	IrEp2
Fault dip (deg)	75	90	75	90	75	90
Fault length (m)	24000		19000		43000	
Fault width (m)	13000		12000		17000	
Fault strike (deg)	266		275		270	
Seismic moment (N*m)	1.323E19		8.811E18		3.650E19	
Geographic coordinates of fault segment (ref_lat, ref_lon) (deg)	37.516, 23.243		37.488, 23.459		37.488, 3.459	
No. of fault segments	1					
Stress drop ($\Delta\sigma$) (Pa)	3.5E06					
High-cut frequency (Hz)	20					
Reference depth (m) (to upper edge of fault)	5000					
Fault rake (deg)	-30					
max. fluctuations strike (deg) (dstmax)	5					
max. fluctuations dip (deg) (ddimax)	5					
max. fluctuations rake (deg) (dramax)	10					
max. extension of composite events subject to Gutenberg-Richter law (lsubmax) (m)	2000					
max. extension of composite events subject to Gutenberg-Richter law (lsubmin) (m)	100					
Rupture time (s) begin of the segment (tstart)	0.0					
Rupture velocity (m/s)	2680					
Hypocenter location from reference point: distance (m) along strike (xstar) and along dip (ystart)	8000, 8500					
Moment distribution option (mdis)	0					
Discretization step (m) (dstep)	500					
Selection (1/0) for geographical coordinate system	1					
If 1: x = latitude, y = longitude (deg)	37.620, 22.770					
Selection for irregular positions (= 0) or a 1D profile (= 1) or a rectangular 2D observation array (= 2): ixy	0					
Number of positions (n)	2					
Latitude/Longitude (deg) of observation point(s): (i.e., Tiryns and Midea)	(37.600, 22.799), (37.649, 22.841)					
Selection for inputting the soft cover parameters: 0 = uniform soft cover for all locations, 1 = via listing, 2 = via an external data file, others (3 for this study) = no site effect	3					
Ir1: Iria-1; Ir2: Iria-2; Ep1: Epidaurus-1; Epidaurus-2; Iria-Epidaurus-1; Iria-Epidaurus-2						

APPENDIX C: Modeling Parameters for Computed Synthetic Earthquakes

Table 5.16: Modeling parameters to stochastically simulate intraplate and interface reverse earthquakes in the Hellenic Subduction Zone.

Modeling Parameter	Fault segment							
	HSZ-1	HSZ-2	HSZ-3	HSZ-4	HSZ-5	HSZ-6	HSZ-7	HSZCrete
Fault strike (deg)	312	312	312	312	312	312	346	292.5
Fault dip (deg)	45	45	25	25	25	25	40	40
Fault length (km)	143 ^a	184 ^a	98 ^a	162 ^a	209 ^a	237 ^a	184 ^a	305 ^a
	139 ^b	183 ^b	83 ^b	141 ^c	188 ^c	217 ^c	183 ^b	288 ^c
	122 ^c	163 ^c	80 ^c				163 ^c	105 ^d
Fault width (km)	66 ^a	76 ^a	53 ^a	71 ^a	82 ^a	88 ^a	76 ^a	101 ^a
	78 ^b	91 ^b	44 ^b	65 ^c	79 ^c	88 ^c	91 ^b	108 ^c
	58 ^c	72 ^c	43 ^c				72 ^c	100 ^d
Depth (km) to upper edge of fault	75.0	80.0	8.0	8.0	8.0	8.0	60.0	6.0
Hypocenter location: i_0/f_0	1,10 ^{a,b,c}	18,7 ^{a,b,c}	1,3 ^{a,b,c}	1,6 ^{a,c}	1,8 ^{a,c}	1,8 ^{a,c}	17,10 ^{a,b,c}	10,10 ^{a,c,d}
No. of subfaults: $N_L \times N_w$	14x10 ^{a,b,c}	18x7 ^{a,b,c}	10x4 ^{a,b,c}	14x6 ^{a,c}	20x8 ^{a,c}	25x4 ^{a,c}	17x10 ^{a,b,c}	10x4 ^{a,c} 10x10 ^d
Stress drop ($\Delta\sigma$) (bars)	30	30	60	60	60	60	30	60
Crustal shear wave velocity (km/s): β	2.1	2.1	2.1	2.1	2.1	2.1	2.1	2.1
Crustal density (g/cm^3): ρ	2.6	2.6	2.6	2.6	2.6	2.6	2.6	2.6
Parameter controlling high frequency level: s_{fact}	1	1	1	1	1	1	1	1
Parameter κ (kappa)	0.035	0.035	0.035	0.035	0.035	0.035	0.035	0.035
Attenuation factor: Q_0	380	380	380	380	380	380	380	380
$Q(f) = Q_0 f^\eta$: η (eta)	0.80	0.80	0.80	0.80	0.80	0.80	0.80	0.80
Geometric spreading: igeom (1/R model)	0	0	0	0	0	0	0	0
Rmin*	0	0	0	0	0	0	0	0
Rdl*	50	50	50	50	50	50	50	50
rdl2*	196	196	196	196	196	196	196	196
Durmin*	5.0	5.0	5.0	5.0	5.0	5.0	5.0	5.0
b1*	0.212	0.212	0.212	0.212	0.212	0.212	0.212	0.212
b2*	0.045	0.045	0.045	0.045	0.045	0.045	0.045	0.045
b3*	0.352	0.352	0.352	0.352	0.352	0.352	0.352	0.352
Windowing function: i_{wind} (Hz) (Saragoni-Hart window)	1	1	1	1	1	1	1	1
Slip distribution model: i_{slip}	0	0	0	0	0	0	0	0

a: Papazachos, 2004; b: Strasser et al., 2010; c: Blaser et al., 2010; d: Stiros, 2010; *: Distance-dependent duration (s) parameters.

APPENDIX C: Modeling Parameters for Computed Synthetic Earthquakes

Table 5.17: Modeling parameters to simulate intraplate and interface reverse earthquakes in the Hellenic Subduction Zone using the Green's Function approach.

Modeling Parameter	Fault segment							
	HSZ-1	HSZ-2	HSZ-3	HSZ-4	HSZ-5	HSZ-6	HSZ-7	HSZCrete
Stress drop ($\Delta\sigma$) (Pa)	3E06 ^{a,b,c}	3E06 ^{a,b,c}	6E06 ^{a,b,c}	6E06 ^{a,b}	6E06 ^{a,c}	6E06 ^{a,c}	3E06 ^{a,b,c}	6E06 ^{a,c,d}
Seismic moment (N*m)	8.913E20 ^{a,b,c}	1.778E21 ^{a,b,c}	3.162E20 ^{a,c}	1.26E21 ^{a,c}	2.512E21 ^{a,c}	3.548E21 ^{a,c}	1.778E21 ^{a,c}	7.079E21 ^{a,c,d}
Geographic coordinates of fault segment (ref_lat, ref_lon) (deg)	36.600, 22.794 ^{a,b,c}	36.194, 23.116 ^{a,b,c}	35.201, 23.263 ^{a,b,c}	35.201, 23.263 ^{a,c}	35.201, 23.263 ^{a,c}	35.201, 23.263 ^{a,c}	36.596, 22.676 ^{a,c}	34.910, 23.925 ^{a,c,d}
Reference depth (m) (to upper edge of fault)	75000 ^{a,b,c}	80000 ^{a,b,c}	8000 ^{a,b,c}	8000 ^{a,c}	8000 ^{a,c}	8000 ^{a,c}	60000 ^{a,b,c}	6000 ^{a,c,d}
Fault length (m)	143000 ^a 139000 ^b 122000 ^c	184000 ^a 183000 ^b 163000 ^c	98000 ^a 83000 ^b 80000 ^c	162000 ^a 141000 ^b	209000 ^a 188000 ^c	237000 ^a 217000 ^c	184000 ^a 183000 ^b 163000 ^c	305000 ^a 288000 ^c 105000 ^d
Fault width (m)	66000 ^a 78000 ^b 58000 ^c	76000 ^a 91000 ^b 72000 ^c	53000 ^a 44000 ^b 43000 ^c	71000 ^a 65000 ^b	82000 ^a 79000 ^c	88000 ^a 88000 ^c	76000 ^a 91000 ^b 72000 ^c	101000 ^a 108000 ^c 100000 ^d
Fault strike (deg)	346 ^{a,b,c}	346 ^{a,b,c}	312 ^{a,b,c}	312 ^{a,c}	312 ^{a,c}	312 ^{a,c}	346 ^{a,b,c}	292.5 ^{a,c,d}
Fault dip (deg)	45 ^{a,b,c}	45 ^{a,b,c}	25 ^{a,b,c}	25 ^{a,c}	25 ^{a,c}	25 ^{a,c}	45 ^{a,b,c}	40 ^{a,c,d}
Fault rake (deg)	130 ^{a,b,c}	130 ^{a,b,c}	90 ^{a,b,c}	90 ^{a,c}	90 ^{a,c}	90 ^{a,c}	130 ^{a,b,c}	90 ^{a,c,d}
max. extension of composite events subject to Gutenberg-Richter law (lsubmax) (m)	2000 ^{a,b,c}	2000 ^{a,b,c}	2000 ^{a,b,c}	2000 ^{a,c}	2000 ^{a,c}	2000 ^{a,c}	2000 ^{a,b,c}	2000 ^{a,c,d}
max. extension of composite events subject to Gutenberg-Richter law (lsubmin) (m)	1000 ^{a,b,c}	1000 ^{a,b,c}	1000 ^{a,b,c}	1000 ^{a,c}	1000 ^{a,c}	1000 ^{a,c}	1000 ^{a,b,c}	1000 ^{a,c,d}
Hypocenter location from reference point: distance (m) along strike (xstar) and along dip (ystart)	5107,62700 ^a 4965,74100 ^b 4357,55100 ^c	178889,70571 ^a 177917,84500 ^b 158472,66857 ^c	4650,33125 ^a 4150,27500 ^b 4000,26875 ^c	5786,65083 ^{a,c} 5036,59583 ^{a,c}	5225,76875 ^a 4700,74063 ^c	231075,77000 ^a 212660,77000 ^c	178588,72200 ^a 172235,86450 ^b 158206,68400 ^c	289750,88375 ^a 273600,94500 ^c 102375,97500 ^d
Moment distribution option (mdis)	0 ^{a,b,c}	0 ^{a,b,c}	0 ^{a,b,c}	0 ^{a,c}	0 ^{a,b,c}	0 ^{a,b,c}	0 ^{a,b,c}	0 ^{a,c,d}
Discretization step (m) (dstep)	5000 ^a 3000 ^{b,c}	2000 ^{a,b,c}	3000 ^{a,b,c}	4000 ^{a,c}	5000 ^{a,c}	6000 ^a 5000 ^c	4000 ^{a,b} 2000 ^c	5000 ^{a,c} 3000 ^d
No. of fault segments	1							
High-cut frequency (Hz)	20							
max. fluctuations strike (deg) (dstmax)	5							
max. fluctuations dip (deg) (ddimax)	5							
max. fluctuations rake (deg) (dramax)	10							
Rupture time (s) begin of the segment (tstart)	0.0							
Rupture velocity (m/s)	2680							
Selection (1/0) for geographical coordinate system	1							
If 1: x = latitude, y = longitude (deg)	37.620, 22.770							
Selection for irregular positions (= 0) or a 1D profile (= 1) or a rectangular 2D observation array (= 2): ixy	0							
Number of positions (n)	2							
Latitude/Longitude (deg) of observation point(s): (i.e., Tiryns and Midea)	(37.600, 22.799), (37.649, 22.841)							
Selection for inputting the soft cover parameters: 0 = uniform soft cover for all locations, 1 = via listing, 2 = via an external data file, others (3 for this study) = no site effect	3							
a: Papazachos, 2004; b: Strasser et al., 2010; c: Blaser et al., 2010; d: Stiros, 2010								

APPENDIX D: Shear-Wave (v_s) Velocity Models

This appendix contains all the site-specific 1D shear-wave velocity models used in all modeling sites.

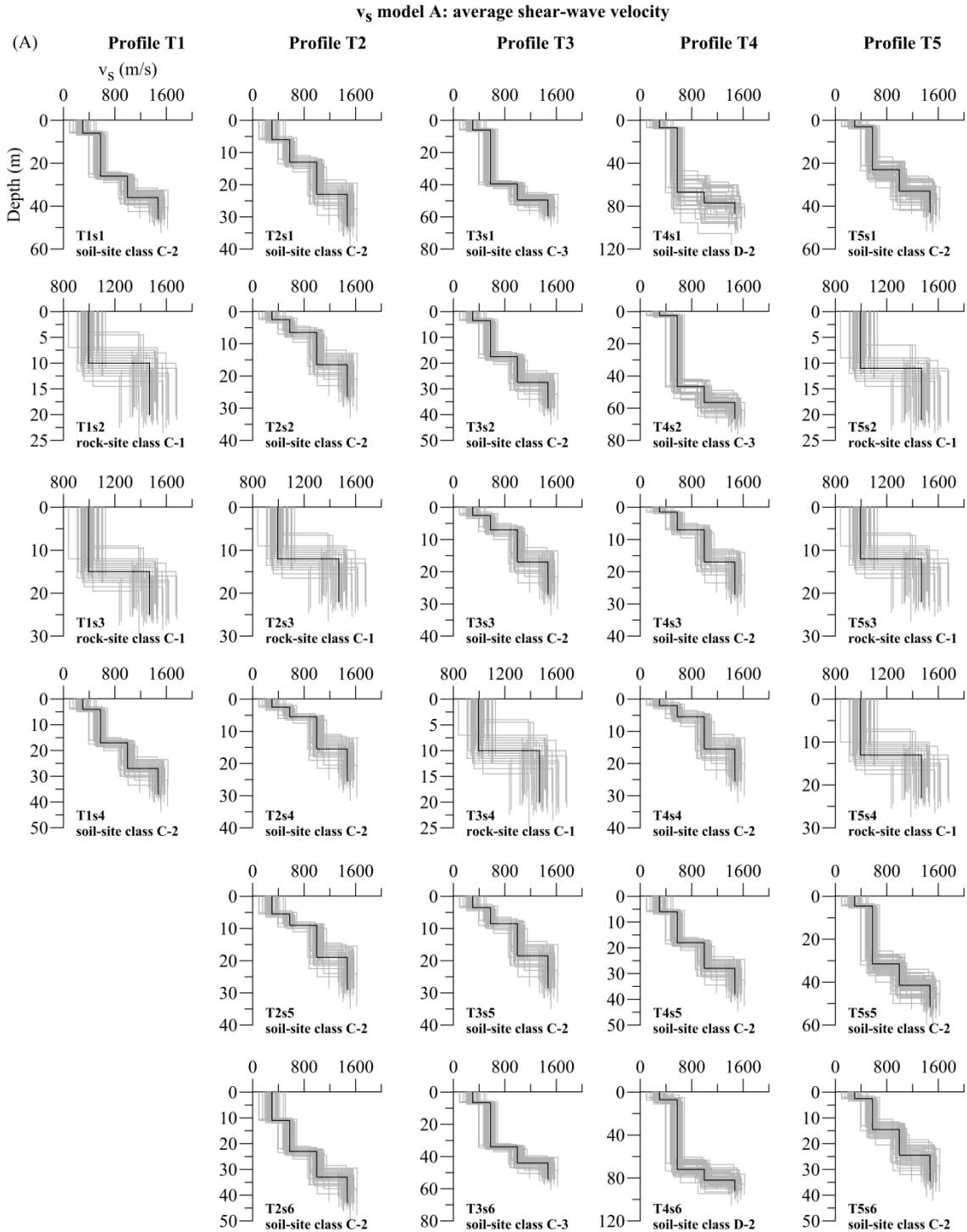


Figure D1: Adopted 1D v_s -depth models of all modeling sites at Mycenaean Tiryns arranged by profile. (A) Average Base Model (v_s model A, black line) and accompanying 50 randomly generated v_s models (gray line). (B) Gradient Base Model (v_s model B, green line) and accompanying 50 randomly generated v_s models (light blue line). Bottom label indicates modeling site (see Figure 6.2 for location) and identified seismic site class.

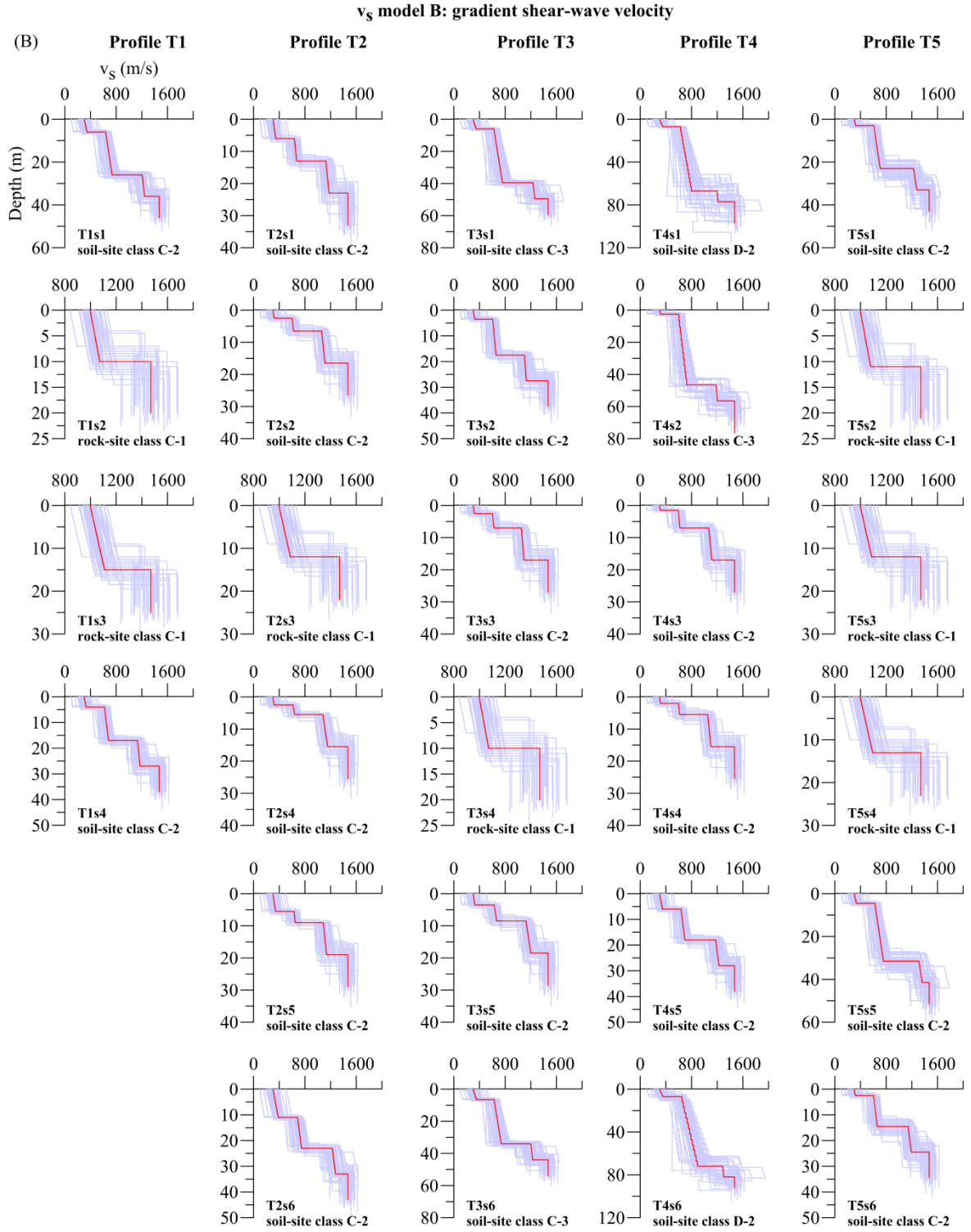


Figure D1: *Continued.*

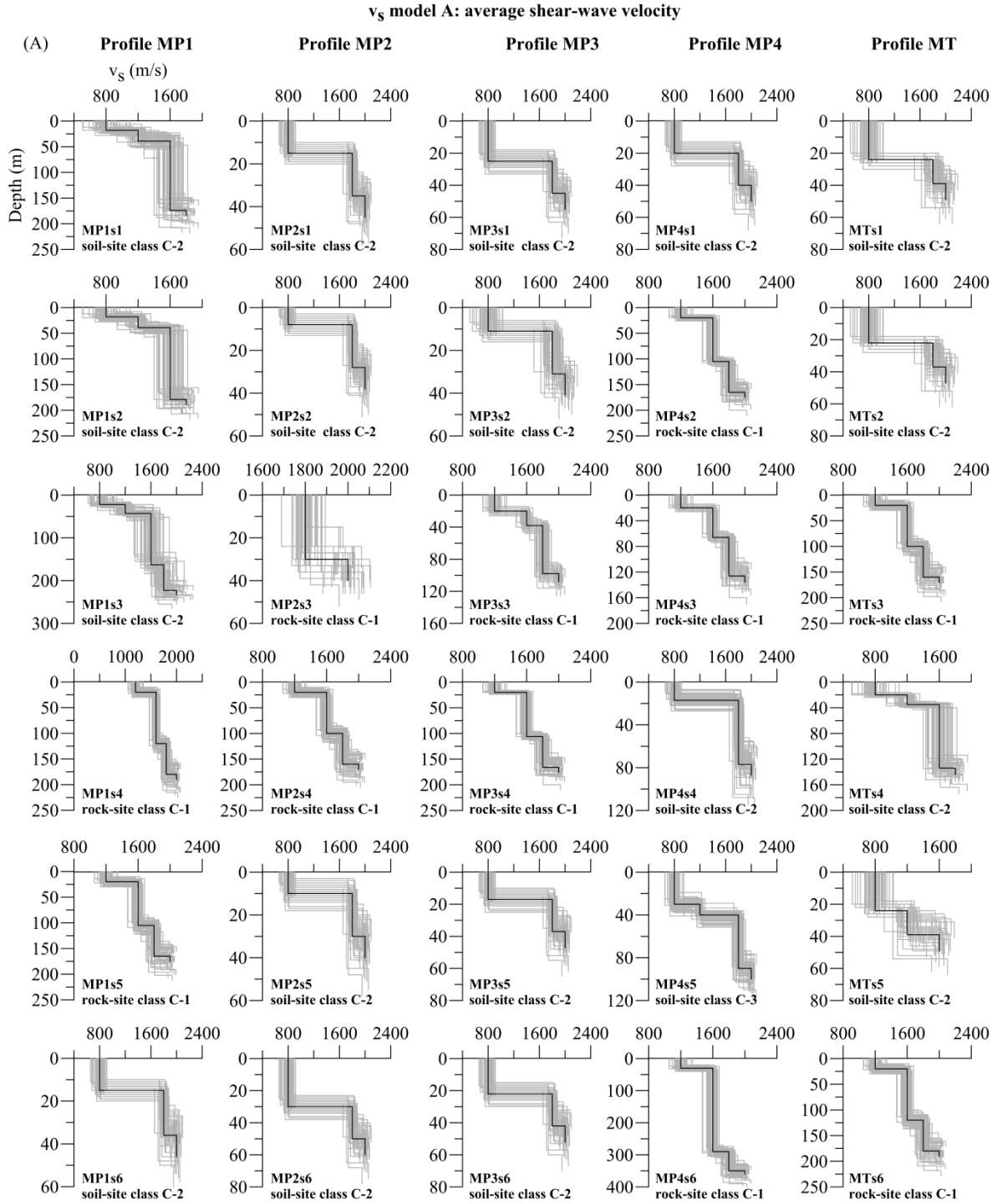


Figure D2: Adopted 1D v_s -depth models of all modeling sites at Mycenaean Midea arranged by profile. (A) Average Base Model (v_s model A, black line) and accompanying 50 randomly generated v_s models (gray line). (B) Gradient Base Model (v_s model B, green line) and accompanying 50 randomly generated v_s models (light blue line). Bottom label indicates modeling site (see Figure 6.3 for location) and identified seismic site class.

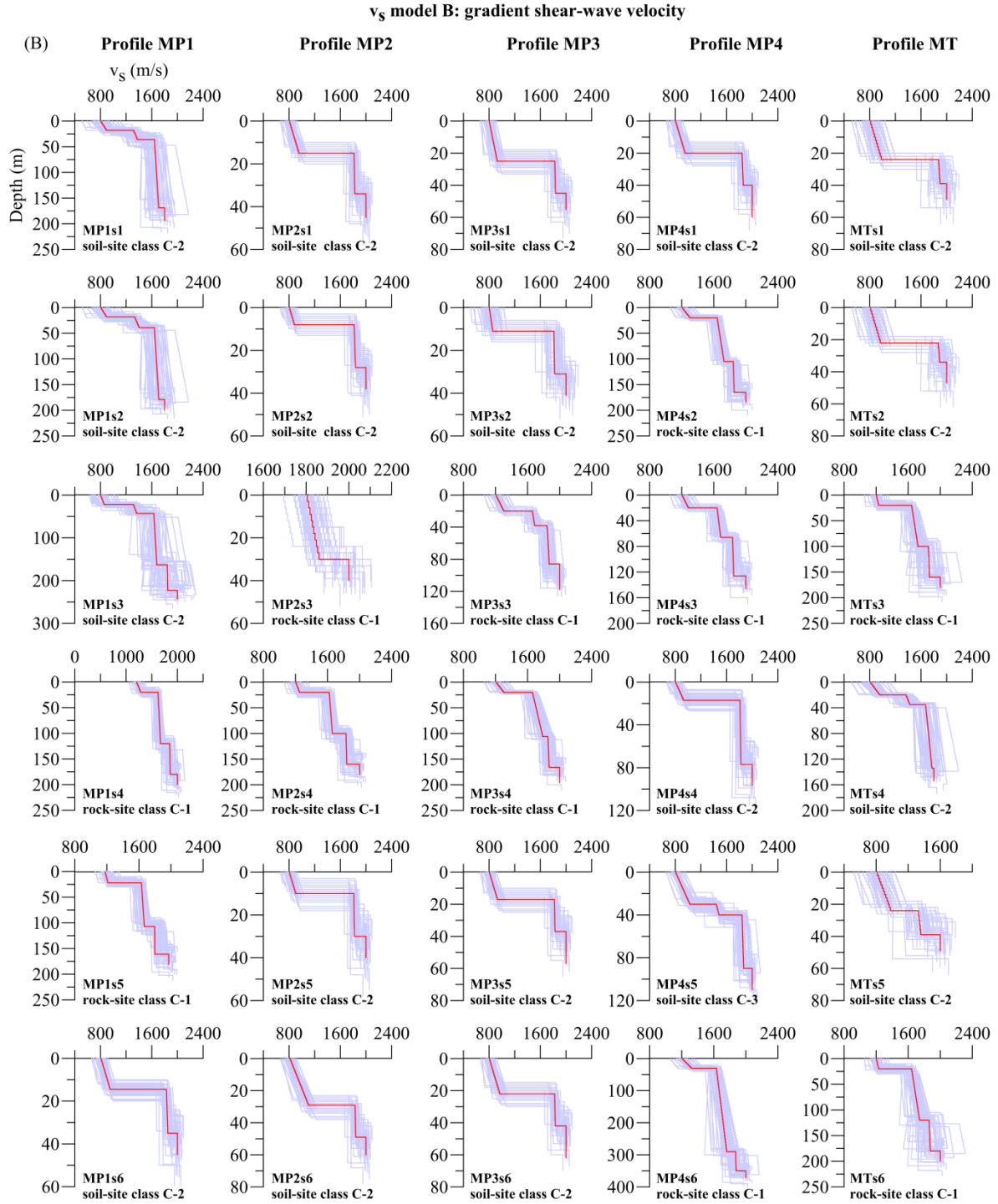


Figure D2: Continued.

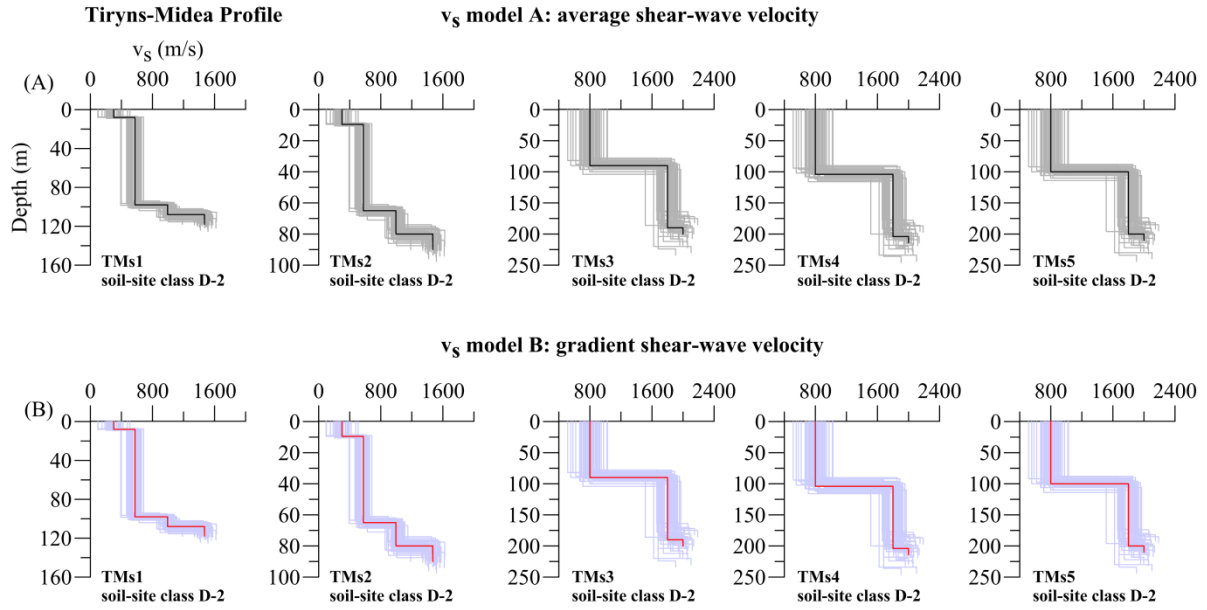


Figure D3: Adopted 1D v_s -depth models of all modeling sites along the Tiryns-Midea profile. (A) Average Base Model (v_s model A, black line) and accompanying 50 randomly generated v_s models (gray line). (B) Gradient Base Model (v_s model B, green line) and accompanying 50 randomly generated v_s models (light blue line). Bottom label indicates modeling site (see Figure 6.4 for location) and identified seismic site class.

APPENDIX E: Site Class Categories and Example of Amplification Factors

This appendix provides the identified seismic site class category of all modeling sites; one example profile for Tiryns, Midea, and the area between them showing the computed amplification factors produced by all seismogenic sources; and the surface geology and geophysical site classification schemes.

Table E6.2: Geotechnical seismic site class categories of all soil- and-rock sites following the seismic site classification scheme of Rodríguez-Marek et al. (2001) (see Figures 6.2 to 6.4 for location of modeling sites).

Modeling site	Geotechnical Site Classification
<i>Tiryns</i>	
T1s2, T1s3, T2s3, T3s4, T5s2, T5s3, T5s4	rock-site class C-1 (weathered/soft rock)
T1s1, T1s4, T2s1, T2s2, T2s4, T2s5, T2s6, T3s2, T3s3, T3s5, T4s3, T4s4, T4s5, T5s1, T5s5, and T5s6	soil-site class C-2 (shallow stiff soil)
T3s1, T3s6, and T4s2	soil-site class C-3 (intermediate depth stiff soil)
T4s1 and T4s6	soil-site class D-2 (deep stiff Pleistocene soil)
<i>Midea</i>	
MP1s4, MP1s5, MP2s3, MP2s4, MP3s3, MP3s4, MP4s2, MP4s3, MP4s6, MTs6, and MTs3	rock-site class C-1 (weathered/soft rock)
MP1s1, MP1s2, MP1s3, MP1s6, MP2s1, MP2s2, MP2s5, MP2s6, MP3s1, MP3s2, MP3s5, MP3s6, MP4s1, MP4s4, MTs1, MTs2, MTs4, and MTs5	soil-site class C-2 (shallow stiff soil)
MP4s5	soil-site class C-3 (intermediate depth stiff soil)
<i>Tiryns-Midea profile</i>	
TMs1, TMs2, TMs3, TMs4, and TMs5	soil-site class D-2 (deep stiff Pleistocene soil)

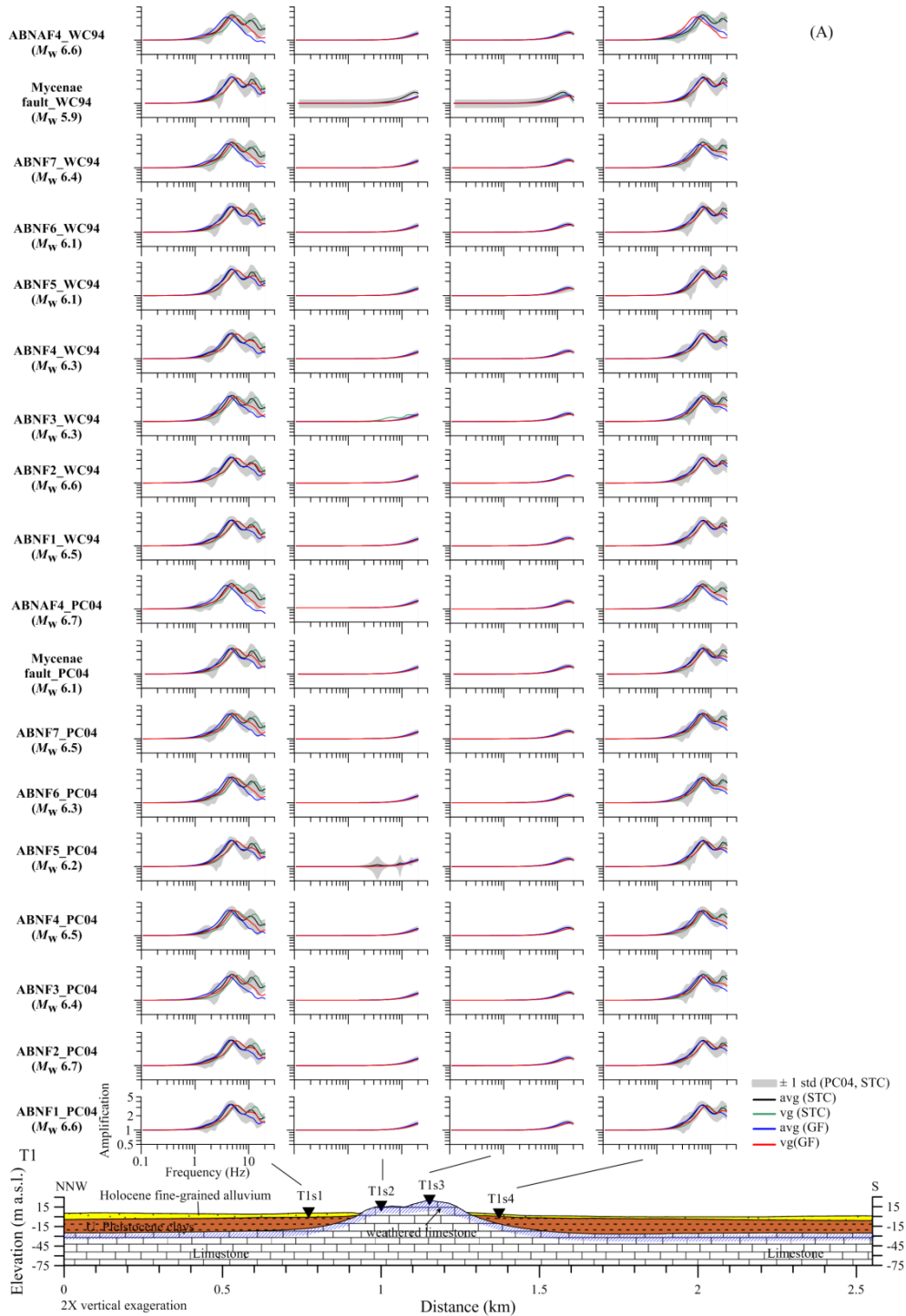


Figure E1: Examples of site-specific amplification response functions of soil- and-rock sites along profile T1 traversing the Tiryns hill and surrounding soils. The label (left-hand side) in each row indicates the input seismic source (A-E): fault segment with related earthquake M_w were calculated using the empirical equations of Pavlides and Caputo (2004) [PC04], Wells and Coppersmith (1994) [WC94], Papazachos (2004) [P04], Strasser et al. (2010) [Str10], and Blaser et al. (2010) [B10]. Results from fault segments corresponding to normal faults in the (A) Argive Basin and (B) Patras–Corinth Continental Rift, (C) strike-slip faults in the Iria–Epidaurus Sinistral Transform fault system, (D) interface and intraplate reverse faults in the Hellenic Subduction Zone, and (E) analytic signal. 1 std: ± 1 standard deviation; avg: average v_s model; vg: v_s gradient model; S10: Stiros (2010); N/A: Not Available (see discussion); STC: Stochastic method; GF: Green’s Function method.

Appendix E: Site Class Categories and Example of Amplification Factors

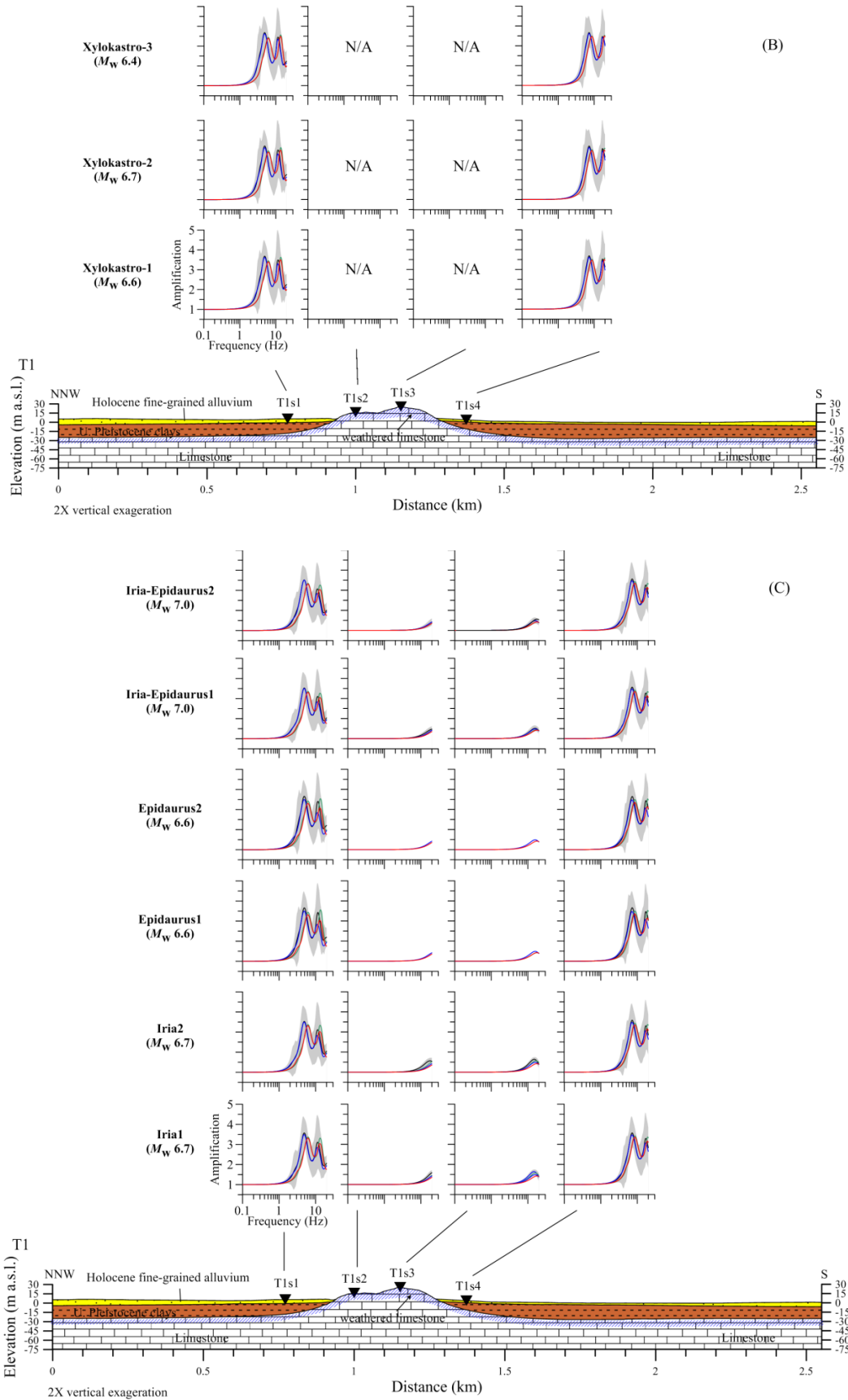


Figure E1: Continued.

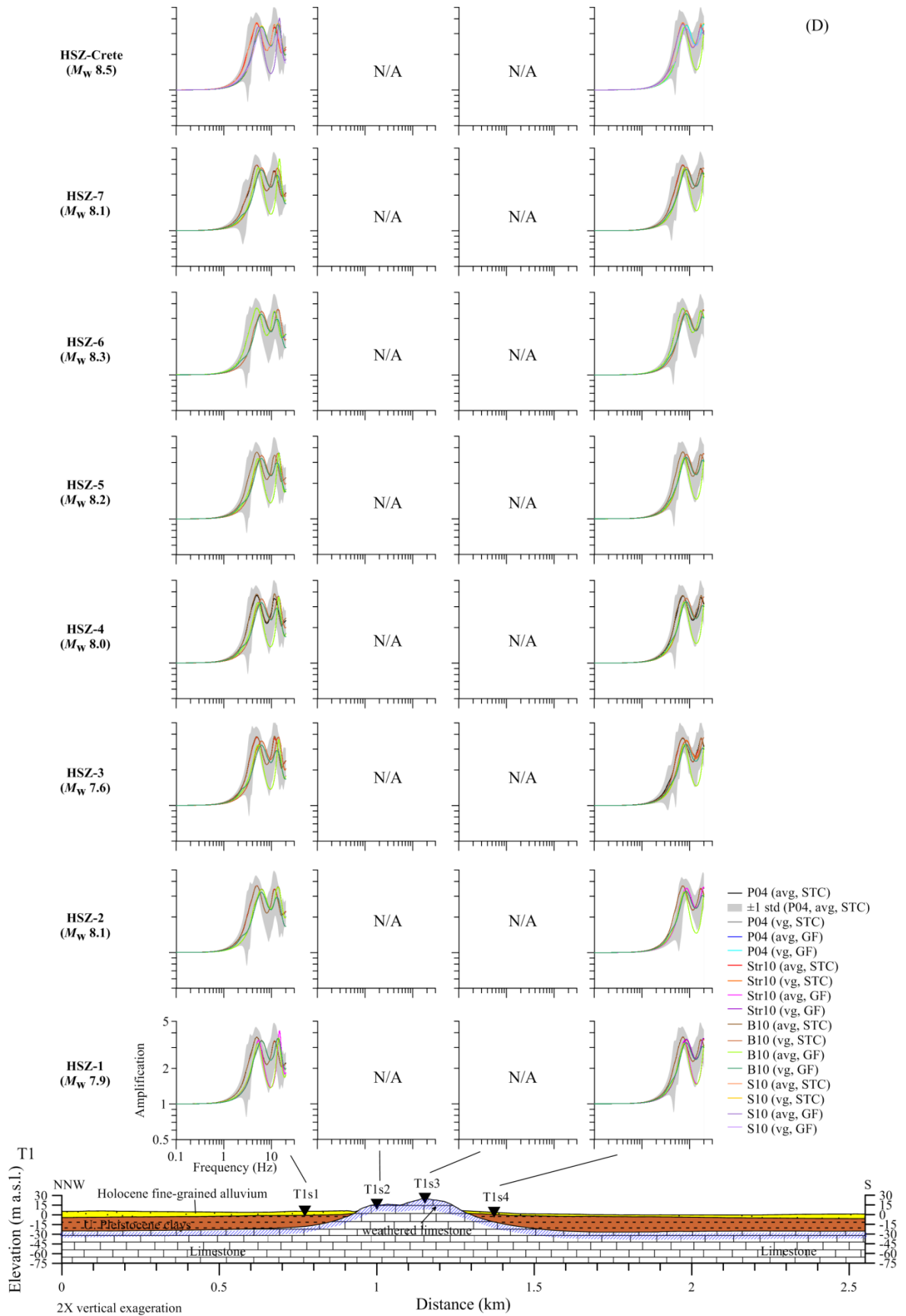


Figure E1: Continued.

Appendix E: Site Class Categories and Example of Amplification Factors

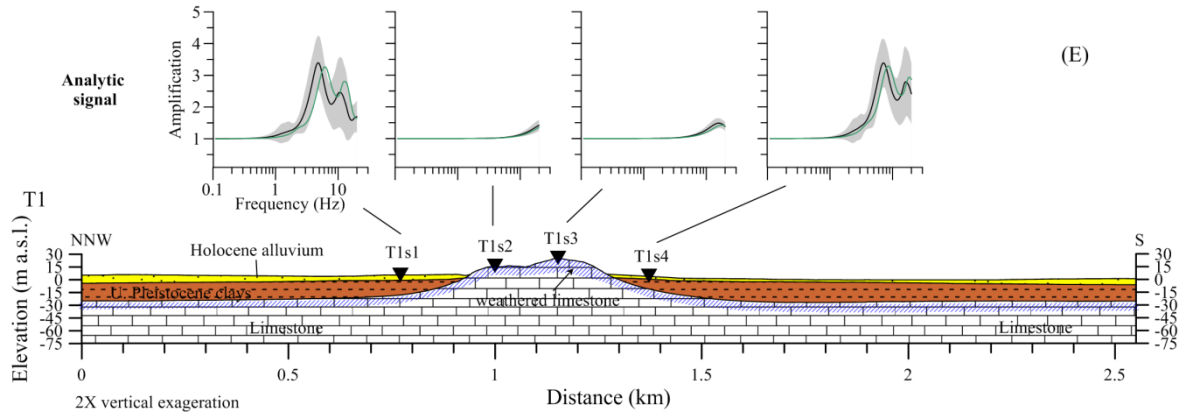


Figure E1: Continued.

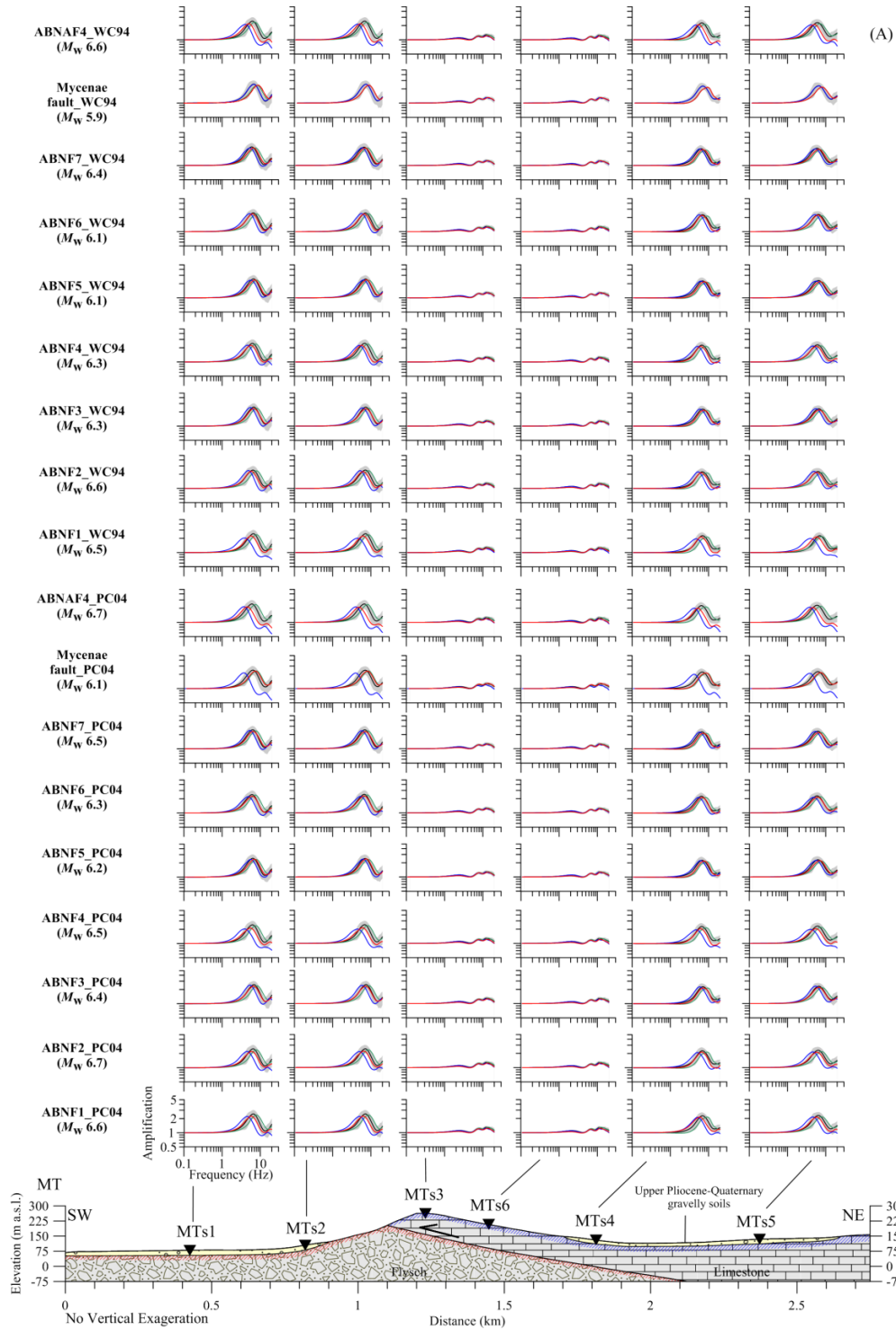


Figure E2: Examples of site-specific amplification response functions of soil-and-rock sites along profile MT traversing the Midea hill and surrounding soils. The label (left-hand side) in each row indicates the input seismic source (A-E): fault segment with related earthquake M_w were calculated using the empirical equations of Pavlides and Caputo (2004) [PC04], Wells and Coppersmith (1994) [WC94], Papazachos (2004) [P04], Strasser et al. (2010) [Str10], and Blaser et al. (2010) [B10]. Results from fault segments corresponding to normal faults in the Argive Basin (A) and Patras–Corinth Continental Rift (B), strike-slip faults in the Iria–Epidaurus Sinistral Transform fault system (C), interface and intraplate reverse faults in the Hellenic Subduction Zone (D), and analytic signal (E). Description of symbols same as in Figure E1.

Appendix E: Site Class Categories and Example of Amplification Factors

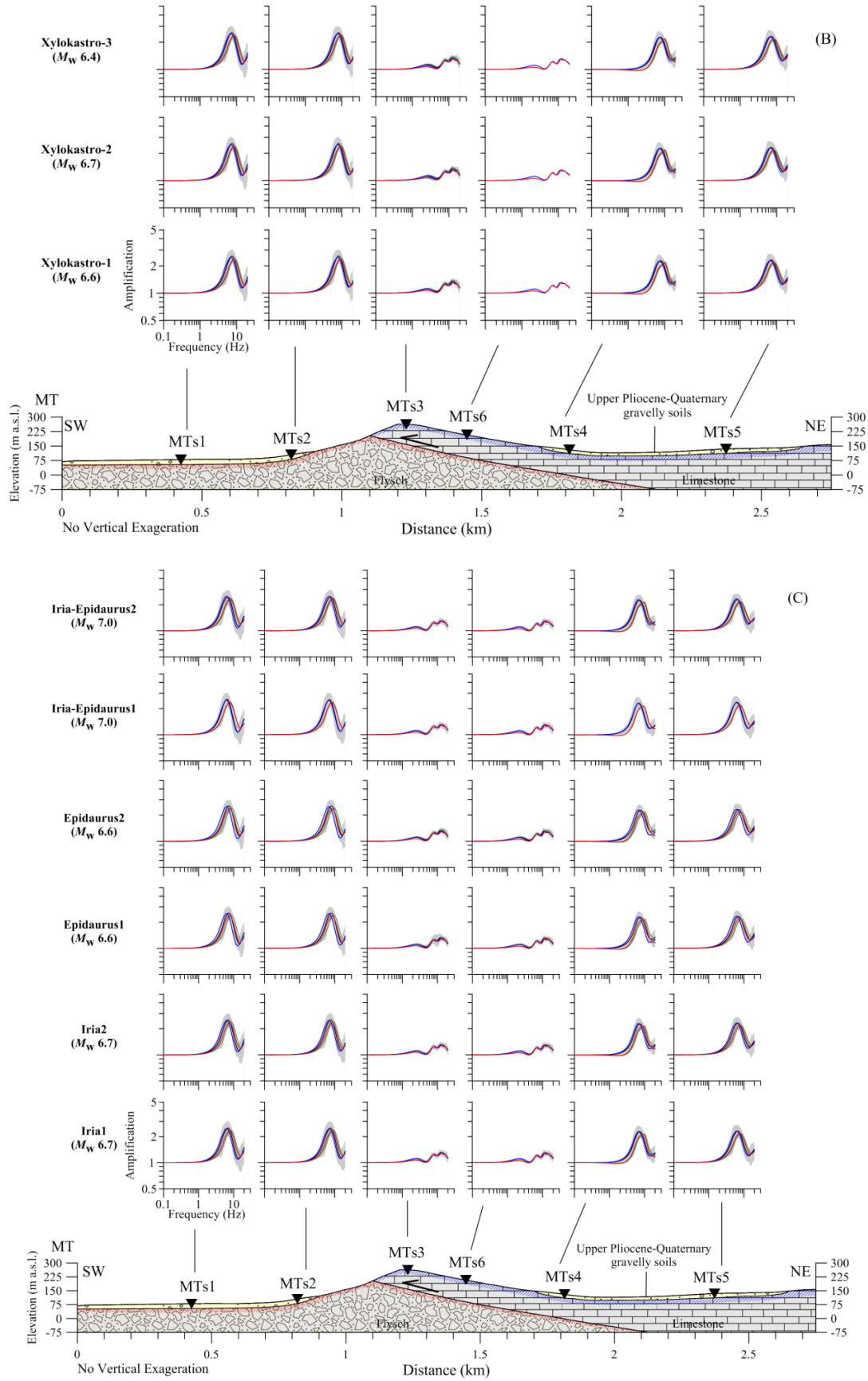


Figure E2: Continued.

Appendix E: Site Class Categories and Example of Amplification Factors

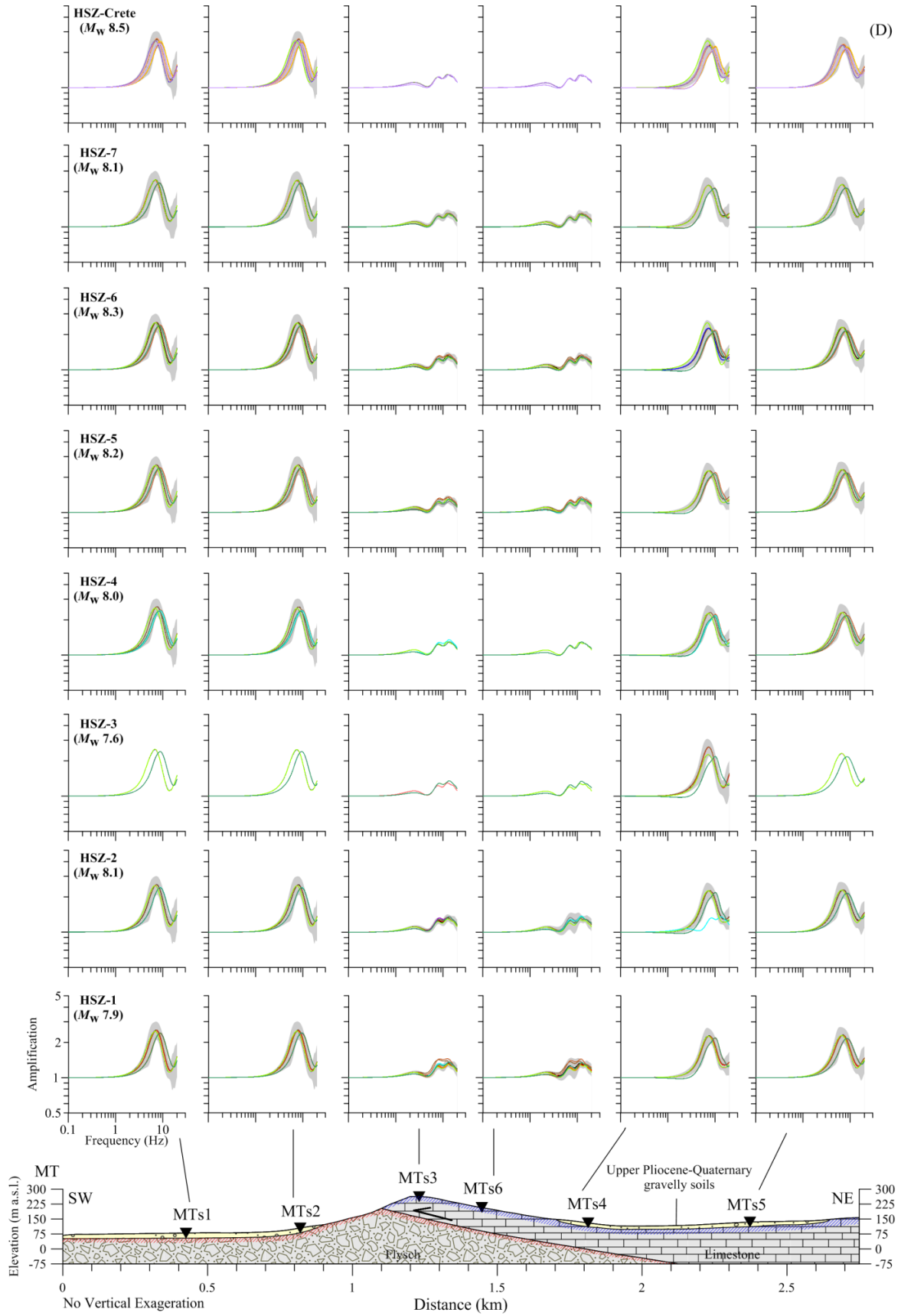


Figure E2: Continued.

Appendix E: Site Class Categories and Example of Amplification Factors

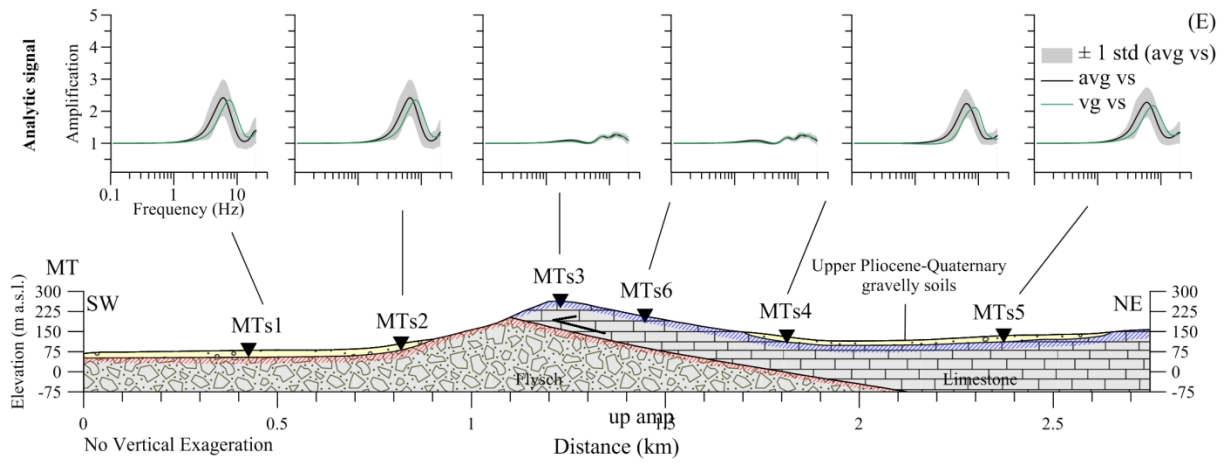


Figure E2: Continued.

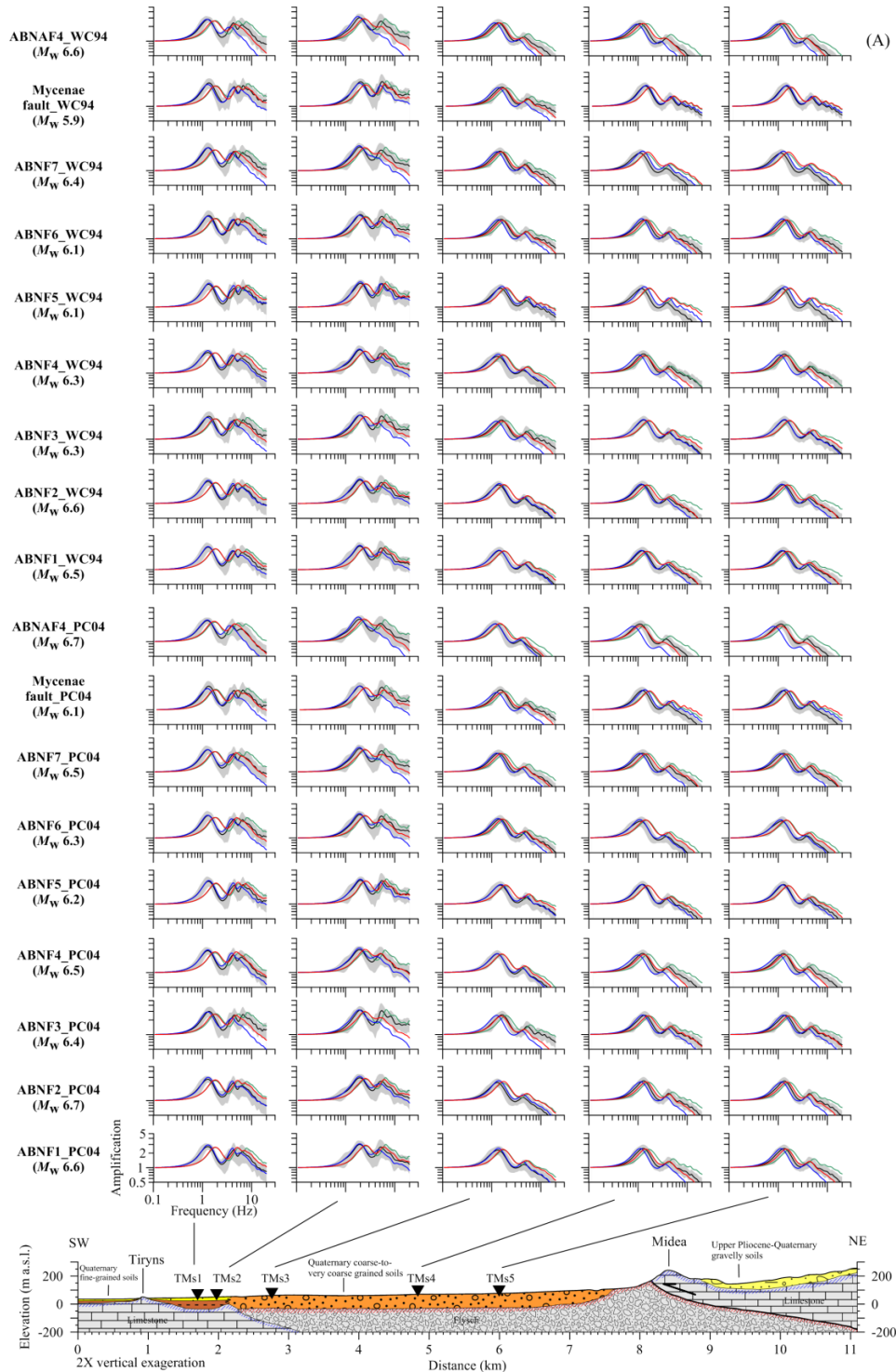


Figure E3: Examples of site-specific amplification response functions of soil- and rock sites along the Tiryns-Midea profile traversing the Quaternary soils between the archaeological Tiryns and Midea hills. The label (left-hand side) in each row indicates the input seismic source (A-E): fault segment with related earthquake M_w were calculated using the empirical equations of Pavlides and Caputo (2004) [PC04], Wells and Coppersmith (1994) [WC94], Papazachos (2004) [P04], Strasser et al. (2010) [Str10], and Blaser et al. (2010) [B10]. Results from fault segments corresponding to (A) normal faults in the Argive Basin and (B) Patras–Corinth Continental Rift, (C) strike-slip faults in the Iria–Epidauros Sinistral Transform fault system, (D) interface and intraplate reverse faults in the Hellenic Subduction Zone, and (E) analytic signal. Description of symbols same as in Figure E1.

Appendix E: Site Class Categories and Example of Amplification Factors

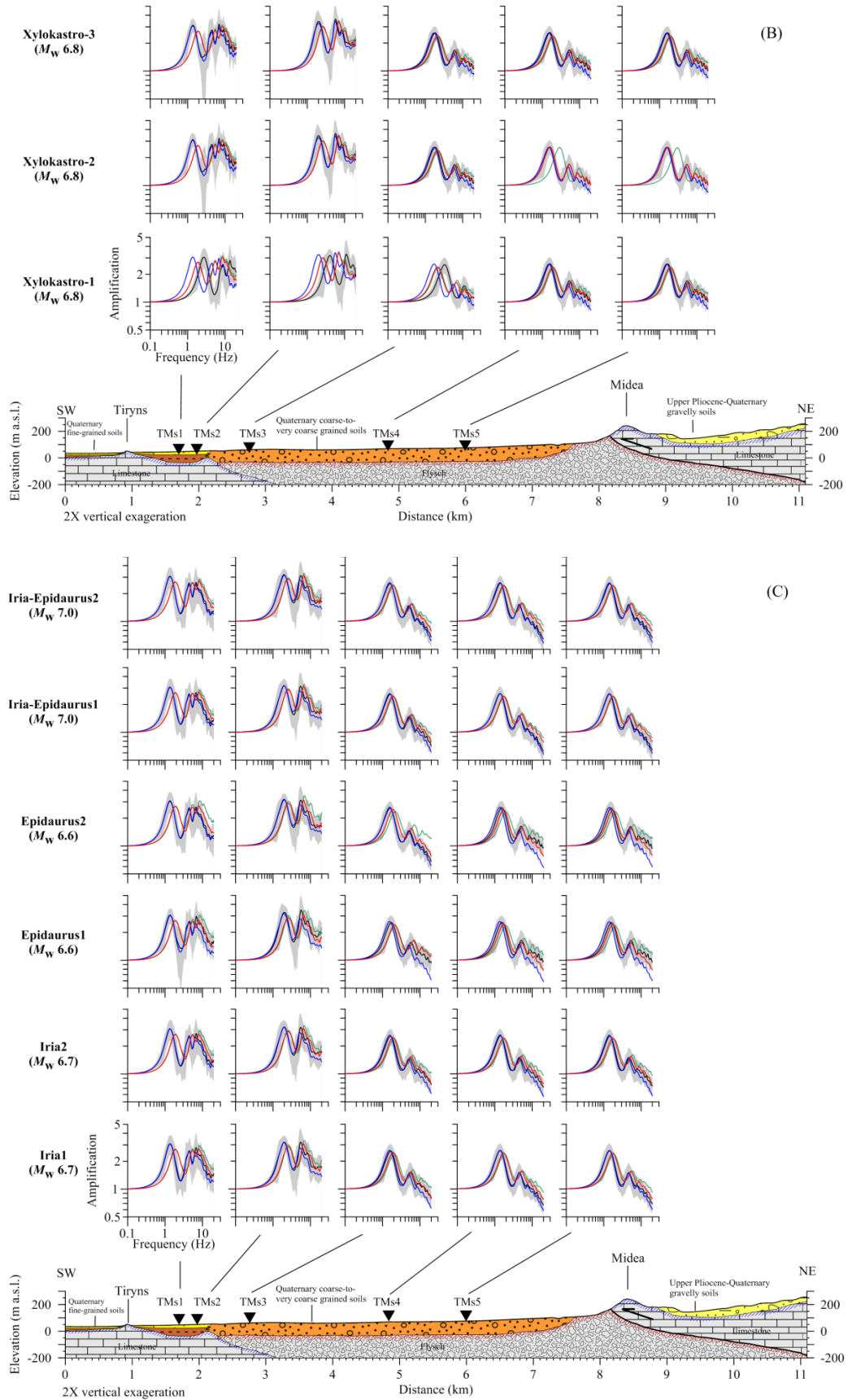


Figure E3: Continued.

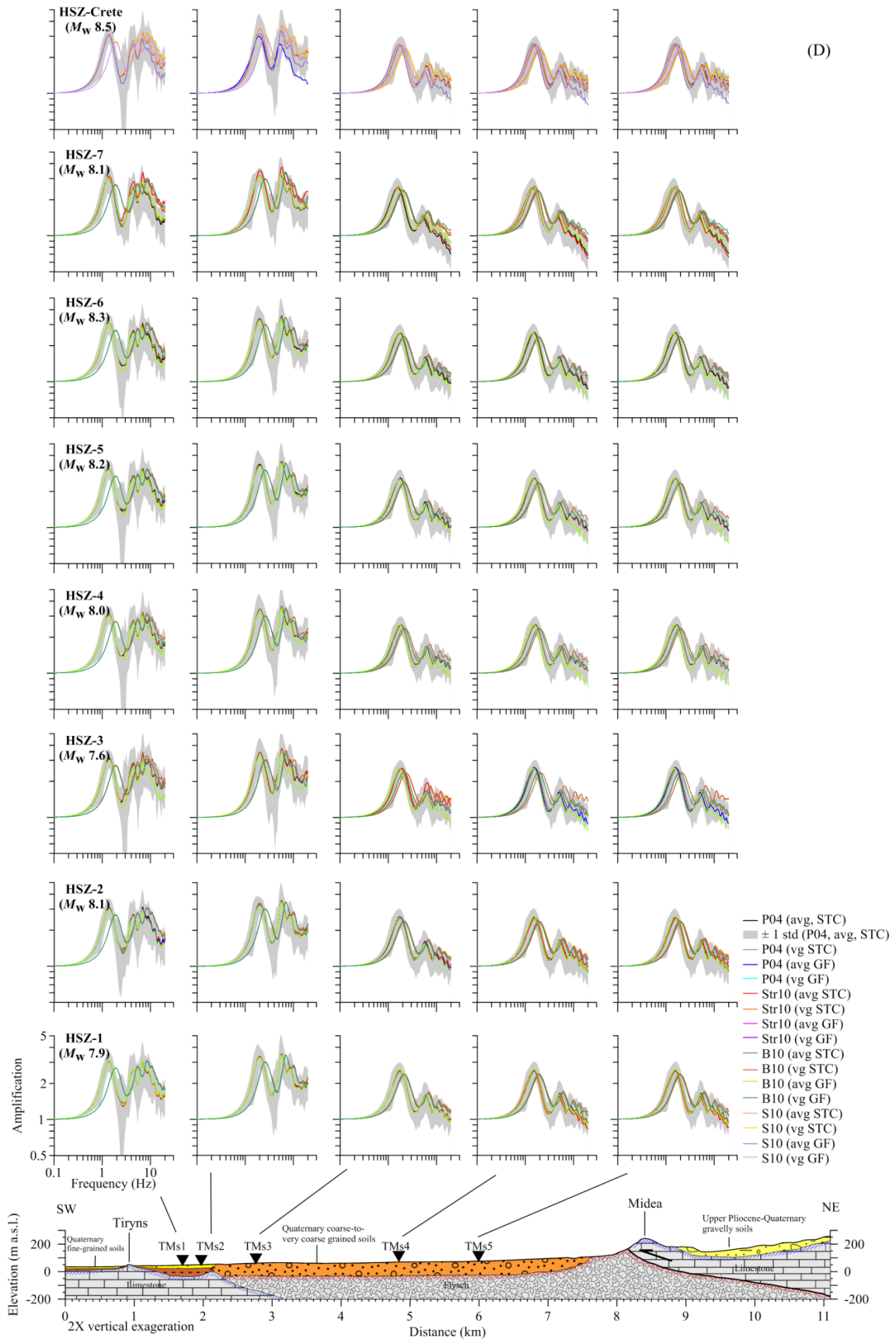


Figure E3: Continued.

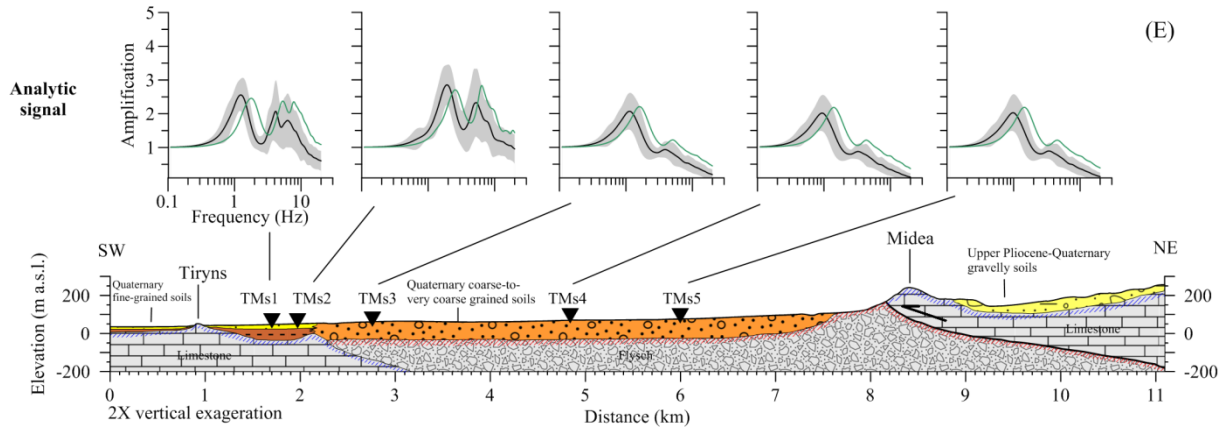


Figure E3: Continued.

Table E7.1: Criteria for Surface Geology seismic site classification scheme (Stewart et al., 2003).

Age	Depositional Environment	Sediment Texture
Holocene	Holocene alluvium	Holocene Coarse
	Pleistocene alluvium	Pleistocene Coarse
Pleistocene	Holocene lacustrine/marine	Holocene Fine-Mixed
	Pleistocene lacustrine/marine	Pleistocene Fine-Mixed
	Aeolian	-
	Artificial fill	-
Tertiary	-	-
Mesozoic and Igneous	-	-

Table E7.2: Criteria for geophysical (v_s^{30} -based) seismic site classification scheme adopted by the 1997 Uniform Building Code (UBC) and the 2003 National Earthquake Hazard Reduction Program (NEHRP) Provisions (NEHRP, 2003; Stewart et al., 2003).

NEHRP Category	Description	Mean v_s^{30}
A	Hard Rock	> 1500 m/s
B	Firm to hard rock	760–1500 m/s
C	Dense soil, soft rock	360–760 m/s
D	Stiff soil	180–360 m/s
E	Soft clays	< 180 m/s
F	Soils that require special study (e.g., liquefiable soils, sensitive clays, organic soils, soft clays > 36-m thick)	

Erklärung

Ich versichere, dass ich die von mir vorgelegte Dissertation selbständig angefertigt, die benutzten Quellen und Hilfsmittel vollständig angegeben und die Stellen der Arbeit - einschließlich Tabellen, Karten und Abbildungen-, die anderen Werken im Wortlaut oder dem Sinn nach entnommen sind, in jedem Einzelfall als Entlehnung kenntlich gemacht habe; dass diese Dissertation noch keiner anderen Fakultät oder Universität zur Prüfung vorgelegen hat; dass sie - abgesehen von der unten angegebenen Teilpublikation - noch nicht veröffentlicht worden ist, sowie, dass ich eine solche Veröffentlichung vor Abschluss des Promotionsverfahrens nicht vornehmen werde.

Die Bestimmungen der Promotionsordnung sind mir bekannt. Die von mir vorgelegte Dissertation ist von Prof. Dr. Klaus-G. Hinzen betreut worden.

Bensberg, 14.10.2015

(Hector R. Hinojosa Prieto)

Teilpublikationen

Hinojosa-Prieto, H.R., and Hinzen, K.-G. (2015). Seismic velocity model and near-surface geology at Mycenaean Tiryns, Argive Basin, Peloponnese, Greece. *Near Surface Geophysics*. 13 (2), 103-113. doi: 10.3997/1873-0604.2015002.

Lebenslauf

Persönliche Daten

Name: Hector Roberto Hinojosa Prieto

Geburtsdatum: 06.11.1979

Nationalität: U.S.A und Mexiko

Anschrift: Tengstraße 20, 80798 München

E-mail: hhinojos@uni-koeln.de

Universitätsstudium

08.2001 – 12.2003 Bachelor in Geosciences,
Studien an der University of Arizona, USA

04.2004 – 05.2006 Master in Geological Sciences
Masterstudium an der Ohio University, USA

08.2007 – 05.2009 Master in Geological Sciences
Masterstudium an der Miami University of Ohio, USA

Promotionsstudium

seit 08.2014 Prüfungsfach: Geologie und Paläontologie
Mathematisch-Naturwissenschaftliche Fakultät,
Universität zu Köln,
Betreuer: Prof. Dr. Klaus-G. Hinzen,
Institut für Geologie und Mineralogie,
Mathematisch-Naturwissenschaftliche Fakultät
Universität zu Köln, Köln, Deutschland